Exciting tin-oxo cages: light-induced chemistry for nanopatterning

Jarich Haitjema

Exciting tin-oxo cages: light-induced chemistry for nanopatterning

Cover design by Tanja van der Heide

ISBN: 978-94-6380-814-9

Full color version of the thesis and the electronic supplementary information are available at http://dare.uva.nl/en

Printed by: ProefschriftMaken

Exciting tin-oxo cages: light-induced chemistry for nanopatterning

ACADEMISCH PROEFSCHRIFT
ter verkrijging van de graad van doctor
aan de Universiteit van Amsterdam
op gezag van de rector magnificus
prof. dr. ir. K.I.J. Maex
ten overstaan van een door het College voor Promoties ingestelde commissie,
in het openbaar te verdedigen
op woensdag 3 juni 2020, te 12:00 uur

door Jarich Haitjema

geboren te Delft

Promotiecommissie:

Promotor:
prof. dr. A.M. Brouwer — Universiteit van Amsterdam

Copromotor:
dr. S. Castellanos Ortega — Advanced Research Center for Nanolithography

Overige leden:
prof. dr. C.J. Elsevier — Universiteit van Amsterdam
prof. dr. A. Meijerink — Universiteit Utrecht
dr. A. Petrignani — Universiteit van Amsterdam
dr. T.A. Schlathölter — Rijksuniversiteit Groningen
prof. dr. P. Swiderek — Universität Bremen
prof. dr. S. Woutersen — Universiteit van Amsterdam

Faculteit der Natuurwetenschappen, Wiskunde en Informatica
Van 't Hoff Institute for Molecular Sciences
Advanced Research Center for Nanolithography (ARCNL)

The research described in this thesis was carried out at the Advanced Research Center for Nanolithography (ARCNL), a public-private partnership of University of Amsterdam (UvA), the VU university Amsterdam (VU), the Netherlands Organization for Scientific Research (NWO) and the semiconductor equipment manufacturer ASML.

Contents

1 Introduction **1**
- 1.1 General introduction . . . 1
- 1.2 Photolithography . . . 3
  - 1.2.1 EUV lithography . . . 5
- 1.3 EUV photoresists . . . 6
- 1.4 Metal-containing resists . . . 9
- 1.5 Tin-containing resists . . . 11
- 1.6 Absorption and absorptivity: definitions . . . 12
- 1.7 Aims and outline of this thesis . . . 13

2 Extreme-ultraviolet patterning of tin-oxo cages **15**
- 2.1 Introduction . . . 16
- 2.2 Experimental . . . 17
  - 2.2.1 Materials . . . 17
  - 2.2.2 Preparation of thin films . . . 17
  - 2.2.3 EUV exposure . . . 17
  - 2.2.4 Post-exposure analysis . . . 18
- 2.3 Results and discussion . . . 18
  - 2.3.1 Open-frame experiments: contrast curves . . . 18
  - 2.3.2 Interference lithography experiments: patterning . . . 23
- 2.4 Conclusion . . . 25
- 2.5 Acknowledgments . . . 26

3 Photochemistry of tin-oxo cages in solution **27**
- 3.1 Introduction . . . 28
- 3.2 Experimental . . . 30
  - 3.2.1 Synthesis . . . 30
  - 3.2.2 UV/Vis spectroscopy . . . 30
  - 3.2.3 NMR spectroscopy . . . 30

3.2.4 DUV exposures . . . 32
3.2.5 Freeze-thaw technique and distillation . . . 32
3.3 Results and discussion . . . 33
3.3.1 UV/Vis spectroscopy . . . 33
3.3.2 NMR spectroscopy on unexposed material . . . 38
3.3.3 Evans method: NMR spectroscopy and spin trapping . . . 41
3.3.4 DUV exposure and product analysis by NMR . . . 45
3.4 Conclusion . . . 61
3.5 Acknowledgments . . . 62

4 UV and VUV-induced fragmentation of tin-oxo cage ions 63
4.1 Introduction . . . 64
4.2 Experimental . . . 65
4.2.1 Sample preparation and measurements . . . 65
4.2.2 Data analysis . . . 66
4.3 Results and discussion . . . 67
4.3.1 Mass spectrum (without photons) . . . 67
4.3.2 UV and VUV irradiation on tin-oxo cage dications . . . 68
4.3.3 UV and VUV irradiation on tin-oxo cage monocations . . . 73
4.4 Conclusion . . . 77
4.5 Acknowledgments . . . 77

5 Soft X-ray fragmentation of tin-oxo cage ions 79
5.1 Introduction . . . 80
5.2 Experimental . . . 81
5.3 Results and discussion . . . 82
5.3.1 Photofragmentation at 91 eV . . . 82
5.3.2 Near edge X-ray absorption fine structure (NEXAFS) . . . 86
5.3.3 Photon energy dependence of mass spectra . . . 89
5.4 Conclusion . . . 93
5.5 Acknowledgments . . . 94

6 Scanning transmission X-ray microscopy on tin-oxo cage films 95
6.1 Introduction . . . 96
6.2 Experimental . . . 98
6.2.1 Synthesis . . . 98
6.2.2 Sample preparation . . . 99
6.2.3 Exposure . . . 99
6.2.4 AFM measurements . . . 100
6.2.5 STXM measurements . . . 100
6.3 Results and discussion . . . 101
6.3.1 AFM measurements . . . 101
6.3.2 Carbon K-edge spectra . . . 103
6.3.3 Elemental composition . . . 111
6.4 Conclusion . . . 124

References **125**

Summary **145**

Samenvatting **149**

Publication list **153**

List of acronyms **155**

Acknowledgments **159**

CHAPTER 1

Introduction

1.1 General introduction

This thesis is about tin-oxo cage materials that can function as photoresists for Extreme Ultraviolet photolithography. In the photolithography process, which is an essential step in the fabrication of integrated circuits or microchips, the photoresist allows to "print" very small structural features.

Microelectronic devices have changed our lives drastically over the past decades. Mobile phones, personal computers, laptops and tablets have become commonplace. This would not have been possible without the invention of the transistor (see Fig 1.1) and its dramatic decrease in size, which enabled billions of them to fit on a small plate: the microchip. Transistors are used as logic gates within the microchips, performing calculations through Boolean logic. It is difficult to imagine a world without microchips; all electronic devices with some level of complexity make use of them.

A precursor to the transistor is the vacuum tube. A first model was invented in 1905 by John Ambrose Fleming.[1] This vacuum tube has about the size of a light bulb and contains a cathode and an anode. The cathode is heated, causing ejection of electrons by thermionic emission. Electrons can thus flow from the cathode to the anode, but not the other way around since the anode is not heated. Later, Lee de Forest invented a version in which the electron flow could be controlled by a grid with a tunable voltage: the *audion*.[2,3] In this device, only a small electrical signal is needed to enable a large current flow from cathode to anode, which means that it can function as an amplifier. This is also the working principle of a transistor. Notable early-age computers that used (more sophisticated) vacuum tubes for their calculations were the Colossus (1943) in Great Britain and ENIAC (1946) in the United States. These computers were enormous (weighing several tonnes), needed a large power supply and frequently had failures as a result of the short lifetime of the vacuum tubes.

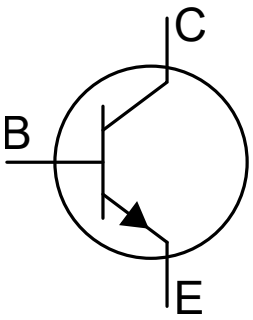

Figure 1.1: Basic layout of a transistor, with a collector (C), a base (B) and an emitter (E). When a small current flows from the base to the emitter, a larger current will flow from the collector to the emitter. Although the used materials are different, the vacuum tube, point contact transistor and MOS-FET have the same working principle.

In 1947, a much smaller and more practical device to perform the function of vacuum tubes was invented by Bardeen and Brattain: the point contact transistor.[5] In this device, a small current from the base to the emitter causes a larger current from the collector to the emitter. The design (see Fig. 1.2b) was significantly smaller and more energy-efficient than a vacuum tube, did not require heating, and had a longer lifetime. Later, their invention was expanded upon by other designs such as the bipolar junction transistor.

In 1959, Atalla and Kahng invented the metal-oxide-semiconductor field-effect transistor (MOS-FET).[7,8] In a MOS-FET, an electric field controls the current flow from source (S) to drain (D), analogous to the collector and emitter in a transistor. Their revolutionary design was very compact, consumed little power, and could be made drastically smaller. This invention enabled the creation of increasingly small integrated circuits.

In 1965, Gordon Moore made the famous prediction:[10]

"The complexity of minimum component costs has increased at a rate of roughly a factor of two per year (...). Certainly over the short term this rate can be expected to continue, if not to increase."

In 1975, Moore revised this to a doubling of components per chip in every *two* years.[11] This became known as Moore's law. Despite frequent predictions of its demise, Moore's prediction has held until the 21st century, although it has slightly slowed down in recent years. It should be noted that Moore's law is not a physical law but a law of economics, driven by the reduced cost of smaller integrated circuits. Additionally, physical limitations start to play a role at very small transistor sizes, such as quantum tunneling.[12]

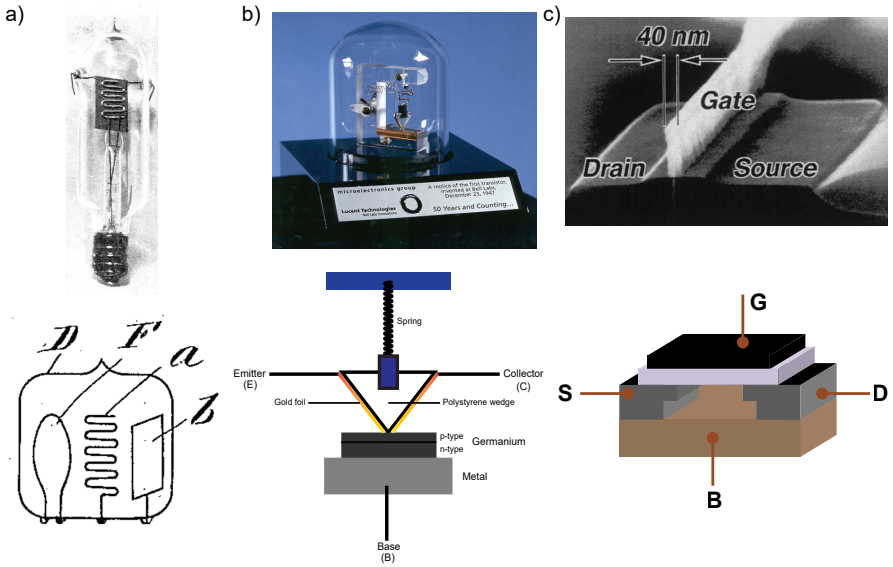

Figure 1.2: (a) Vacuum tube triode or audion,[3,4] (b) point contact transistor,[5,6] and (c) MOSFET.[7,8] On the top, images are shown (for the audion the first prototype, for the point contact transistor a replica of the original, and for the MOS-FET an SEM image)[9]. Schematic structures are shown on the bottom (for the audion, the scheme is reproduced from Ref. 3, the original patent by De Forest).

1.2 Photolithography

Scaling down MOS-FETs was enabled by photolithography. In this technique, a photosensitive film (photoresist) is exposed to a light pattern, changing the solubility of the exposed parts (see Fig. 1.3). This is followed by a development step, during which the substrate is immersed in a solvent or solvent mixture (called "developer"). This either removes the exposed parts (positive-tone resist) or the unexposed parts (negative-tone resist) of the film. The pattern can then be transferred to the underlying oxide layer during an etching step. The parts that are covered with photoresist are protected from etching, while the non-covered parts are etched away. After etching, the photoresist can be removed, leaving behind a pattern in the oxide layer.

In the fast few decades, feature sizes that are written by photolithography have shrunk dramatically. The minimum size (resolution) that can be reached is given by Equation 1.1:[13]

$$CD = k_1 \frac{\lambda}{NA} \tag{1.1}$$

In Eq. 1.1 k_1 is a prefactor, λ is the used wavelength, and NA is the numerical aperture. CD is the critical dimension, which is the minimum feature size that can

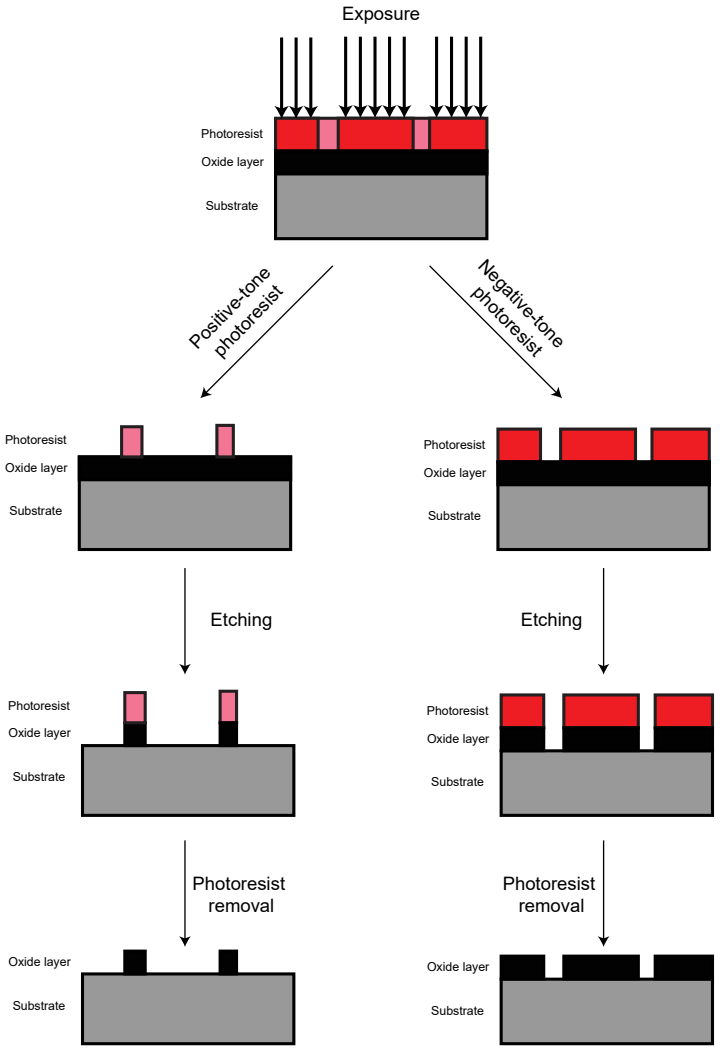

Figure 1.3: Step-by-step lithography process: exposure, development, etching, and photoresist removal. This process can be repeated multiple times.

be obtained. It is desirable to decrease *CD* as much as possible. While decreasing the prefactor k_1 is an option, this is generally difficult to achieve.[14] The numerical aperture cannot be increased much beyond ∼1.4. The largest improvements have been made by decreasing the wavelength of the used light. In the early days of lithography, mercury arc lamps were used that produced well-defined spectral lines: $\lambda = 435.8$ nm ("g-line"), 404.7 nm ("h-line"), and 365.4 ("i-line").[15] In the 1980s, the switch was made to excimer lasers: KrF (emitting at 248 nm) and ArF (193 nm).[16] Decreasing the wavelength further runs into practical difficulties; since air starts to absorb below these wavelengths, the optical system needs to be under vacuum. Although steps were taken towards the use of an F_2 laser (emitting at 157 nm),[17] this turned out not to be cost-effective. Instead, the next development was immersion lithography, in which water instead of air is present between the lens and the wafer. This improves the resolution by enabling an increase in the numerical aperture. The technique was invented in the 1980s and further developed in the 21st century.[18,19]

The resolution limit for immersion lithography at 193 nm is around 36 nm for a single exposure. To improve resolution even further, other methods have to be used, such as EUV lithography, which uses 13.5 nm radiation. Currently, smaller features are produced by multiple-patterning techniques, but EUV lithography, despite all challenges in its development, is more effective.

1.2.1 EUV lithography

In the late 1980s, the first studies were carried out on lithography using soft X-rays.[20–25] This research was performed while optical lithography was still dominating the market, and therefore it took a long time before it was considered industrially relevant. The first pattern with soft X-rays ($\lambda = 11$ nm, close to the EUV wavelength) was written in 1985: an array of 4 μm dots (see Fig. 1.4), written in poly(methyl methacrylate) (PMMA).[20,25] EUV lithography was further developed by ASML, which is currently the only provider of EUV scanners.

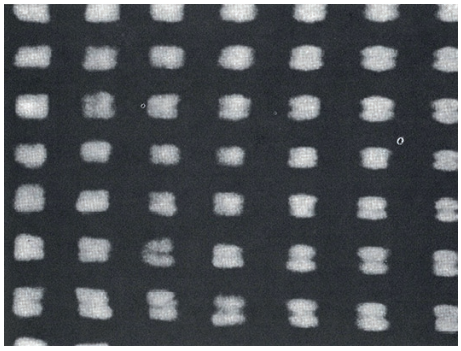

Figure 1.4: Array of 4 μm dots in PMMA, written using soft X-ray lithography in 1985 by Kinoshita and coworkers.[20,25]

EUV lithography is a significant departure from conventional optical lithography, and comes with its own challenges. One major limitation is that projection lenses can no longer be used at these short wavelengths, because no material would be transparent to this radiation and the refractive indices are small. Instead, reflective optics are called for. At that time, multilayer mirrors that can efficiently reflect soft X-rays under normal incidence were not yet available, making the development of a high-throughput tool very difficult.

The exposure wavelength was an important choice, and wavelengths between 4 and 85 nm have been suggested.[26] After continued research, it was found that soft X-rays with an energy of around 13.5 nm could be relatively efficiently reflected by alternating layers of molybdenum and silicon.[27] These multilayer mirrors reflect around 70% of the light. Since typically 11 reflections are required for focusing, this means that a large amount of light is still lost.

EUV radiation cannot be produced by conventional light sources. The industrial method to generate EUV is by using a laser-produced plasma, which features droplets of tin that are irradiated with a very powerful CO_2 laser.[28] The tin droplet is then converted to a plasma, emitting a wide range of wavelengths, among which EUV (13.5 nm).[29] Such light sources are clearly not easy to build and operating them in an industrial setting is expensive as well. Therefore, it is clear that the photons need to be used efficiently.

1.3 EUV photoresists

EUV lithography cannot be performed without a photosensitive film capturing the photons (the photoresist). This film can either become more soluble in a specific developer upon irradiation (positive-tone photoresist) or become less soluble upon irradiation (negative-tone photoresist) (see Fig. 1.3). In either case, the pattern written in the photoresist can be transferred into the underlying layer.

The performance of a photoresist can be described by three important parameters (see Fig. 1.5): resolution, line edge roughness (LER) and sensitivity. **Resolution** describes the minimum feature size that can be obtained. For testing of a resist, a pattern of alternating lines and spaces is often written. The resolution can then be expressed as *half pitch* (HP), half the space between two identical features. **Line edge roughness** or LER describes the average deviation of the printed lines from a perfectly straight line. A too large deviation can lead to printing defects. Lastly, **sensitivity** describes the light dose per unit of area that is required for pattern formation. It is usually expressed in mJ/cm^2. Sensitivity is an important factor since it is directly related to throughput in a lithography machine: the lower the dose needed for an acceptable pattern, the higher the throughput.[30]

An often used mechanism to generate more solubility change per photon (higher sensitivity) is chemical amplification, in which a photon is absorbed by a so-called photoacid generator (PAG) that is irreversibly converted to acid. This acid can chemically react with the side groups of polymer chains in a catalytic process. Since the acid is recovered upon photoreaction, each photon can induce multiple reactions. However,

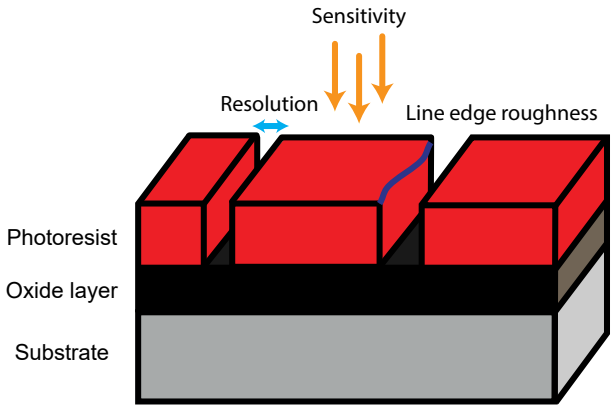

Figure 1.5: Pattern printed in a photoresist by photolithography. Performance of the photoresist is characterized by resolution (minimum feature size), sensitivity (number of photons required to obtain an acceptable pattern), and line edge roughness or LER (deviation of a line edge from a perfectly straight line).

the acids should not diffuse too far from their point of generation, as this leads to undesirable blurring effects. Therefore, quenchers that neutralize the acids are added to the resist formulation to limit blurring. Resist materials that make use of the described amplification mechanism are called chemically amplified resists (CARs), and they have been known since the 1980s.[31]

Like the source and optics, EUV photoresist chemistry implies its own challenges and limitations compared to resist chemistry using deep UV (DUV) light ($\leq$ 248 nm). DUV generates molecular excited states within the material, ultimately leading to the solubility change. EUV has a completely different mechanism of action, with photon absorption leading to ionization, and the ejected (primary) electron producing a cascade of secondary electrons. These secondary electrons then initiate chemical reactions. In addition, the positively charged ions ("holes") that are left behind can also initiate reactions.[32]

Several limitations start to play a role for EUV resists at small(er) dimensions. First, the absorptivity to EUV is usually lower than that to DUV. This is especially the case for organic polymer-based films that are usually employed as photoresists.[33] This means that a relatively thick resist is required to absorb enough photons. This runs into issues during the development step, with the sidewalls sometimes not staying in place as a result of capillary forces. This is known as "pattern collapse".[34,35]

Another major issue is photon stochastics, also known as "shot noise". The *average* light dose per area can be controlled, but the number of received photons per irradiated area of resist film varies. This variation in light dose can be described by a Poisson distribution, with an average light dose and a standard deviation. For a Poisson distribution, the standard deviation scales with the square root of the mean. This means that the higher mean leads to a lower relative variation in the mean. This can

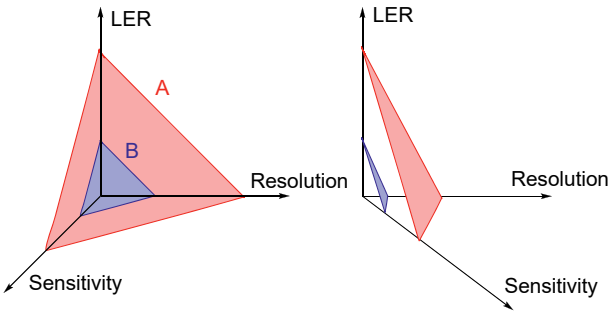

Figure 1.6: RLS triangle, showing the trade-off between LER (Line Edge Roughness), sensitivity and resolution. Typical requirements are: resolution < 16 nm, LER < 2 nm, sensitivity < 10 mJ/cm^2.[36] Adapted from Ref. 37.

be intuitively understood by a simple statistical experiment such as a coin flip: at a large number of throws, the number of heads and tails will be approximately equal, whereas large deviations are possible with only a limited number of throws. The same is the case for light exposure; the larger the dose, the lower the relative variation in the dose.

The change from DUV to EUV has exacerbated the shot noise problem. Since EUV photons are 14.3× more energetic than DUV photons, 14.3× fewer photons are used for the same light dose. This means that the number of EUV photons will vary much more strongly than the number of DUV photons (given the same light dose). The problem also gets worse for smaller feature sizes. A 10×10 nm^2 feature will receive a hundred times more photons than a 1×1 nm^2 feature (at the same light dose in mJ/cm^2).

Photon shot noise directly relates to a well-known problem in photolithography, known as the "RLS trade-off" (see Fig. 1.6). This is the notion that it is not possible to improve one of the resist parameters (resolution, line edge roughness, sensitivity) without simultaneously worsening at least one of the others. This can be understood from the shot noise perspective: a smaller resolution or a higher sensitivity both imply a lower number of photons per feature. This automatically leads to worse stochastics, leading to line edge roughness.

Although the RLS problem is unavoidable on account of photon noise, it is generally believed to be different for photoresists that are composed of different material classes. In Fig. 1.6, it can be seen that material class B has much better specifications than material class A.[37] The performance of a photoresist is also sometimes quantified by the Z-factor, defined by $Z = R^3 \cdot (LER)^2 \cdot S$,[38] in which R is the resolution, LER is the line edge roughness and S is the sensitivity.

The better performance for different material classes can be understood from many different points of view. First, photon *absorption* events are also governed by a statistical distribution,[39], with a stronger absorbing material generally having less photon

absorption noise. Secondly, photon noise is not the only type of noise that occurs within a photoresist material; molecules are also randomly distributed within a material. This can be described as "chemical noise". For example, a CAR has different components (polymer, photoacid, quencher); the concentration of these components also varies locally within a photoresist film. These fluctuations also lead to stochastic effects such as line edge roughness. Especially the quencher was shown to have a large contribution to line edge roughness, as a result of its low concentration within the resist film.[40] Therefore, CARs may not be ideally suited to meet the increasing demands of EUV lithography. A homogeneous material that does not contain photoacids or quenchers, may have much less severe "chemical noise". The low absorptivity of CARs is also detrimental to their sensitivity. Still, creative ways to counter stochastic effects have been proposed, such as the use of photodecomposable quenchers,[41] multi-trigger resists,[42–44] or photosensitized chemical amplification.[45]

1.4 Metal-containing resists

As can be seen in Fig. 1.7, carbon and hydrogen (main elements of PAGs) are relatively poor absorbers of EUV light. An obvious method to increase sensitivity in a photoresist is to increase the absorptivity: if more photons are absorbed, this can (in principle) lead to more chemical reactions per incident photon. One way to increase absorptivity is to incorporate metal atoms, which have large EUV cross sections.

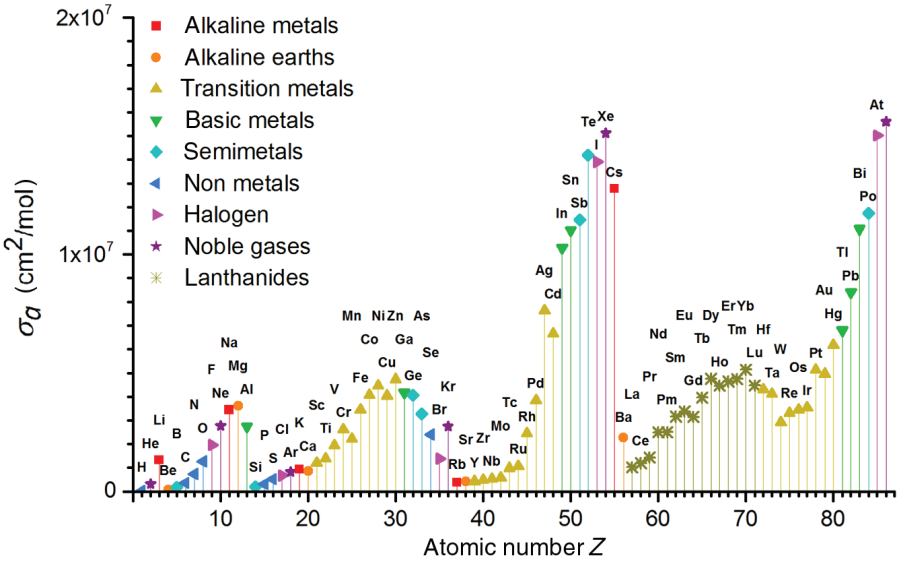

Figure 1.7: EUV absorption cross sections (in cm^2/mol) of all elements up to $Z = 86$. Adapted from ref. 46.

Absorptivity is not the only consideration for incorporation in EUV resist materials. Besides obvious exclusions (noble gases, radioactive elements), some elements are undesirable in a semiconductor manufacturing process. For example, it is known that sodium ions can diffuse through MOS-FETs, leading to threshold voltage instability.[47] For this reason, developer solutions containing sodium ions (NaOH solutions) were replaced with solutions containing non-metallic cations. Another concern is that metal compounds outgas during exposure, causing poorly cleanable contamination on EUV optics.[48] In general, metals to be avoided are alkali metals, alkaline earth metals, and certain transition metals (Au, Ag, Cu, Fe, Pd, Pt, Co, Mn, and Ni).[49]

Chemistry of the elements and their compounds should also be considered. The compound should undergo a photochemical solubility switch upon irradiation. This cannot be achieved for any material. Above all, the solubility switch should be efficient: a higher absorption cross section will not lead to a higher photosensitivity if only a small fraction of absorbed photons leads to the desired solubility switch. These loss mechanisms are an important (and poorly understood) factor.

Over the past years, several methods have been attempted to increase EUV absorptivity of photoresist films. For example, fluorine is a good EUV absorber; fluorinated polymeric compounds can be used that are similar to those that are conventionally employed.[50,51] Doping with other elements such as tellurium has been attempted as well.[52]

Another approach is to use metal oxide nanoparticles that turn insoluble upon illumination. These materials have shown potential for both DUV immersion lithography[53] and EUV lithography.[54–58] Alternatively, such nanoparticles can be used to dope polymer thin films, with the idea that absorption on the nanoparticles eventually also leads to the solubility switch.[59]

Aside from nanoparticles, smaller molecular-sized compounds can be used as well. This has the advantage that the building blocks are smaller and better defined, and the chemical reaction mechanisms are therefore easier to study. It has been shown that various metal-oxo organometallic hybrid compounds can be spin coated onto a substrate.[60–63] Such thin films can be converted into their respective metal oxides, which in itself already has various applications.[64–66]

Recently, researchers have investigated the potential of metal-oxo/organic hybrid materials as photoresists. The idea is that exposure to EUV initiates cross linking within the material, rendering the compounds insoluble. Studies on such resists have mainly focused on zirconium, hafnium and titanium compounds.[67–69] Recently, zinc clusters have shown to be another viable option.[70]

1.5 Tin-containing resists

An interesting element for EUV photoresists is tin, which clearly has high absorptivity (see Fig. 1.7) Another interesting property of tin is that the bond between tin and carbon (Sn–C) is relatively stable, with a bond energy of ∼2.2 eV.[71] This means that general knowledge on organic chemistry can be applied to organotin compounds. This gives rise to a wealth of possibilities, and several books have been written on organotin chemistry.[72–74]

Recently, researchers from Oregon State University studied several organotin compounds for their potential as photoresists.[75–80] Similar materials have also attracted industrial attention. Inpria Corporation is the main player in this field, publishing several patents.[49,81,82]

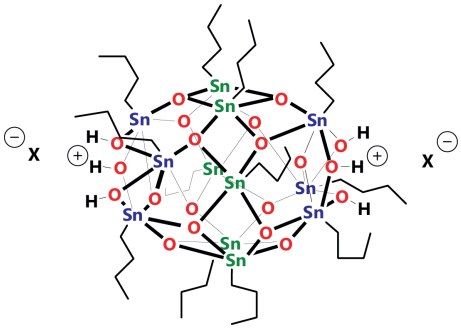

Figure 1.8: The dication $[(BuSn)_{12}O_{14}(OH)_6]^{2+}$, "tin-oxo cage". Green tin atoms are 5-coordinated, blue tin atoms are 6-coordinated. X denotes a counterion, which can be altered to tune the material properties.

Various other tin-containing compounds have been prepared, including smaller tin compounds (Sn_3, Sn_6),[83,84] larger compounds (up to Sn_{34}),[85] and tin compounds containing other elements such as tellurium.[86] It is difficult to evaluate the potential of such compounds as EUV photoresists, since practical limitations (such as formation of homogeneous films and long-term stability) are also very important. It is clear, however, that many options are available in this field of chemistry.

The work described in this thesis concerns one particular tin compound: the tin-oxo cage (see Fig. 1.8), first described in 1989 by Puff and Reuter.[87] Its possible use as an EUV photoresist was described by Cardineau and coworkers in 2014.[88] This tin-oxo cage is small, well-defined, and has promising patterning capabilities as a negative-tone photoresist: it becomes insoluble in organic solvents upon EUV radiation. Both the counterions and side groups attached to the tin atoms can be tuned.[88,89] The mechanism of action behind the solubility switch is not known yet. In general, the mechanism for such materials is thought to be related to aggregation of units into larger networks,[90] but the exact chemical reactions that occur (leading to these networks) are unclear. Elucidating the fundamental photochemistry of the tin-oxo cage is the main aim of this work.

1.6 Absorption and absorptivity: definitions

Throughout this work, light absorption of a photoresist or photoresist material is an important factor. Different definitions are used to quantify how strongly a material absorbs light, and it is important to distinguish between them:

- Absorbance (A): A dimensionless quantitative measure of the absorption of light (of a particular wavelength) by a sample. It is related to the transmittance $T = \frac{I}{I_0}$ (the fraction of incident power I_0 that is transmitted) as $A_{10} = -\log T$ or $A_\mathrm{e} = -\ln T$.[91] In chemistry, A_{10} is used, while in the X-ray community A_e is the standard. Unfortunately, in both communities the same symbol A is used.
- Absorption coefficient (ϵ) in L mol^{-1} cm^{-1} or M^{-1} cm^{-1}: related to A by Beer-Lambert's law: $A_{10} = \epsilon c l$ in which c is the concentration (in mol L^{-1}) and l is the path length (in cm).
- Absorption cross section (σ, sometimes μ) in cm^2 mol^{-1} or cm^2 g^{-1}: defined by either $\sigma = \frac{10^3 \ln 10}{N_\mathrm{A}} \cdot \epsilon$ (N_A is Avogadro's number) or $A_\mathrm{e} = \sigma c l$.
- Linear absorptivity (α) (in m^{-1}): defined by the equation $T = e^{-\alpha d}$ in which d is the layer thickness. This can be rewritten to $\alpha = -\frac{1}{d} \ln T$.
- Attenuation coefficient (in m^{-1}): the distance after which the light intensity has dropped to $1/e$.

1.7 Aims and outline of this thesis

This thesis focuses on tin-oxo cages and their reactions to various types of light, ranging from Ultraviolet to Extreme Ultraviolet to soft X-rays. This is done by several types of experiments.

In **Chapter 2**, we study the lithographic properties of the tin-oxo cage by exposing films to EUV light, obtained at the SLS synchrotron in Switzerland. We confirm the finding of Cardineau and coworkers[88] that spin coated films of tin-oxo cages can be succesfully used as EUV photoresists. In addition, we improve upon earlier work in terms of resolution and sensitivity by using different counterions, and demonstrate that photoresist properties (such as sensitivity and resolution) critically depend on processing conditions, such as post-exposure baking (PEB).

In **Chapter 3**, we investigate reactions of tin-oxo cages to DUV (225 nm) light in a solution, using various NMR techniques for product analysis. Several photoproducts are found, which are produced from initially formed butyl radicals.

In **Chapter 4**, we investigate the DUV ($\lambda = 200 - 300$ nm) and VUV ($\lambda = 35 - 200$ nm) photoreactions of tin-oxo cages that were brought into the gas phase by electrospray ionization, and trapped using a linear ion trap. Monochromatic DUV and VUV light is obtained from a synchrotron (SOLEIL, France) and photoproducts are detected by mass spectrometry. Cleavage of butyl groups occurred upon light absorption, sometimes involving the ejection of an electron (ionization).

In **Chapter 5**, the results of Chapter 4 are expanded upon by exposing trapped tin-oxo cage ions to EUV light (92 eV, 13.5 nm) as well as higher energy photons, up to an energy of 550 eV. This was done at a different synchrotron (BESSY-II, Germany). Two different ion traps were used for this, of which one was cooled to cryogenic temperatures. It was shown that absorption of an EUV or X-ray photon can initiate cleavage of several butyl groups of the tin-oxo cage. Different reactivities were observed with the cooled and non-cooled experiment.

In **Chapter 6**, EUV and DUV-exposed films of tin-oxo cages were studied by Scanning Transmission X-ray Microscopy (STXM) at the SLS synchrotron. Absorption edges of the elements are investigated, and the elemental composition of the films is additionally tracked. The results support the assumption made in other work that tin compounds are not outgassed from the thin films after EUV exposure.

CHAPTER 2

Extreme-ultraviolet patterning of tin-oxo cages*

Abstract

We report on the extreme ultraviolet (EUV) patterning performance of tin-oxo cages. These cage molecules were already known to function as negative tone photoresists for EUV radiation, but in this work we significantly optimized their performance. Our results show that sensitivity and resolution are meaningful photoresist parameters only if the process conditions are optimized. We focus on contrast curves of the materials using large area EUV exposures and patterning of the cages using EUV interference lithography. It is shown that baking steps, such as post-exposure baking, can significantly affect both the sensitivity and contrast in the open-frame experiments as well as the patterning experiments. A layer thickness increase reduced the necessary dose to induce a solubility change but decreased the patterning quality. The patterning experiments were affected by minor changes in processing conditions such as an increased rinsing time. In addition, we show that the anions of the cage can influence the sensitivity and quality of the patterning, probably through their effect on physical properties of the materials.

*This work was published as: J. Haitjema, Y. Zhang, M. Vockenhuber, D. Kazazis, Y. Ekinci, A.M. Brouwer, "Extreme-ultraviolet patterning of tin-oxo cage", *J. Micro/Nanolith. MEMS MOEMS* **16**, 033510 (2017).

2.1 Introduction

Extreme ultraviolet lithography (EUVL) is a powerful technique, which can further improve the resolution of patterning in advanced semiconductor manufacturing. Nevertheless, there are still many challenges to be overcome for the introduction of EUVL into high volume manufacturing. One of these challenges is the photoresist performance. The high energy per photon means fewer photons for the same dose, which exacerbates stochastic noise.[92] This leads to increased line edge roughness and puts limits on the achievable resolution for a given dose. One way to get more chemical conversion per absorbed photon is to use chemical amplification mechanisms such as in acid-sensitive resists.[93] However, the photoacid generators and their quenchers are randomly distributed, causing further stochastic effects.[94] Quenchers, in particular, are known to have a large contribution to stochastic noise, as a result of their low concentration in the photosensitive layer.[40]

For these reasons, it is interesting to search for alternative materials with improved properties, such as metal-containing compounds. These have larger absorption cross sections for EUV photons than organic materials, which contributes to an increase in sensitivity.[95] This may eliminate the need for chemical amplification, removing statistical uncertainties in the position of photoacid generators and quenchers. Metal-containing compounds also have an improved etch resistance compared to conventional chemically amplified resists (CARs).[54,57]

Nanoparticles, introduced by Trikeriotis and coworkers,[54] and organic-inorganic hybrid compounds have demonstrated photoresist performance.[96,97] Since the latter materials are molecular, they are well defined with a single particle size, as opposed to the nanoparticle systems. Tin-oxo cages are the subject of the present work (see Fig. 2.1).[88] The cage has a 2+ charge and is therefore stabilized by one or two counterions.

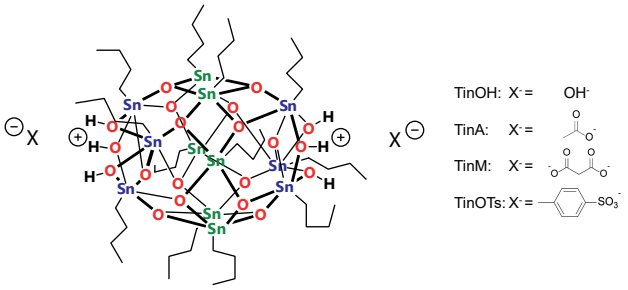

Figure 2.1: Tin-oxo cages with four different anions: hydroxide (TinOH), acetate (TinA), malonate (TinM), and tosylate (TinOTs). For the malonate, the ratio of tin-oxo cages to malonate anions is 1:1

The tin-oxo cage molecules can be regarded as the tin analog of the silicon-containing silsesquioxane class of compounds. Hydrogen silsesquioxane (HSQ) is the most prominent member of this family, and it has been used to achieve high-resolution

patterning with both e-beam and EUV lithography.[98] However, the sensitivity of HSQ is very low, mainly due to the low EUV absorption. EUV absorption can be increased significantly by incorporating metal atoms that strongly absorb EUV light. It is not possible to directly replace silicon with tin in HSQ due to the larger size of the tin atom. However, the tin-oxo cage material is a similar building block with a slightly different shape. The calculated linear absorption coefficient (α) for TinOTs is 13.3 μm^{-1} assuming a density of 1.9 g/cm^3 taken from the crystal structure,[99] and using atomic EUV absorption coefficients reported in the literature.[100] In 2017, the absorption coefficients α for some of the tin-oxo cage materials were measured[46] and found to be in good agreement with the predicted ones.

The absorption coefficient α of organic polymer-based resists is typically $\sim$5 μm^{-1}, whereas tin-based materials from Inpria Corp. show higher absorption coefficients, even up to 20 μm^{-1}.[101] While a large absorption coefficient favors sensitivity, it is not known how efficiently absorbed photons induce a change in solubility of these materials, nor is it known what the maximum achievable efficiency is.

The tin-oxo cage system has the advantage that two properties can be readily altered: the anions at the side of the cage (X^-) and the organic groups (*n*-butyl chains in this case). In this study, we focus on the EUV patterning of some selected materials of this class. The chemical changes upon exposure to short-wavelength UV light are discussed elsewhere.[102,103]

2.2 Experimental

2.2.1 Materials

2.2.2 Preparation of thin films

For a typical thin film of $\sim$40 nm thickness, a solution is made of 15 mg/mL of the tin-oxo cage (with any of the counterions) dissolved in toluene using sonication (30 s). The malonate form did not sufficiently dissolve in toluene and was therefore dissolved in methanol. Particulates were removed by filtering the solutions using a 0.2-µm syringe filter before spin coating. The solutions were spun on Si wafers (for interference lithography) and 2 × 2 cm^2 Si chips (for open-frame experiments) with a spin speed of 2500 rpm for 45 s, with a subsequent soft bake of 30 s at 90 °C. Both wafers and chips were treated with hexamethyldisilazane (HMDS) before spin coating. After exposure, the samples were developed using a 2:1 iPrOH/H_2O mixture for 30 s and rinsed for 10 s.

2.2.3 EUV exposure

EUV exposures were carried out at the XIL-II beamline of the Swiss Light Source (SLS) synchrotron at the Paul Scherrer Institute (PSI) with EUV light at λ = 13.5 nm.[98] For the open-frame experiments, 0.5 × 0.5 mm^2 areas were exposed to EUV light through a square aperture. For the patterning experiments, a transmission mask was used providing line/space patterns with pitches of 100, 80, 60, and 44 nm.

2.2.4 Post-exposure analysis

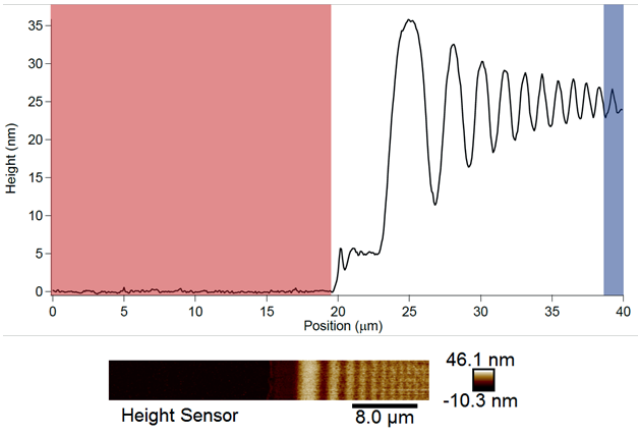

Figure 2.2: AFM image of the material edge (bottom). Image height was corrected using a second-order flattening procedure. The height values of the image were then averaged along the y-axis to produce an edge cross section (top). The average substrate height (red) was compared with the average photoresist height far from the edge (blue).

Atomic force microscopy (AFM) images were made using a Bruker Dimension Icon, using the PeakForce tapping (ScanAsysAir) mode. Perpendicular to the resist edge, fields of 40 × 5 μm^2 were scanned with 128 samples/line, using a scan speed of 0.5 Hz. The raw images were corrected for bowing using first- and second-order corrections, and the film thickness was measured by comparing the height of the film with the height of the substrate, as shown in Fig. 2.2. Scanning electron microscopy (SEM) imaging was performed using a Carl Zeiss SUPRA 55VP SEM with a voltage of 1 kV.

2.3 Results and discussion

2.3.1 Open-frame experiments: contrast curves

Contrast curves (also known as H-D curves or characteristic curves) were obtained by measuring the remaining thickness after development as a function of EUV exposure dose using AFM imaging (see Section 2.2.4).

A typical AFM image of the material edge is shown in Fig. 2.2. Here, the left part of the image is the blank Si substrate, because the unexposed material was removed by the developer. The right part of the image shows exposed and therefore insoluble material. It can be seen that the edge of the profile is partly covered by a wave pattern, caused by interference effects (knife-edge effect). To measure the remaining thickness

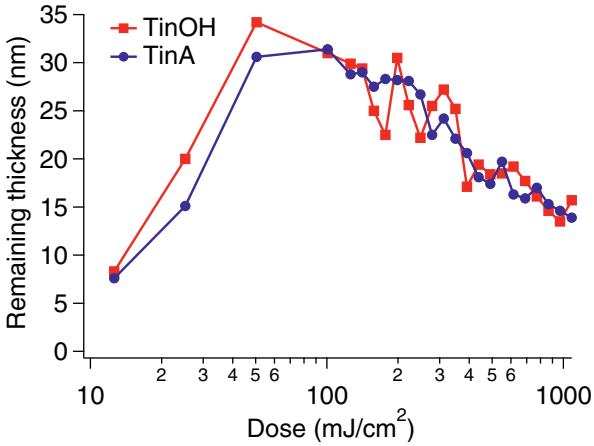

Figure 2.3: Remaining layer thickness after development as a function of EUV dose for TinOH and TinA. Initial thickness was ∼40 nm. No post-exposure baking step (PEB) was applied.

correctly, the height of the resist was measured as far from the edge as possible and averaged over a certain distance window.

Contrast curves were first used to compare compounds with different counterions, TinOH and TinA. The anion of the tin-oxo cage can not only alter the reaction of the material to EUV excitation[88] but also its physical properties such as solubility. For instance, doubly charged anions such as malonate combined with the cage compound render the material more polymeric in nature because the tin-oxo cage can form elongated chains with the doubly charged counterion.[89]

TinOH and TinA were spin coated, followed by a post-application bake (90 °C, to remove residual solvent) and EUV exposure (see Experimental). They did not differ significantly in their performance judging from the contrast curves (Fig. 2.3). The material's response (quantum efficiency and solubility properties) thus appears to be similar when these different counterions are used. We can observe the onset of gelation at ∼10 mJ/cm^2 and a maximum thickness at ∼50 mJ/cm^2. At higher doses, the thickness decreases again. This is likely due to loss of more of the butyl chains, in analogy to the results of deep UV exposures.[102]

In addition to the anion effect, improvements to the process can also alter the contrast curves. In fact, photoresist parameters such as sensitivity and resolution are meaningful concepts only if the process conditions are optimized. Parameters that were optimized were: developer, development time, post-application bake (PAB), and post-exposure bake (PEB). First, the use of a different developer may improve resist performance because of a larger difference in the solubility rates of the exposed and unexposed areas. A few other developers instead of the 2:1 iPrOH/H_2O mixture[88] were tried, such as 2-heptanone.[82] None of them, however, seemed to significantly

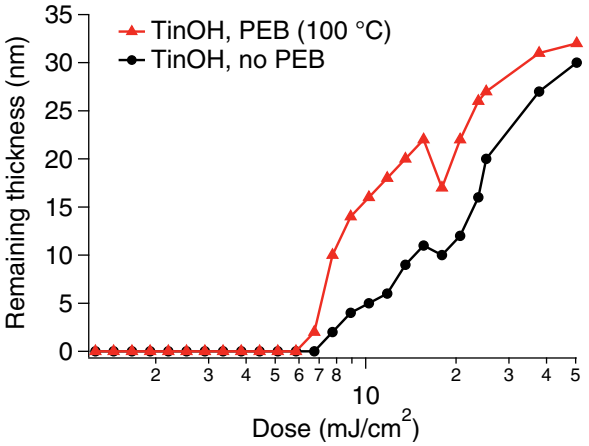

Figure 2.4: Contrast curves of TinOH, measured without PEB (black) and with PEB at 100 °C (red). Initial thickness was ∼40 nm.

improve resist performance. We will therefore only show results obtained with the 2:1 iPrOH/H_2O developer.

Another important processing step is post-exposure baking (PEB). This is well known for CARs: heating the resist after exposure allows diffusion of the photoacids and induces the removal of the dissolution inhibiting protecting groups.[104] For non-CARs, this connection is less clear. Although photoacid diffusion does not apply here, the heating could still induce additional chemical reactions of species that were formed during the exposure step. This is especially the case since EUV exposures take place in vacuum. The photoresist material is baked under ambient atmosphere, enabling reactions of reactive species with oxygen and moisture.

However, the conditions of the PEB should be carefully tuned, since the unexposed material may also change solubility. This can lead to loss of contrast. In the case of a negative tone resist, it is essential that the unexposed part can still be fully cleared by the developer.

The baking effect was studied for two different anions: the hydroxide and the malonate. The malonate form is more polymeric in nature and may, therefore, have a different response to heating. The effect of baking at 100 °C for the hydroxide form is shown in Fig. 2.4.

PEB (100 °C, 2 min) has a significant effect on the sensitivity of the tin-oxo cage material. A lower dose is required to reach the onset of gelation (7 mJ/cm^2 PEB, 8 mJ/cm^2 non-PEB) and to achieve a remaining thickness of 20 nm, the dose needed is 2× smaller. Additionally, the contrast seems to increase as the initial increase of remaining thickness with dose is ∼4× larger for the baked samples. However, we note that the contrast measured in this way can be different from the theoretical contrast, which is defined as the difference in solubility rate between the exposed and

nonexposed parts of the resist.[105] Measuring this more directly, for instance using a quartz crystal microbalance (QCM), would be needed to get an accurate value for the contrast.

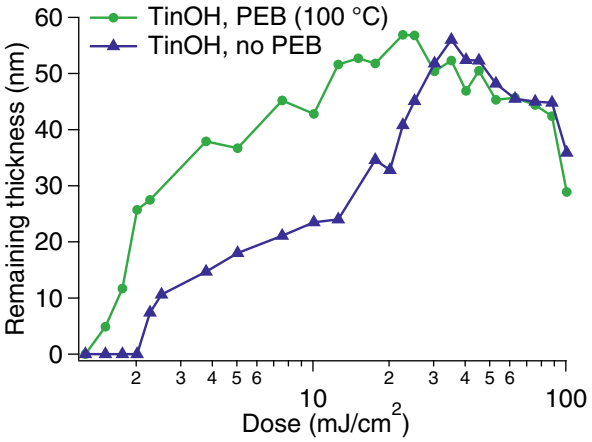

Figure 2.5: The PEB effect for TinOH with a higher initial layer thickness (60 nm).

The effect of baking was also investigated for a layer with higher initial thickness (60 nm instead of 40 nm).The baking effect was consistent there (see Fig. 5.4). However, we also note a large increase in the sensitivity for a thicker layer of TinOH. Only 2 mJ/cm^2 was needed for a reasonable remaining thickness (26 nm). Calculations by others show that a reasonable dose at the bottom is required for this type of materials, in order to make the converted material attach to the substrate.[90] However, these results contradict this. Apparently, converted material attaches easily even if it is not in direct connection with the substrate. A thicker layer leads to a larger amount of converted material, which apparently leads to a higher remaining thickness as well. The effect of resist thickness was investigated for CARs in previous work,[106] which also showed dependence of lithographic performance on layer thickness. For CARs, pattern collapse occurred more often upon increasing layer thickness (25 to 30 nm), though on the other hand, LER decreased. Pattern quality also worsened for the tin-oxo cage material upon increasing layer thickness (results not shown).

The films were also post-exposure baked at two higher temperatures: 120 °C and 150 °C. The unexposed parts of the film became partly insoluble. In the case of 120 °C, the unexposed resist layer was still lower in height than the exposed material, except at very low doses (<5 mJ/cm^2). We suspect that, at these low doses, the shrinkage of the material (caused by outgassing of hydrocarbons) was a larger factor than the solubility change. In the case of a 150 °C PEB, the unexposed layer was barely soluble, leading to a decrease in height of the exposed parts for all used doses (2 to 50 mJ/cm^2). PEB at these higher temperatures is probably not suitable for patterning.

The effect of temperature on the materials was investigated by means of TGA,

with which mass loss as a function of temperature can be measured. This can give additional information about the temperature stability of the unexposed material. A TGA curve of TinOH is shown in Fig. 2.6.

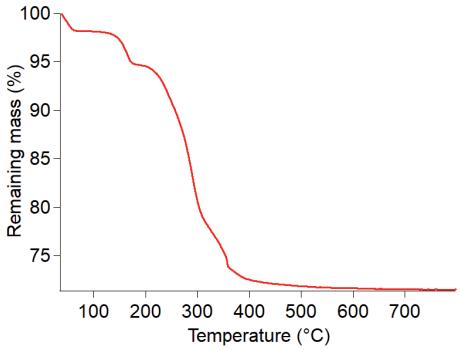

Figure 2.6: TGA analysis for TinOH powder, in an 80%/20% N_2/O_2 atmosphere.

It can be seen that the remaining mass of TinOH first has a slight drop at the onset of the curve (<100 °C). This can be attributed to the loss of some loosely attached iPrOH, the solvent that was used in the conversion step from TinOTs to TinOH (see experimental section). The remaining mass reaches a first plateau around 100 °C, but drops suddenly above 150 °C, at which temperature we observe a change in solubility. Banse et al.[107] reported that the crystal structure of TinOH contains four molecules of iPrOH, but they observed that powders are easily obtained that contain less iPrOH. The weight loss at ∼150 °C could be due to the loss of the most tightly bound solvent. It is also conceivable that water is eliminated, accompanied by deprotonation of the bridging OH-groups. Above ∼200 °C, a gradual loss of ∼22% of the original weight occurs that can be attributed to the loss of organic content (cleavage of the butyl groups). The final remaining mass is 72%, which is close to the theoretical remaining mass of 73% assuming complete conversion to SnO_2. The slightly lower remaining mass can be attributed to the presence of iPrOH or H_2O in the initial sample.

The temperature response can be different for different tin-oxo cage materials. The malonate form (TinM) was also baked at 120 °C. Surprisingly, the non-exposed TinM was still completely soluble even at this temperature. In addition, the sensitivity of the material seems to be high (see Fig. 2.7), although the high initial layer thickness also plays a role. If we compare the results to TinOH (Fig. 2.7), we see that in both cases a higher initial thickness leads to a higher remaining thickness. However, the measured contrast of TinM under these conditions appears to be lower than that of TinOH (PEB at 100 °C, Fig. 5.4), which could explain why the patterning results of TinM were not significantly better.

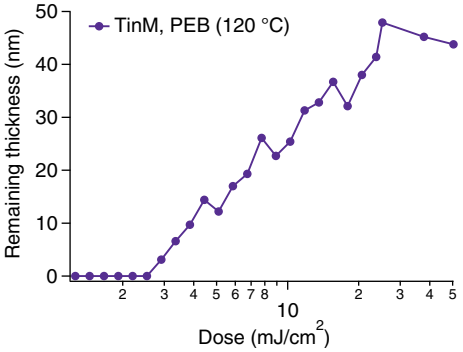

Figure 2.7: Contrast curve of TinM, using a PEB of 120 °C. Initial thickness was ∼50 nm.

2.3.2 Interference lithography experiments: patterning

Line patterns were printed in ∼30 nm thick films of the tin-oxo cage materials using EUV interference lithography. Transmission diffraction gratings on a Si_3N_4 membrane were used (mask) to create mutually coherent beams, which in turn interfere to form the desired interference pattern. In our case, by utilizing two gratings we obtained line/space patterns with half the periodicity of the gratings on the mask.[108] Patterning experiments are important to demonstrate the potential of materials for photoresist applications: a performance is sought with the resolution and sensitivity being as high as possible, and the line edge roughness being minimized.

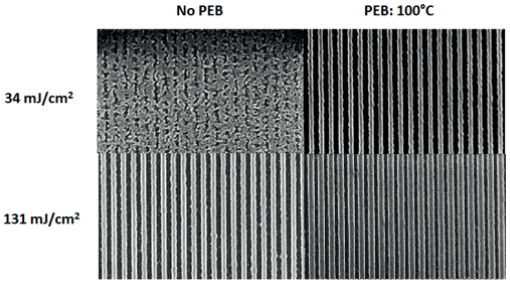

Figure 2.8: The effect of PEB on TinOH measured at two different doses (34 and 131 mJ/cm^2) for 50-nm half-pitch lines.

In Fig. 2.8, the effect of PEB can be seen. The pattern is almost invisible when a dose of 34 mJ/cm^2 is applied without PEB, but clearly present when a post-exposure bake (100 °C, 30 s) is applied before development. In the case of the 131 mJ/cm^2 patterns, the lines increase in width with respect to the spaces. The lines are around 50 nm for the non-PEB sample but increase in width to around 68 nm for the PEB

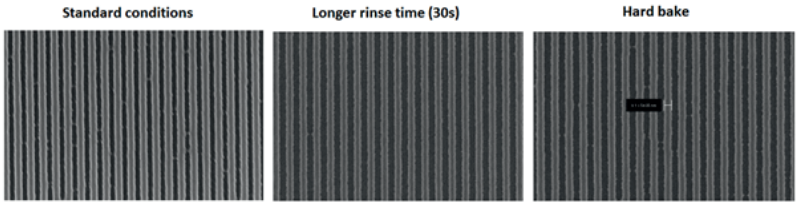

Figure 2.9: Minimization of bridging effect, for TinOH using a dose of 110 mJ/cm^2 on 50-nm HP lines. The regular rinsing time was 10 s. PEB was performed at 100 °C for 2 min for all three patterns. Hardbaking (postdevelopment baking) was performed at 200 °C for 1 min.

sample. This must mean that kinetically stable reaction products are formed during the EUV exposure, which reacts further during the PEB step.

Other parameters that were investigated were rinsing time and hard baking (post-development baking). These parameters were investigated because they could have a favorable effect on microbridging, an undesirable phenomenon that was encountered during interference lithography experiments. The effect of rinsing and hard bake on this phenomenon is shown in Fig. 2.9.

The images show that the bridging effect is reduced if a longer rinsing time is used. Longer rinsing time also leads to smaller lines relative to the spaces. Under standard conditions, the lines are around 60 nm, whereas longer rinsing decreases this to around 50 nm. This implies that the resist is still partially soluble in the rinser (H_2O) and that the rinsing should not be performed for too long time. Hard baking (200 °C for 1 min) does not significantly change the pattern, although it slightly reduces the linewidth to around 55 nm.

The materials were also tested at a higher resolution. Although 80-nm pitch lines could be printed, the 60- and 44-nm pitch lines were significantly more difficult to print. Significant bridging between lines was observed. This is probably related to a problem in the development or rinsing process. Pattern collapse does not seem very likely, however, since the aspect ratio of the pattern is close to 1:1. Rather, the lines seem to detach from the substrate, signaling poor adhesion of the resist film or pattern collapse. For none of the presently studied materials, patterns at 22-nm HP could be resolved. Further investigations and improvements are needed to reach high resolution, such as reducing the aspect ratio, changing and optimization of the rinsing solvent, and improving adhesion of the resist to the substrate using surface treatments or underlayers.

Similarly to the open-frame experiments, we also patterned thicker layers (30 nm instead of 20 nm). However, a higher sensitivity was not found here. A reason could be that adhesion of the lines is very important for patterning experiments. A thicker layer receives less light at the bottom, making this adhesion more difficult.

The best patterns were created for the tin-oxo cage with acetate (CH_3COO^-) anions. This material was significantly less prone to pattern collapse or bridging,

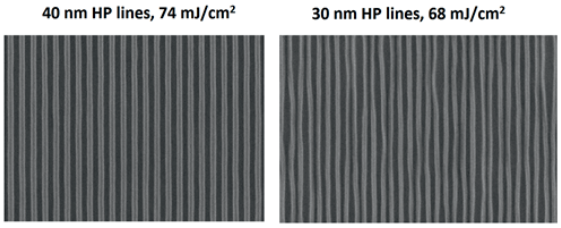

Figure 2.10: Interference lithography on TinA. Processing conditions: PAB 90 °C (1 min), PEB 100 °C (1 min), and hard bake 200 °C (1 min).

perhaps owing to its better stability. Two patterns at half pitches of 40 and 30 nm for this anion can be seen in Fig. 2.10. As it is seen in the figure, patterning with high quality is obtained down to 30-nm HP and the resolution is limited by the pattern collapse, as a result of the adhesion problems.

2.4 Conclusion

We studied the EUV patterning of thin films of a small set of tin-oxo cage compounds. The relatively high packing density of Sn atoms provides a highly absorbing material,[46] since Sn is one of the elements most strongly absorbing at 13.5 nm.[100] Optimization of the processing conditions provided a better sensitivity than was reported previously.[88] Large area exposure (contrast curve) experiments showed a dependence on initial layer thickness and PEB temperature. Post-exposure baking also substantially improved the negative tone photoresist performance in patterning experiments. This suggests that EUV photoreaction products are formed that can further react during the baking step. Identification of such photoproducts is a target of our ongoing research. Loss of carbon, in any form, leaves the Sn atoms in a coordinatively unsaturated state, making them potentially more reactive. While we have achieved progress, it is clear that further improvements are needed to make the materials competitive with the state-of-the-art EUV resists. The process of improvement would benefit greatly from a better understanding of the photochemical processes at work. For instance, the relatively low sensitivity suggests that loss mechanisms may be at play in which EUV photons are not converted into the desired solubility change. Reduction of these loss mechanisms could pave the way toward more sensitive resist materials.

2.5 Acknowledgments

Part of this work was performed at the Swiss Light Source; this includes preliminary AFM results obtained at the Scanning Probe Microscopy Laboratory of the Laboratory for Micro and Nanotechnology, Paul Scherrer Institut. We thank Lianjia Wu (ARCNL) for performing the TGA analysis. We thank Elizabeth Buitrago and Roberto Fallica for helping with the experiments, and ASML for providing the initial access to EUVL experiments at PSI. This project has received funding from the EU-H2020 research and innovation program under grant agreement No. 654360 having benefited from the access provided by PSI in Villigen within the framework of the Nanoscience Foundries and Fine Analysis Europe Transnational Access Activity.

CHAPTER 3

Photochemistry of tin-oxo cages in solution*

Abstract

n-Butyl tin-oxo cages with hydroxide counterions (TinOH) or acetate counterions (TinA) were exposed to deep ultraviolet (DUV) light (225 nm) in solution, after which the photoproducts were characterized. UV/Vis spectroscopy confirmed that Sn–C bonds are broken upon DUV exposure by detecting a decrease in absorbance from the $[\sigma^*_{\mathrm{Sn–C}} \leftarrow \sigma_{\mathrm{Sn–C}}]$ transitions. The quantum yield of Sn–C cleavage was determined to be 60−80% by UV/Vis experiments. The cleavage of Sn–C bonds in TinOH upon DUV exposure was confirmed further by ^{1}H NMR spectroscopy. This showed that the Sn–C bond cleavage is homolytic, by indirect detection of transient radicals with a spin trap. NMR spectroscopy also showed a decrease in integrals of *n*Bu protons from TinOH. Four main photoproducts were identified with 1D ^{1}H, 2D TOCSY, DOSY and selective TOCSY NMR spectroscopy: *n*-octane, 1-butene, 1-butanol and 1,1-dimethoxybutane (selectivity 79.1%, 6.0%, 6.2% and 7.9%, respectively). When the solution was deoxygenated before DUV exposure and volatile compounds were distilled, only *n*-octane and 1-butene were detected. This indicates that 1-butanol and 1,1-dimethoxybutane form upon reaction with dissolved oxygen. A quantitative NMR experiment was carried out in a quartz NMR tube, which was exposed to increasing amounts of DUV radiation. The quantum yield of Sn–C bond cleavage was determined to be at least 20%, based on the observed generation rate of photoproducts. This quantum yield may, however, be underestimated because a lot of light is lost by reflection on the cylindrical quartz NMR tube. Reaction mechanisms for product formation were proposed; it is clear that radical chemistry plays a major role in the photochemistry of TinOH.

*J. Haitjema, Y. Boeije, A.W. Ehlers, A. M. Brouwer, "Photochemistry of tin-oxo cages in solution", *Manuscript in preparation.*

3.1 Introduction

Understanding the photochemistry of tin-oxo cages is one of the main aims of the research discussed in this thesis. In this chapter, deep ultraviolet light (DUV, 225 nm) is used to expose tin-oxo cages in solution, followed by photoproduct analysis. While DUV photoreactions are different from EUV photoreactions, the generated excited states or photoproducts may be similar.[109] Moreover, EUV lithography machines may produce out-of-band radiation in the deep UV region, which could be detrimental to pattern resolution.[110] DUV photoreactions should therefore be understood to develop better EUV photoresists. In the ideal case, an EUV photoresist would respond only to EUV but not (or only very weakly) to DUV radiation.

Photoreactions that occur upon DUV exposure of tin-oxo cage thin films have been studied previously by X-ray photoelectron spectroscopy as well as UV/Vis spectroscopy.[102,111] It was shown that the solubility switch occurs upon exposure to DUV light as well. A photoreaction mechanism was proposed for this solubility switch, making a distinction between reactions performed under air and under nitrogen atmosphere (see Scheme 3.1). In both cases, DUV exposure led to the loss of carbon as a result of Sn–C bond cleavage. Under air atmosphere, immediate oxidation processes are possible, leading to a larger amount of oxygen in the photo-exposed tin-oxo cage product. Although EUV exposures are performed under either vacuum or reductive (H_2) atmosphere,[112] reactions with oxygen are still relevant on account of the post-exposure baking (PEB) step, which is usually performed in air. It is hypothesized that intermediary products react further during this step (see Chapter 2). These intermediary products have thus far not been firmly identified.

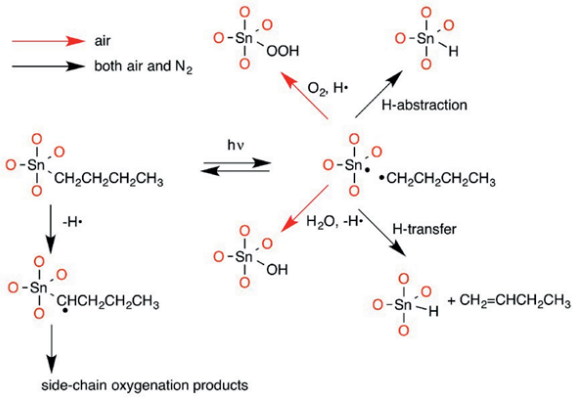

Scheme 3.1: Proposed photochemical reactions for TinOH thin films exposed to DUV in air and N_2, as proposed by Zhang and coworkers. Adapted from ref. 102.

Analyzing photoproducts and intermediates in thin films is challenging, because only a small amount of converted material is produced. Exposing in solution, followed by post-exposure analysis, significantly broadens the choice of spectroscopic

techniques.

One such method is UV/Vis spectroscopy. UV/Vis spectra of tin-oxo cage films show a broad absorption band ($\lambda_{max} \approx 220$ nm).[102] This absorption band decreased upon DUV exposure, indicating cleavage of Sn–C bonds and possible Sn–O bond formation. However, film inhomogeneity and roughness complicated quantification of the observed changes. In solution, the light exposure is distributed homogeneously because diffusion can take place and the solution can be stirred during exposure.

NMR spectroscopy can also be used to analyze the photoproducts. The chemical shifts (δ) and coupling constants (J) can provide unambiguous identification. Furthermore, NMR spectroscopic studies on tin-oxo cages are abundant,[89,99,107,113–117] providing a good starting point for analysis. 1D ^{1}H, ^{13}C and ^{119}Sn NMR have all been used for studies on tin-oxo cages. ^{13}C and ^{119}Sn NMR, however, have only low sensitivity and are therefore less suitable for photoproduct identification, although they can be used for confirmation of the starting material (TinOH). ^{1}H NMR is sufficiently sensitive for identification of photoproducts. This identification can be strengthened by more sophisticated NMR methods, such as TOtal Correlated SpectroscopY (TOCSY).

In ^{1}H–^{1}H 2D TOCSY, coupling between protons of the same "spin system" is observed.[118] Separation of signals is caused by a spin-lock in the pulse program, in which all the protons that are correlated to each other in sequence will get polarized and thus give a signal in the acquisition phase.[119] In the case of TinOH, the *n*Bu groups attached to 5-coordinated tin (Sn_5) and 6-coordinated tin (Sn_6) can be distinguished.

Selective TOCSY (or 1D TOCSY) is a method similar to 2D TOCSY, but the spectrum is obtained after selectively pulsing one proton signal. Accordingly, 1D spectra are obtained in which only the proton signals are seen that correlate to the specifically pulsed proton signal. In this way, overlapping signals in the 2D TOCSY can be easily separated by pulsing at different proton signals.

Diffusion Ordered SpectroscopY (DOSY) NMR is a method to distinguish differently sized particles in a sample. It is a pulsed field gradient NMR technique that separates each signal according to diffusion rate, and has been used to determine the associative behavior of tin-oxo cages.[89,115] It can also be used to study the size (hydrodynamic radius) of starting material and photoproducts.

The downside of solution exposure is that use of EUV light is not practical owing to the ultrashort absorption length of EUV in liquids. Therefore, only exposure to DUV (225 nm) was performed. Only a few solvents are sufficiently transparent in this spectral region; methanol (MeOH) and ethanol (EtOH) were chosen for the experiments, since tin-oxo cages can be readily dissolved in them.

Solution photochemistry is different from solid-state chemistry. For radical chemistry in solution, an important aspect is the "radical cage effect",[120,121] in which two formed radicals are surrounded by solvent molecules, making it difficult for the radicals to diffuse out of each other's vicinity. This effect explains why photodissociation yields are lower in solution than in the gas phase; in solution recombination of radicals is much more likely.[122] In the solid state, diffusion is even slower.[123,124] Therefore, it should be kept in mind that the quantum yield of photo-exposure in solution is expected to be higher than the quantum yield in a photoresist film.

3.2 Experimental

3.2.1 Synthesis

Tin-oxo cage materials were prepared as mentioned before (see Chapter 2).[88] The tin-oxo cage was prepared with tosylate counterions, after which the material was converted to hydroxide form (TinOH) by ion exchange using aqueous tetramethyl ammonium hydroxide.[114] Conversion to the acetate form (TinA) was performed by reacting TinOH with two molar equivalents of acetic acid.[89]

3.2.2 UV/Vis spectroscopy

For UV-visible samples, approximately 5–10 mg of TinOH or TinA were dissolved in 3 mL of solvent. This was then further diluted to achieve a final concentration of 1–10 μM in 3 mL. UV/Vis spectra were recorded using a Shimadzu 2700 spectrometer, using spectroscopic grade solvents (methanol, ethanol, cyclohexane, isopropanol). The spectra for quantitative analysis were baseline-corrected by setting the absorbance at 320 nm (far from the absorption band) to zero.

3.2.3 NMR spectroscopy

TinOH (21 mg ≈ 8.2 μmol) was dissolved in 1.8 mL of MeOH-d_4, leading to a concentration of approximately 4.6 mM. A solution of TinOH in deuterated solvent (4.6 mM) inside a 1×1 cm^2 quartz cuvette was exposed by a laser (see Section 3.2.4). After multiple time intervals, a sample was taken out of the cuvette to obtain an NMR spectrum after DUV exposure.

A quartz NMR tube was used for the quantitative NMR experiment. The sample was directly measured (no aliquots were taken), after which the sample was exposed to the next dose of DUV. In this experiment, 21 mg of TinOH powder was dissolved in 0.6 mL of MeOH-d_4.

1D ^{1}H NMR

1D ^{1}H NMR spectra were recorded on a Bruker AVANCE NEO 500 MHz spectrometer. The solvent used was MeOH-d_4 (Sigma Aldrich or VWR, ≥99.8 atom % D, ≥99% purity). At least 16 scans per sample were recorded, or more (up to 512) if low quantities of product needed to be detected. Typical concentration of tin-oxo cages was 5 mM (12 mg/mL).

1D ^{119}Sn NMR

1D ^{119}Sn NMR spectra were recorded on a Bruker AVANCE NEO 500 MHz spectrometer. The solvent was MeOH-d_4 (Sigma Aldrich or VWR, ≥99.8 atom % D, ≥99% purity) or CD_2Cl_2, measuring at least 2000 scans per sample. Typical concentration of tin-oxo cages was 60 mM (140 mg/mL).

1D/2D TOCSY

The same concentration was used as for 1D ^{1}H NMR. 1D and 2D TOCSY spectra were recorded on a Bruker AVANCE NEO 500 MHz spectrometer. Total Correlated Spectroscopy NMR (TOCSY-NMR) was performed based on a method by Bax and coworkers.[119] For 2D TOCSY, 16 scans were performed in the f1 direction and 256 scans were performed in the f2 direction, with a total measurement time of around 2 h. Spin-lock (mixing) time was 200 ms for all TOCSY experiments.

DOSY NMR

The same concentration was used as for 1D ^{1}H NMR. At the start of each diffusion-ordered spectroscopy (DOSY) experiment, the diffusion delay (D20) was tuned to get a clear signal at 98% gradient strength, and 2–3% of the signal at 2% gradient strength. The optimal value for D20 was found to be 0.12 s. Pulse duration (P30) was 0.5 µs for each scan.

Spectra were then recorded at 16 different gradient strengths (between 98 and 2%). Each spectrum was recorded 16 times. The result is an NMR spectrum in which the signals decrease as a function of gradient strength. This decrease was fitted to a mono-exponential decay function, with each peak having a different decay rate which is related to its diffusion constant. The fitting procedure was carried out using Bruker Dynamics software.

The diffusion axis of the DOSY plots was calibrated by using literature values for the self-diffusion constant of methanol ($\log(D) = -8.63$).[125] The chemical shift axis was calibrated by using a literature value for the chemical shift of the CH_3 groups in MeOH (3.34 ppm).[126]

Quantitative NMR

Quantitative NMR measurements were carried out in a quartz NMR tube, which was directly exposed to DUV irradiation. 21 mg of TinOH (8.5 µmol) were dissolved in 0.6 mL MeOH-d_4. iPrOH, which was already present in all prepared TinOH powders,[107] was used as an internal standard. It was assumed that all photons were absorbed by the solution, because of the high absorption coefficient of TinOH at 225 nm (approximately 10^5 $M^{-1}\,cm^{-1}$)[103] and high concentration, leading to an absorbance $A > 100$. The actual number of absorbed photons may be lower as a result of reflection losses.

Evans method

A stock solution of spectroscopic grade acetonitrile (MeCN, 0.1 mL) and TinOH (20 mg; 8.5 µmol) in MeOH-d_4 (2 mL) was prepared. 1 mL of this stock solution and 2,2,6,6-tetramethylpiperidinyloxyl ("TEMPO", 3.2 mg) were added to a 1 × 1 cm^2 quartz cuvette. 0.6 mL of this solution was added to a glass NMR tube and a glass capillary with stock solution (TinOH/MeCN in MeOH, but no TEMPO) was placed inside this tube, after which an ^{1}H NMR spectrum was obtained. After measurement, the solution was added back to the cuvette and the sample was exposed at 225

nm at multiple durations, while stirring at 400 rpm. After 1 h and 2 h of DUV exposure, ^{1}H NMR spectra were obtained. In each measurement the capillary with stock solution was placed inside the NMR tube. Two different blank experiments were performed to correct for the possible radical photochemistry of TEMPO independent of TinOH (blank 1) and the possibility that TinOH reacts with TEMPO without light absorption (blank 2). For blank 1, a stock solution of TEMPO in MeOH-d_4 (without TinOH) was prepared and the ^{1}H NMR spectrum of unexposed TEMPO as well as exposed TEMPO (1 h and 2 h) was measured. For blank 2, the same stock solution of MeCN and TinOH in MeOH-d_4 was prepared. ^{1}H NMR spectra were obtained at multiple time intervals of a solution of TEMPO (3.2 mg) and 1 mL stock solution (1 h and 2 h waiting time).

3.2.4 DUV exposures

DUV exposures were carried out using an Ekspla NT342B tunable laser system, using a wavelength of 225 nm. Pulse repetition rate was 10 Hz with a pulse width of 3–6 ns and typical pulse energy of around 1 mJ. The solution was stirred by a stirring bar (400 rpm) during exposure. Aliquots were taken out of the cuvette and transferred into NMR tubes.

3.2.5 Freeze-thaw technique and distillation

Selected samples of TinOH dissolved in MeOH-d_4 (1 mL of solution, approximately 5 mM) were deoxygenated before DUV exposure by using the freeze-pump-thaw technique. This was done using a custom-made setup in which a flask was connected to a quartz cuvette, in which gas and liquid flow can be controlled by various valves (see Fig. 3.1).

The flask with solution was frozen using liquid N_2 after which the atmosphere was pumped off ($p < 0.01$ mbar). The vacuum connection was closed and the solution was warmed to room temperature (water bath). After this, the flask was frozen and evacuated again, repeating the procedure three times. The deoxygenated solution was transferred to the cuvette for DUV exposure, without any exposure to oxygen. After exposure, the solution was transferred back to the flask for distillation. First, the flask was frozen (N_2) and the atmosphere was pumped off. The valve connecting to the vacuum was then closed and the flask was warmed to room temperature. At the same time, the setup was connected to an NMR tube which was cooled down using liquid N_2 and evacuated. The connection to the NMR tube was then opened, after which volatile compounds condensed in the NMR tube.

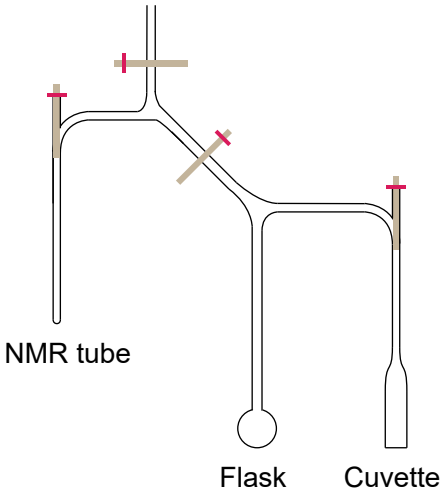

Figure 3.1: Schematic representation of the setup used for the freeze-thaw cycle (deoxygenation), followed by DUV exposure and distillation.

3.3 Results and discussion

3.3.1 UV/Vis spectroscopy

UV-visible (UV/Vis) spectroscopy is a useful tool to track chemical (photo)-reactions of tin-oxo cages in solution. It has the advantage of high sensitivity, being able to detect species at very low concentrations (micromolar or even lower).

The DUV photochemistry of TinOH primarily arises from [σ^* ← σ Sn–C] transitions, which give rise to a collective absorption maximum (λ_{max}) around 220 nm. In these transitions, an electron is promoted from the sp^3-hybridized Sn–C bond, mostly at the 6-coordinated tin atom, to an empty σ^* orbital.[103] The calculations show that this excited state also has significant σ^* Sn–C character. This electronic transition weakens the Sn–C bond, leading to bond cleavage. Therefore it is expected that the intensity of the [σ^* Sn–C ← σ Sn–C] transition will decrease upon DUV exposure. Since fewer transitions are available and the transition moments are smeared out over multiple transitions, the absorption band corresponding to the [σ^* Sn–C ← σ Sn–C] transitions broaden and decrease in intensity.

UV-visible spectra of unexposed TinOH

First, UV/VIS absorption spectra were obtained from unexposed samples of TinOH in methanol (MeOH), isopropanol (iPrOH) and cyclohexane (cHex) and show a strong absorption near 220 nm with a molar absorption coefficient $\epsilon \sim 10^5$ M^{-1} cm^{-1} (see Fig. 3.2). A red shift is observed moving from the most polar solvent (MeOH) to the least polar (cHex). UV/Vis spectra of other tin-oxo cages, such as TinA, show a very similar absorption band (see below).

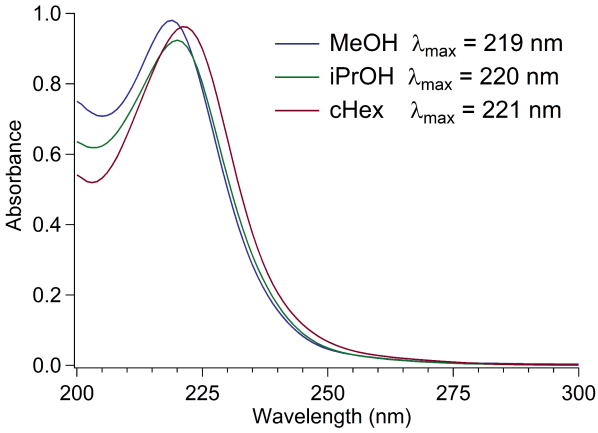

Figure 3.2: UV/VIS Absorption spectra of TinOH in MeOH (blue), iPrOH (green) and cHex (red). Concentrations are 9.1 µM. $\epsilon \sim 10^5$ M^{-1} cm^{-1} at λ_{max}.

UV-visible spectra of DUV-exposed tin-oxo cages

Tin-oxo cages were irradiated in solution, after which the UV/Vis spectrum was measured. The results are shown in Fig. 3.3. These experiments were done on TinA (acetate counterions) in spectroscopic ethanol. The used materials therefore deviate slightly from the NMR experiments shown later in this chapter, which were performed in a solution of TinOH in methanol. In the ESI (Fig. 9.2), UV/Vis results for photo-exposure of TinOH in methanol are also shown; the results are very similar to those shown in Fig. 3.3. In the absorption band, the absorbance A decays with increasing exposure dose D, as can be seen in Fig. 3.4. This decay can be described as mono-exponential:

$$A = a + be^{-cD} \tag{3.1}$$

where a, b and c can be obtained by fitting. a can be viewed as the absorbance value at infinite exposure dose. b is a scaling factor and c gives the rate at which the absorbance decreases (in mJ^{-1}).

a is clearly not zero, which means that even at exceedingly high doses, there is still absorption remaining. This can be explained in two ways. First, other transitions could

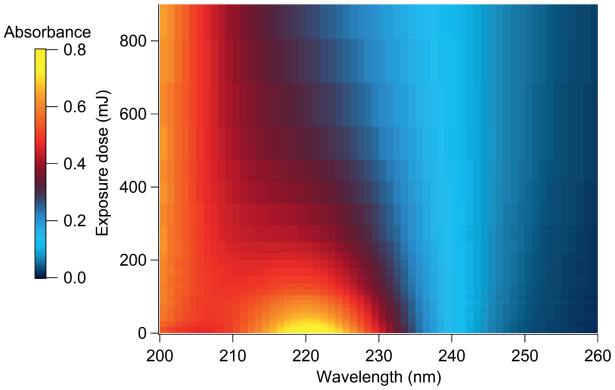

Figure 3.3: UV/Vis absorption spectra of TinA (6.9 µM in EtOH) as a function of exposure dose.

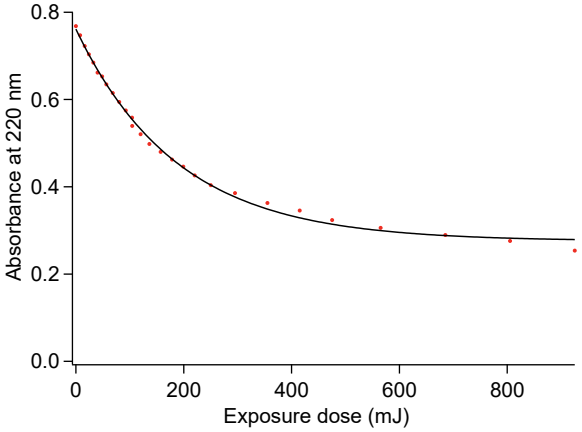

Figure 3.4: Absorption at 220 nm plotted vs. DUV (225 nm) irradiation dose, for 3 mL of a 6.9 µM solution of TinA (tin-oxo cage with acetate counterions) in EtOH. Fitted to function $A = a + be^{-cD}$, with $a = 0.28$, $b = 0.49$ and $c = 5.3 \times 10^{-3}$ mJ^{-1}.

give rise to absorption at 220 nm which do not lead to Sn–C cleavage, and therefore no decrease in absorption. This gives rise to a background a. Secondly, photoproducts can also be formed that give rise to absorption. This would also give rise to an apparent decrease in the rate c and a background a. It should be noted that formation of photoproducts normally does not lead to bi-exponential behavior, because the rate of photoproduct formation will usually be equal to the rate of irreversible Sn–C cleavage. Because both these explanations have a similar effect, they are difficult to separate from each other; both are probably correct.

DUV-induced conversion of tin-oxo cages to photoproducts can be studied quantitatively. Both the initial amount of tin-oxo cage and the number of absorbed photons are known. The latter can be calculated from the laser power ($\sim$ 10 mW) and the absorbance values.

In a simple approximation, the strength of the absorption band ($\lambda_{\text{max}} \approx 220$ nm) scales linearly with the number of Sn–C bonds present and the DUV source is monochromatic. This approximation may be the most valid at short exposure times (0–60 sec.), because only small amounts of products are generated in this case.

The number of absorbed DUV photons can be approximated by Eq. 3.2:

$$N_{\text{photons}} = \frac{P \cdot t \cdot (1 - 10^{-\bar{A}})}{E_{\text{phot}}} \tag{3.2}$$

In Eq. 3.2, P is the laser power (in Watt), t is the exposure time (s), $\bar{A}$ is the average absorbance during exposure, and E_{phot} is the energy of one DUV photon (8.8×10^{-19} J, as given by $\frac{hc}{\lambda}$). $\bar{A}$ can be approximated by taking the average of the absorbance between dose 0 and dose D_1. The average value of a function in the interval between x_0 and x_1 is given by:

$$\frac{1}{x_0 - x_1} \int_{x_0}^{x_1} f(x)\, dx \tag{3.3}$$

Substituting 3.1 for $f(x)$, the exposure dose D_1 for x_2, and 0 for x_1, we obtain:

$$\begin{aligned} \bar{A} &= \frac{1}{D_1} \int_0^{D_1} a + b\mathrm{e}^{-cD}\, dD \\ &= a + \frac{b}{cD_1} - \frac{b}{cD_1}\mathrm{e}^{-cD_1} \end{aligned} \tag{3.4}$$

In Eq. 3.4, D is the exposure dose and D_1 is the exposure dose at which the number of absorbed photons is evaluated. a, b and c are fit parameters, obtained by fitting the absorbance vs. exposure dose plot to an exponential decay. The number of photochemical events (Sn–C bond cleavage in this case) can be calculated by Eq. 3.5:

$$N_{\text{Sn–C bond cleaved}} = (n_0 - n) \cdot N_{\text{A}} \cdot 12 \tag{3.5}$$

In Eq. 3.5, n is the amount of TinOH (in mol) at time t, n_0 is the amount of TinOH for the unexposed material, and N_{A} is Avogadro's number. The factor 12 appears because each TinOH molecule contains 12 Sn–C bonds.

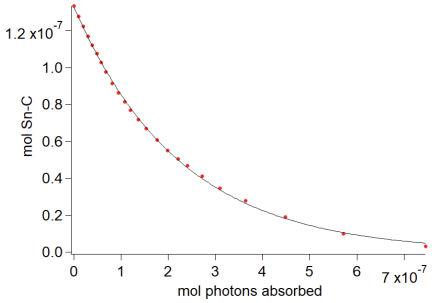

Figure 3.5: Mol Sn–C bonds plotted vs. the number of absorbed photons for 3 mL of a 6.9 µM solution of TinA in EtOH. The number of Sn–C bonds was corrected for baseline absorption. The fitted curve is an exponential decay: $a + be^{-cD}$ with $a = 0$, $b = 1.3 \cdot 10^{-7}$ mol, $c = 4.9 \cdot 10^{6}$ mol^{-1}.

For an initial TinA concentration of 6.9 µM, $a = 0.28$, $b = 0.49$, and c is 5.3×10^{-3} mJ^{-1}. Using the integration procedure described in Eq. 3.4, the absorbed dose can be calculated for each data point. This can be plotted vs. the remaining number of Sn–C bonds (see Fig. 3.5), which can be calculated using the molar concentration of tin-oxo cage and the total volume of the solution (3 mL).

One would expect Fig. 3.5 to show a linear decay, since each absorbed photon is expected to break a fixed number of Sn–C bonds (the quantum yield). This is clearly not the case; the plot again shows a mono-exponential decay. This means that the quantum yield decreases with increasing exposure dose. This can be explained by the loss of Sn–C over time, which means that an increasing number of photons that are absorbed do not cause Sn–C cleavage and do not lead to a decrease in absorption.

To determine the quantum yield, it is the most reasonable to choose the slope at zero dose. In this case, no other products are formed yet that complicate the analysis. The quantum yield is then given by the derivative at $D = 0$, which is $-bc$ in case of an exponential decay ($a + be^{-cD}$).

The quantum yield as calculated is shown for different samples of TinA with different concentrations. At higher tin-oxo cage concentration the quantum yield appears to be higher, as shown in Fig. 3.6. This could indicate a reaction with other tin-oxo cages after exposure, which would become more probable as the concentration increases. However, this conclusion is only preliminary on account of the limited number of data points.

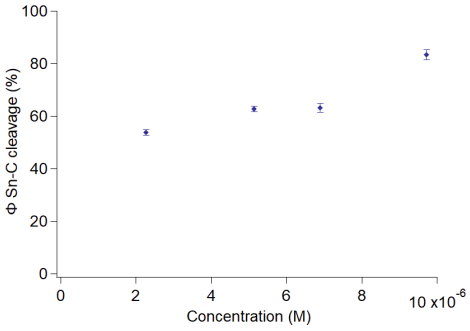

Figure 3.6: Quantum yield Φ of Sn–C cleavage as function of TinA concentration. Concentration was calculated using the absorption spectrum and the molar absorption coefficient. Error bars are standard deviations, as calculated using the standard deviation obtained from the fitting procedure and the "propagation of errors" formula (see Chapter 6).

3.3.2 NMR spectroscopy on unexposed material

NMR spectroscopy yields much more structural information on photoproducts than UV/Vis spectroscopy. To study DUV-induced changes on tin-oxo cages in solution, a clear understanding of spectra of non-exposed tin-oxo cage is necessary. In various previous works, NMR studies on the tin-oxo cage have already been conducted. This includes ^{119}Sn NMR, ^{13}C NMR, ^{1}H NMR, DOSY NMR, etc.[89,99,107,113–115]

^{119}Sn NMR

Sn NMR is a useful tool to probe the chemical structure of organotin compounds, and is therefore commonly used in organotin chemistry.[127] ^{119}Sn NMR spectra of TinOH and TinOTs can be found in the ESI (Fig. 9.3 and 9.4). These spectra are in agreement with the literature.[114]

^{1}H NMR

In Fig. 3.7 the ^{1}H NMR spectrum of unexposed TinOH in MeOH-d_4 is shown. 2D TOCSY NMR (Fig. 3.8) was used for signal assignment. The spectrum and assignment are in agreement with the literature.[107] A detailed analysis of the ^{1}H NMR spectrum can be found in the ESI (Section 9.3.2). A small impurity of tetramethyl ammonium ions (TMA, a leftover from the synthesis, see Section 3.2.1) is detected at 3.2 ppm, but the compound is otherwise pure.

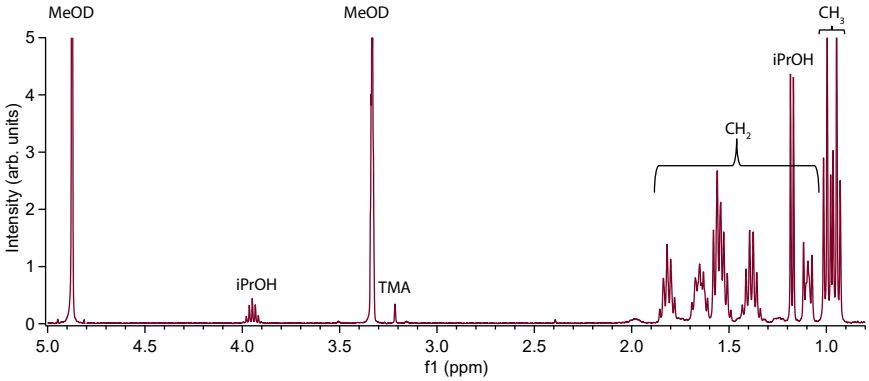

Figure 3.7: 400 MHz ^{1}H NMR spectrum of TinOH in MeOH-d_4.

2D TOCSY NMR

TOCSY is an NMR method that creates couplings between all protons within a "spin system", a chain of nuclei in which each is coupled to its neighbor.[118] Even protons at large distances can couple to each other. The 2D TOCSY spectrum of unexposed TinOH in MeOH-d_4, including the assignments, is shown in Fig. 3.8. This spectrum is zoomed-in on the *n*Bu region, where all the ^{1}H–^{1}H couplings are expected. The couplings between a chemically distinct group of *n*Bu protons can easily be derived by looking at one F2 peak and see which cross peaks on the F1 axis below that peak belong to that F2 signal. For example, starting right above on the F2 axis, Sn_6-CH_2-CH_2-CH_2-**CH_3** is found at 0.92 ppm as was found in the ^{1}H spectrum (Fig. 3.7). By scanning down the F1 axis, it can be seen that these methyl protons couple to signals at 1.07 ppm, 1.36 ppm and 1.63 ppm. This shows that with TOCSY only shows couplings between protons of the same *n*Bu. A table showing all couplings is shown in the ESI (Tab. 9.3).

Selective TOCSY

In a selective TOCSY experiment, a specific proton signal is pulsed. This leads to suppression of all signals that are not coupled to the proton signal via the "spin system". The selective TOCSY spectrum of unexposed TinOH in MeOH-d_4 is shown in Fig. 3.9, for two different pulsed signals. In the blue spectrum (top), Sn_6-CH_2-**CH_2**-CH_2-CH_3 at 1.63 ppm is pulsed, causing all the signals corresponding to the *n*Bu chain bound to the six-coordinated tin atom to evolve, while suppressing all the Sn_5 signals. In the green spectrum (middle), Sn_5-CH_2-**CH_2**-CH_2-CH_3 is pulsed, leading to suppression of all signals that do not correspond to this butyl chain. The red spectrum (bottom) is the normal ^{1}H spectrum, which is approximately the sum of the green and blue spectra, with an added signal for iPrOH.

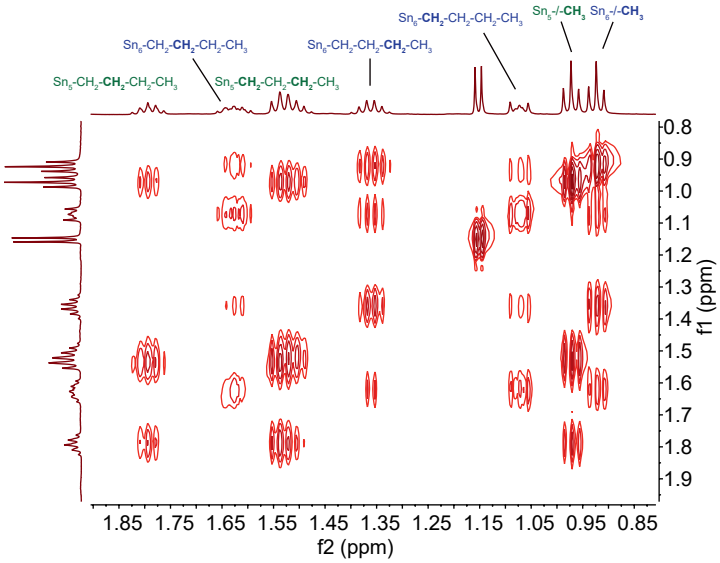

Figure 3.8: 500 MHz 2D TOCSY spectrum of TinOH in MeOH-d_4, zoomed-in on the nBu region. The assignments are shown as well.

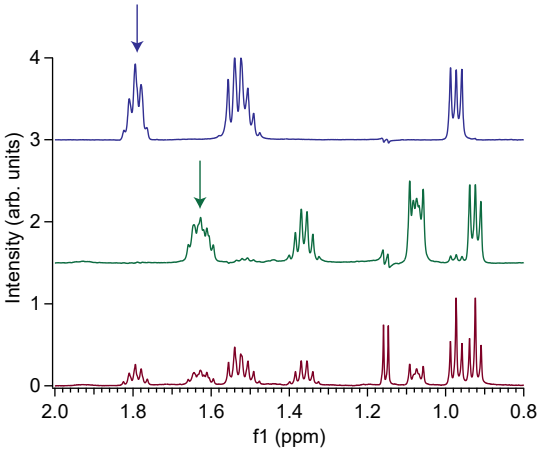

Figure 3.9: 500 MHz selective TOCSY spectra of TinOH in MeOH-d_4. Red: ^{1}H spectrum. Green: pulsed at 1.63 ppm (indicated with green arrow). Blue: pulsed at 1.79 ppm (indicated with blue arrow). A vertical offset was used on the y-axis.

3.3.3 Evans method: NMR spectroscopy and spin trapping

Cardineau and coworkers hypothesized first that the photochemistry of tin-oxo cages involves the formation of radicals after homolysis of Sn–C bonds, based on a mild correlation between EUV photosensitivity and strength of Sn–C bonds.[88] Quantum chemical calculations support the breaking of the Sn–C bond as the primary process after DUV photon absorption.[103] Zhang and coworkers performed DUV radiation induced solid-state chemistry of tin-oxo cage films, followed by XPS analysis.[102] From these results mechanistic pathways were suggested, which involved initial homolytic bond cleavage. However, this has not been definitively proven, because the volatile reaction products could not be identified yet.

In this work, the Evans method was used to demonstrate formation of transient radicals upon photon absorption by TinOH.[128] This method is based on the dependence of the NMR chemical shift of reference compounds on the concentration of unpaired electrons (paramagnetic species) in a sample. These unpaired electrons have an interaction with the hydrogen nuclei of the reference compound, changing the chemical shift of its signal. Both the contact interaction and the dipolar interaction between the unpaired electron and nucleus are involved in this paramagnetic shifting.[129] Besides the shift, paramagnetic species decrease the relaxation times of protons, significantly broadening all signals.

The paramagnetic shift of the reference compound scales linearly with the concentration of paramagnetic species. By observing the frequency difference (Δf) of a resonance in the presence and absence of paramagnetic species, the magnetic susceptibility (χ_m) can be obtained. This is quantified in Eq. 3.6.

$$\chi_\mathrm{m} = \frac{3\Delta f}{4\pi F c} \tag{3.6}$$

In Eq. 3.6, χ_m is the magnetic susceptibility (mL/mmol), Δf is the frequency difference between the shifted resonance and the pure solvent resonance (Hz), F is the spectrometer radiofrequency (Hz), and c is the concentration of paramagnetic species (mmol/mL).

The frequency difference between shifted resonance and the pure solvent resonance can be measured directly, using a capillary (reference) within an NMR tube (see Fig. 5.2a). The NMR tube contains a paramagnetic substance that shifts the signal, while the capillary does not and shows a signal which is not paramagnetically shifted. The NMR spectrum shows a shift in ppm value ($\Delta\delta$) which can be converted to Δf using the spectrometer frequency.

The measurement of transient radicals is limited by the short lifetime of radical species. In an ideal case, the radical species are measured *in situ*. In our case, however, it would involve intersecting a DUV light source with an NMR spectrometer, which for practical reasons was not possible. A way to prove formation of radicals after they have terminated is through the use of spin traps that selectively react with radicals. In this work, the paramagnetic spin trap TEMPO was used (Fig. 5.2b), which contains an unpaired electron at the oxygen atom but is sufficiently stable.

TEMPO converts to a stable diamagnetic species upon reaction with a radical.

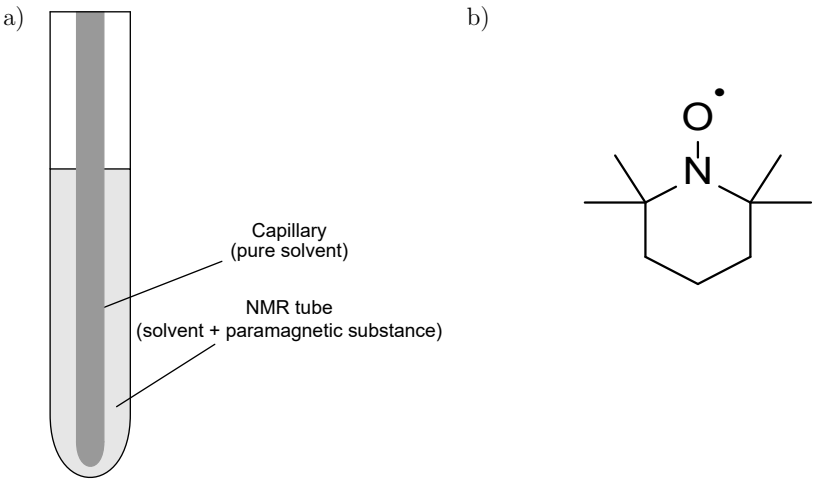

Figure 3.10: (a) Schematic representation of the Evans method, (b) chemical structure of the spin trap used (2,2,6,6-Tetramethylpiperidin-1-yl)oxyl (TEMPO).

The larger the amount of TEMPO, the larger the shift (Δf) between the capillary and NMR-tube signals. If this shift decreases upon DUV exposure, this indicates a radical mechanism in the photochemistry of TinOH. In addition, the number of generated radicals can be quantified if the initial amount of TEMPO is known.

In our experiments, acetonitrile (MeCN) was used as a reference compound, because it is both chemically inert and transparent to DUV light. The chemical shift of a TinOH/MeCN solution in MeOH was then compared to a TinOH/MeCN/TEMPO solution in MeOH that was exposed to DUV light (225 nm), using a sealed capillary within an NMR tube. In Fig. 3.11, the resulting ^{1}H NMR spectra are shown, with increasing DUV exposure. In all spectra, two resonances corresponding to MeCN are shown. The larger peak corresponds to the signal in the capillary, which is not paramagnetically shifted. The smaller peak corresponds to the signal in the NMR tube, which is affected by paramagnetic shifting by TEMPO. Clearly, the paramagnetic shift is decreasing upon DUV exposure, indicating loss of paramagnetic species. This can be explained by the reaction of TEMPO with radicals arising from the DUV photochemistry of TinOH.

This reasoning is explained further in Fig. 3.12. Upon DUV exposure two radicals are expected to be created: a tin-centered radical and a butyl radical. As a spin trap, TEMPO can react with one of these highly reactive radicals, leading to a decrease in concentration of TEMPO. It is expected that TEMPO reacts faster with butyl radicals than with the bulkier tin-centered radicals. Upon DUV exposure, a triplet at 3.8 ppm is evolving, which indeed indicates the formation of a butyl-TEMPO adduct. The CH_2 protons adjacent to oxygen in this adduct are expected to appear at this chemical shift.[130] The other NMR peaks of the butyl-TEMPO adduct are

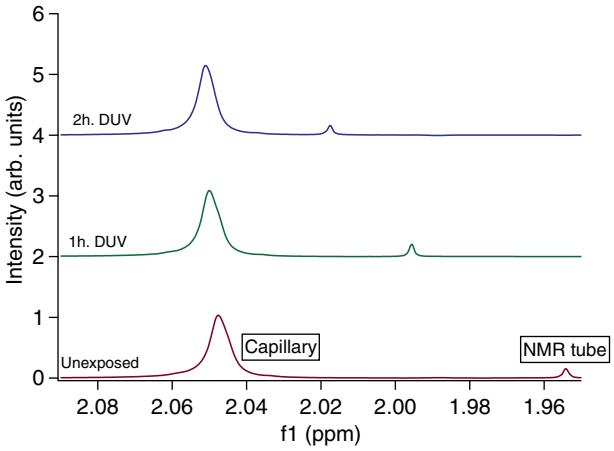

Figure 3.11: Evans method: ^{1}H NMR spectra of DUV exposed TinOH and TEMPO in MeOH-d_4, using MeCN as a reference. Bottom: unexposed. Middle: 1 h DUV exposed. Top: 2 h DUV exposed. $\Delta\delta = 0.035$ ppm after 1 h, 0.055 ppm after 2 h).

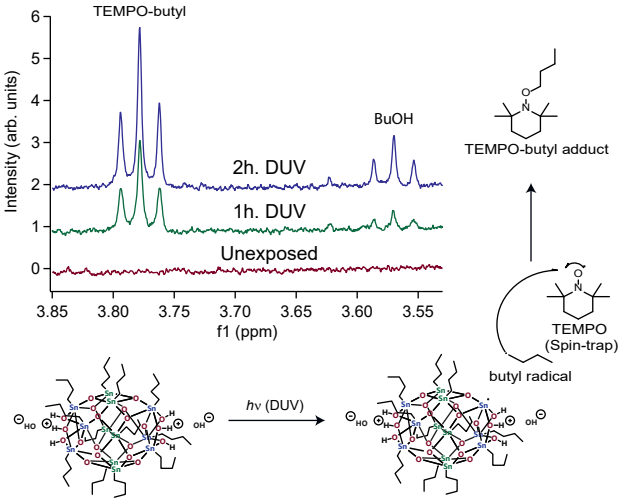

Figure 3.12: Spin-trapping of butyl radical with TEMPO and ^{1}H NMR measurement of formed TEMPO-adduct. A vertical offset was used on the y-axis.

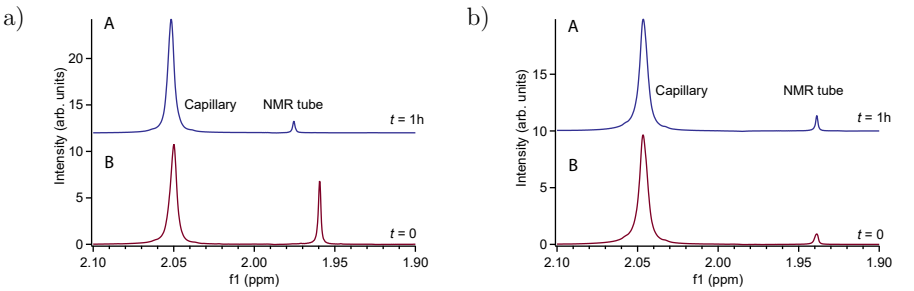

Figure 3.13: Blanks Evans Method. (a) Blank 1 (solution of TEMPO and MeCN in MeOH-d_4), without TinOH. Blue: 1 h DUV exposed. (b) Unexposed. $\Delta\delta$ (MeCN) = 0.01 ppm. Right: Evans Method (solution of TinOH, TEMPO and MeCN in MeOH-d_4), without DUV exposure. A (blue): $t = 1$ h. B (red): $t = 0$. $\Delta\delta$ (MeCN) = 0 ppm). Vertical offsets were used on the y-axes.

obscured by TinOH proton peaks. In addition, a large singlet at 1.14 ppm is appearing upon DUV exposure, which represents the methyl protons of a TEMPO adduct (see ESI, Fig. 9.7).[131] This confirms the loss of TEMPO radical upon DUV exposure and the formation of a diamagnetic TEMPO adduct. The presence of this adduct after exposure is a strong confirmation of the radical mechanism. Without TEMPO, the discussed peaks do not show up in the spectrum.

Tin-centered radicals could in principle react with TEMPO as well. However, this TEMPO-adduct was not detected by ^{1}H NMR spectroscopy. Its formation is likely sterically hindered. The tin-centered radicals are apparently unstable, as they do not contribute to the paramagnetic shielding. One possibility is that they decompose by breaking a second Sn–C bond to give a closed-shell tin compound and another Bu·, which is trapped by TEMPO.

In Fig. 3.12, it can also be seen that a triplet at 3.55 ppm is evolving. As shown below (Section 3.3.4), this signal corresponds to 1-butanol, which is a photoproduct after DUV absorption of TinOH.

To ensure that the decrease in TEMPO radical is caused by the photochemistry of TinOH, two blank experiments were performed. Blank 1 (without TinOH) checks the possibility of the radical photochemistry of TEMPO itself. As shown in Fig. 3.13a, there is a small difference in the peak distances from MeCN before and after exposure of $\Delta\delta = 0.01$ ppm. TEMPO thus appears to have a DUV photochemistry on its own, forming a diamagnetic species. However, this change in frequency difference is much smaller than the frequency shift seen in the photochemistry of TinOH ($\Delta\delta = 0.035$ ppm, see Fig. 3.11). Blank 2 (Fig. 3.27b) is the Evans experiment performed without DUV exposure, using a waiting time of 1 h. As can be seen, no paramagnetic shift occurs, which means that DUV irradiation must cause the paramagnetic shift.

In Table 3.1, the results from Figure 3.11 are quantified using Eq. 3.6. From Δf and the known starting concentration of TEMPO (11.3 mM), the concentration of TEMPO at different exposure times can be calculated. In this calculation, Δf of

Table 3.1: Frequency shifts for MeCN and corresponding conversion derived from Evans Method spectra in Fig. 3.11 and Eq. 3.6

DUV exp. (h)	**$\Delta\delta$ MeCN (ppm)**	**Δf MeCN (Hz)**	**Conc. TEMPO (mM)**	**Sn–*n*Bu conversion[a] (%)**
0	0.090	36.0	11.3	0
1	0.065	26.0	8.16	5.5
2	0.050	20.0	6.28	8.9

[a]Assuming conversion of one TEMPO molecule per Sn–*n*Bu.

TEMPO (Blank 1) is corrected for by extracting the shifts in this blank for 1 h of DUV exposure and extrapolating to 2 h of DUV exposure. Then, the conversion of the total number of *n*Bu chains from TinOH can be calculated with the known starting amount (8.5 µmol; 102 µmol *n*Bu), by assuming every TEMPO molecule has reacted with a cleaved butyl radical. In this way, it has been calculated that 5.5% of all Sn-*n*Bu chains have been converted after 1 h of DUV exposure, and 8.9% after 2 h. Using the laser power, we can calculate a quantum yield Φ (converted Sn–C bonds per photon). This was found to be 0.54%. In this calculation, it is assumed that every TEMPO molecule that has been converted to a diamagnetic species reacts with a *n*Bu radical from TinOH. However, the generated *n*Bu radicals can also react with the solvent or with each other. Furthermore, tin-centered radicals could contribute to the loss of TEMPO by generation of radicals (e.g. by H-atom abstraction) which could react with TEMPO. Therefore, Φ could be underestimated. Nevertheless, the Evans method has clearly proven the homolytic cleavage of Sn–C upon DUV exposure.

3.3.4 DUV exposure and product analysis by NMR

1D ^{1}H NMR

In Fig. 3.14, NMR spectra of unexposed and exposed solutions of TinOH in MeOH-d_4 are shown. Clearly, new signals appear in the NMR spectrum, which correspond to photoproducts. These are 1,1-dimethoxybutane ("acetal") at 4.49 ppm (t), 1-butanol at 3.55 ppm (t), and *n*-octane at 1.3 ppm (multiplet) and 0.88–0.91 ppm (triplet). Further, some low intensity signals can be observed at 9.70 ppm (butyraldehyde), 5.86 ppm (1-butene), 5.42 ppm, 4.98 ppm (1-butene), 2.41 ppm (butyraldehyde), 2.19 ppm and 2.06 ppm (1-butene) upon long exposure (see ESI, Fig. 9.8). Reference spectra were taken after short exposure times (on the order of minutes) to ensure that these product peaks also appeared after short exposure (i.e. they are not secondary products). Evidence for signal assignment will be shown in the upcoming discussion.

1-Butanol (BuOH) and butyraldehyde could be formed by reaction of formed Bu· with dissolved oxygen. This reaction is known from previous literature.[132,133] The

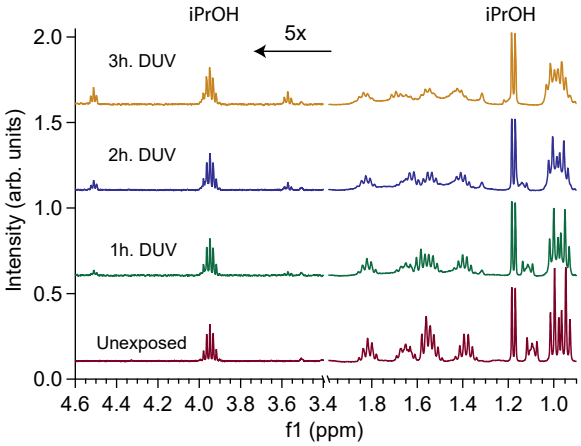

Figure 3.14: Zoomed-in 400 MHz ^{1}H NMR spectra of TinOH in MeOH-d_4 after multiple DUV exposure times. From bottom to top: 0 h (red), 1 h (green), 2 h (blue) and 3 h (purple) DUV exposure. The intensity in the left part of the graph was multiplied by five to show the product formation clearly. The spectra were normalized to the iPrOH C–H peak (3.95 ppm). A vertical offset was used on the y-axis.

intermediate peroxide BuOOH could be formed in this reaction, which could react further to form BuOH or butyraldehyde (see Scheme 3.2).[134] Butyraldehyde could further react with MeOH-d_4 to form the acetal 1,1-dimethoxybutane-d_6. This reaction is possibly catalyzed by TinOH (see below).

n-Octane and 1-butene are probably formed by reaction of butyl radicals with the formed Sn· or butyl attached to the tin-oxo cage (see Scheme 3.3). A tin (II) compound is formed if a butyl is abstracted by the initially formed butyl radical, while a tin hydride is formed if the tin radical abstracts a hydrogen atom from a butyl radical. Tin hydrides were not observed in the ^{1}H NMR spectrum, which could be due to their short lifetime.

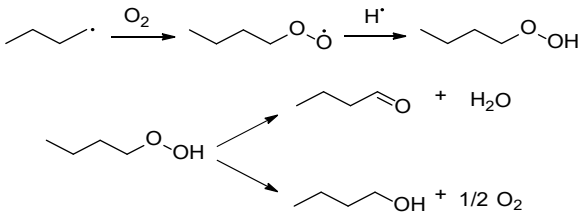

Scheme 3.2: Generation of BuOOH (top), a precursor to BuOH or butyraldehyde (bottom).

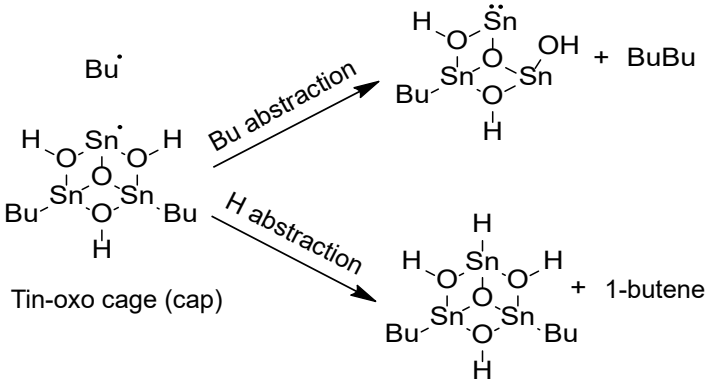

Scheme 3.3: Formation of *n*-octane (BuBu) by butyl abstraction by Bu· (top), and formation of 1-butene by H abstraction (bottom), at the cap of the tin-oxo cage (6-coordinated tin atoms). Each tin atom is bound to two more oxygen atoms, which have been omitted for clarity. The initial radical pair is formed by photodissociation.

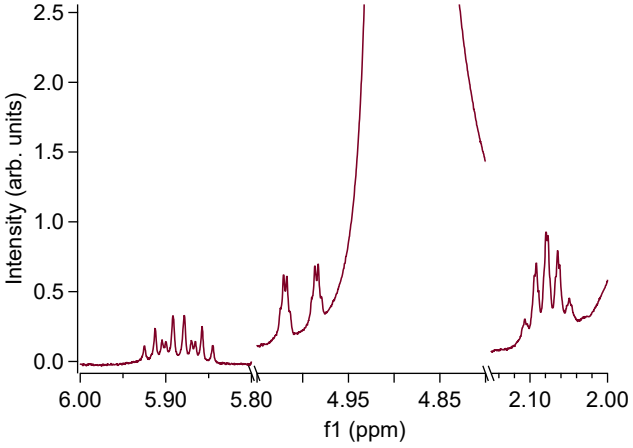

Figure 3.15: 500 MHz ^{1}H NMR spectrum of 2 h DUV exposed TinOH in MeOH-d_4, zoomed-in to show 1-butene peaks.

When zoomed in on the alkene region and acquiring the 1D spectrum after DUV exposure with 512 scans on a 500 MHz NMR spectrometer, 1-butene can be assigned unambiguously as shown in Fig. 3.15 (a full assignment, including coupling constants, is shown in the ESI, Tab. 9.5).[135] Two signals of 1-butene, at 4.90 and 1.00 ppm, are not visible because they overlap with other signals. The signal at 4.90 can be made visible by cooling the sample down to –80 °C, shifting the CD_3OH peak significantly downfield (see ESI, Fig. 9.10).

The *n*Bu peaks all broaden, decrease in intensity and shift slightly downfield. This shows that cleavage of Sn-*n*Bu bonds from the tin-oxo cage is occurring upon DUV absorption. Although calculations suggest that the *n*Bu is cleaved off primarily at the six-coordinate tin atoms,[103] the decrease in intensity of five-coordinated *n*Bu chain signals shows that chemistry is clearly occurring at the five-coordinated tin atoms as well.

The downfield shift is especially pronounced for the Sn_6-$\mathbf{CH_2}$-CH_2-CH_2-CH_3 signal (initially at 1.1 ppm), which at 2 h of DUV exposure overlaps with the iPrOH signal and at 3 h DUV exposure is partially downfield from this iPrOH signal. It is tempting to assign this shifted peak to a butyl chain bound to a Sn_6 atom at which some chemical change (such as a nearby butyl cleavage) has occurred. However, in such case there would be two Sn_6-$\mathbf{CH_2}$-CH_2-CH_2-CH_3 signals, one for unconverted and a shifted signal for converted TinOH. This is clearly not the case. Therefore, the downfield shift of the *n*Bu peaks is likely due to a changed chemical environment, induced by photochemical reactions. The coordination of solvent and/or pH changes after DUV exposure could influence the chemical shift of *n*Bu protons. In addition, rapid exchange of butylstannoic acid (Sn–BuOOH) between tin-oxo cages could occur, leading to an NMR signal that is averaged out.

Upon DUV exposure white insoluble material started to form. These white particles did not dissolve in either polar (H_2O) or non-polar (*n*-hexane) solvents. This could indicate the formation of agglomerated tin-oxo cages.

A control experiment (without exposure) was performed to ensure that the changes in NMR signals arise from the photochemistry. The sample was also stirred the same way as in the photochemistry experiments. The ^{1}H NMR spectrum did not show any significant difference after 2 hours of waiting time (see ESI, Fig. 9.6).

Distillation of volatile photoproducts

The NMR spectrum of DUV-exposed tin-oxo cages contains both photoproduct and tin-oxo cage signals. These signals partly overlap, which complicates product identification. A way to separate photoproducts from remaining tin-oxo cages is distillation. Photoproducts such as 1-butanol, 1-butene, *n*-butane and *n*-octane are volatile, whereas tin-oxo cages are not. Therefore, we performed distillation after exposing tin-oxo cages to DUV in solution (see Section 3.2.5 for details). A custom-made setup (see Fig. 3.1) was used to distill after exposure without exposing the solution to air. The setup also enabled deoxygenation prior to exposure, using the freeze-thaw cycle. In this way, reaction pathways that involve oxygen are excluded.

In Fig. 3.16, the spectrum of distilled volatile photoproducts is shown. Because

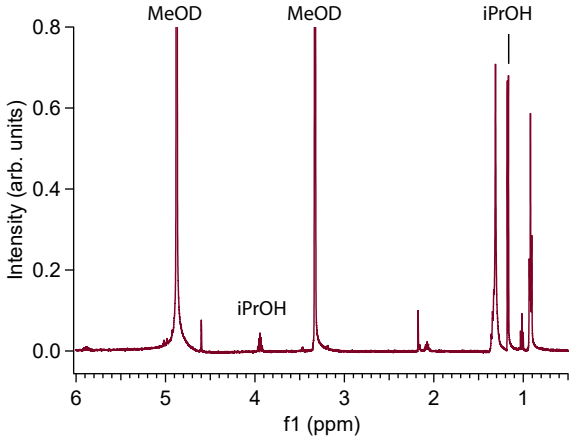

Figure 3.16: 500 MHz ^{1}H NMR spectrum of TinOH in MeOH-d_4, exposed to 45 min. of DUV radiation and distilled. Formed photoproducts are 1-butene (5.89 ppm, 4.99 ppm, 2.08 ppm, 1.02 ppm) and *n*-octane (1.3 ppm and 0.92 ppm). iPrOH peaks (3.94 ppm and 1.17 ppm) are visible as well.

tin-oxo cages are not volatile, they do not give rise to any signal in this spectrum. Signals of 1-butene are present, with an extra triplet at 1.02 ppm (–CH_3) which was previously invisible as a result of overlap with tin-oxo cage signals. The signals at 1.3 and 0.9 ppm are also present, showing a much clearer fine structure. This fine structure matches poorly with *n*-butane,[136] but very well with *n*-octane (see Fig. 3.17). The NMR spectrum of *n*-octane is complex as a result of magnetically inequivalent hydrogen atoms. This is seen in both the experimental spectrum and the literature spectrum.[137] No signals for *n*-butane are found; these would show up as two shoulders slightly downfield of the strongest *n*-octane signal.[136] Its presence cannot be completely excluded; if a small amount were present, its NMR signal could be obscured by the *n*-octane peak.

Other photoproduct signals, such as the triplets at 4.49 (1,1-dimethoxybutane) and 3.55 ppm (1-butanol) (see Fig. 3.14), are not visible in the distilled sample. These products could be formed by a reaction with dissolved O_2 (see Fig. 3.2), which was thoroughly removed before DUV exposure in the case of the distilled sample.

To ensure that the formed photoproducts were a result of DUV photoreactions, two blank experiments were performed. First, pure MeOH-d_4 was distilled in the vacuum setup, after which the NMR spectrum was recorded. The only signals that were recorded besides CD_3OH (4.9 ppm) and $CHCD_2OD$ (3.3 ppm) were acetone at 2.2 ppm (which was used for cleaning the setup before the experiments) and a signal at 4.6 ppm. This signal corresponds to an unknown contamination, but certainly not a photoproduct.

Secondly, a non-exposed solution of TinOH in MeOH-d_4 was distilled as well. The only difference with the first blank is the presence of iPrOH, which is also volatile.

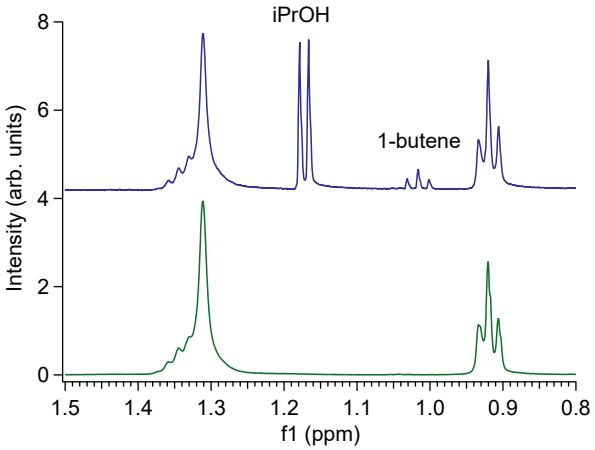

Figure 3.17: 500 MHz ^{1}H NMR spectra, bottom (green): *n*-octane in MeOH-d_4, and TinOH in MeOH-d_4, DUV-exposed for 45 min. and distilled, top (blue). A vertical offset was used on the *y*-axis.

NMR spectra of both blank samples are shown in the ESI (Fig. 9.10).

It should be noted that the NMR analysis of the distilled sample is not very quantitative because no internal standard was added and the amount of distilled iPrOH is unknown. However, with some certainty it can be assumed that more *n*-octane than 1-butene is formed, and that *n*-butane is present only in small quantities if at all.

2D TOCSY NMR

2D TOCSY is a useful method to assign photoproduct signals. The 2D TOCSY spectra after 2.5 h of DUV exposure, zoomed-in on the *n*Bu region and downfield, are shown in Fig. 3.18 and Fig. 3.19 respectively. In the ESI, the couplings are tabulated (Tab. 9.3). Overall, the signals are less well resolved compared to the unexposed sample in Figure 3.7, mainly as a result of broadening of all the *n*Bu peaks. It is notable that all the *n*Bu signals have shifted slightly downfield, with the $Sn_{5/6}$-$\mathbf{CH_2}$-CH_2-CH_2-CH_3 experiencing the largest shift (0.11 ppm for Sn_6 and 0.15 ppm for Sn_5). The shifting of Sn_5-$\mathbf{CH_2}$-CH_2-CH_2-CH_3 resolves this signal from $Sn_{5/6}$-CH_2-CH_2-$\mathbf{CH_2}$-CH_3, which makes it possible to observe that this methylene group appears as a triplet.

The most pronounced new signals after DUV exposure in the downfield region are those of *n*-octane (1.3 and 0.9 ppm) and the two triplets at 4.48 ppm and 3.55 ppm (1,1-dimethoxybutane and 1-butanol). The signals at 1.3 and 0.9 ppm couple with each other, which is consistent with the *n*-octane assignment. Both the 4.48 and 3.55 ppm signals couple with signals overlapping with the Sn_5-CH_2-CH_2-$\mathbf{CH_2}$-CH_3, Sn_6-CH_2-CH_2-$\mathbf{CH_2}$-CH_3 and Sn_6-CH_2-CH_2-CH_2-$\mathbf{CH_3}$ peak.

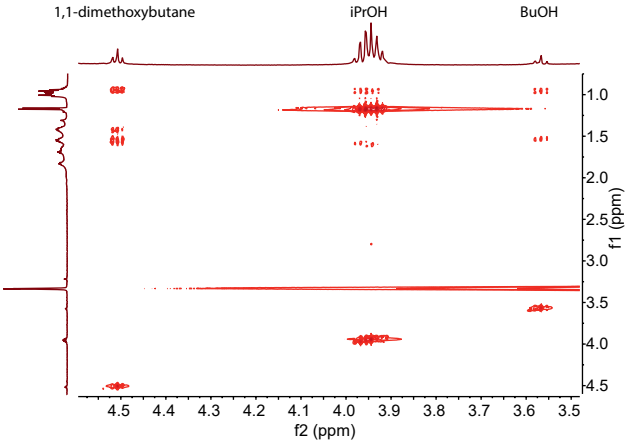

Figure 3.18: Partial 2D TOCSY spectrum of TinOH in MeOH-d_4 after 2.5 h of DUV exposure, zoomed-in downfield.

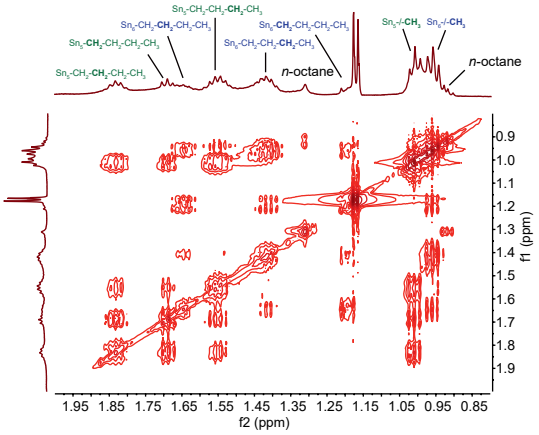

Figure 3.19: Partial 2D TOCSY spectrum of TinOH in MeOH-d_4 after 2.5 h of DUV exposure, zoomed-in on the nBu region. Assignments for the nBu protons are shown as well.

1D selective TOCSY NMR

Recording selective TOCSY spectra is a valuable method to assign signals that are overlapping. For example, except for the 3.55 ppm signal, BuOH proton signals overlap with TinOH nBu signals. Using selective TOCSY and obtaining all couplings to 3.55 ppm, signals at 0.94 ppm (t), 1.38 ppm (sextet), 1.51 ppm (m) and 1.63 ppm are observed. Aside from the signal at 1.63 ppm, this spectrum perfectly matches

a spectrum from BuOH in MeOH-d_4, as shown in Fig. 3.20. The couplings of the amplified signals in the selective TOCSY spectrum match the couplings of BuOH as well. The small peak at 1.63 ppm is probably due to other proton signals that are excited by the 3.55 ppm pulse (see ESI, Fig. 9.11).

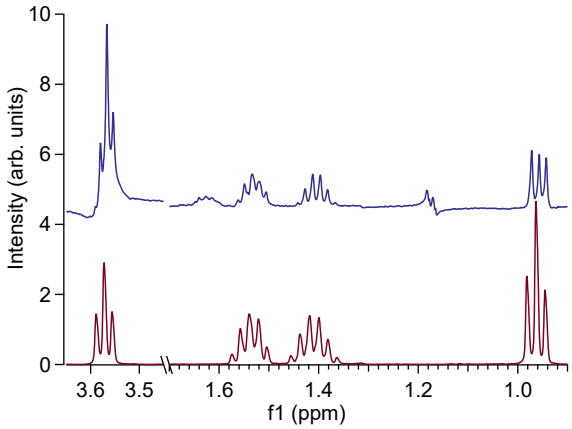

Figure 3.20: Red: BuOH in MeOH-d_4. Blue: Selective TOCSY spectrum of TinOH in MeOH-d_4 after 3.5 h DUV exposure, pulsed at 3.55 ppm. A vertical offset was used on the y-axis.

Signals corresponding to 1,1-dimethoxybutane (acetal of butyraldehyde) also show significant overlap with tin-oxo cage nBu signals, except for the 4.52 ppm signal. The selective TOCSY spectrum that is obtained when pulsed at 4.52 ppm shows similar peaks to the TOCSY spectrum in Fig. 3.20: 0.93 ppm (t), 1.40 ppm (sextet), 1.48–1.58 (overlapping multiplets), as shown in Fig. 3.21. Dissolving butyraldehyde and TinOH in MeOH-d_4 provided a good match with the 1D TOCSY spectrum of 4.52 ppm (see Fig. 3.21). Butyraldehyde reacts with MeOH-d_4 to form the acetal 1,1-dimethoxybutane, as is apparent from the disappearance of the signal at 9.7 ppm (aldehyde proton). This reaction is apparently catalyzed by TinOH, since the aldehyde signal is still present in the red spectrum (butyraldehyde in MeOH-d_4 without TinOH).

A selective TOCSY spectrum was obtained by pulsing at 1.29 ppm (n-octane) as well. The singlet at 1.29 ppm shows a coupling with a triplet at 0.90 ppm (Fig. 3.22), which is consistent with the n-octane assignment. This coupling was also observed in the 2D TOCSY spectrum (see Section 3.3.4).

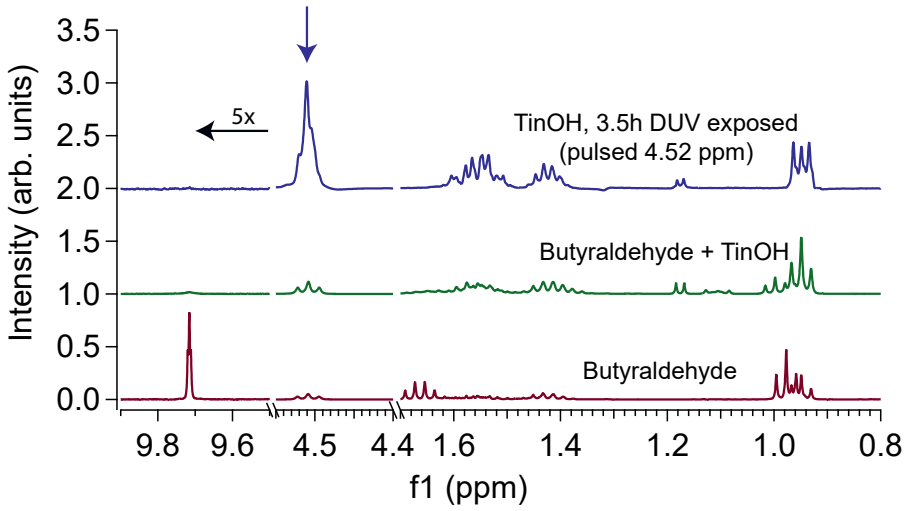

Figure 3.21: Acetal formation in MeOH-d_4, catalyzed by TinOH. Red: NMR spectrum of butyraldehyde in MeOH-d_4. Green: butyraldehyde and TinOH in MeOH-d_4. Blue: selective TOCSY spectrum of TinOH in MeOH-d_4 after 3.5 h DUV exposure, pulsed at 4.52 ppm. A vertical offset was used on the y-axis.

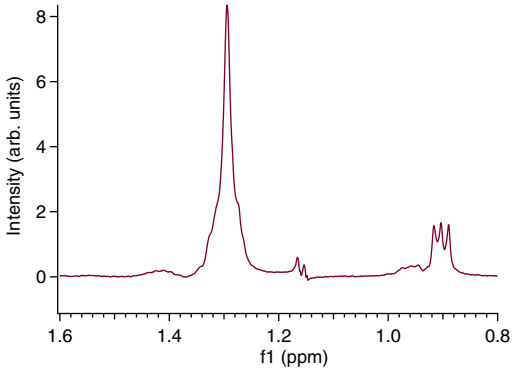

Figure 3.22: Selective TOCSY spectrum of TinOH in MeOH-d_4 after 2.5 h DUV exposure, pulsed at 1.29 ppm.

DOSY NMR

The DOSY spectrum of exposed and unexposed TinOH in MeOH-d_4 is shown in Fig. 3.23. The diffusion coefficient D (f1 axis) of a certain signal is related to its size; smaller molecules diffuse faster. This is described by the Stokes-Einstein equation (Eq. 3.7):

$$R_{\mathrm{H}} = \frac{k_{\mathrm{B}}T}{6\pi\eta D} \tag{3.7}$$

In Eq. 3.7, R_{H} is the hydrodynamic radius (in m), k_{B} is the Boltzmann constant (1.38×10^{-23} m^2 kg s^2 K^{-1}), T is the temperature (in K), η is the viscosity of the solvent (in kg m^{-1} s^{-1}) [MeOH: 5.45×10^{-4}][138] and D is the diffusion coefficient (in m^2 s^{-1}). The hydrodynamic radius is related to the type of solvent and the dynamics of motion and can be viewed as the radius of a hypothetical hard sphere that diffuses with the same speed as the particle under examination.[139] For spheroidal molecules much larger than solvent molecules, R_{H} is considered a good measure for the actual molecular radius.[89]

The value of R_{H} for the tin-oxo cage can be calculated using the diffusion coefficient of the signals corresponding to nBu in the tin-oxo cage material in the DOSY. The four peaks with the lowest log(D) value, at ppm values of 1.83, 1.66, 1.55 and 1.01, were assumed to be the most representative for the diffusion constant. This is because any small impurity in the sample that overlaps in signal with nBu will likely be smaller than the tin-oxo cage. This would shift log(D) to higher values. Additionally, these four signals appear at an almost identical log(D) value. This could mean that these are "clean" signals, without any impurity present that induces signals at the same ppm values. The hydrodynamic radius of the tin-oxo cage, calculated from the average log(D) value of the 4 peaks, is calculated to be 0.78 nm using Eq. 3.7, which is identical to the value reported by Van Lokeren and coworkers.[89]

The 2D DOSY spectrum of TinOH in MeOH-d_4 after 2.5 h DUV exposure (green) is superimposed with the unexposed sample (blue) in Fig. 3.23. The solvent peaks (3.31 ppm and 4.85 ppm) appear at large log(D) values. The peaks in the nBu region are more spread out over multiple log(D) values and appear on average at larger log(D) values in the exposed sample. Since DOSY provides the average diffusion coefficient for one chemical shift and some resonances of small photoproducts overlap with Sn-nBu protons, small photoproducts could significantly shift the measured log(D) to higher values. Although in such cases the intensity vs. gradient strength data can be fitted to a multi-exponential (instead of mono-exponential) decay, obtaining multiple D values, this was not feasible as a result of the limited number of available data points.

The overall shift to higher log(D) values can also be attributed to modifications on the tin-oxo cage itself. For example, a tin-oxo cage in which the nBu chains have been substituted with either –OH or –H would be smaller, giving rise to higher log(D).

The photoproduct signals A (acetal), B (BuOH), C (unknown), D (1-butene) and E (octane/butane) all appear at larger log(D), and therefore smaller R_{H}, than the nBu signals. The R_{H} values for the photoproducts may not be accurate, because the

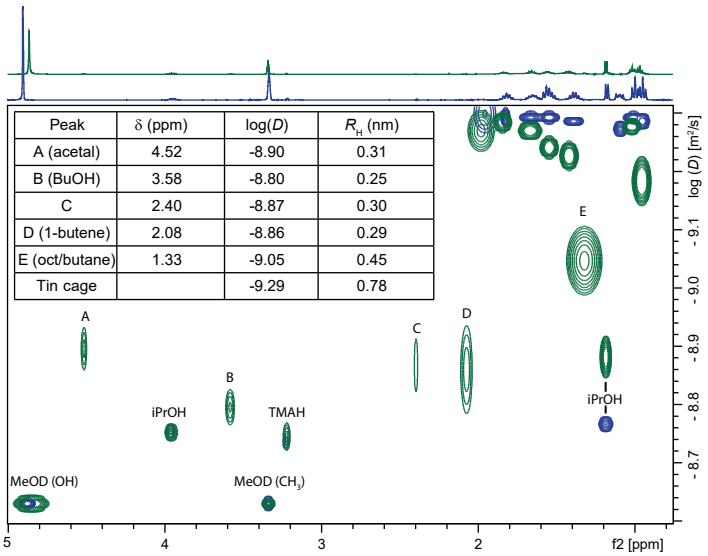

Figure 3.23: 2D DOSY spectra of TinOH in MeOH-d_4. Blue: unexposed. Green: 2.5 h DUV exposed. Product peaks are indicated with capital letters. Inset table shows calculation of the hydrodynamic radius for the product peaks and tin-oxo cage peaks. 1,1-dimethoxybutane is denoted as 'acetal'.

conditions under which the Stokes-Equation applies (spherical molecule of much larger size than the solvent molecules) do not hold. Still, the small size of these molecules is unequivocal. The signals A, B, C, D and E clearly correspond to small photoproducts rather than functional groups that are attached to the tin-oxo cage (for instance a Sn-O-CH_2-CH_2-CH_2-CH_3 group).

Quantitative NMR

In the previous sections, we have assigned signals in the ^{1}H NMR spectrum to photoproducts. Formation of these photoproducts was not yet quantified, however. ^{1}H NMR spectroscopy inherently contains a method for quantification, because peak areas can be a reliable measure for the relative amount of a chemical species. Because the starting amount of tin-oxo cage (in g or in mol) is known, this can be converted to an amount of converted material or to amounts of formed photoproducts.

The quantitative measurements were performed in a quartz NMR tube instead of a quartz cuvette. This has the advantage that sample transfer (from cuvette to NMR tube) need not take place, limiting oxidation and evaporation effects.

^{1}H NMR spectra at different exposure times are shown in Fig. 3.24. The signals in the *n*Bu region are less broadened compared to the ^{1}H NMR spectra at different exposure times when irradiated in a quartz cuvette (Fig. 3.14). Furthermore, photo-

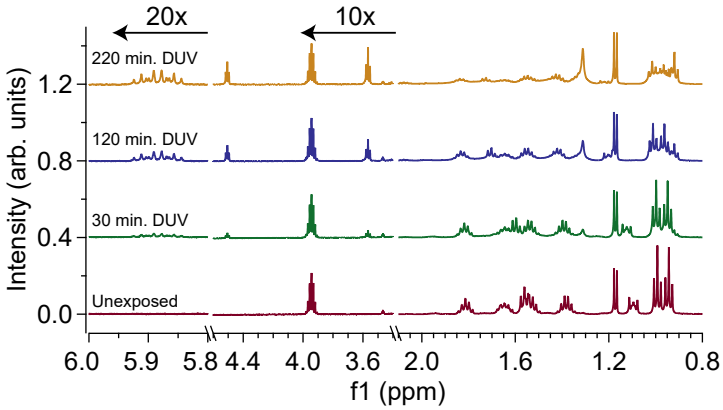

Figure 3.24: Zoomed-in ^{1}H NMR spectra (500 MHz) of TinOH in MeOH-d_4 after multiple DUV exposure times, performed in a quartz NMR tube. From bottom to top: 0 h (red), 30 min. (green), 120 min. (blue) and 220 min. (purple) DUV exposure. A vertical offset was used on the y-axis. The spectra were normalized to the iPrOH C–H peak at 3.95 ppm.

product peaks (especially 1-butene) are sharper.

For a quantitative analysis, we first need to consider solubility of the photoproducts. Material that is above the solubility threshold will not appear in the NMR spectra; especially gases can easily escape. Although butane and 1-butene are both gases at standard temperature and pressure, their solubility in methanol is considerable: both around 4 mol%.[140,141] In the ESI (Section 9.3.2), it is shown that this is more than sufficient for dissolution of all formed butane or 1-butene.

iPrOH was used as internal standard for this measurement. iPrOH is present in TinOH powder because it is part of its crystal structure.[107] The septet at 3.95 ppm (C–H) is well isolated from photoproduct and Sn-nBu signals. By comparing the intensity of other peaks to this iPrOH peak, the amount of generated products (in mol) and the loss of Sn-nBu can be calculated. This is shown in the ESI (Section 9.3.2).

A clear difference with the quartz cuvette measurement is that the signals for n-octane at 1.3 ppm and 0.9 ppm are much more prominent for the quartz NMR tube measurement (compare e.g. Fig. 3.24 with Fig. 3.14). This can be explained by the smaller involvement of oxygen in the reaction; the NMR tube remained closed at all times whereas the cuvette was opened several times to take aliquots. If oxygen is present in lower concentrations, butyl radicals are more likely to react with other butyl groups attached to the tin-oxo cage (see Fig. 3.3).

Product peaks increase upon exposure while peaks corresponding to Sn–nBu decrease. This can be quantified by peak integrals. For most product peaks this is straightforward, but for n-octane the signal overlaps with Sn_6-CH_2-CH_2-$\mathbf{CH_2}$-CH_3 (see Fig. 3.25). Additional issues are a non-constant baseline and a downfield shift

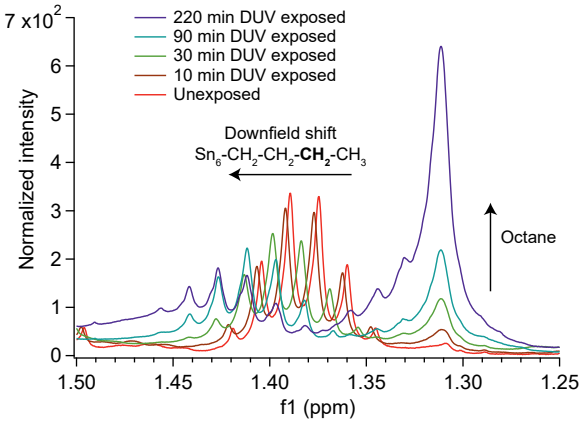

Figure 3.25: Evolution of octane and decrease and downfield shift of the 1.38 ppm signal (Sn_6-CH_2-CH_2-$\mathbf{CH_2}$-CH_3) upon DUV exposure. All spectra were normalized to the iPrOH C–H peak at 3.95 ppm.

of (especially) the Sn_6-*n*Bu signals. This complicates quantification of *n*-octane formation and loss of Sn_6-*n*Bu. An approximation for these effects was made as follows. First, the baseline was corrected by correcting for the slope between approximately 1.48 ppm (downfield from both signals) and 1.26 ppm (upfield from both signals). *n*-octane formation was quantified by calculating the integral between 1.32 and 1.28 ppm (no overlap). This was multiplied by the ratio between the complete peak area (1.375–1.26 ppm) and the area between 1.32 and 1.28 ppm. This ratio was calculated using the 220 min. exposed spectrum, which has negligible overlap between the Sn_6-*n*Bu and *n*-octane signals. A baseline (complete peak area 1.32–1.28 ppm at $t = 0$, resulting from small impurities in the MeOH-d_4) was subtracted from the resulting area values.

For the Sn_6-CH_2-CH_2-$\mathbf{CH_2}$-CH_3 signal, the integral was taken between the middle of the signal (as determined by the minimum of the sextet structure) and 0.04 ppm downfield from it (end of sextet structure). This downfield half of the peak has no significant overlap with the *n*-octane signal. The full peak integral was calculated by multiplying with 2. This integral was used to track loss of Sn_6-*n*Bu.

For the other peaks, calculation of peak integrals was more straightforward. All other photoproducts give rise to at least one peak that does not significantly overlap with the Sn-*n*Bu signals: 1-butene at 5.9 ppm, 1,1-dimethoxybutane at 4.5 ppm, BuOH at 3.55 ppm, and butyraldehyde at 2.4 ppm. The amount of Sn_5-*n*Bu was determined using the peak at 1.82 ppm (Sn_5-CH_2-$\mathbf{CH_2}$-CH_2-CH_3). Although this peak also undergoes downshift, and a correction for the baseline was necessary, this peak does not significantly overlap with any known photoproducts.

In Fig. 3.26, the amount of formed products is plotted vs. exposure time. It can be seen that photoproduct formation scales approximately linearly with exposure time; there is no evidence that formation of any product occurs via a secondary mechanism

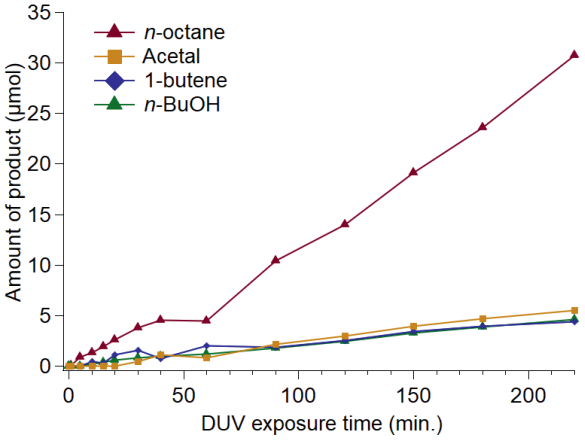

Figure 3.26: Amount of product arising from the DUV photochemistry of TinOH (8.5 µmol in 0.6 mL MeOH-d_4), as a function of exposure time.

Table 3.2: Yield of the five most important photoproducts (in µmol), starting from an 8.2 µM solution of TinOH. Rate of formation is shown (as calculated by linear fit), as well as selectivity (assuming no other product formation). 1,1-dimethoxybutane is denoted as 'acetal'.

	1-butanol	Acetal	1-butene	Butyraldehyde	*n*-octane
10 min.	0.22	0	0.43	0	2.76
30 min.	0.86	0.43	1.58	0	7.61
90 min.	1.79	2.15	1.86	0.14	21.1
220 min.	4.66	5.59	4.44	0.57	62.2
Rate (nmol/min.)	21.0	26.7	20.1	2.62	133
Selectivity	10.3%	13.1%	9.9%	1.3%	65.4%

(i.e. a photoproduct is converted by DUV into a secondary product). Fluctuations can be attributed to either statistical errors (signal to noise ratio of the NMR spectrum) or systematic errors such as insufficient homogeneity of the measured solution. Clearly, the main formed product is *n*-octane; the other products are formed in much lower quantities (see Table 3.2).

The quantitative analysis can also be used for measuring conversion of Sn_5-*n*Bu and Sn_6-*n*Bu. Some complications arise, however. The area of the Sn_5-CH_2-$\mathbf{CH_2}$-CH_2-CH_3 peak (1.81 ppm) is not equal to that of Sn_6-CH_2-CH_2-$\mathbf{CH_2}$-CH_3 (1.41 ppm), even without photo-exposure. This is possibly due to differences in the relaxation time T_1.[142] As a result, it was difficult to accurately quantify loss of Sn-*n*Bu. Therefore, a "relative loss" of Sn_5-*n*Bu and Sn_6-*n*Bu was calculated by dividing areas of 1.81 ppm and 1.41 ppm peaks with their values at $t = 0$. This is shown in Fig. 3.27a. In

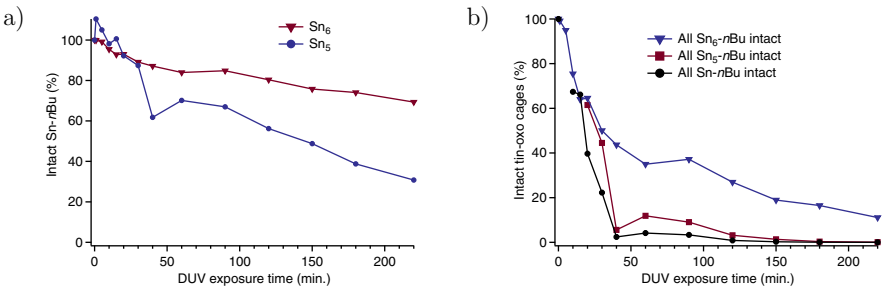

Figure 3.27: (a) Relative loss of Sn_5-*n*Bu (blue) and Sn_6-*n*Bu (red), as calculated from 1.81 ppm and 1.41 ppm peak areas. (b) Amount of intact tin-oxo cages: tin-oxo cages with all Sn_6-*n*Bu intact (blue), tin-oxo cages with all Sn_5-*n*Bu intact (red), and tin-oxo cages with all Sn-*n*Bu intact (black).

contrast with predictions,[103] the Sn–C cleavage appears to take place predominantly at the 5-coordinated site.

To calculate the chance P that a TinOH molecule has lost *at least one* 5-*n*Bu chain, we need to consider that this chance is equal to one minus the chance that it has lost *no* 5-*n*Bu chains ($P_{\text{no 5-butyl loss}}$). If we assume that all cleavage events are independent, $P_{\text{no 5-butyl loss}}$ is equal to the chance that one particular 5-*n*Bu chain is cleaved off to the power of six (because there are six butyl groups bound to 5-coordinated tin). This is described in Eq. 3.8. This equation is valid under the assumption that each Sn–C cleavage is random (i.e. does not depend on whether a previous Sn–C cleavage has taken place on the same tin-oxo cage). The chance that one particular butyl group is cleaved is then equal to the total fraction of cleaved butyl groups in the entire population of tin-oxo cages.

$$P_{\text{at least one 5-butyl loss}} = 1 - P_{\text{no 5-butyl loss}} = 1 - \left(\frac{N_{\text{5-butyl non-cl.}}}{N_{\text{5-butyl initial}}}\right)^6 \tag{3.8}$$

In Eq. 3.8, $N_{\text{5-butyl initial}}$ is the total initial number of 5-butyl chains in the entire population of tin-oxo cages. $N_{\text{5-butyl non-cl.}}$ is the total number of 5-butyl chains (in the entire population) that have not been cleaved off. Obviously, the same equation applies to the loss of 6-butyl chains. The results are shown in Fig. 3.27b, which shows the relative amount of intact tin-oxo cages. It can be seen that after 50 minutes of DUV exposure, almost no intact tin-oxo cages remain, even though the majority of *n*Bu groups have not yet been cleaved off (see Fig. 3.27a).

The quantum yield (Φ) of Sn–C cleavage can be measured as well. Φ was defined by the number of cleaved Sn–C bonds (calculated from photoproduct signals) divided by the number of absorbed photons. The number of absorbed photons was calculated by dividing the total amount of energy for a certain exposure time by the energy of a DUV photon (8.8×10^{-19} J). It was assumed that all light from the laser pulses was absorbed.

The amount of converted Sn_5-*n*Bu and Sn_6-*n*Bu as calculated by the 1.41 and

1.81 integrals (see Fig. 3.27a) may not be completely accurate. As discussed before, their initial values are already different. Therefore, it may be better to calculate the quantum yield by using the photoproduct signals. As a measure for the quantum yield, it is most accurate to use the reaction rate (in mol/min.), which was obtained by fitting the lines in Fig. 3.26 to linear functions. It was found that approximately 0.23 µmol of photoproduct was formed per minute of DUV exposure. If we convert this to the number of Sn–C cleavage events per number of photons, and assume that *n*-octane is formed by only one cleaved butyl, we obtain a quantum yield of around 20% for Sn–C cleavage. This is significantly lower than the quantum yield found by the UV-Vis spectroscopy experiments in methanol (60–70%, see Section 3.3.1). This is probably due to reflection losses, which lead to an overestimation of the number of absorbed photons. The used NMR tube (5 mm) was slightly smaller than the laser spot, and reflection losses occur on the cylindrical NMR tube.

Formation of *n*-octane can occur either through simple combination of two butyl radicals, or by butyl abstraction from another Sn–Bu (see Scheme 3.3). Given the high quantum yield, the latter appears to be more probable. In this scenario, only one photo-induced Sn–Bu cleavage would be required to yield one *n*-octane molecule.

3.4 Conclusion

In this chapter, the DUV photochemistry of TinOH and TinA was studied in solution. Clearly, Sn–C cleavage is the dominant photoreaction upon DUV photon absorption on tin-oxo cages. In UV/Vis experiments, the initial quantum yield of this cleavage was estimated to be 60–80%.

The nature of the Sn–C cleavage was studied using a spin trapping experiment. The molecule TEMPO (containing an unpaired electron) induces a paramagnetic shift on the chemical shift of a reference compound. This paramagnetic shift decreased upon DUV exposure of a TEMPO+TinOH solution, indicating a decrease in the concentration of TEMPO. This decrease was induced by a chemical reaction between TEMPO and butyl radicals. This proves that the Sn–C cleavage is homolytic, producing a butyl radical and a tin-centered radical. Formation of a TEMPO-butyl adduct, visible in the NMR spectrum, formed additional proof of this photoreaction. Photoproducts were further studied using NMR spectroscopy. In the 1D ^{1}H NMR spectrum of DUV exposed TinOH in MeOH-d_4, several new signals appeared, corresponding to photoproducts. Diffusion-ordered (DOSY) NMR showed that these signals corresponded to small molecules, rather than functional groups attached to the tin-oxo cage. Using total correlation NMR spectroscopy (TOCSY), the signals were assigned to *n*-octane, 1-butene, 1-butanol and 1,1-dimethoxybutane. Formation mechanisms for these products are proposed (see Scheme 3.4).

When the solution of TinOH was degassed before DUV exposure and the solution was distilled, only *n*-octane and 1-butene were found in the NMR spectrum. This indicates that the other products (1-butanol and 1,1-dimethoxybutane) are formed by reaction with dissolved oxygen. No signals for *n*-butane could be seen, which means that it is probably formed only in low quantities. This is quite different from EUV photochemistry in thin tin-oxo cage films, where *n*-butane and 1-butene are major products, and *n*-octane is minor.[111]

The formation of products was quantified using the NMR peak areas. Production of *n*-octane was found to be by far the most prominent photoreaction (65% selectivity). *n*-Octane can be formed by recombination of two *n*-butyl radicals or by abstraction of a butyl group from the cage by a butyl radical. The generation rate of *n*-octane was found to be much higher for a sample that was irradiated in a quartz NMR tube instead of a cuvette. Less involvement of oxygen is a possible reason for this. The quantum yield was found to be around 20%, which is however a lower bound because reflection losses are not taken into account.

This chapter shows that radical chemistry plays a major role in the initial photoreaction. Initially formed radicals can either recombine or react further. Possible intermediates are tin (II) and Sn–H. In the solid state, the quantum yield was generally found to be lower than the results shown in this chapter.[111] This can be attributed to the formation of a "radical cage pair", which is much more stable in a solid film than in solution. Inhibiting recombination of the Sn·/C· caged pair could drastically increase the sensitivity of organometallic photoresist materials in thin films.

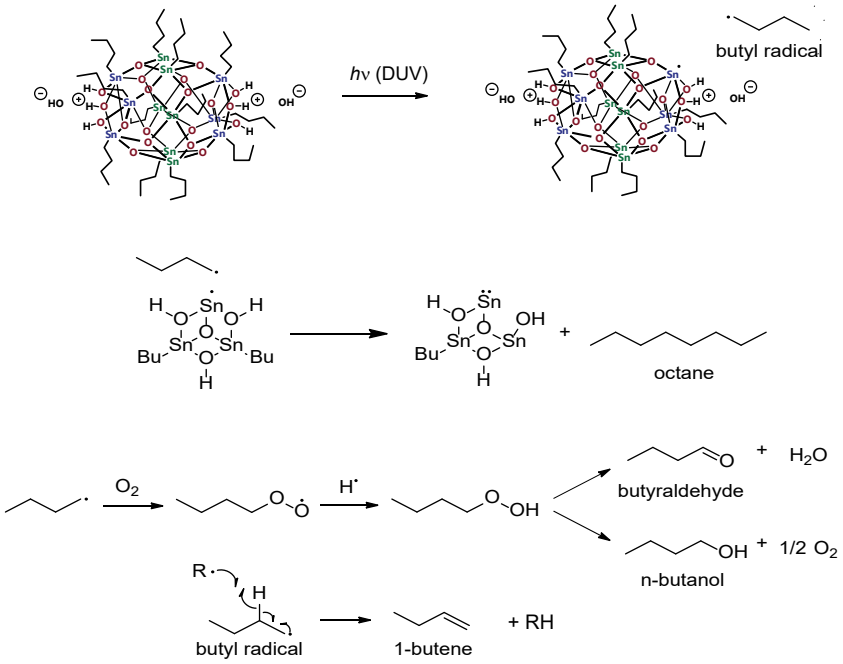

Scheme 3.4: Photoreaction scheme describing formation of photoproducts upon DUV exposure of a TinOH solution in MeOH-d_4.

3.5 Acknowledgments

The author acknowledges Jan Meine Ernsting, Eline van den Heuvel, Michiel Hilbers, Xander Schaapkens, Daniel Smith and Janita Vermeulen for their contribution to this work.

CHAPTER 4

UV and VUV-induced fragmentation of tin-oxo cage ions*

Abstract

Tin-oxo cage materials are of interest for use as photoresists for EUV (Extreme Ultraviolet) lithography (13.5 nm, 92 eV), owing to their large absorption cross section for EUV light. In this work we exposed tin-oxo cage cations in the gas phase to photons in the energy range 4–35 eV to explore their fundamental photoreactivity. At all energies above the onset of electronic absorption at ∼5 eV (∼250 nm), homolytic cleavage of tin-carbon bonds was observed. With photon energies > 12 eV (< 103 nm), dissociative photoionization occurred for the dication (M^{2+}), competing with the regular fragmentation process. The photoionization threshold is lowered by approximately 2 eV if one counterion (triflate or tosylate) is attached to the tin-oxo cage ($MOTf^+$ and $MOTs^+$), as a result of the weaker electrostatic force. Addition of counterions also affects the fragmentation pathways; photoexcitation of $(MX)^+$ (X = counterion, OTf or OTs) always leads to formation of $(MX–2Bu)^+$ rather than $(MX–Bu)^+$. $MOTs^+$ was found to be much more reactive than $MOTf^+$ in terms of reaction products per absorbed photon. A possible explanation for this is proposed, which involves the counterion reacting with the initially formed tin-based radical.

*Some of the results presented in this chapter were published in: J. Haitjema, L. Wu, A. Giuliani, L. Nahon, S. Castellanos, A. M. Brouwer, *J. Photopolym. Sci. Tec.*, 2018, **31**, 243–247

4.1 Introduction

Photoresists that are specifically designed for extreme ultraviolet (EUV, 13.5 nm) radiation have attracted considerable interest recently.[97,143,144] For instance, incorporating metal atoms in the resist formulation can increase the EUV absorption considerably.[101,145] The more efficient use of the photon flux may compensate for the absence of chemical amplification, which is the sensitivity enhancement mechanism of current photoresists that are based on photo-acid generation. A photoresist without photo-acid generators may have lower chemical noise, because the photo-acids (and quenchers) have an inherent random distribution within the photoresist layer. Additionally, acid diffusion contributes to blurring of the pattern.[94,146] Most importantly, strong absorption of the photoresist allows the use of thinner layers. Smaller aspect ratios can then be achieved, which are more suitable for small critical dimensions, because they are less prone to pattern collapse.[34] Therefore, a highly absorbing photoresist without photo-acid generators may have better photoresist performance in terms of the well-known parameters resolution (scale of patterning), sensitivity (number of photons needed) and line edge roughness (deviation of the resist pattern from the intended image).

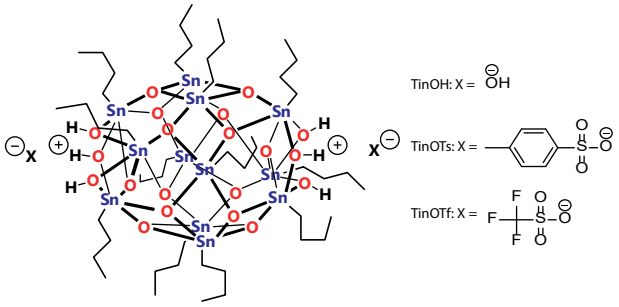

Figure 4.1: Tin-oxo cage in the three forms used in this chapter: TinOH (hydroxide counterions), TinOTs (tosylate counterions), and TinOTf (triflate counterions). For TinOH, the dication (M^{2+}) was isolated, for TinOTf and TinOTs the monocations ($MOTf^{+}$, $MOTs^{+}$).

An example of such a material is the tin-oxo cage (see Fig. 4.1).[88,103,114] This cage consists of a tin-oxo core with 12 organic groups (in the present case *n*-butyl chains) attached to the tin atoms. The absorption of a thin film of this material at 13.5 nm is very high ($\sim$13 μm^{-1} compared to $\sim$5 μm^{-1} for conventional polymer-based resists).[46] The tin-oxo cage materials turn insoluble upon EUV radiation, thus having the properties of a negative tone resist. The solubility change upon irradiation also occurs for electron-beam and UV radiation. The mechanism behind the solubility change of the tin-oxo cages (and related materials) is still under investigation. Knowledge of the chemical mechanism is paramount for the design of novel metal-containing

materials with even better resist performance.[147] Ideally, one would expose the photoresist to EUV radiation and analyze the reaction products afterwards, or even *in situ*. However, the analysis of chemical changes in nanometric films is challenging and a combination of surface analysis and other techniques is necessary to unequivocally identify the products of radiation.

Another way to study the reaction mechanism is through gas-phase photofragmentation experiments on trapped ionic species.[148–151] This method was very recently used for a study on organometallic molecular hybrid materials that can potentially be used as photoresists.[67] The bare tin-oxo cage can conveniently be isolated in the gas phase as the 2+ ion (Fig. 4.1) using electrospray, without any need for prior photoionization, and trapped in a linear ion trap or quadrupole trap.[113] Monocations, with one counterion attached, can also be isolated in the gas phase. In this work, we have chosen to study the counterions trifluoromethylsulfonate (triflate, OTf^-) and *p*-toluenesulfonate (OTs^-). It was found that the complex of the tin-oxo cage bound to (one of) these counterions could be conveniently isolated in the gas phase. The counterion could have an influence on the reactivity; for example, the tin-oxo cage with trifluoroacetate counterions (TinF) was found to be less responsive to EUV light than the tin-oxo cage with acetate or hydroxide counterions, even though the fluorine atoms enhance EUV absorptivity.[111] The reason for this lower sensitivity is still not completely clear.

The aim of this chapter is to thoroughly study UV and VUV fragmentation and ionization pathways for the tin-oxo cage dication and monocations (with one counterion). These pathways depend on the photon energy. At low energies, only excitation to bound electronic states (e.g. HOMO $\rightarrow$ LUMO) is possible, whereas at higher energies valence electrons can be ejected into the continuum (ionization). Tin 4d electrons could in principle also be ejected; their binding energy was found to be about 27 eV,[152] which is accessible with the used synchrotron source. While further reaction steps occur in a photoresist film, the gas phase experiments pinpoint reactive sites within the molecule and allow us to elucidate the initial reaction steps.

4.2 Experimental

4.2.1 Sample preparation and measurements

Tin-oxo cage materials were prepared as described before (see Chapter 2).[88] The tin-oxo cage was synthesized with tosylate counterions (TinOTs), after which the material was converted to hydroxide form (TinOH) by ion exchange using aqueous tetramethyl ammonium hydroxide.[114] The tin-oxo cage in triflate form (TinOTf) was prepared by reacting TinOH with two molar equivalents of trifluoromethanesulfonic acid.[89] A characterization of TinOTf (^{1}H and ^{19}F NMR spectra) can be found in the ESI (Fig. 9.12). UV absorption spectra were recorded with a Shimadzu 2700 spectrometer, using spectroscopic grade ethanol (EtOH) as a solvent.

The tin-oxo cage compounds were dissolved in methanol (concentration $\sim$10 µM), filtered and electrosprayed for the gas phase VUV exposure experiments, using a sy-

ringe pump with a flow rate of about 5 µL/min. Ions with m/z 1218 (M^{2+}), 2585 ($MOTf^{+}$) and 2607 ($MOTs^{+}$) were trapped in a commercial linear ion trap (Thermo Finnigan LTQ XL) coupled to the DESIRS VUV beamline of the SOLEIL synchrotron.[153,154] The trapping range was 30 m/z for all fragments; for example for the dication (m/z 1218) all ions with an m/z between 1203 (1218 − 15) and 1233 (1218 + 15) were trapped.

Photofragmentation was monitored for different photon energies, using 0.1 eV steps between 4.1 and 22.0 eV and 0.15 eV steps between 20.15 and 35.0 eV. The UV and VUV photons had an approximate spot size of 0.3 mm^2, a small energy bandwidth (approximately 12 meV at 10 eV)[151] and were free of high harmonics owing to the use of a Kr gas filter (7–14 eV) and a quartz window (4–7 eV). The photon flux was in the 10^{12}–10^{13} photons/s range and was measured independently in a reference scan, using an AXUV100 photodiode (International Radiation Detectors) under the measurement conditions. The light dose was kept low to limit (sequential) two-photon processes, aiming for ≤10% conversion of the primary ions to photoproducts. The dose was controlled by the exit slit and a mechanical shutter that controlled the irradiation time of the trapped ions between 65 and 2000 ms.

4.2.2 Data analysis

Results were obtained in the form of mass spectra for each photon energy, with intensity (I) obtained as a function of the mass-to-charge ratio (m/z). All shown mass spectra in this chapter were normalized to the precursor ion intensity.

To quantify formation of fragments as a function of photon energy, *action spectra* were also obtained. These spectra show the relative yield of fragments at each photon energy. To obtain meaningful results, this relative yield should be corrected for the number of incident photons (to correct for dose fluctuations) and for the total ion current *TIC* (to correct for fluctuations in the electrospray source). The relative intensity of fragment A can thus be calculated in the following way:

$$I_{\mathrm{A(rel)}} = \frac{I_{\mathrm{A}}}{TIC \cdot N_{\mathrm{phot}}} \tag{4.1}$$

In Eq. 4.1, I_{A} is the relative intensity for fragment A, measured by the peak area. The integration range was chosen to be the predicted average mass-to-charge ratio plus or minus 7 (3+ ions), 14 (2+ ions) or 28 (1+ ions), rounded to the nearest whole number. *TIC* is the total ion current, measured by calculating the area of the complete mass spectrum. The number incident of photons N_{phot} is given by:

$$N_{\mathrm{phot}} = \Phi_{\mathrm{q}} \cdot t \cdot \frac{w_{\mathrm{exp}}}{w_{\mathrm{ref}}} \tag{4.2}$$

In Eq. 4.2, Φ_{q} is the photon flux in s^{-1} measured in the reference scan, t is the irradiation time in s, w_{meas} is the slit width during the experiment (in µm), and w_{ref} is the slit width during the reference scan (in µm).

4.3 Results and discussion

4.3.1 Mass spectrum (without photons)

The ESI-MS mass spectrum of the tin-oxo cage was reported earlier by Dakternieks and coworkers,[113] who observed a main peak at m/z 1218, assigned to the dication $[(n\mathrm{BuSn})_{12}\mathrm{O}_{14}(\mathrm{OH})_6]^{2+}$. This peak is quite broad and shows an intricate structure, as a result of the 10 stable isotopes of tin. The high mass resolution of our instrumentation allowed us to resolve the isotope pattern (see Fig. 4.2). The pattern reveals the 2+ charge, because the spacing between the subpeaks is half an m/z unit.

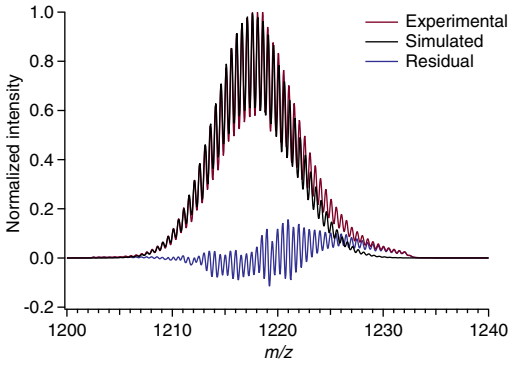

Figure 4.2: Electrospray ionization (ESI) mass spectrum of $[(n\mathrm{BuSn})_{12}\mathrm{O}_{14}(\mathrm{OH})_6]^{2+}$ (M^{2+}), showing the precursor peak centered at m/z 1218 and a broad isotope pattern. This experimental spectrum is an average of the 36 photofragmentation spectra in the range 4.1–7.6 eV. The precursor peak did not show a significant difference at different incident photon energies. For comparison, the black line shows a spectrum predicted by the online tool "Chemcalc" (resolution: 3200, full width half max. ≈ 0.38).[155] The bottom blue line shows the residual.

A similar isotope pattern was predicted by the online tool Chemcalc,[155] which is based on a method by Yamamoto and McCloskey.[156] Predicting mass spectra for isotopically complex molecules such as the tin-oxo cage is by no means trivial,[157] but a reasonable approximation can be made. As can be seen, the experimental spectrum mostly matches the predicted one. A slight deviation can be observed towards higher masses. The residuals show a periodic structure, which suggests that the masses are slightly misaligned. This could be related to imperfections in the experimental m/z calibration.

Depending on electrospray conditions, a peak with a lower m/z (1190) also appeared in the mass spectrum. This corresponds to a tin-oxo cage of which one of the butyl chains has been lost. By tuning the electrospray settings and applying a mass filter, we made sure that only $[(n\mathrm{BuSn})_{12}\mathrm{O}_{14}(\mathrm{OH})_6]^{2+}$ (precursor ion, M^{2+}) was present in the ion trap before irradiation.

4.3.2 UV and VUV irradiation on tin-oxo cage dications

In an initial set of experiments, we exposed the tin-oxo cage dication to UV light ranging from 4 to 7 eV (310–177 nm). In this range the tin-oxo cage in solution shows a strong absorption centered around 220 nm (see Chapter 3). According to DFT calculations (LANL2DZ basis set, B3LYP and ωB97DX density functionals), the Highest Occupied Molecular Orbital (HOMO) is primarily located on the six-coordinated Sn atoms and has a Sn–C bond character. The LUMO is located on the central belt of the cage and consists mainly of tin 5d-orbitals, although it also has significant Sn–C σ* character.[103]

The tin-oxo cage undergoes photoreactions upon 225 nm exposure in solution, as described in Chapter 3. In the current chapter, we aim at shedding light onto the photofragmentation in the gas phase, i.e. onto the intrinsic reactivity of the isolated dications and monocations (with attached counterion).

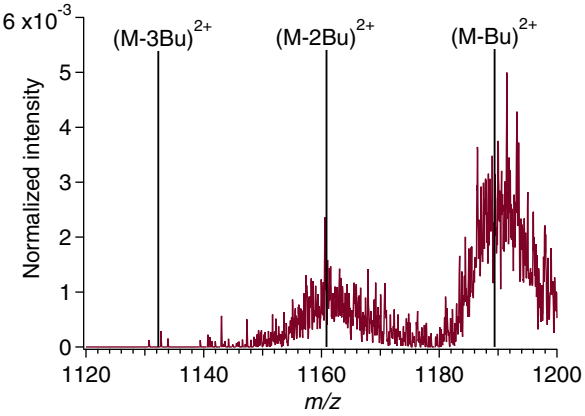

Figure 4.3: Mass spectrum with 7 eV (177 nm) incident photon energy at m/z values just below the precursor ion peak (m/z 1218). Vertical lines indicate the m/z corresponding to loss of butyl (Bu): M–3Bu (m/z 1132.5), M–2Bu (m/z 1161) and M–Bu (m/z 1189.5). Number of incident photons: 5.5×10^{11}.

The photofragmentation spectrum of the tin-oxo cage at a photon energy of 7.0 eV is shown in Fig. 4.3. It can be seen that the precursor ion (M^{2+}) easily loses a butyl chain (Bu) upon photon absorption. This indicates cleavage of Sn–C bonds as the primary process in the electronically excited state. The isotope pattern shows that the fragments are doubly charged. It can be seen that one or two butyl chains are lost, but there are no peaks corresponding to loss of three or more butyl chains.

In Fig. 4.4, the *action spectrum* of $(M–Bu)^{2+}$ and $(M–2Bu)^{2+}$ is shown (see Experimental for data processing details). It can be seen that the fragmentation yield of $(M–Bu)^{2+}$ is low below 5 eV, peaks around 5.6 eV and increases again at higher energies (see Fig. 4.4). Although the 1204–1232 m/z peak area <5 eV is slightly above zero, a closer examination shows that this is caused by spectral background and not

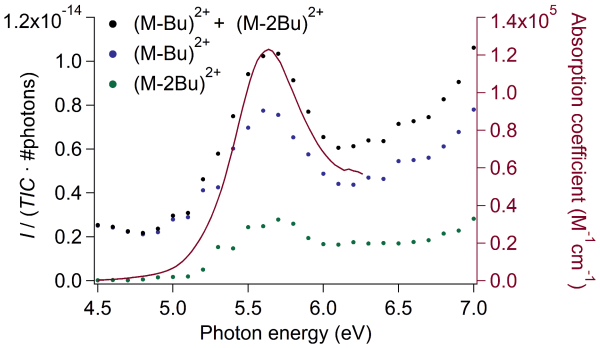

Figure 4.4: Comparison between absorption spectrum of TinOH in EtOH solution (red line) and action spectrum of $(M–Bu)^{2+}$ and $(M–2Bu)^{2+}$ in the gas phase (blue and green dots, sum of both given by black dots).

by the presence of $(M–Bu)^{2+}$ (see ESI, Fig. 9.13). Presumably, there are always some background counts that give rise to a signal.

A similar excitation onset was found for $(M–2Bu)^{2+}$. This fragment could be formed as a result of excess energy that remains in the system after cleavage of the first butyl group, which requires only about 2.2 eV.[71] Cleavage of the second butyl group is expected to require even less energy, according to DFT calculations.

The spectral shape of both action spectra is the same as the shape of the absorption spectrum of TinOH in EtOH (blue line), which indicates that photofragmentation in this energy regime scales more or less linearly with the absorption coefficient. At photon energies > 6.3 eV, no reliable solution absorption spectrum could be recorded, because the solvent (EtOH) absorbs too strongly in this range. The gas phase experiment, however, shows a clear increase in absorption above 6.5 eV.

At VUV energies (between 7 and 13.5 eV), other fragments could additionally be observed (see Fig. 4.5). $(M–Bu)^{2+}$ is still the most abundant, although multiple butyl chain losses (up to M–5Bu) are now detected as well. The subsequent fragmentation reactions are likely a result of the higher internal energy that remains in the various $(M–n\mathrm{Bu})^{2+}$ intermediates at higher photon energies. We cannot, however, exclude photoreactions occurring from higher electronically excited states.

Between M–2Bu and M–3Bu, a broad feature is present in the mass spectrum, of which the origin is unclear. It could correspond to the loss of 2 butyl groups and one or multiple hydroxide(s).

As can be seen, fragmentation is much stronger at these higher photon energies. The relative intensity of the main fragment peak is only 5×10^{-3} of that of the total in Fig. 4.3, but $\sim 60\times$ larger in Fig. 4.5, although the photon number in the latter case is only $3\times$ larger. The fragmentation yield of $(M–Bu)^{2+}$ increases gradually with photon energy (see Fig. 4.7) until it reaches a maximum around 13 eV, after which it gradually decreases. This decrease is due to competition with other fragmentation and ionization processes.

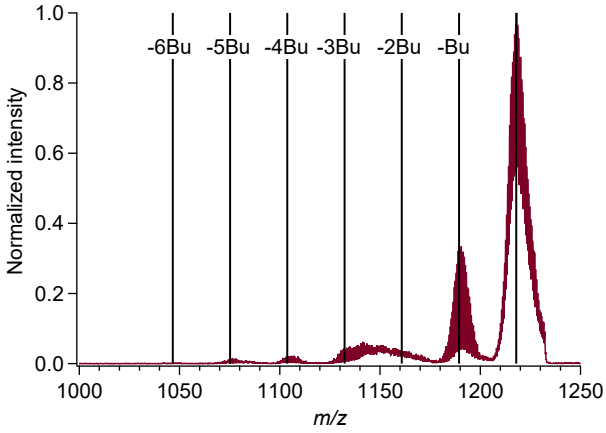

Figure 4.5: Mass spectrum of the tin-oxo cage dication with incident light of 92 nm (13.5 eV), showing only 2+ ions. Vertical lines indicate the main peak (m/z 1218) and peaks indicating various butyl chain losses. Number of incident photons: 1.7×10^{12}.

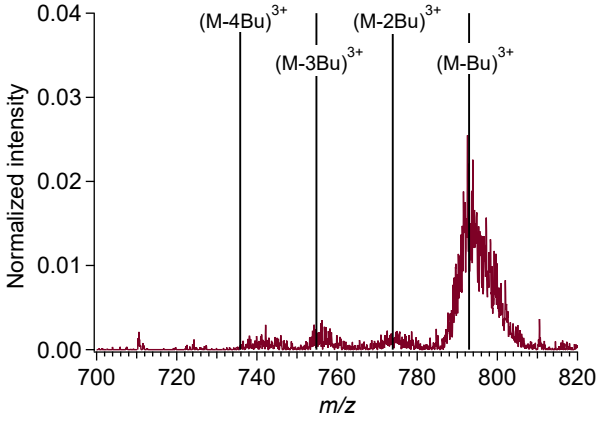

Figure 4.6: Mass spectrum of the tin-oxo cage dication with incident light at 92 nm (13.5 eV), in the 3+ range of the spectrum. Vertical lines indicate the peaks corresponding to loss of multiple butyl groups. Number of incident photons: 1.7×10^{12}.

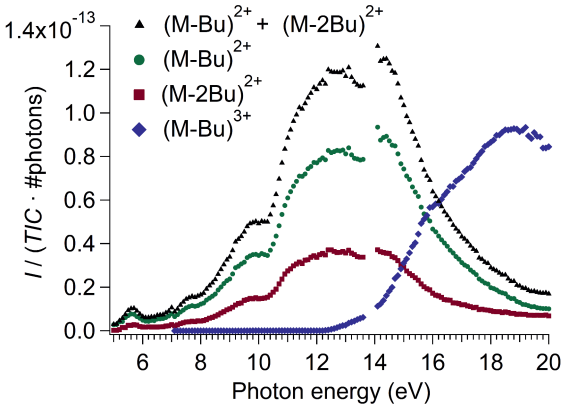

Figure 4.7: Action spectra of $(M–Bu)^{2+}$, $(M–2Bu)^{2+}$ and $(M–Bu)^{3+}$ formation between 5 and 20 eV.

Photons with energy > 12 eV can ionize the dication, promoting it from a 2+ to a 3+ charge. This ionization can either take place directly (short time scale) or by internal conversion to an auto-ionizing excited state, which contains sufficient internal energy to emit an electron (longer time scales). The intact tin-oxo cage with a 3+ charge could not be detected, but a 3+ cage having lost one butyl chain could (see Fig. 4.6).

It is likely that upon photoionization of the cage, the resulting radical trication is unstable and cleaves off one butyl group. The isotope pattern of the peaks unequivocally indicates a 3+ charge. 3+ fragments only appear with a photon energy above the ionization threshold, clearly visible in Fig. 4.7 around 12.1 eV.

The increasing yield of $(M–Bu)^{3+}$ upon increasing the photon energy is accompanied by a decreasing yield of $(M–Bu)^{2+}$ and $(M–2Bu)^{2+}$. This indicates that the ionization process is competitive with simple bond cleavage leading to an $(M–Bu)^{2+}$ fragment. In contrast, the $(M–2Bu)^{2+}$ yield scales with the $(M–Bu)^{2+}$ yield. Therefore, it is likely that $(M–2Bu)^{2+}$ is formed directly from $(M–Bu)^{2+}$, as shown in Eq. 4.3, which shows the main fragmentation pathways:

$$\begin{aligned} M^{2+*} &\rightarrow (M–Bu)^{2+\cdot} + Bu\cdot \rightarrow (M–2Bu)^{2+} + 2Bu\cdot \quad (> 5\ eV) \\ M^{2+**} &\rightarrow [M^{3+\cdot}] + e^- \rightarrow (M–Bu)^{3+} + Bu\cdot + e^- \quad (> 12\ eV) \\ [M^{3+\cdot}] &+ e^- \rightarrow (M–Bu)^{2+\cdot} + Bu^+ + e^- \quad (> 12\ eV) \end{aligned} \tag{4.3}$$

In Eq. 4.3, M^{2+*} is the tin-oxo cage dication in the first excited state, while M^{2+**} is in an autoionizing higher excited state. As can be seen, the tin-oxo cage dication (M^{2+}) can lose a butyl radical upon irradiation if the photon energy is sufficiently high (> 5 eV). At photon energies > 12 eV, ionization can take place, which implies the ejection of a (primary) electron to form $[M^{3+\cdot}]$, a radical trication. Since this species is not observed in the mass spectrum, it is likely to be short-lived (transient) and

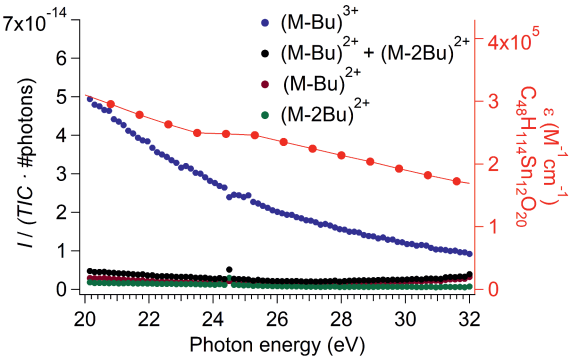

Figure 4.8: Action spectra of $(M–Bu)^{2+}$, $(M–2Bu)^{2+}$ and $(M–Bu)^{3+}$ formation between 20 and 35 eV. The bright red dotted line (right axis) shows the molar absorption coefficient of the tin-oxo cage dication (molecular formula: $C_{48}H_{114}Sn_{12}O_{20}$) as calculated from tabulated values.[100]

therefore noted between brackets. In a thin film of tin-oxo cages, primary electrons induce further reactions,[158] but in this gas-phase experiment the electron is lost in the vacuum environment. This loss can lead to triply charged cations, but also to doubly charged ones if a charged butyl group is lost. The ionization process appears to compete with homolytic cleavage (without ionization); the $(M–Bu)^{3+}$ fragment increases in intensity as the $(M–n Bu)^{2+}$ fragments decrease in intensity. The relative probability to reach a non auto-ionizing state and an auto-ionizing state could change; upon increasing the photon energy, reaching the non-ionizing state is still possible but less probable.

The yield of $(M–Bu)^{3+}$ keeps increasing with photon energy until it reaches a maximum around 19 eV. Above this energy, the fragmentation yield gradually decreases with increasing photon energy, with no evidence of ionization from a Sn 4d level (see Fig. 4.8). Although a small outlier is observed at 24.5 eV, this was not reproduced in other experiments. The absorption cross section of a tin-oxo cage, as predicted by the CXRO database for the hypothetical compound, is additionally shown.[100] At these higher photon energies, the "atomic approximation" becomes increasingly valid.[159] In this approximation, the total cross section is approximated by the sum of the cross sections of all individual atoms. It can be seen that the fragment yield drops faster upon increase of photon energy than the predicted absorption coefficient. Apparently, the fragmentation process becomes less efficient with the increase of energy. This could be due to formation of smaller fragments, that are no longer detected within the m/z range of the experiment. Alternatively, there could be an error in the absorption cross section as calculated from the tabulated values (Henke).[100] Since the photon energy is still quite low, the atomic approximation (adding together cross sections of all individual atoms) could be not completely valid.[159]

4.3.3 UV and VUV irradiation on tin-oxo cage monocations

Besides irradiations on the doubly charged tin-oxo cage (dication), irradiation on mono-cations is also of interest. In a tin-oxo cage film, the 2+ charge of each cage is balanced by two counterions. For the gas phase dication, the electrons are more tightly bound as a result of Coulomb forces. Therefore, the value found for the ionization potential of the tin-oxo cage ($\sim$ 12 eV, see previous section) is higher than the ionization potential in solid tin-oxo cage films.[111]

The tin-oxo cage with two attached counterions has a net charge of zero, and is therefore difficult to isolate and study by ESI-MS. However, isolation of a tin-oxo cage with only one counterion (net charge +1) is very well possible. The counterions triflate (OTf) and tosylate (OTs) were chosen for this purpose. These counterions can interact with the tin-oxo cage dication through hydrogen bonding,[99] Other such structures, with the sulfonate group being attached either covalently or electrostatically, have been reported before.[83] Because the tosylate anion is a stronger base, its hydrogen bonding with the tin-oxo cage is expected to be stronger than for the triflate.[160]

Mass spectra of the isolated (non-irradiated) monocations $MOTf^+$ and $MOTs^+$ clearly are in good agreement with predicted mass spectra for $M(OTf)_2$ and $M(OTs)_2$ that have lost one of their counterions (see Fig. 4.9).

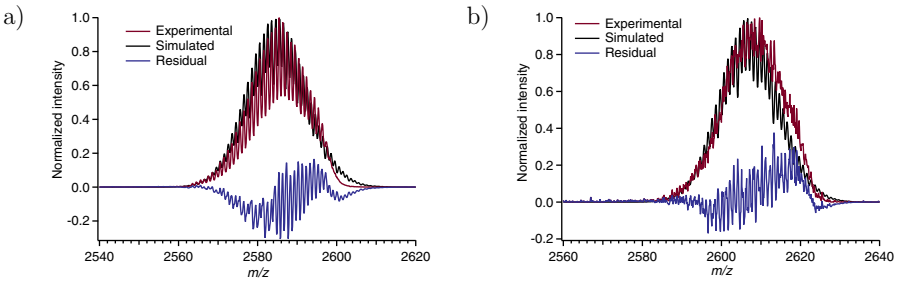

Figure 4.9: Mass spectrum of the precursor peaks (a) $MOTf^+$ and (b) $MOTs^+$. The black lines show simulated spectra using the online tool "Chemcalc" (resolution: 3200, full width half max. $\approx$ 0.81).[155] The bottom blue lines show the residuals.

Similarly to the study on tin-oxo cage dications (described in Section 4.3.2), photofragmentation of these monocations was studied. A mass spectrum of $MOTf^+$, exposed to 7.0 eV photons, is shown in Fig. 4.10a. In contrast with the results on dications, simple butyl loss can hardly be observed. Rather, the major photoproduct at low energies appears to be $(MOTf–2Bu)^+$. As is the case for the dication, excess energy could play a role in initiating the second butyl cleavage. Apparently, this process is more efficient than for the dication. For the monocation $MOTs^+$ the same result was found (see Fig. 4.10b). However, the tosylate monocation ($MOTs^+$) is more reactive than the triflate monocation ($MOTf^+$), judging from the relative height of the $(MOTs–2Bu)^+$ peak.

This can be explained if the counterion performs a nucleophilic attack once a Sn· radical is formed upon Sn–C bond cleavage (see Scheme 4.1). Because the resulting

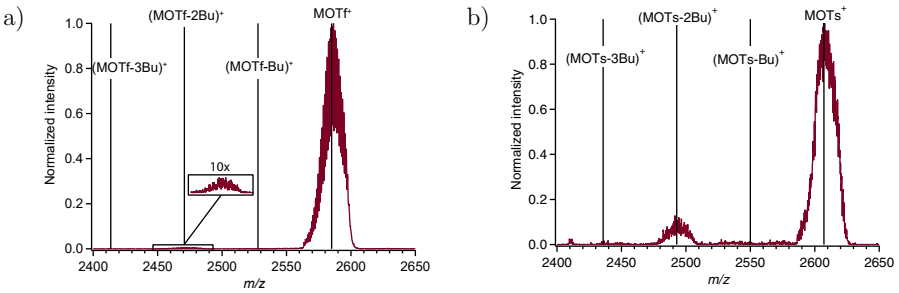

Figure 4.10: Photofragmentation of $MOTf^+$ (a) and $MOTs^+$ (b) with incident light at 177 nm (7.0 eV), in the 1+ region of the spectrum. Vertical lines indicate the peaks corresponding to loss of multiple butyl groups. Number of incident photons: 8.3×10^{11}.

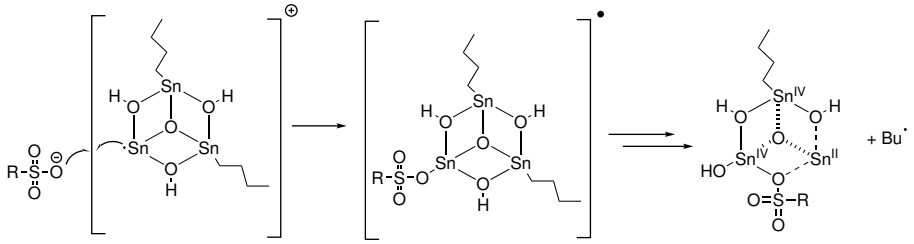

Scheme 4.1: Reaction mechanism for the loss of two butyl groups upon photo-excitation of $MOTf^+$ (R = CF_3) or $MOTs^+$ (R = MePh), taking place at the positively charged cap of the tin-oxo cage (6-coordinated tin atoms; extra bonds are omitted for clarity). The initially formed Sn· radical is formed by cleavage of a Sn–C bond. The reactive intermediate (middle) reacts further to form an $(MX–2Bu)^+$ structure (X = OTf or OTs) with a bridging sulfonate functional group.

structure still contains an unpaired electron, further reactions can lead to another butyl loss while forming a bridging sulfonate group, a structural feature that was also observed by Prabusankar and coworkers.[83] This reaction could be mediated by electrostatic force (the cap of the tin-oxo cage has a net +1 charge while the anion has a –1 charge) and by formation of two Sn–O bonds, which is thermodynamically favorable. Additionally, formed Bu· are simply lost into the continuum, meaning that they are unlikely to get involved in the chemical reactions.

Since $MOTs^+$ is more reactive than $MOTf^+$, the reaction scheme shown in 4.1 could be more efficient if tosylate rather than triflate is attached. The stronger basicity of the tosylate anion could be a reason for this.

Similarly to the tin-oxo cage dication, the onset of photofragmentation corresponds to the onset of photo-absorption (see Fig. 4.11). This indicates that the initial excitation (leading to Sn–C cleavage) is not affected by the presence of counterions.

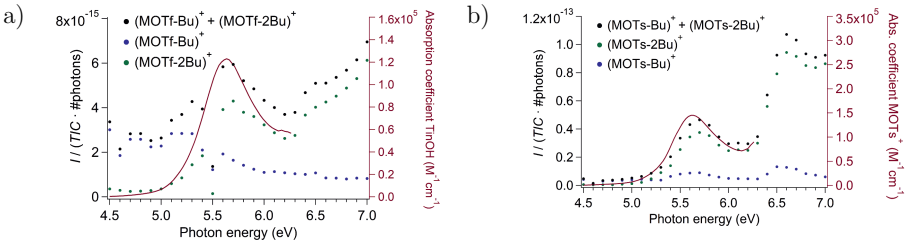

Figure 4.11: Action spectrum of $(MOTf–2Bu)^+$ (a) and $(MOTs–2Bu)^+$ (b). Red lines indicate absorption coefficients: TinOH (a) and $MOTs^+$ (b, predicted, see Fig. 4.12).

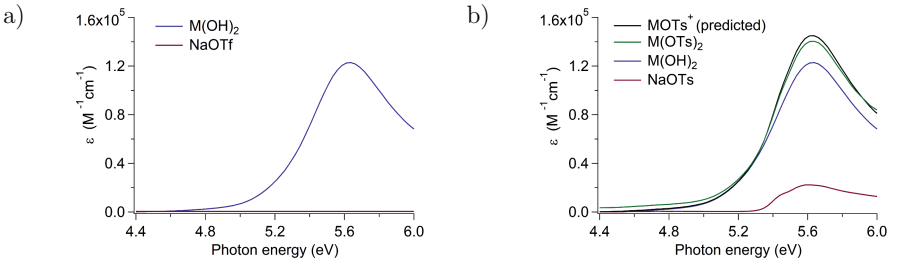

Figure 4.12: UV/Vis absorption spectra of the counterions (a) triflate and (b) tosylate, measured in their sodium salt form in H_2O (for NaOTf) and in EtOH (for NaOTs). For tosylate, a prediction for the absorption spectrum of the monocation $TinOTs^+$ is also given, calculated by adding the NaOTs and TinOH ($M(OH)_2$) spectra together. The experimental spectrum of TinOTs ($M(OTs)_2$) is shown as well.

A difference between the two counterions OTf and OTs is that OTf is mostly transparent at low photon energies (< 6 eV), whereas OTs is absorbing (see Fig. 4.12). Absorption on OTs could also lead to fragmentation, but it is difficult to see how excitational energy could be transferred from OTs to the tin-oxo cage. Therefore, absorption properties of the counterions are not expected to affect the photoreactivity.

At higher photon energies (> 10 eV), photoionization is observed, similarly to the results of the tin-oxo cage dication; $MOTf^+$ and $MOTs^+$ are converted to doubly charged fragments. This photoionization is always dissociative and leads to the fragment $(MOTf–Bu)^{2+}$ or $(MOTs–Bu)^{2+}$ (see Fig. 4.14). For $MOTf^+$, a small peak is observed just below 1220 m/z, which could correspond to the bare dication (m/z 1218). The fragment $(MOTf–2Bu)^{2+}$, however, is not observed, contrary to the photoionization of the bare M^{2+} (see reaction scheme below).

$$MOTs^+ \rightarrow (MOTs–2Bu)^+ + 2Bu\cdot \qquad (> 5 \text{ eV})$$
$$MOTs^+ \rightarrow (MOTs–Bu)^{2+} + Bu\cdot + e^- \qquad (> 10 \text{ eV})$$

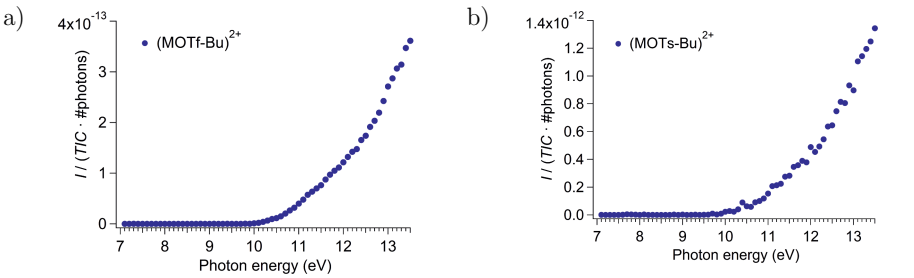

Figure 4.13: Fragmentation yield of (a) $(MOTf–Bu)^{2+}$ and (b) $(MOTs–Bu)^{2+}$ upon irradiation of $MOTf^+$ and $MOTs^+$. Integration ranges: 1250–1278 m/z for $MOTf^+$, 1261–1289 m/z for $MOTs^+$.

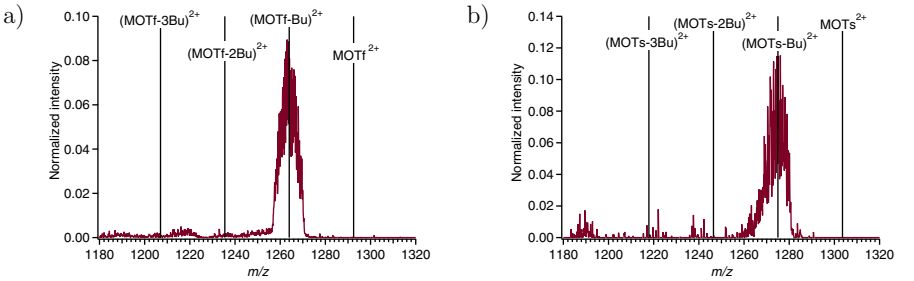

Figure 4.14: Photofragmentation of (a) $MOTf^+$ and (b) $MOTs^+$ with incident light at 92 nm (13.5 eV), in the 2+ region of the spectrum. Vertical lines indicate the peaks corresponding to loss of multiple butyl groups. Number of incident photons: 1.4×10^{11} for $MOTf^+$, 3.3×10^{10} for $MOTs^+$

The ionization threshold is approximately 10 eV if a counterion (OTs^- or OTf^-) is attached (see Fig. 4.13). This ionization threshold appears to be identical for the two counterions; however, $MOTs^+$ is more reactive towards ionization ($\sim 3.5\times$). Both $MOTf^+$ and $MOTs^+$ are more reactive than the bare cage, however (see Fig. 4.6).

The ionization threshold is significantly lower than the 12 eV for the bare dication (compare with Fig. 4.7). As discussed before, this is due to electrostatic force; at higher charge, the electrons are more tightly bound. Additionally, a matrix effect could play a role, which causes further reduction of the ionization potential as a result of polarization of the medium surrounding the molecule. This is only expected to be a minor effect, however. In solid films, the ionization threshold is expected to be even lower because for each dication, two counterions are present instead of one. If we extrapolate our finding of a 2 eV Coulombic shift upon addition of one counterion, the ionization energy would be about 8 eV in solid films. This does not completely match XPS results by Zhang and coworkers, who reported valence electrons having a minimum binding energy of about 4 eV.[111]

4.4 Conclusion

Tin-oxo cage ions in the gas phase were exposed to UV and VUV light (4–35 eV) and the fragmentation pathways were studied. For the tin-oxo cage dication (M^{2+}), single butyl loss was the main photoreaction channel, occurring above the electronic absorption threshold of about 5 eV (∼250 nm). Double butyl loss, as a result of excess energy after the first butyl cleavage, also occurred. Above the ionization threshold of ∼12 eV, the charge of the tin-oxo cage dication is promoted from 2+ to 3+. This ionization was always dissociative, leading to the $(M–Bu)^{3+}$ fragment. No evidence was found for ejection of electrons from the 4d orbitals of tin, even at high photon energies (up to 32 eV).

When counterions (triflate or tosylate) were attached to the tin-oxo cage and the monocations ($MOTf^+$ and $MOTs^+$) were exposed to light, the ionization threshold was lower (∼10 eV). The fundamental reactivity also changed, since loss of 2 rather than 1 butyl group was much more prominent upon electronic excitation. $MOTs^+$ was found to be much more reactive than $MOTf^+$. These two phenomena can possibly be explained by a reaction between a tin radical with the tosylate counterion.

Although the energies used in this work are much lower than those used in EUV lithography, these lower energy experiments are relevant to EUV lithography for two reasons. Firstly, EUV photons (92 eV) induce a cascade of secondary electrons, which have lower energies and may cause excitations much like the photons used here. Secondly, EUV sources often contain VUV out-of-band radiation, which implies that the effect of VUV on photoresist materials should be considered. Most importantly, this study gives fundamental insight into the properties of the tin-oxo cages and emphasizes the facile breaking of the tin-carbon bonds as a key reaction.

4.5 Acknowledgments

The authors acknowledge Ed Zuidinga (UvA) for initial testing of the electrospray conditions and thank Niklas Ottosson, Thomas Schlathölter (RUG) and Ronnie Hoekstra (ARCNL/RUG) for performing preliminary experiments that initiated this research. We thank Mees Trouwborst for help with synthesis of tin-oxo cage compounds. We warmly thank the whole SOLEIL staff for running the facility under project 20161099.

CHAPTER 5

Soft X-ray fragmentation of tin-oxo cage ions*

Abstract

"Tin-oxo cage" organometallic compounds (general formula $[(RSn)_{12}O_{14}(OH)_6]X_2$) are considered as photoresists for extreme ultraviolet (EUV) photolithography. To gain insight into their photoreactivity, we brought an ion cloud of tin-oxo cage dications into the gas phase and investigated their fragmentation upon XUV and soft X-ray photoabsorption by means of mass spectrometry. Secondary electrons and intermolecular interactions are ubiquitous in photochemistry at EUV energies. However, in this gas phase study these can be neglected almost completely, which means that it is a unique study on initial photochemistry. Tin-carbon bond cleavage was found to be the major initial bond dissociation process, leading to loss of up to seven butyl groups. Additionally, photofragments such as SnO_2 and $Sn_4O_6^+$ were formed, but not when the ion cloud was continuously cooled, indicating that they are thermally generated. At different photoexcitation energies (range 82–550 eV), essentially the same fragments were observed but with very different branching ratios. Sharp increases in fragmentation yield were observed around absorption edges of carbon (K), oxygen (K) and tin (N_1). For carbon, two major resonant transitions are seen: a characteristic transition to Sn–C σ^* and one to a mix between C–H σ^* valence states and Rydberg (3s and 3p) states. Our results show that a high degree of fragmentation per soft X-ray photon can be reached for the tin-oxo cage, even though secondary electrons that induce additional reactions are absent in the gas phase. This suggests that the tin-oxo cage as a photoresist has an efficient initial reaction to EUV or X-rays.

*J. Haitjema, T.A. Schlathölter, Y. Zhang, R. Lindblad, M. Timm, C. Bülow, V. Zamudio-Bayer, B. von Issendorff, J. T. Lau, R. Hoekstra, A. M. Brouwer, "Soft X-ray fragmentation of tin-oxo cage ions", *Manuscript in preparation.*

5.1 Introduction

Organotin compounds based on tin-oxo cage structures are candidates for a new generation of extreme ultraviolet (EUV) photoresists: light-sensitive materials that change their solubility upon exposure to EUV light (13.5 nm, 92 eV).[77,81,82,88,161,162] A material that has a larger absorption cross section can be used as photoresist at smaller layer thicknesses (∼20 nm) than conventionally employed. Patterns with small critical dimensions can then be written on the photoresist while keeping the aspect ratio (ratio between height and width of a feature) small enough to avoid pattern collapse.[35] Tin atoms strongly absorb EUV radiation.[100] The EUV absorption coefficient of tin-oxo cage films was measured[46] to be around 12 μm^{-1} (depending on the counterion), around 2.5× higher than that of conventional photoresists based on organic polymers. The chemical reaction pathways in organometallic photoresists are relatively unexplored. The formation of a condensed (insoluble) metal oxide-like network, induced by removal of organic side groups, is generally suggested,[67,75,90,144] but little is known about the EUV-induced photoreactions on a molecular level. Therefore, mechanistic studies are necessary to improve our understanding.

The first step upon EUV exposure is well-known: absorption of EUV photons leads to photoionization,[145,163–165] ejecting either valence or inner-shell semi-core electrons. For a number of metal atoms, semi-core (e.g. 4d) photoionization with 92 eV photons is energetically possible, which is a major contribution to the larger EUV absorption cross section of compounds containing the respective elements. The resulting inner-shell vacancies typically have short lifetimes (1–10 fs range)[166] and decay either by internal conversion or Auger processes.[167,168] The ejected electrons generate a cascade of secondary electrons in surrounding photoresist molecules.[169] These electrons are assumed to induce the majority of the chemical conversions that lead to the solubility change in EUV photoresists.[170,171]

For the tin-oxo cage, EUV can eject both valence and Sn 4d electrons,[111,172] but no carbon or oxygen 1s electrons since they are bound much more strongly (see Table 9.6 in the ESI). Small clusters, complexes and molecules in the gas phase mainly relax through Auger decay after ejection of a (semi-)core electron. Antimony (Sb, $Z = 49$) is known to undergo Auger decay involving the 4d vacancy and 5s/5p valence states, for example in small metal clusters.[173] Tin (Sn, $Z = 50$) has a similar inner-shell electronic structure, suggesting a high probability for Auger emission for this element as well, even though the 4d level of Sn is more weakly bound (24.4 eV vs. 32.7 eV).[152]

Cardineau et al.[88] proposed cleavage of the weak (∼2.2 eV)[71] Sn–C bond as the first dissociation step in the tin-oxo cage. This could be followed by cross-linking and formation of an insoluble network, as suggested by Hinsberg and Meyers.[90] The full chemical reaction mechanism, however, is currently unknown. Reactions in EUV photoresists are difficult to study, because the photoresist layers for EUV photoresists are typically thin and standard chemical analysis techniques (NMR, IR) lack the sensitivity to detect subtle changes.

It is clear that different methods are needed to study these chemical conversions. A possible method is to expose ions corresponding to the compounds under study to XUV and VUV photons in the gas phase. Fragmentation of the ions can then

be studied directly using mass spectrometry. Soft X-ray induced photofragmentation of complex molecular systems has been previously studied for biomolecules such as proteins,[148,174] peptides,[175] and oligonucleotides[176] but also for size-selected metallic clusters.[177,178] However, an EUV photofragmentation study on an organometallic system that is relevant for EUV lithography, such as the tin-oxo cage, has to our knowledge never been reported. Photofragmentation with lower photon energies has been reported before, however.[67,179] Excitation with EUV (or higher energy) light could provide new insights in the fundamental EUV photochemistry. By applying the obtained knowledge, new ways to improve photoresist performance of organometallic-type photoresists can be obtained; for example, weakening the Sn–C bond by attaching different groups than butyl could be a good method to improve efficiency.

5.2 Experimental

All photo-exposure experiments were performed at the BESSY II synchrotron radiation source (Helmholtz-Zentrum Berlin für Materialien und Energie, Germany) using two different tandem mass spectrometer systems interfaced with two beamlines. In both cases, tin-oxo cage dications $[(BuSn)_{12}O_{14}(OH)_6]^{2+}$, were brought into the gas phase using electrospray ionization (ESI) of a 40 µM solution of the tin-oxo cage (with hydroxide counterions) in methanol.[113] After phase space compression of the ion beam in a radiofrequency (RF) ion funnel and a multipole RF ion guide, the ions were mass selected using a quadrupole RF mass filter. Eventually, the dications were collected in a 3D ion trap.[180] The charged photoproducts, originating from the trapped and irradiated tin-oxo cage dications, were analyzed by means of time-of-flight (TOF) mass spectrometry.

In the Groningen Tandem Mass Spectrometer ("Groningen setup")[148,181] the ions are trapped in a classical Paul trap with a capacity of 10^4–10^5 ions. This system was interfaced with the U49/2-PGM1 beamline at BESSY-II, providing small bandwidth soft X-ray photons ($h\nu$ = 85–1600 eV, resolution: 90 meV at 100 eV and 1000 meV at 535 eV). The cloud of trapped ions had a diameter of about 400 µm and the photon beam diameter was about 100 µm at photon fluences up to 10^{13} s^{-1}. The photoexposure time (1.0 s–2.2 s) was chosen to guarantee single absorption conditions for more than 90% of the ions. After each photoexposure period, the entire trap content was extracted into a linear TOF mass spectrometer. Detection of the ions was done using a multi-channel plate (MCP) detector bearing a charge of 4 kV.

The Nanocluster Trap[177,182,183] is permanently installed at the UE52-PGM beamline and it was custom built to record partial ion yields as a function of photon energy. Here, ions are collected continuously in a linear RF Paul trap of much larger ion capacity than a classical Paul trap, and the trap content is continuously exposed to synchrotron radiation. While the photon energy is slowly scanned over the energy region of interest (bandwidth approximately 300 meV at carbon K-edge, 350 meV at oxygen K-edge), ion bunches are extracted into a reflectron TOF system with a repetition rate of 19 Hz. From the resulting mass spectra, partial ion yields as a function of photon energy can be extracted. In this setup, it is only possible to record a

region of the mass spectrum that corresponds to a couple of 100 Da at a time. Further experimental details can be found in the ESI.

5.3 Results and discussion

5.3.1 Photofragmentation at 91 eV

As a reference, Fig. 5.1 shows the mass spectrum of $[(BuSn)_{12}O_{14}(OH)_6]^{2+}$, the isolated precursor ion with m/z = 1218 (black line), measured using the Groningen setup. The ESI-MS spectrum of this species was observed earlier (see Chapter 4).[113,179] A small peak (barely visible in Fig. 5.1) is observed at m/z = 1189, which is attributed to loss of one butyl (Bu) group, but no other fragments were detected. In a first series of experiments, we exposed these ions to synchrotron radiation with $h\nu$ = 91 eV, close to the industrially relevant energy of 92 eV. The resulting difference spectrum is shown in Fig. 5.1 as a red line.

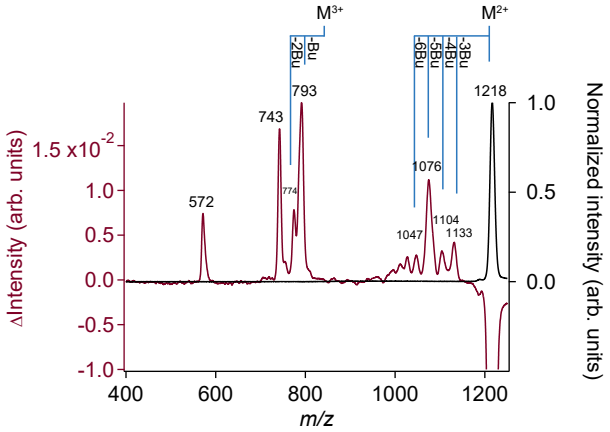

Figure 5.1: Photofragment spectrum (Groningen setup) of the tin-oxo cage for $h\nu$ = 91 eV, using 4.5 × 10^{12} photons/s and an exposure time of 1 s. The reference spectrum of the isolated precursor ion (without photofragmentation, black, right axis) was subtracted from the mass spectrum with photofragmentation. The difference spectrum is shown in red (left axis, ∼ 60× magnified). Both spectra were normalized to the height of the original precursor peak (m/z = 1218, Peak intensity ≡ 1). M denotes the precursor dication and Bu a butyl group.

The negative peak centered at m/z 1218 corresponds to the precursor ion, which is depleted due to photoionization and fragmentation. On the low mass side of the precursor peak, a series of peaks is observed with masses between m/z 1000 and 1200 at values around m/z 1047, 1076, 1104 and 1133. These peaks correspond to the loss

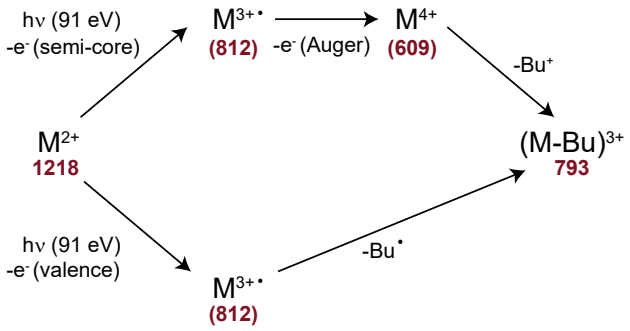

Scheme 5.1: Two possible reaction pathways for the initial photoreaction. M denotes the precursor ion, -Bu denotes a butyl group. Theoretical peak m/z values are indicated in red.[155] Peaks that are not observed in the mass spectrum are shown in brackets.

of 6, 5, 4 or 3 Bu chains (m_{Bu} = 57 Da), respectively, from the precursor dication. Minor peaks are located just below m/z 1047. They are difficult to assign but may be due to additional loss of small molecules such as water or OH. At even lower m/z values, peaks can be observed at 774 and 793, which correspond to the loss of 2 or 1 butyl groups from the photoionized precursor ion M^{3+}. Additionally, there is a peak at m/z 743, and one at even lower m/z (572), which have to be due to more complex photofragmentation processes. Recent photoemission experiments have shown that at 91 eV photon energy ionization from the Sn 4d orbitals is favored,[111] producing about half of the primary photoelectrons. The intermediate trication M^{3+} (m/z 812), formed via 4d photoionization, can undergo subsequent Auger decay to an intermediate M^{4+} (m/z 609). Both M^{3+} and M^{4+} are not observed in the mass spectrum. Loss of a Bu cation from M^{4+} or loss of a Bu radical from M^{3+} can both lead to the observed $(M–Bu)^{3+}$ (m/z 793) (Scheme 5.1). In case of initial photoionization of a valence electron, Auger de-excitation of the intermediate M^{3+} is energetically inhibited, leaving only the butyl loss channel opened. The absence of intact M^{3+} and M^{4+} implies that every absorbed photon induces fragmentation.

The facile cleavage of the tin-carbon bond (∼2.2 eV)[71] is supported by density functional theory calculations, which show that this process takes place spontaneously upon geometry optimization after one electron is removed from the stable tin-oxo cage dication.[103] The tin-carbon bond cleavage is also supported by the observed loss of carbon upon EUV exposure of tin-oxo cage thin films.[102,162] The presence of doubly charged fragments $(M–n\text{Bu})^{2+}$ (n = 3–6) from a triply charged precursor implies charge separation processes, where one of the Bu groups is lost as a cation from an intermediate M^{3+}. In the low m/z range, the corresponding Bu^+ cation is indeed observed (see Fig. 9.17 in the ESI). Loss of H^+ could be an alternative pathway to charge reduction, but the loss of 1 Da cannot be distinguished with the available mass resolution.

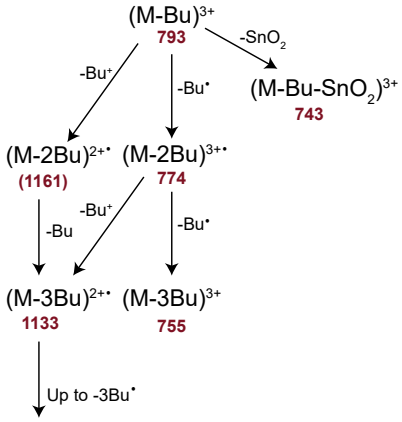

Scheme 5.2: Possible photofragmentation pathways of the tin-oxo cage ion starting from the $(M–Bu)^{3+}$ species. Theoretical peak m/z values of the fragments are indicated in red. $(M–2Bu)^{2+}$ (m/z value between brackets) was not observed in the mass spectra. The initial m/z 793 ion can either lose a charged Bu chain or a neutral Bu chain. The fragment with m/z 774 can lose a charged butyl chain or a neutral butyl radical. The fragment with m/z 1133 further loses up to 3 Bu radicals.

An overview of all fragmentations, starting from $(M–Bu)^{3+}$, is shown in Scheme 5.2. In the sketched scenario, the ion $(M–Bu)^{3+}$ with an m/z value of 793 can lose a neutral butyl group to form $(M–2Bu)^{3+}$. We do not clearly observe an $(M–3Bu)^{3+}$ peak, i.e. further fragmentation processes most likely are charge separation processes where a butyl chain is lost as a cation, leading the system into the 2+ manifold. This could explain that $(M–3Bu)^{3+}$ is almost absent in the mass spectrum.

Most likely, the strong peak at m/z 743 corresponds to $(M–Bu–SnO_2)^{3+}$, i.e. the triply charged precursor cation which lost a butyl group and a SnO_2 group. This loss could also occur in one step by loss of butylstannoic acid (BuSnOOH) which is a precursor in the synthesis of the tin-oxo cage.[114] The remaining intense peak in Fig. 5.1 (m/z 572) likely corresponds to the singly charged fragment cation $Sn_4O_6^+$ (or $Sn_4O_6H^+$). This could be an unusually stable tin oxide structure that is either easily cleaved from the tin-oxo cage ion or an end product of successive dissociation processes. The Sn_4O_6 structure has been observed earlier as a building block for a tin-ferrocenyl complex,[184] and as a core structure of an organotin telluride complex.[185] However, its appearance in photofragmentation or other mass spectra has not been reported before. $Sn_4O_6^+$ or $Sn_4O_6H^+$ could be formed after the cleavage of several Bu groups; for example, if the cap of the tin-oxo cage (three 6-coordinated Sn atoms) has lost all its butyl groups, it could be entirely cleaved from the rest of the cage along with one Sn atom from the belt of the cage (5-coordinated Sn atoms). The loss of the tin-containing fragments SnO_2 and Sn_4O_6 could have practical significance for EUV photolithography, because outgassing of metals from an EUV photoresist can lead to

(poorly cleanable) contamination inside EUV scanners.[48]

The fragmentation sketched in Scheme 5.2 can in principle be due to two fundamentally different processes. Typically, a distinction is made between 'statistical' and 'fast' dissociation channels.[186] For statistical fragmentation (time scale ranging from ns to s, depending on bond energies and temperature), electronic energy is converted by internal conversion and internal vibrational redistribution (IVR) into vibrational excitation (heat). Fast dissociation usually involves the population of antibonding states, meaning that the bonds can break before the energy has equilibrated.

For 91 eV photo-absorption by the tin-oxo cage, high energy, excited valence states can be reached by an Auger decay that involves electrons from deeper (more tightly bound) valence levels. A calculated density of states spectrum for the tin-oxo cage, involving these valence levels, can be seen in the ESI (Fig. 9.16). In such case, the ion can thermalize through IVR. In earlier work, the average amount of thermal energy deposited on a peptide ion was estimated to be 18.5 eV.[148] The tin-oxo cage is relatively large; it can readily redistribute the internal energy over its many ($3N - 6 = 576$) vibrational modes,[187] but the remaining temperature is expected to be high. A remaining internal energy of 18.5 eV would lead to an internal temperature of around 930 K (based on DFT calculated vibrational frequencies, see Fig. 9.22 in the ESI).

In the statistical fragmentation scenario, the sequential loss of butyl units could be viewed as an evaporation-like process which removes energy from the molecular complex. This evaporation normally involves neutral butyl groups, unless the Coulomb repulsion of the remaining charge renders a charge separation process energetically more favourable. In the fast dissociation scenario, however, the ion can dissociate before the energy has equilibrated.

To obtain information on the effect of heat dissipation (which is relevant for photodissociation) in a photoresist layer, cooling techniques were applied. In the NanoclusterTrap setup, the wall of the ion trap was continuously cooled using liquid He and a constant He buffer gas pressure. In the Groningen setup, buffer gas pulses (He, room temperature) were applied before irradiation (100 ms long) and after irradiation (20 ms after the light pulse, 180 ms long) to cool down the ions. For the latter experimental setup, the thermal dissociation may occur before the buffer gas pulse, although the ions could already start to cool down before the buffer gas pulse by emitting infrared photons.[148,188] The different cooling mechanisms in the two experimental setups could thus give additional information, as statistical fragmentation is suppressed for the Nanocluster Trap experiments, but not for the experiments with the Groningen setup.

5.3.2 Near edge X-ray absorption fine structure (NEXAFS)

In the previous section we have assigned the different peaks in the photofragmention mass spectrum obtained at 91 eV. The initial process there was photoionization from Sn 4d or valence levels. In the soft X-ray range, electrons can also be ejected from the carbon and oxygen K-shells.

The increase in photoabsorption cross section around the carbon and oxygen K-edges can be studied quantitatively by means of partial ion yield spectroscopy, i.e. by recording the peak areas as a function of photon energy. We have employed the Nanocluster Trap apparatus for such partial ion yield spectroscopy.

Photofragmentation mass spectra in the range between 700 and 800 m/z are shown in Fig. 5.2a and 5.2b, along with the resulting NEXAFS spectra for the carbon and oxygen K-edge. The tin $M_{4,5}$ edge (480–500 eV) was also scanned but no clear resonances were found.

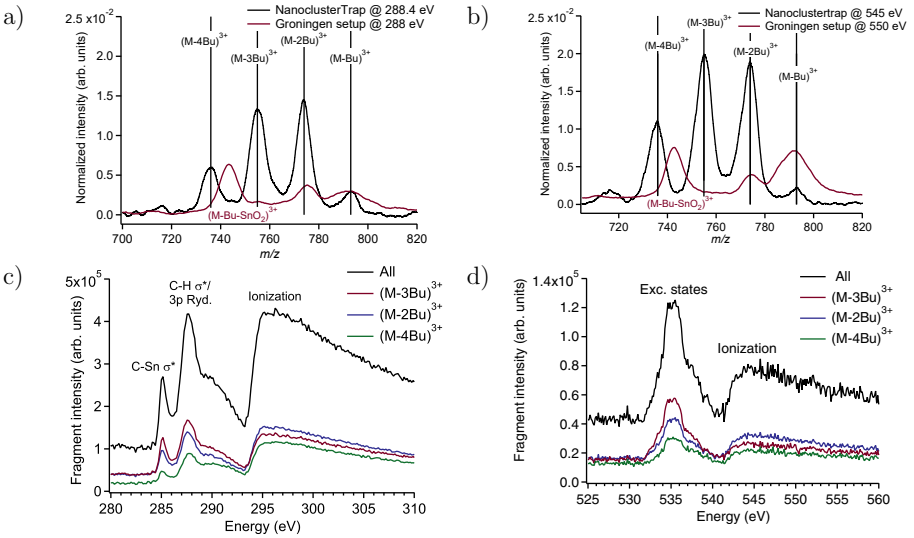

Figure 5.2: (a) and (b): photofragmentation mass spectra obtained at the Nanocluster Trap (288 eV and 545 eV irradiation) and (c) and (d) carbon K-edge and oxygen K-edge NEXAFS spectra, obtained by measuring the partial ion yields of three different peaks in the mass spectrum as a function of photon energy, (corrected for background and normalized to the number of photons).

In the Groningen setup, helium buffer gas pulses are only applied to cool down the ions to room temperature prior to photoabsorption and no further collisional cooling is possible. As a consequence, statistical fragmentation such as loss of butyl groups only competes with the relatively slow cooling by means of infra-red photoemission.[148,188] In the Nanocluster Trap setup on the other hand, the trapped ions are continuously collisionally cooled by He buffer gas at cryogenic temperatures (∼10–100 K), limiting

statistical fragmentation to µs timescales. As a consequence, for instance the fragment $(M–Bu–SnO_2)^{3+}$ (m/z 743) is not observed in Fig. 5.2a when statistical fragmentation is quenched. As we will see later, this absence cannot be explained by the higher photon energy (see Fig. 5.3). $(M–Bu–SnO_2)^{3+}$ thus originates from long-timescale statistical fragmentation processes, resulting from the high initial temperature of the photoionized precursor dication. Likewise and for similar reasons, the fragment $Sn_4O_6^+$ (m/z 572) is not detected in the Nanocluster Trap setup either. On the other hand, quenching of statistical fragmentation allows for the formation and detection of trications that lost 3 or 4 Bu chains ($(M–3Bu)^{3+}$, $(M–4Bu)^{3+}$), which are not observed in Fig. 5.2a (Groningen spectrum, in red).

The carbon K-edge NEXAFS spectrum (see Fig. 5.2c), obtained from the sum of all $(M–n Bu)^{3+}$ fragments, consists of an excitation regime ($E < 295$ eV) characterized by two well-defined resonances and a broad ionization regime ($E > 295$ eV). Urquhart and Gillies have systematically studied carbon K-edge NEXAFS in gas-phase alkanes and for the pre-edge region always observed a dominating 1s–3p transition as well as a much weaker 1s–3s transition at lower photon energy. These transitions also have a slight valence (C–H σ^*) character, and they are accompanied by the respective vibrational series as well as by transitions into higher Rydberg states.[189] Clearly, the richness of these spectra does not resemble our observations for the tin-oxo cage. In the tin-oxo cage $[(BuSn)_{12}O_{14}(OH)_6]^{2+}$, each Bu group is attached to the tin-oxo cage and surrounded by 11 additional Bu groups, a situation that might resemble the condensed phase. For the model alkane neopentane, a direct comparison between gas-phase and condensed phase reveals that in the latter, the lifetime of the core excited state is strongly reduced as a result of Rydberg quenching and/or an increase in valence character of the excited states.[190] The resulting broadening of the peaks gives rise to a spectrum dominated by two broad resonances ($\sigma^*_{C–H}$/3s and $\sigma^*_{C–H}$/3p) with a high energy shoulder, very similar to the pre-edge spectrum in Fig. 5.2c. However, the first resonance (at 285.1 eV) is at an energy much lower than the value reported by Urquhart for $\sigma^*_{C–H}$/3s (287.3 eV). Therefore, it is likely that the 285.1 eV resonance has a different origin; a transition to Sn–C σ^* is the most likely assignment. In that case, the transition to $\sigma^*_{C–H}$/3s is not observed; because this transition is dipole forbidden (1s → 3s), it could be easily hidden below other resonances as a result of its low intensity.

The sharp increase around 295 eV is due to the onset of carbon 1s ionization. The ionization threshold is higher than in earlier studies,[191–193] which is a result of the initial +2 charge of the cage, increasing the binding energies of all electrons. We do not observe further resonances in this section of the spectrum.

Apart from the total yield of different ions, looking at separate partial ion yields for different fragments is a fruitful method to elucidate photofragmentation mechanisms.[178,194] The colored spectra in Fig. 5.2c are based on the separate partial ion yields for loss of 2, 3 and 4 Bu groups ($(M–2Bu)^{3+}$, $(M–3Bu)^{3+}$, $(M–4Bu)^{3+}$). The photoresponse is different for the three different fragments: loss of 3 Bu is significantly stronger at the 1s–3p/σ^* transition than at the maximum of the ionization continuum. For loss of 2 Bu, resonant 1s–3p/σ^* excitation and ionization give approximately equal yields and for loss of 4 Bu, the ionization case is dominant.

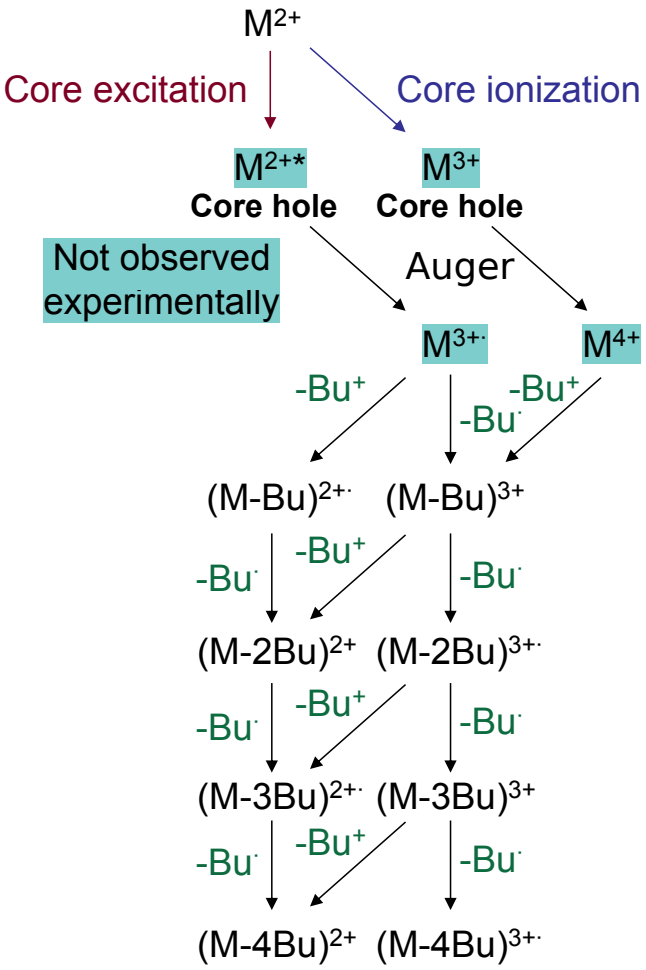

Scheme 5.3: Expanded photofragmentation pathways of the tin-oxo cage ion, starting from either ejection of an inner-shell (core) electron to a bound excited state (left, excitation) or to the continuum (right, ionization). Auger decay then occurs, after which a cascade of butyl losses (charged or neutral) takes place.

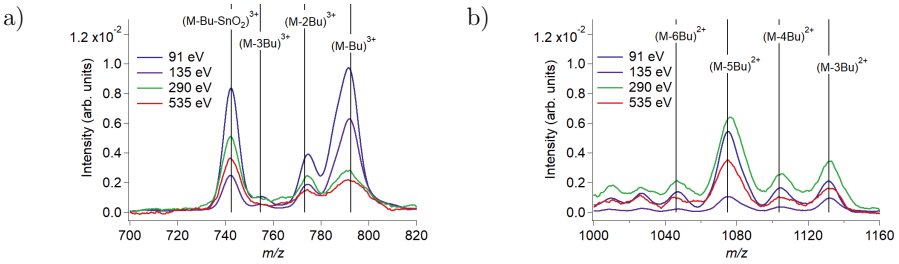

Figure 5.3: Comparison between photofragmentation mass spectra for photon energies of 91 eV (blue), 135 eV (purple), 290 eV (green) and 535 eV (red). The 3+ fragment range is shown in (a), the 2+ fragment range is shown in (b). The spectra were normalized to the photon count and target fluctuations, and smoothed using the moving average algorithm. Additional spectra (between 100 eV and 130 eV) and a non-smoothed version of this figure can be found in the ESI (Figs. 9.18 and 9.19)

The photofragmentation pathways for precursor single ionization (resonant excitation followed by Auger emission) and double ionization (direct ionization followed by Auger emission) are shown in Scheme 5.3. This scheme does not yet explain why the ratio between fragmentation yield for excitation (left) and ionization (right) differs for certain fragments (see Fig. 5.2c and 5.2d). This phenomenon cannot easily be understood.

In the oxygen K-edge spectrum (Fig. 5.2d), a main resonance was found at 535 eV with a shoulder at higher energies. These features are comparable to those seen in studies on SnO_2,[195] but are otherwise difficult to assign. Scheme 5.3 also applies here; excitation to a bound excited state leads to the initial intermediate $M^{3+\cdot}$, while direct ionization leads to the intermediate M^{4+}.

5.3.3 Photon energy dependence of mass spectra

Aside from comparing intensities within absorption edges, a comparison of photofragmentation over a wide range of photon energies is of interest, because it allows to investigate the influence of absorption site and the difference between valence and inner shell absorption. This was again studied using the Groningen setup (see Fig. 5.3). This figure displays mass spectra for the trication (a) and the dication (b) mass range for four representative energies (91, 135, 292 and 535 eV).

For the trication case (Fig. 5.3a), the single Bu loss peak is the strongest ($(M–Bu)^{3+}$ is relatively stable) for 91 eV, while Bu loss accompanied by SnO_2 loss leading to $(M–Bu–SnO_2)^{3+}$ is similarly pronounced. For 135 eV (weaker Sn 4d absorption), the fragment $(M–Bu–SnO_2)^{3+}$ is scarce but single butyl loss is prominent.

At the lowest energies, only valence electrons and Sn 4d electrons can be removed. The photoelectron spectra[111] show that the yields of Sn 4d and valence electrons are approximately equal at 91 eV, while at 135 eV relatively more valence ionization occurs. For the dication case (Fig. 5.3b), lowest intensities are observed for 135 eV.

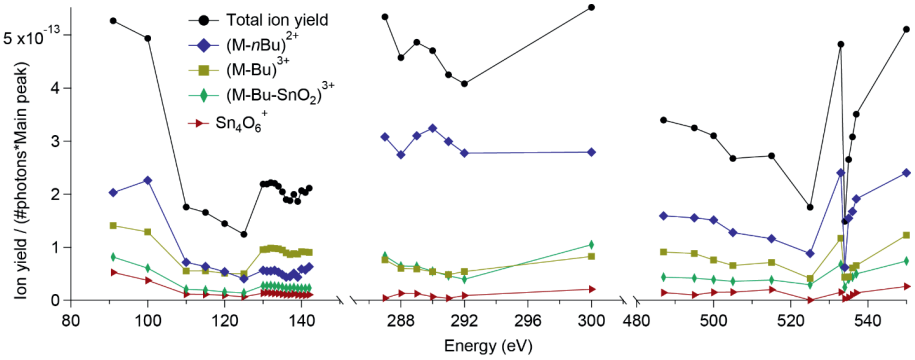

Figure 5.4: Partial ion yields: integration of fragments that appear in the mass spectrum. $(M–nBu)^{2+}$ represents the sum over all fragments with $n = 3 - 7$. The line representing the fragment $(M–2Bu)^{3+}$ has been omitted for clarity, but it is included in the total ion yield. The ion yields are corrected for the detection efficiency (see Fig. 9.15 in the ESI), photon count and target fluctuations.

Clearly, at this photon energy formation of a trication is favored and charge separation is weak. At 135 eV, a higher fraction of ionization is on valence electrons, after which no Auger decay can take place. In this case, most of the excitation energy is left through the ejected (primary) electron. This could lead to a lower internal temperature, reducing the fragmentation yield. The 535 eV spectrum is again more similar to the 91 eV spectrum; at this energy Auger processes on oxygen are likely. The peak intensities for the carbon K-edge spectrum (290 eV) are the strongest, indicating a strong contribution of Bu^+ loss for photoionization directly within the Bu chains. Furthermore, for all four energies, loss of 3 and 5 Bu chains appears most probable.

The ion yield of different fragments in the "Groningen setup" was also studied quantitatively, as shown in Fig. 5.4. In the left part of this figure (90–135 eV) we can see that the total ion yield sharply decreases with increasing photon energy. The decrease appears to be most pronounced for $(M–n\text{Bu})^{2+}$. Between 125 and 130 eV, a steep increase in total ion yield was observed. This can be explained by 4s $\rightarrow$ 5p transitions; no other absorption edge is near this energy. At the carbon K-edge (287–300 eV) the total ion yield is even higher, mainly as a result of the higher yield of $(M–n\text{Bu})^{2+}$. Going from 292 to 300 eV, the yield of the triply charged $(M–\text{Bu})^{3+}$ and $(M–\text{Bu}–SnO_2)^{3+}$ increases significantly. At the oxygen K-edge the fragment yield peaks at 533 eV and exhibits a minimum at 534 eV, after which it increases all the way up to 550 eV. The yield of $(M–n\text{Bu})^{2+}$ is much lower at the oxygen K-edge compared to the carbon K-edge, while the yield of $(M–\text{Bu})^{3+}$ is similar.

To explain these trends, we have to consider the possible processes that eventually cause fragmentation. For all photon energies, photoionization is the first step upon photon absorption. This ionization either removes a valence electron or a core electron. At some specific energies below the ionization edge, promotion of core level electrons to bound levels is possible. Valence ionization is possible as well; previous XPS results

Table 5.1: Absorption cross sections (σ_X) at different photon energies of elements that are present in the tin-oxo cage dication. The relative cross section ($\sigma_{X,rel}$), given as the fraction of the total absorption, is calculated by multiplying the cross section with the number of atoms of each element (12 × Sn, 20 × O, 48 × C) in the tin-oxo cage dication. It gives the relative chance that a photon is absorbed by the element. Values were calculated using tabulated values by Henke and coworkers.[100]

	91 eV	135 eV	300 eV	550 eV
σ_C (cm^2/mol)	$3.5 \cdot 10^5$	$1.5 \cdot 10^5$	$5.5 \cdot 10^5$	$1.3 \cdot 10^5$
$\sigma_{C,rel}$ (cm^2/mol) (48 atoms)	0.10	0.17	0.69	0.18
σ_O (cm^2/mol)	$3.6 \cdot 10^5$	$5.7 \cdot 10^5$	$7.9 \cdot 10^4$	$3.3 \cdot 10^5$
$\sigma_{O,rel}$ (cm^2/mol) (20 atoms)	0.14	0.26	0.04	0.19
σ_{Sn} (cm^2/mol)	$1.1 \cdot 10^7$	$2.0 \cdot 10^6$	$8.5 \cdot 10^5$	$1.9 \cdot 10^6$
$\sigma_{Sn,rel}$ (cm^2/mol) (12 atoms)	0.75	0.56	0.27	0.64

on the tin-oxo cage have shown this to be weak at $h\nu = 2005$ eV,[102] but it could be significant at the lower photon energies used in this work. Molecular photoabsorption cross sections can be approximated by adding the respective cross sections of all constituent atoms, as tabulated in the CXRO database.[100] Such an approximation was previously found to be inaccurate at $h\nu = 16.7$ eV[196] but increasingly accurate for higher photon energies, with virtually no difference with experimental values for 92 eV photons.[159] The thus obtained approximated relative contributions to the photoabsorption cross section are shown in Table 5.1. Because absorption on hydrogen is very weak, it is not shown in this table, nor considered in the subsequent discussion.

Not only the cross sections of elements have been calculated; subshell photoionization cross sections for the elements are also available.[197] For $h\nu$ between 80 eV and 100 eV, mainly the Sn 4d orbital is contributing (binding energy ∼25 eV), since the Sn 4p orbital has a small cross section at these energies.[145] At $h\nu = 135$ eV, the Sn 4d photo-ionization cross section reaches the Cooper minimum, dropping lower than the Sn 4p cross section (see Fig. 9.20 in the ESI).[197] Sn 4s absorption is weak here, but absorption on oxygen and carbon is almost twice as likely for 135 eV compared to 91 eV (see Table 5.1). It is known that 4p core holes in heavy elements decay very rapidly through the Coster-Kronig type of Auger transitions,[198] leading to a 4d core hole plus an additional valence core hole, or to two 4d core holes in case of a "super Coster-Kronig" process. These processes have been studied for Xe ($Z = 54$)[199] and are expected to be even stronger for Sn ($Z = 50$).[172] 4d excitation leads to an initial single $4d^{-1}$ core hole, while for 4p excitation the double core hole $4d^{-2}$ can be formed in case of the super Coster-Kronig process. Although Sn 4s absorption is supposedly weak here, resonant transitions from 4s to 5p-like orbitals may very well take place. The 5p atomic orbital participates in σ and σ* molecular orbitals (Sn–C or Sn–O).

Now we can use this information to explain the different yields of fragments at different energies. The decrease in photofragments between 100 and 125 eV is evidently due to the decreasing cross section of the Sn 4d level (and other accessible levels) at this energy, leading to a lower photoabsorption in the ion cloud (the total

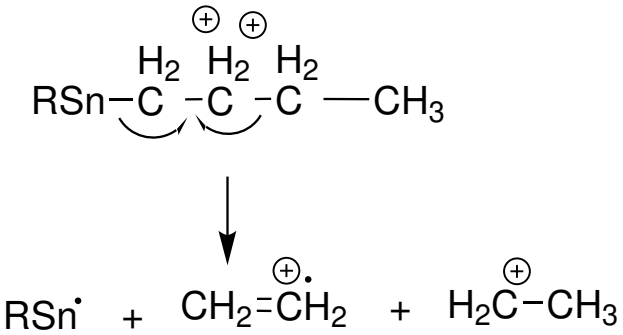

Scheme 5.4: Proposed photofragmentation pathway within a butyl chain, occurring upon 300 eV irradiation (above the carbon K-edge), resulting from a double ionization (Auger).

cross section of the tin-oxo cage, as a function of energy, is shown in Fig. 9.21 in the ESI). In contrast, the sharp increase of the fragment $(M–Bu)^{3+}$ going from 125 to 130 eV cannot be explained by atomic cross sections, as the theoretical absorption still drops going from 125 to 130 eV. However, the resonant transition 4s → 5p/σ* (Sn–C) may directly induce butyl cleavage, because the Sn–C bond would be weakened by populating the anti-bonding σ* orbital.

At higher photon energies the situation is a bit different. At $h\nu$ = 300 eV, the absorption event predominantly involves carbon 1s electrons (∼70%, see Table 5.1). It is expected that one or more Auger decays then take place on the carbon atoms, leaving a double charge that is located on carbon. Possibly, one of the charges transfers towards the tin-oxo cage while the other charge remains on the butyl, after which the Sn–C bond is cleaved. Because in this process $(M–Bu)^{3+}$ and Bu^+ are formed, it can explain the increase in yield of $(M–Bu)^{3+}$ going from 292 to 300 eV. This result is in line with the Nanocluster Trap NEXAFS results (see Fig. 5.2c). $(M–n\text{Bu})^{2+}$ can still be formed through double Bu^+ loss or cleavage reactions that occur within the butyl chains (see Scheme 5.4).

For $h\nu$ = 535 eV, cross sections are generally lower but both the Sn 3d and O 1s core levels are accessible. Absorption on oxygen appears to dominate, since an increase in fragmentation yield is observed at the oxygen K-edge (see Fig. 5.4). Excitation or ionization on oxygen (1s) is likely followed by an Auger process (KL_1L_1, KL_1V or KVV).[200] In case of KL_1L_1 there is a large amount of remaining energy in the system, as a result of the two O 2s semi-core vacancies. This could cause a drastic fragmentation of the ions into much smaller fragments (such as Sn^+, SnO_2^+ or Bu^+) that can no longer be detected simultaneously with the larger photofragments. This may be the reason why the yield of $(M–n\text{Bu})^{2+}$ is relatively lower (compared to $(M–Bu)^{3+}$) around the oxygen K-edge. Another indication of this scenario is the absence of the $Sn_4O_6^+$ fragment in this energy region, suggesting that fragments smaller than $Sn_4O_6^+$ are being formed.

Similarly to the C edge, the yield of $(M–Bu)^{3+}$ increases sharply going from 537 eV (below ionization edge) to 550 eV (above the ionization edge). This could similarly be related to the initial formation of M^{4+} above the ionization edge, which then breaks up into $(M–Bu)^{3+}$ and Bu^+.

The $(M–Bu–SnO_2)^{3+}$ fragment yield is more or less constant across all energy ranges. Probably, a large amount of energy is required to break the four Sn–O bonds, required to obtain this fragment. However, the internal energy upon ∼91 eV and ∼135 eV excitation is apparently sufficient. Once the SnO_2 molecule is split off, no further fragmentation is observed, possibly owing to the large amount of energy required for the splitting-off of SnO_2.

5.4 Conclusion

In this study we use soft X-ray and EUV photons to fragment the "tin-oxo cage" ion $[(BuSn)_{12}O_{14}(OH)_6]^{2+}$, which acts as a (model) photoresist in EUV lithography. Gas phase EUV photoexcitation on the tin-oxo cage $[(BuSn)_{12}O_{14}(OH)_6]^{2+}$ leads to the loss of at least one butyl group (Bu), which can be observed in the mass spectrum as Bu^+. Up to seven Bu chains can be lost by absorption of a single soft X-ray or EUV photon. The initial $(M–Bu)^{3+}$ fragment that is formed (m/z 793) can undergo (neutral) butyl loss or SnO_2 loss. Further butyls can be either lost as a radical (forming $(M\text{-}n Bu)^{3+}$) or a charged species (forming $M–nBu)^{2+}$. The photoproduct $Sn_4O_6^+$ was also formed, which may be an end product of successive butyl losses.

More photoproducts are formed if the energy of irradiation is resonant with electronic transitions. This is due to the stronger photo-absorption, but it could also be partly due to another effect: formation of tin-oxo cages in specific excited states, which are more likely to fragment. For example, the photofragmentation yield peaks at 285 eV. This was attributed to carbon 1s → C–Sn σ* transitions, which weaken the C–Sn bond and thus increase the yield of $(M–Bu)^{3+}$. When the photon energy corresponded approximately to the carbon and oxygen 1s binding energy (∼290 eV and 535 eV) the yield of $(M–Bu)^{3+}$ was comparatively lower while the yield of $(M–nBu)^{2+}$ (n = 3–7) was enhanced. This is because excitation on 1s orbitals leads to a high internal energy, inducing further butyl loss. A different response to excitation (to a bound valence state) or ionization (to the continuum) was clearly observed; ionization leads in general to a higher yield of $(M–nBu)^{3+}$ as a result of the higher initial charge.

To translate these findings into information that can be applied to EUV photochemistry in a photoresist layer, we must consider the differences between gas phase and solid phase photoreactions. In the gas phase, secondary electron interactions (which are ubiquitous in a photoresist film) are mostly absent, as are intermolecular reactions. However, thermally-induced processes are more likely to occur in the gas phase, as a result of poorer heat dissipation. Comparing the results of experiments with different cooling conditions (Nanocluster Trap) allowed us to separate thermally induced processes from faster "direct" fragmentation channels. For example, it was shown that the fragments $(M–Bu–SnO_2)^{3+}$ and $Sn_4O_6^+$ were not formed in the (cooled) Nanocluster Trap experiment. Therefore, formation of these species in a photoresist

film, in which heat redistribution occurs rapidly compared to the gas phase, is not deemed very likely. However, loss of butyl (Bu) also occurs within photoresist films.[102] Additionally, processes such as Auger decay are still relevant, since they take place before heat dissipation plays a role. This work contributes further to understanding of initial photoreactions and chemical pathways in organotin photoresists, which hopefully leads to improved structural design. For instance, weakening the Sn–C bond, by using other groups than *n*-butyl, may lead to a higher reaction efficiency. This would mean that lower doses are needed for patterning, leading to the desired increase in sensitivity of the photoresist.

5.5 Acknowledgments

The authors acknowledge Ed Zuidinga (UvA) for initial testing of the electrospray conditions. We thank Niklas Ottosson for helpful discussions and for performing preliminary experiments that initiated this research. We thank Helmholtz-Zentrum Berlin for the allocation of synchrotron radiation beamtime under proposal number 17105145-ST. R.L. acknowledges funding from the Swedish Research Council (637-2014-6929). The ion trap setup at HZB is partially funded by BMBF under project number BMBF-05K16Vf2.

CHAPTER 6

Scanning transmission X-ray microscopy on tin-oxo cage films*

Abstract

In this chapter we study tin-oxo cage films using Scanning Transmission X-ray Microscopy (STXM). The carbon K-edge spectrum of the tin-oxo cage in hydroxide form (TinOH) shows electronic transitions from C 1s to Sn–C σ^*, C–H σ^*/3p Rydberg, and C–C σ^*. The films were exposed to extreme ultraviolet (EUV) or deep ultraviolet (DUV) radiation, after which the changes in the STXM spectrum were studied. Expected photoproducts, such as *n*-butane, 1-butene and *n*-octane, likely desorb before they can be detected. Therefore, it was difficult to observe chemical changes. The elemental composition of the tin-oxo cages was additionally determined by measuring the X-ray absorbance at three different photon energies. This could be converted to elemental compositions by using elemental absorption cross sections. It was found that using tabulated values for these absorption cross sections yielded an elemental composition for TinOH that did not match the molecular formula. Therefore, absorption cross sections were determined independently through measurements on reference compounds: polystyrene (PS) for carbon, polymethyl methacrylate (PMMA) for oxygen, and metallic tin for tin. Using the obtained values for elemental cross sections, elemental compositions for TinOH were found that agreed with the molecular formula. Upon EUV exposure, the amount of carbon strongly decreased, while no conclusive evidence was found for outgassing of tin or tin compounds. For the tin-oxo cage with trifluoroacetate counterions (TinF), reactivity to EUV was lower, as is apparent from the smaller carbon loss and higher dose needed to convert to insoluble material. The approach for obtaining elemental composition by STXM could be used for other photoresist-like systems or even for completely different material classes.

*J. Haitjema, K. Witte, I. Bespalov, O. Lugier, N. Thakur, L. Wu, M. Vockenhuber, B. Watts, S. Castellanos, A. M. Brouwer', "Scanning transmission X-ray microscopy on tin-oxo cage films", *Manuscript in preparation.*

6.1 Introduction

Extreme ultraviolet lithography (EUVL) is a powerful way to write patterns with high resolution, as a result of the short wavelength used ($\lambda = 13.5$ nm).[201] The semiconductor industry makes continuous improvements in terms of EUV source power, mask performance and optics. Another important factor is the photoresist, which faces stringent requirements on resolution, line edge roughness, and sensitivity.[98] Sensitivity (the light dose required for obtaining an acceptable pattern) determines the speed of the lithographic process, and is therefore an important factor in high-volume manufacturing. Organometallic compounds (such as the tin-oxo cage, Fig. 6.1) absorb EUV radiation more strongly than conventionally used photoresists,[46] which should be beneficial to the sensitivity. Another approach to enhance absorptivity is to employ (partially) fluorinated polymers,[50] since fluorine is a good EUV absorber as well. However, sensitivity also depends on the efficiency with which photons are converted into chemical reactions that change solubility; some photons are converted to heat instead of leading to the desired chemical reactions.[32] Understanding such loss mechanisms is key to improving photoresist sensitivity.

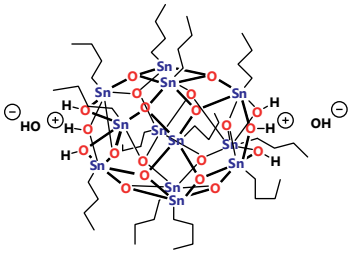

Figure 6.1: Structural formula of the tin-oxo cage with hydroxide counterions (TinOH), $[(BuSn)_{12}O_{14}(OH)_6](OH)_2$.[88,99] TinF (with trifluoroacetate anions) was also used in the work described in this chapter.

Organometallic photoresists have been much less explored than the conventionally employed chemically amplified resists. Therefore, for many such materials it is not clear how EUV absorption leads to the solubility switch. Tracking photoproducts as a function of exposure dose is a path towards such understanding. When it becomes clear what the chemical reaction towards the solubility change entails, the chemistry can be tuned to amplify this reaction and to eliminate undesired side reactions. Chemical analysis is, however, impeded by the small amount of material in the thin films used, limiting the quantity of converted material. This makes it a difficult task to identify the photoproducts.

One promising method for product identification is X-ray Photoelectron Spectroscopy (XPS),[79,102,202,203] which detects photoelectrons that are ejected from a material upon absorption of X-rays. From the kinetic energies of these electrons, electron binding energies can be obtained, which are an important indicator for the chemical

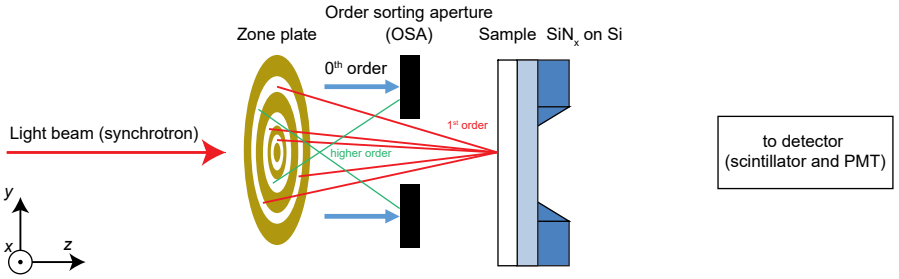

Figure 6.2: Schematic layout of the Scanning Transmission X-ray Microscope (STXM) used. The synchrotron beam is focused on the sample by a zone plate, which focuses on the sample. The sample is usually a thin film spin coated on the substrate, which has free-standing SiN_x membrane in the middle. Zeroth and higher order light is removed by the ordering sorting aperture. The actual detection system is located further to the right. The sample can be moved in x, y and z direction by moving the sample holder.

structure within the material. A drawback of this technique is that mainly electrons originating from atoms close to the surface (top $\sim$ 3 nm) can be detected, as a result of the short electron inelastic mean free path. This makes XPS particularly sensitive to surface phenomena such as oxidation, adsorption and desorption, including poorly defined contaminations.

An alternative technique is Scanning Transmission X-ray Microscopy (STXM), which detects X-rays that are transmitted through a material as a function of photon energy, with spatial resolution down to nanometers.[204] In contrast with XPS, X-ray absorption is related to the chemical composition of the entire film, with no effect of enhanced surface signal. Strong absorption features are typically found around the absorption edges, where the photon energy matches a core electron binding energy. Here, characteristic absorption resonances emerge that originate from transitions in which core electrons are promoted to low-lying vacant orbitals, producing bound states. Such an absorption edge structure is named the Near-Edge X-ray Absorption Fine Structure (NEXAFS), and it gives information on the chemical structure. NEXAFS information is complementary to XPS, because in XPS only ejected electrons are measured, meaning that transitions to bound states are not directly visible in XPS.

STXM is a relatively new technique because it largely relies on the availability of synchrotron sources. The first experimental K-edge transmission spectrum using synchrotron light was reported in 1954, on a beryllium metal foil.[205] A working STXM with fully operational microscopic resolution was first reported in 1972.[206] Since then the technique has found applications in scientific areas such as catalysis,[207] polymer science,[208,209], life sciences,[210] and magnetism.[211,212]

Soft X-ray photons have a short attenuation length in almost all solids. This means that STXM can detect a signal even for thin photoresist films ($\sim$ 30 nm). Despite

this, only few STXM studies have been conducted on materials that are relevant for EUV lithography. Most of them focus on chemically amplified photoresists[213] or on silicon-based materials.[214,215] Studies on organometallic photoresists are still scarce. Fallica and coworkers recently published a pioneering STXM study on such materials, reporting clear photo-induced degradation upon exposure.[216] However, they did not study photoreactions induced by EUV (92 eV) but by much higher energy X-rays (500 eV), and the used exposure dose was not quantified.

Two synchrotron beamlines at the Swiss Light Source (SLS) are employed in this study: EUV exposures were performed at XIL-II while STXM was performed at the PolLux beamline. The SLS was fully operational around 2001.[217] This synchrotron consists of a 2.4 GeV storage ring with undulators that provide tunable sources of X-rays. The XIL-II beamline is mainly used for EUV interference lithography, but can also be used for simple flood (open-frame) EUV exposures.[218,219] After exposure, the samples were transferred to the PolLux STXM beamline. This beamline was specifically built for microspectroscopy, with a spatial resolution up to 40 nm. X-ray energies between 270 and 1500 eV can be used in this beamline.[220]

STXM was employed for two different experiments on tin-oxo cage compounds: NEXAFS spectra (for detection of resonant transitions) and elemental analysis. The former was done to study photo-induced degradation as evident from changes in the carbon K-edge spectra. The latter was performed by measuring absorbance at three different energies, which provides sufficient information to solve for elemental compositions (in mol/cm^2). The used approach for calculating elemental composition is similar to previous work by de Smit and coworkers,[207] who also measured STXM raster scans at three different energies to obtain chemical information. Elemental mapping using STXM is well-known, for example for characterization of aerosol particles.[221–223] Our approach differs in the used photon energies, which were chosen to be far away from the absorption edges rather than at resonant transitions. Advanced data analysis, such as fitting of NEXAFS spectra, was therefore not necessary to obtain elemental compositions. The elemental analysis can be used to detect whether any tin-containing species is lost upon EUV exposure, which is relevant because outgassing of tin compounds can lead to ill-cleanable contamination on EUV optics.[48,224]

Because the elemental analysis depends strongly on accurate elemental absorption coefficients, these were independently measured on three reference materials with a known elemental composition: polystyrene (PS), polymethyl methacrylate (PMMA) and tin (Sn).

6.2 Experimental

6.2.1 Synthesis

Tin-oxo cage materials were prepared as described before.[88] The tin-oxo cage was synthesized with tosylate counterions, after which the material was converted to hydroxide form (TinOH) by ion exchange using aqueous tetramethyl ammonium hydroxide.[114] The tin-oxo cage in its trifluoroacetate form (TinF) was prepared by reacting

TinOH with two molar equivalents of trifluoroacetic acid.[89] ^{1}H and ^{19}F NMR spectra of TinF can be found in the ESI (see Fig. 9.23)

6.2.2 Sample preparation

The tin-oxo cage materials were spin coated onto 7.5×7.5 mm^2 substrates obtained from Norcada, composed of a silicon nitride (SiN_x) membrane covering a silicon substrate, with a 3×3 mm^2 window of freestanding silicon nitride ($d = 30$ nm) in the middle. In some cases, specially produced substrates containing 5×5 arrays of freestanding windows (0.15×0.15 mm^2, $d = 30$ nm) were used, obtained from Silson Ltd. Spin coating of tin-oxo cage materials was performed using either a Suss Delta 10 or Chemat Technology Inc. Spin Master 50 spin coater. Spin coating was performed at 2500 rpm for 35 s, using a 20 mg/mL solution of TinOH/TinF in toluene. The solutions were filtered using a 0.2 µm PTFE filter prior to the spin coating. A post-application bake step of 30 s at 90 °C was performed. The resulting thicknesses were approximately 30 nm (TinOH) and 60 nm (TinF).

Reference materials were prepared as follows: a layer of polymethyl methacrylate (PMMA, average MW ≈ 100.000 Da) or polystyrene (PS, average MW ≈ 100.000 Da) was prepared by spin coating glass cover slips with these materials, using a Chemat Technology Inc. Spin Master 50 spin coater. The spin coated films were removed from the glass substrates using a water bath. Parts of the spin coated layer were picked up and placed on Si/SiN_x substrates (Silson, frame size: 5×5 mm^2, window size 1×1 mm^2, membrane thickness 100 nm). Flakes of PMMA/PS (thickness 77 nm and 240 nm, respectively) were made to partially cover the SiN_x window. Ultra-thin tin (Sn) flakes in metallic (β) form were prepared by microtoming from a tin wire (99.999%, 0.5 mm diameter, Sigma Aldrich) using a Leica Ultracut EM UC7 microtome set at a cutting thickness of 150 nm, leading to tin flakes of approximately 180 nm. These were picked up using the Si/SiN_x substrates mentioned above (Silson).

The substrates with spin-coated films were attached to a sample holder that contained holes at the position of the freestanding silicon nitride windows (see Fig. 6.3).

6.2.3 Exposure

EUV exposures (92 eV, 13.5 nm) were carried out at the XIL-II beamline at SLS (PSI).[218,219] 500×500 µm^2 square areas of the samples were exposed to a homogeneous dose (open frame exposure).

Selected samples were developed for 30 s using a 2:1 mixture of iPrOH:H_2O and rinsed using demineralized H_2O for 10 s. Partial development (removing approximately one half of the layer) was carried out on selected samples by using a cotton swab dipped in the 2:1 iPrOH:H_2O developer solvent.

DUV exposures were carried out using an Ekspla NT342B tunable laser system set at a wavelength of 225 nm. Pulse repetition rate was 1 Hz with a pulse width of 3-6 ns and total pulse energy of around 1 mJ. The beam profile was approximately Gaussian with a diameter of around 0.2 cm. The exposures were carried out under N_2 flow, using a cell with quartz windows.

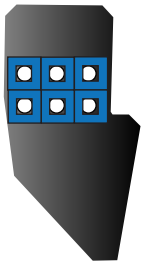

Figure 6.3: STXM sample holder (grey) with attached Si/SiN_x substrates, shown in blue. The transparent squares in the middle of the substrates are free-standing SiN_x membranes; these are sufficiently transparent to X-rays to enable X-ray measurements on spin coated films.

6.2.4 AFM measurements

Atomic force microscopy (AFM) measurements were carried out using a Bruker DimensionIcon AFM, operating in Tapping mode, using Bruker OLTESPA AFM probes with a frequency between 70 and 80 kHz. 512 lines (512 samples per line) were recorded on areas of around 20 × 20 μm^2, using a scan rate of 1 Hz.

6.2.5 STXM measurements

STXM was performed at the PolLux beamline at SLS (PSI).[220] The X-rays (energy range 270–590 eV) were monochromated using a 300 lines/mm Ni grating and focused using a gold Fresnel zone plate, having an outermost zone width of 35 nm and a diameter of 240 µm, with a focal length of approximately 2.2 mm. Higher order light was suppressed by using higher order suppressor mirrors. A 50 µm diameter order sorting aperture (OSA) was used to block 0^{th} and higher order light. X-ray photons were converted to visible photons by means of a scintillator (Phosphor technology, phosphor: UKL59CF/UF-R1, Gd_2O_2S:Pr,Ce,F, median size: 2.5 microns) and visible photons were detected by a Hamamatsu photomultiplier tube (PMT). Scanning of the raster scans and line spectra was performed using a coarse and piezoelectric (interferometrically calibrated) fine XY stages that move the sample holder. To limit X-ray induced damage to the sample, the beam was defocused by moving the sample back 100 µm with regard to the focusing distance. Carbon K-edge spectra were recorded with an energy range of 270 – 350 eV, using steps of 0.5 eV between 270 and 282 eV, steps of 0.1 eV between 282 and 293 eV, steps of 0.25 eV between 293 and 300 eV, and steps of 1 eV between 300 and 350 eV. The spectra were averaged 25 times by measuring 25 µm lines, with a spatial step size of 1 µm, across the region of interest, with a dwell time of 100 ms. Tin $M_{4,5}$ edge spectra (for the Sn flake) were obtained in a range from 480 to 590 eV. Spectral resolution using these settings was 0.46 eV at 300 eV and 1.68 eV at 500 eV. The Sn,O spectrum of the tin flake was corrected for dark counts (measured by closing the shutter and detecting background signal on

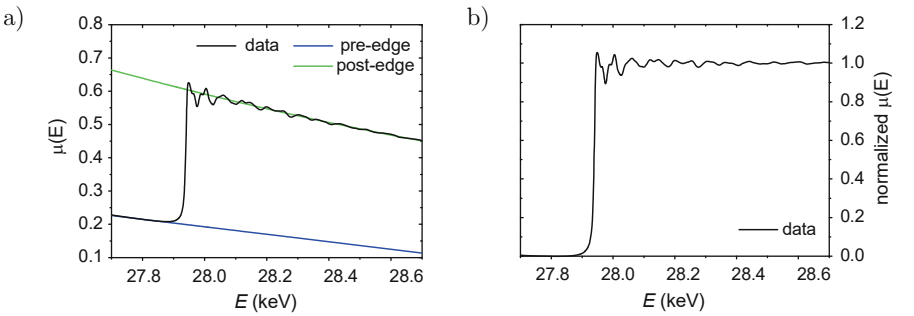

Figure 6.4: Illustration of normalization procedure (adapted from ref. 229). (a) Raw $\mu(E)$ (X-ray absorption coefficient) data measured at the In K-edge of crystalline InP together with the fitted pre-edge and post-edge lines. (b) Normalized $\mu(E)$ obtained from the spectrum in panel (a).

the photomultiplier tube). Fitting of carbon K-edge spectra was performed using the Levenberg-Marquardt algorithm.[225,226]

The ATHENA software was used for spectra normalization of selected K-edge spectra.[227,228] In this software, the pre-edge region is fitted to a linear function and the post-edge region to a polynomial. The edge step μ_0 is then obtained as the difference between pre-edge and post-edge lines at the absorption threshold E_0. A normalized spectrum is obtained by subtracting the pre-edge line from the measured spectra over the whole energy range, dividing by the step height μ_0 and flattening the spectra above the threshold to account for the different slopes of pre-edge and post-edge lines (see Fig. 6.4).[229]

For absorption measurements (calculation of elemental composition), 150 × 150 μm^2 raster scans (300 × 150 or 150 × 150 pixels) were recorded at photon energies 320, 515 and 550 eV, using a dwell time of 12 ms.

6.3 Results and discussion

6.3.1 AFM measurements

The sample thickness d plays a major role in the interpretation and data analysis of the STXM results. The thickness was measured using atomic force microscopy (AFM) for both reference and tin-oxo cage samples. The AFM tip was scanned across an edge of the material with the bare SiN_x membrane. For EUV-exposed materials, a corner of the exposed area was scanned. The scans were performed for both exposed non-developed material (see Fig. 6.5a) and exposed developed material (see Fig. 6.5b). For an exposed but not developed sample, the EUV exposed part will generally have a lower film thickness, as a result of outgassing of volatile compounds. For an exposed developed sample, the non-exposed part will be dissolved by the developer, while the exposed part has been (at least partially) converted into insoluble material, which

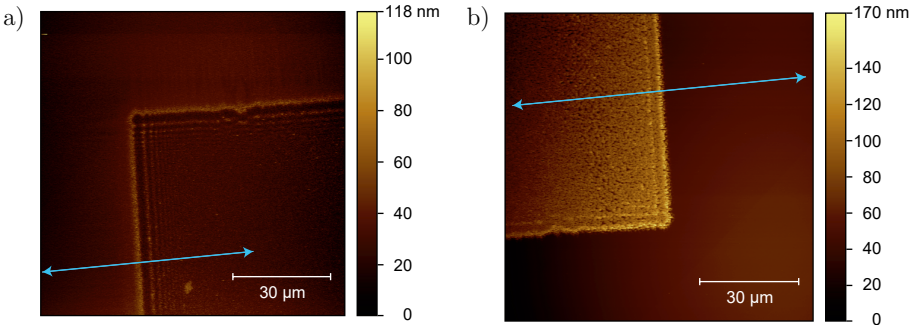

Figure 6.5: AFM image of TinF spin coated on SiN_x, partially exposed (0.5×0.5 mm^2 square area) to 150 mJ/cm^2 of EUV irradiation. Non-developed (a) and developed using a 2:1 mixture of iPrOH/H_2O (b). Examples of cross sections taken are shown as light blue arrows.

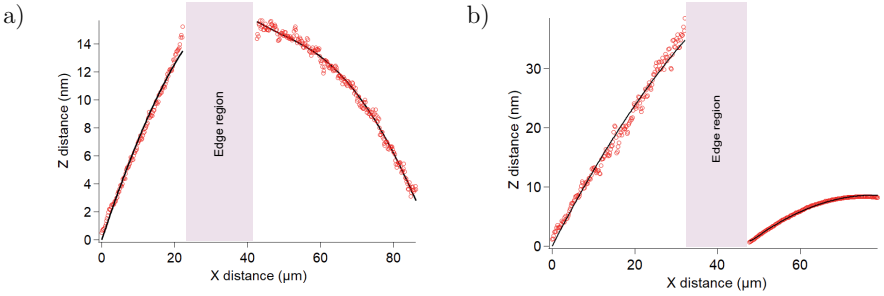

Figure 6.6: Cross sections of the AFM images on TinF (Fig. 6.5) taken perpendicular to the exposure edge area, masking the edge region (pink rectangle). Open circles: experimental results, black lines: fit using bent step function. Fitted thickness loss ± one standard deviation, provided by the fitting procedure: (a) 5.7 ± 0.4 nm. Fitted remaining thickness (b): 44.6 nm ± 0.3 nm.

means it will remain on the substrate.

The film thickness can be extracted from Figs. 6.5a and 6.5b by taking cross sections perpendicular to the square edge. The step height can be calculated by fitting the cross section to a step function, described by Eq. 6.1:

$$f(x) = y_0 + \frac{h}{2}\tanh(\xi/w) + \alpha\xi + \beta\xi^2, \xi = x - x_0 \tag{6.1}$$

in which y_0 is the vertical offset, h is the step height and x_0 is the x position of the step's inflection point. As is apparent from Figs. 6.6a and 6.6b, AFM images always have some inherent drift in the z signal, which is corrected for by the terms $\alpha\xi$ and $\beta\xi^2$. The fitting procedure was carried out using the open-source Gwyddion software, in which the bent step function is built-in.[230]

It is known that the XIL-II beamline provides flood exposures that contain some

dose fluctuations at the edges, as a result of the knife-edge effect.[161] Therefore, this edge was masked in the fitting procedure (see Figs. 6.6a and 6.6b). The same was done for the reference samples. Removing these data from the fitting procedure has the additional advantage that the result is independent on the type of step function that is chosen.

For reference samples (PS, PMMA, Sn) the edge between the flake and bare SiN_x was measured. The same procedure using a bent step function was applied.

6.3.2 Carbon K-edge spectra

NEXAFS spectra arise from resonant transitions from atomic core levels to excited states, and (at higher energies) ejection of core electrons into the continuum. The NEXAFS provides useful information on excited states that are present within the material. In particular, we have studied the carbon K-edge. The oxygen K- and tin $M_{4,5}$-edge of the tin-oxo cage films were also scanned, but the signal-to-noise ratio was found to be too low to obtain satisfactory spectra. We will first discuss the NEXAFS spectrum of unexposed TinOH, as shown in Fig. 6.7. This spectrum was obtained by combining two separate measurements: acquisition of carbon K-edge spectra of TinOH spin coated on SiN_x (I) vs. the (unblocked) X-ray beam (I_0), and bare SiN_x (I) vs. the X-ray beam (I_0). An absorption spectrum of TinOH can then be obtained by subtraction:

$$A_{\mathrm{TinOH}} = A_{\mathrm{TinOH+SiN_x}} - A_{\mathrm{SiN_x}} \tag{6.2}$$

In Eq. 6.2, A is given by $-\ln(I/I_0)$. Note that in contrast to chemists, X-ray scientists commonly use natural instead of 10-based logarithms to define absorbance. To minimize the effect of beam instability, I and I_0 were measured almost simultaneously for each measurement. This was done by measuring in two lines, one on the sample (I) and one on a hole (I_0). For each photon energy in the spectrum, the values of I and I_0 were measured directly after each other before moving to the next energy. Measurements through a hole were made possible by using an array of SiN_x windows, with one of the windows intentionally being broken after spin coating. To obtain the absorption spectrum of TinOH, the spectrum of the bare membrane was subtracted from the TinOH+membrane spectrum, as shown in Fig. 6.7.

It can be seen that the absorbance of SiN_x decreases going from 270 to 350 eV. This is a well-known phenomenon that can be understood by applying a classical oscillator model to estimate the absorption of an electromagnetic wave. The absorbance then falls with $1/E^3$ as function of the energy.[229] As an approximation, a polynomial or linear fit can be used.

As can be seen in Fig. 6.7, the absorption spectrum of SiN_x does not completely match the calculation using tabulated values (dashed line).[100] This can be related to a different stoichiometry of SiN_x than Si_3N_4,[231] or to a larger film thickness than 30 nm. After subtraction of the SiN_x background, the STXM spectrum of TinOH can be described in further detail by a fitting procedure. A fit function for the NEXAFS can be made by using a sum of Gaussians (resonant transitions) plus a step function for the ionization, which can be described as an exponential decay convoluted with a

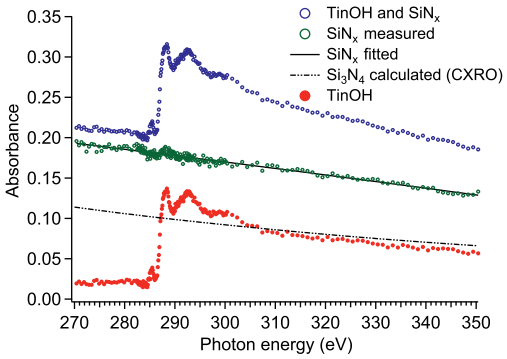

Figure 6.7: Absorption of TinOH spin coated on 30 nm of SiN_x (blue open circles), absorbance of bare SiN_x (green open circles, average of three independent measurements, $d = 30$ nm) and absorbance of TinOH (red closed circles, obtained by subtraction). Black line: second degree polynomial fit for the SiN_x absorbance ($ax^2 + bx + c, a = -4.4 \times 10^{-7}, b = -5.3 \times 10^{-4}, c = 0.36$). The fitting result was used to subtract SiN_x absorbance values from SiN_x + TinOH absorbance values. The bare membrane spectrum is an average of three separate measurements. The dashed line indicates absorbance calculated using tabulated values[100] for a 30 nm Si_3N_4 membrane.

Gaussian function:[216,232,233]

$$f(E) = \sum_{i=1}^{N} \frac{A_i}{\sigma_i\sqrt{2\pi}} e^{-\frac{(E-E_i)^2}{2\sigma_i^2}} + Ae^{-\frac{E-IP}{\sigma}} \otimes \frac{1}{\sigma_C\sqrt{2\pi}} e^{-\frac{(E-IP)^2}{2\sigma_C^2}} \tag{6.3}$$

In Eq. 6.3, N is the number of Gaussians (usually 4 in our case). A_i, σ_i and E_i are respectively the amplitude, standard deviation and center position of Gaussian i. The $\otimes$ sign denotes convolution of the exponential decay $Ae^{-\frac{E-IP}{\sigma}}$ with the Gaussian function $\frac{1}{\sigma_C\sqrt{2\pi}} e^{-\frac{(E-IP)^2}{2\sigma_C^2}}$, in which IP is the ionization potential, and σ_C is the Gaussian width related to the continuum states. It is noted in ref.[232] that convolution with a Gaussian function (rather than a Lorentzian) is sensible as long as the instrumental resolution is not too high. Fitting the TinOH spectrum in Fig. 6.7 to Eq. 6.3 yields the result shown in Fig. 6.8. For comparison, a spectrum of TinF (tin-oxo cage with trifluoroacetate anions) and the fitting result is shown in this figure as well.

Four main resonances can be distinguished in Fig. 6.8, denoted by the numbers 1–4. First, a small absorption resonance (1) is present at 285.4 eV. Because this energy is too low to be related to C–H σ^*, and the tin-oxo cage lacks the double bonds necessary for transitions to π^* orbitals, this feature is assigned to a transition from 1s to Sn–C σ^*. To the best of our knowledge, this is the first time a resonant transition to Sn–C σ^* is reported. Although an STXM study on an organotin compound has been reported previously,[234] this compound contained no Sn–C bond.

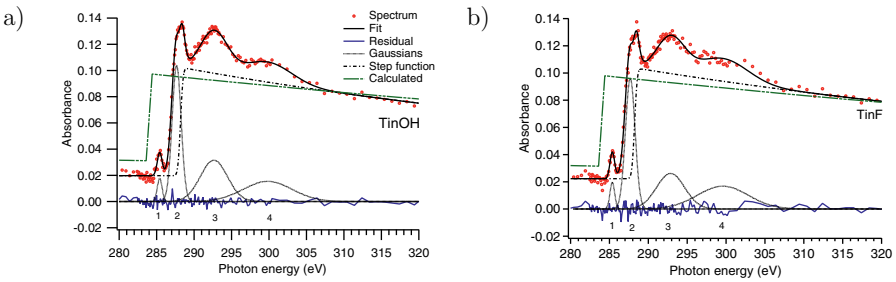

Figure 6.8: Carbon K-edge spectra of (a) TinOH and (b) TinF. Open circles: measured spectrum, solid black lines: fitting results, dashed lines: Gaussian and step function components, blue lines: fitting residuals. The dashed green lines indicate absorbance values calculated by Henke et al,[100] assuming a film thickness of 30 nm and density of 1.9 g/cm^3 for both TinOH and TinF.

It has to be noted that toluene, the solvent used for spin coating, also has a strong 1s $\rightarrow \pi^*$ resonance at 285 eV.[235] Although toluene is volatile and should evaporate, small amounts could remain trapped inside the film. However, the resonance at 285 eV is also present in photofragmentation experiments (Chapter 5), in which the tin-oxo cage ion was isolated and no toluene was used. Therefore, it is unlikely that toluene is responsible for the 285 eV peak.

The second (strong) resonance at 287.7 eV (2) likely originates from transitions from 1s to σ* C–H mixed with Rydberg 3p. Similar results were obtained by Urquhart and Gillies,[190] who studied carbon K-edge NEXAFS on linear and branched alkanes in the gas phase as well as the solid state, and observed a strong peak at 288.1 eV. They also observed a σ* C–H/3s peak at 287.1 eV, which is not present in our results. However, this resonance is expected to be weak because the 1s $\rightarrow$ 3s Rydberg transition is dipole-forbidden (selection rule: $\Delta\ell = \pm 1$) and could be hidden beneath the strong σ* C–H/3p peak.

The third strong resonance (3), located around 292.6 eV, likely originates from transitions from 1s to C–C σ* orbitals. The origin of the fourth (very broad) resonance (4) is unclear. Its Gaussian width σ is as large as 37 eV, which is unlikely for a single transition. Additionally, its position appears to be variable among different spectra. It is therefore probable that it is composed of multiple Gaussian peaks, which are however difficult to distinguish because of overlap with each other and with the ionization step function. A similar result was obtained by Fallica and coworkers.[216]

The residuals (in blue) show a good agreement of the fits with the experimental data. Some deviation can be seen around the position of the second Gaussian function. Therefore, we hypothesize that this peak is actually composed of two or more peaks. This could be either a σ* C–H/3s peak which is hidden underneath the strong σ* C–H/3p peak, or the σ* C–H/3p peak could be split into multiple components because not all C–H bonds in the tin-oxo cage are equal (calculations show that hundreds of transitions are possible, all having different energies). For example, the C–H (CH_3) is

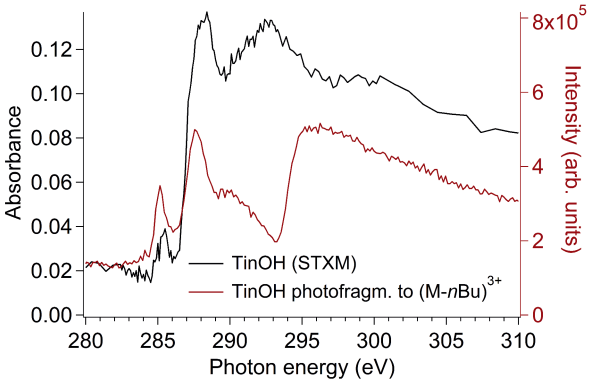

Figure 6.9: STXM spectrum of TinOH (black line) and photofragmentation spectrum of M^{2+} leading to $(M\text{-}n\text{Bu})^{3+}$, n = 2–4 (red line), as described in Chapter 5.

different from the C–H (CH_2) while the CH_2 next to the tin atom is also chemically different, as indicated by earlier NMR studies.[107] Furthermore, Rydberg transitions are possible to other orbitals such as 4s, 3d etc. which lie very close in energy. An obvious way to solve this problem would be to add extra Gaussian bands to the fitting procedure. Care should be taken to avoid overfitting the data, however. For this reason, we stuck to four Gaussian bands in the analysis.

The fitting result can be compared to photofragmentation spectra, as described in Chapter 5. Fig. 6.9 shows the STXM and photofragmentation spectrum plotted in the same graph. It can be seen that there are some major differences between these two spectra. The fitting results are described and compared in Table 6.1.

Table 6.1: Comparison of fitting results for TinOH (STXM results), TinF (STXM results), and gas phase photofragmentation of the tin-oxo cage dication M to $(M\text{-}nBu)^{3+}$ (BESSY experiments, Chapter 5). The standard deviation in the peak position is also given. We define the onset of ionization as the energy at which the step function has increased by 1% compared to its initial value (at 270 eV).

Assignment	**Band 1** C–Sn σ* Center pos.	**Band 2** C–H σ*/3p Ryd. Center pos.	**Band 3** C–C σ* Center pos.	**Band 4** C–C σ* various Center pos.	**Step function** Ionization Onset
Tin2+ photofragm.	285.2 ± 0.01	287.6 ± 0.02	289.5 ± 0.07	-	292.4 ± 0.04
Ampl.	16%	22%	20%	-	42%
TinOH STXM	285.4 ± 0.03	287.7 ± 0.02	292.6 ± 0.08	299.8 ± 0.3	287.4 ± 0.1
Ampl.	7.0%	41%	13%	6.1%	33%
TinF STXM	285.4 ± 0.03	287.7 ± 0.02	292.9 ± 0.09	299.0 ± 0.4	287.5 ± 0.03
Ampl.	8.2%	40%	11%	7%	34%

First, the ionization energy is shifted down approximately 5.0 eV for the STXM spectrum. This is a direct effect of the hydroxide counterions, which are present in the STXM experiment but not in the photofragmentation studies. As a result of lower

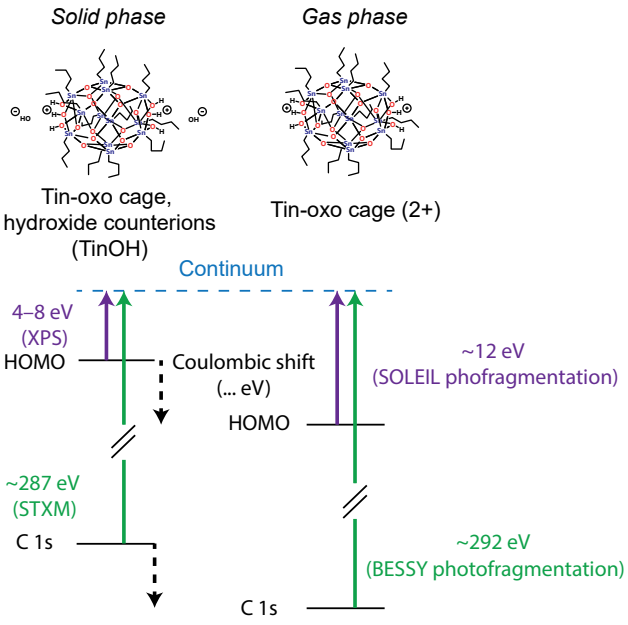

Figure 6.10: Ionization processes studied by four different experiments: XPS (valence electrons of solid-phase tin-oxo cages),[111] STXM (core electrons of solid-phase tin-oxo cages), SOLEIL photofragmentation (valence electrons tin-oxo cage dication, Chapter 4) and BESSY photofragmentation (core electrons of dication, Chapter 5).

attractive Coulombic force compared to the bare dication, the binding energy of all electrons is decreased ('Coulombic shift') as compared to gas phase experiments on the tin-oxo cage dication. This Coulombic shift can be compared to the observed shift in the ionization energy of valence electrons in the highest occupied molecular orbital (HOMO) (see Fig. 6.10). In an earlier XPS study,[111] the lowest threshold for valence ionization was found to be $\sim$ 4 eV, although recent experiments indicate a higher threshold of around 8 eV.[236] In photofragmentation experiments on the doubly charged tin-oxo cage at SOLEIL (see Chapter 4), the threshold was found to be $\sim$ 12 eV.

These experiments suggest that the Coulombic shift is between 4 and 8 eV for valence electron ejection. A comparison between STXM and photofragmentation results (see Table 6.1) shows a Coulombic shift of about 5 eV, which is in line with the shift for valence electron ejection. This was checked with quantum chemical calculations, which indicate that all electron binding energies are $\sim$5 eV higher in the bare dication compared to species with two counterions (see ESI, Fig. 9.24).

The second main difference between STXM and photofragmentation results is that the first resonance, attributed to Sn–C σ^*, has much higher intensity for the photofragmentation measurements. This could be because ions that undergo excita-

tion into a state in which an anti-bonding Sn–C σ* orbital is occupied more readily undergo fragmentation relative to other transitions, which involve for example C–H orbitals. In STXM measurements, not the efficiency of fragmentation is measured, but purely the absorption of the material.

EUV exposures

Now that we have assigned features in the TinOH (unexposed) spectrum, we can move on to spectra of films that have been exposed to EUV. We have chosen exposure doses ranging from 37.5 to 375 mJ/cm^2. The lowest dose (37.5 mJ/cm^2) is approximately the dose needed to get sufficient conversion for pattern formation,[161] while the higher doses are also relevant to study compression and outgassing processes within the material.

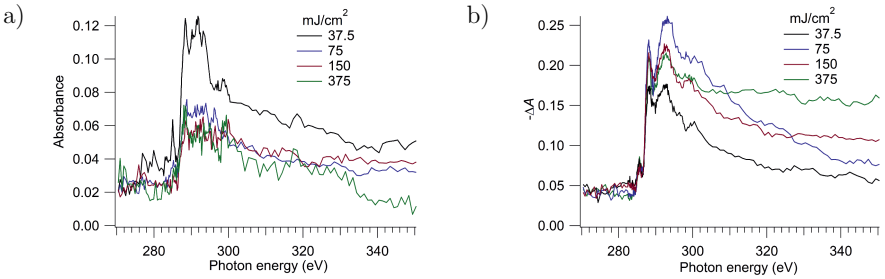

Figure 6.11: STXM spectra of TinOH, exposed to various doses of EUV radiation (92 eV, 13.5 nm): (a) developed using a 2:1 iPrOH/H_2O mixture, (b) non-developed. For (a), the unexposed part (removed by the developer) was used as reference (I_0). Therefore, these spectra arise from material that is remaining on the substrate. For (b), the unexposed part of the sample was used as the reference (I_0) while an exposed part was used as sample measurement (I). Therefore, these spectra arise from material that has outgassed or reacted.

Two main approaches are used here. First, we study developed samples and directly obtain an absorption spectrum by measuring transmitted light through sample + SiN_x and pure SiN_x. Because the exposure area edge is sharp, this can be conveniently done in a single line scan that measures both exposed and unexposed parts of the sample. The resulting spectra are shown in Fig. 6.11a. Clearly, these spectra are of insufficient quality for further analysis. The remaining film thickness is small (< 30 nm), and the percentage of carbon in this remaining film has also decreased as a result of outgassing. Therefore, little carbon is left to yield a carbon K-edge spectrum that is sufficiently above the noise level. Intensity fluctuations are an additional concern. If the light intensity drops or rises during an I_0 or I measurement, this will lead to a slope in the absorption spectrum. This effect is more severe if the measured film is thin.

Another approach for studying EUV-induced change is to compare transmitted light through non-exposed material and exposed material, which is bleached and

therefore has lower absorption than the unexposed material. Absorbance values can in this case not be obtained because an absolute I_0 measurement is not available. Rather, the difference in absorbance ($-\Delta A$) is measured. This difference in absorbance is directly related to compounds that have reacted or outgassed. For instance, the C–Sn bond could be cleaved upon exposure, releasing butane/butene or other volatile organic compounds. This would lead to a difference spectrum that is (almost) identical to the NEXAFS of the starting material. This is indeed what is observed in Fig. 6.11b. As can be seen, the difference spectra have a higher signal and much better signal to noise ratio than the spectra in Fig. 6.11a. This is because the amount of outgassed carbon is larger than the amount of remaining carbon after exposure and development. The STXM difference spectra have the same overall spectral shape as the spectrum of non-exposed material. If only butyl loss occurs, the difference in absorbance would be almost the same as the spectrum of non-exposed material. The only deviation from this could come from the remaining butyl groups having a different chemical environment. Apparently, this difference is too small to be noticeable.

Formation of other products would also be possible. This would lead to negative peaks in the difference spectrum. For example, formation of 1-butene would lead to C=C π^* resonances around 285.0 eV. This overlaps with the C–Sn σ^* resonance, however, making this difficult to observe experimentally. Moreover, small molecules such as 1-butene would likely desorb in the STXM measurement chamber ($p < 1{\times}10^{-5}$ mbar).

DUV exposure

Aside from exposure to EUV, DUV exposure is also of high interest. As was noted in previous work (see Chapter 3), the tin-oxo cage has a strong absorption band in the DUV region.[103] Exposure of the tin-oxo cage to DUV radiation also leads to a solubility switch. In previous work by Zhang and coworkers, the XPS spectrum of DUV-exposed material was studied.[102] For comparison, the DUV exposures were performed using the same laser (225 nm pulsed laser, 1 Hz, approximately 1 mJ/pulse). Exposures were carried out under nitrogen flow to avoid immediate reaction with oxygen from the atmosphere.

Because of the previously mentioned issues with beam stability, an alternative approach was used to obtain I_0 spectra. The materials were spin coated on a 5×5 array of 0.15 mm $\times$ 0.15 mm^2 freestanding SiN_x membranes on silicon (obtained from Silson Ltd.). One membrane was intentionally broken. The spectra were then recorded by alternately measuring I (spin coated sample on a freestanding membrane) and I_0 (broken membrane), moving back and forth between sample and reference measurement at each energy. This was enabled by the close proximity of the freestanding membranes. The SiN_x spectrum was subtracted from the obtained absorption spectrum (see Fig. 6.7) to yield absorption of the spin coated film. Spectra recorded in this way can be seen in Fig. 6.12a (developed samples) and Fig. 6.12b (non-developed samples). It has to be noted that in this case, the non-developed spectra yield actual absorbance values instead of a difference in absorbance (as was the case for the EUV exposed samples).

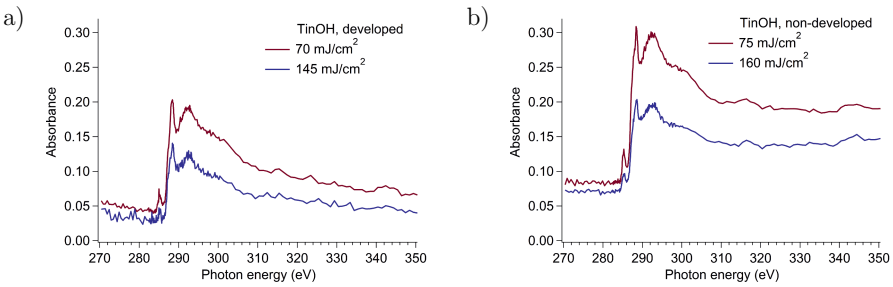

Figure 6.12: STXM spectra of TinOH, exposed to various doses of DUV radiation (225 nm). (a): developed using a 2:1 iPrOH/H_2O mixture, (b) non-developed. The free beam (through a broken membrane) was used as reference (I_0). Absorption values from a reference measurement on bare SiN_x vs. the bare X-ray beam (see Fig.6.7) were subtracted from the spectra.

As can be seen, there is a clear decrease in the amount of carbon upon exposure, evident from the loss in absorbance and the lower step edge. The step edge is approximately 0.16 (70 mJ/cm^2) and 0.1 (145 mJ/cm^2) for the developed samples, and approximately 0.2 (75 mJ/cm^2) and 0.12 (160 mJ/cm^2) for the non-developed samples. The carbon loss is a result of outgassing of volatile hydrocarbons, and is even stronger for developed samples, which indicates that not all carbon-containing material has been converted to insoluble material.

The spectra in Fig. 6.12 are difficult to compare to each other, as they have a varying negative slope in the absorbance values and a difference in the step height. Therefore, we take a closer look at spectra that have been normalized by using the ATHENA software.[227,228] Normalization sets the pre-edge absorbance to 0, the step height to 1, and removes any pre-edge and post-edge slope (see Experimental).[229] Normalization was successful for DUV-exposed samples (see Fig. 6.13), but unsuccessful for EUV-exposed samples. This is due to the improved I_0 measurement for DUV-exposed samples (measuring I and I_0 alternately for each energy). In Fig. 6.13, there are clear differences between DUV-exposed and non-exposed material. The second absorption resonance has shifted to a higher energy. This could be due to newly formed products with a different NEXAFS structure, to the selective loss of material, or to a different chemical environment of the remaining material. For example, a butyl group attached to a 5-coordinated tin atom could have a different transition energy to C–H σ^* than one attached to a 6-coordinated tin. If one type of butyl chain (6- or 5-coordinated) is predominantly cleaved off, the absorption resonance may shift because the remaining butyl groups are predominantly of the other type. Previous NMR studies have shown that the chemical difference between the two different butyl groups is not negligible, even for –CH_3 groups, which are located far away from the tin atom.[107] Hardly any difference can be observed between developed and non-developed films, or between films exposed to different doses. Probably, the development process has no or very little selectivity to a specific material.

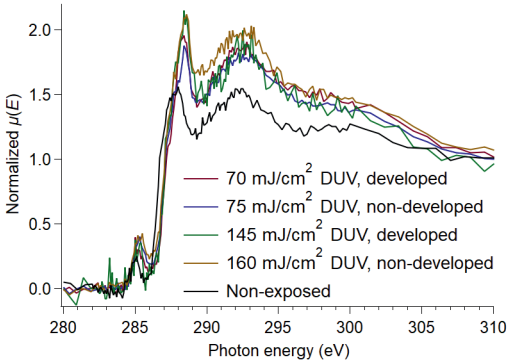

Figure 6.13: STXM spectra of TinOH, exposed to various doses of DUV radiation (225 nm) and non-exposed. These spectra were normalized using the ATHENA software.[227,228]

6.3.3 Elemental composition

Approach

Elemental composition of tin-oxo cage films was recorded by means of STXM, using absorbance values at 320, 515 and 550 eV. Here, the absorption can be assumed to be independent of chemical structure, enabling calculation of elemental composition.

At 320 eV, mainly carbon is absorbing (K-edge), at 515 eV mainly tin is absorbing ($M_{4,5}$-edges) while at 550 eV both tin and oxygen (K-edge) absorb strongly. Hydrogen absorbs X-rays very weakly; its absorbance was neglected if the amount of hydrogen was unknown (e.g. exposed tin-oxo cage films) and calculated using the molecular formula (PMMA and PS reference samples, unexposed tin-oxo cage films). Absorption from fluorine was approximated using the molecular formula of TinF (unexposed TinF samples). Fluorine was estimated to contribute at most 2% to the total absorbance (at 320 eV) in TinF, which means that its influence on the results is relatively small. For exposed TinF samples, the fluorine absorbance was neglected because the elemental composition after exposure is unknown. It was found that this leads to a small overestimation of the amount of carbon ($\sim$ 3%), while the effect on other elemental quantities is negligible.

Recorded STXM raster scans contained both an exposed and an unexposed part of the tin-oxo cage film. Unexposed parts of the film were removed by the development process, which means that a bare membrane remains in the unexposed region.

The intensity through the tin-oxo cage film (I) and intensity through the bare membrane (I_0) can be measured by selecting parts of the raster scan which are known to be either exposed or non-exposed. The exposed part is darker because it contains an X-ray absorbing film (see Fig. 6.14). As can be seen, horizontal stripes appear as a result of fluctuations in the synchrotron source (top-ups). To avoid unwanted effects from these fluctuations, parts of the raster scan were selected for analysis that

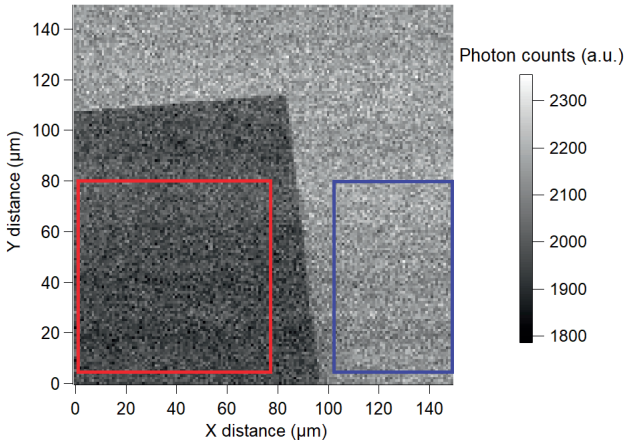

Figure 6.14: STXM raster scan of a TinOH thin film spin coated on top of a SiN_x membrane, partially exposed by EUV light (75 mJ/cm^2, 500 × 500 µm^2) and developed to remove unexposed material. 550 eV X-ray photons were used in the measurement.

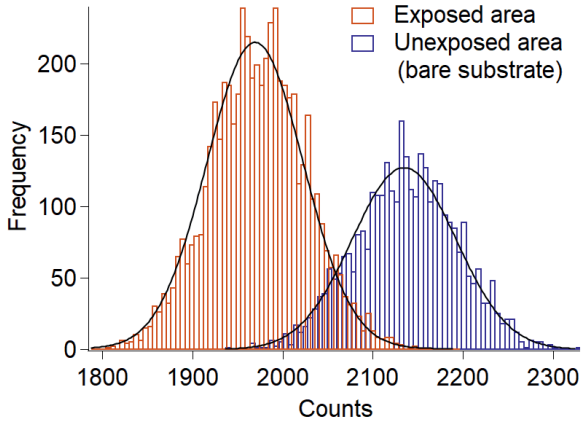

Figure 6.15: Histograms for the number of counts in the exposed area (red) and the unexposed area (blue) shown in Fig. 6.14, after development. Gaussian fits of the data are indicated by solid black lines. Standard error of the mean (SEM) is 0.72 counts for the exposed, 0.97 counts for the non-exposed area.

correspond to the same time period. As the raster scans are composed of consecutively recorded horizontal lines, rectangular areas with the same Y coordinates have been recorded during the same time period (see red and blue rectangles in Fig. 6.14). Histograms for the light intensity in both the unexposed and exposed areas can be seen in Fig. 6.15. The distribution is described as Gaussian (black lines). The areas represented by the rectangles can thus be characterized by an average intensity ($\bar{I}$) and standard deviation (s_I). An absorbance value can be obtained by Eq. 6.4:

$$A = -\ln(\frac{\bar{I}}{\bar{I}_0}) \tag{6.4}$$

In Eq. 6.4, $\bar{I}$ is the average photon intensity recorded through the membrane and the sample, and $\bar{I}_0$ is the average photon intensity recorded through the bare membrane. Three different absorbance values for the X-ray energies 320, 515 and 550 eV are thus obtained. They depend on the amounts of each element (carbon, oxygen and tin) and the elemental absorption coefficient. This can be described using the Beer-Lambert law, as follows:

$$\begin{aligned} A_{320} &= \alpha_{320} \cdot d = (c_C\sigma_{C(320)} + c_O\sigma_{O(320)} + c_{Sn(320)}\sigma_{Sn(320)}) \cdot d \\ A_{515} &= \alpha_{515} \cdot d = (c_C\sigma_{C(515)} + c_O\sigma_{O(515)} + c_{Sn(515)}\sigma_{Sn(515)}) \cdot d \\ A_{550} &= \alpha_{550} \cdot d = (c_C\sigma_{C(550)} + c_O\sigma_{O(550)} + c_{Sn(550)}\sigma_{Sn(550)}) \cdot d \end{aligned} \tag{6.5}$$

In Eq. 6.5, α_E is the total absorption coefficient at energy E in cm^{-1}, d is the film thickness in cm, c_X is the concentration of element X in mol/cm^3 and $\sigma_{X(E)}$ is the absorption cross section (in cm^2/mol) of element X at energy E. Because d is constant within the same absorption measurement, the set of equations can be solved for the three unknowns (c_C,c_O and c_{Sn}) by converting it to a matrix form:

$$\begin{pmatrix} A_{320} \\ A_{515} \\ A_{550} \end{pmatrix} = d \begin{pmatrix} \sigma_{C(320)} & \sigma_{O(320)} & \sigma_{Sn(320)} \\ \sigma_{C(515)} & \sigma_{O(515)} & \sigma_{Sn(515)} \\ \sigma_{C(550)} & \sigma_{O(550)} & \sigma_{Sn(550)} \end{pmatrix} \begin{pmatrix} c_C \\ c_O \\ c_{Sn} \end{pmatrix} \tag{6.6}$$

The solution is then given by:

$$\begin{pmatrix} c_C \\ c_O \\ c_{Sn} \end{pmatrix} d = \begin{pmatrix} \sigma_{C(320)} & \sigma_{O(320)} & \sigma_{Sn(320)} \\ \sigma_{C(515)} & \sigma_{O(515)} & \sigma_{Sn(515)} \\ \sigma_{C(550)} & \sigma_{O(550)} & \sigma_{Sn(550)} \end{pmatrix}^{-1} \begin{pmatrix} A_{320} \\ A_{515} \\ A_{550} \end{pmatrix} \tag{6.7}$$

The solution contains the concentrations of each element multiplied by the film thickness d, and can thus be expressed in mol/cm^2. If d is known (AFM measurements), the concentration of the element in mol/cm^3 can be easily obtained through division by d. However, reporting the values in mol/cm^2 has the advantage that different EUV doses can be conveniently compared. This is because the value in mol/cm^2 is unaffected by densification of the material. The values in mol/cm^2 can therefore easily be compared to study losses or gains of elements. In contrast, elemental density values in mol/cm^3 depend on both compression of the material and elemental gain or loss; they are therefore less straightforward to interpret. The elemental cross sections $\sigma_{X(E)}$ at selected

energies can be approximated by tabulated values such as those by Chantler,[237,238] who uses a purely computational approach, or by Henke and coworkers[100] who use a combination of computation and experimental results. The elemental cross sections were also independently measured, as will be described later in this chapter.

In addition to measurements on exposed developed samples, non-developed samples were studied as well. In this case, raster scans were recorded that contained both an exposed and an unexposed part of the tin-oxo cage film. Absolute absorbance values cannot be obtained, but the difference in absorbance (ΔA) can be easily calculated using the formula:

$$\Delta A = -\ln(\frac{\bar{I}_\mathrm{e}}{\bar{I}_\mathrm{u}}) \tag{6.8}$$

in which ΔA is the difference in absorbance, $\bar{I}_\mathrm{e}$ is the average number of counts through the exposed part and $\bar{I}_\mathrm{u}$ the average number of counts through the unexposed part. ΔA is usually negative because the number of counts through the exposed part will be higher as a result of photobleaching. From ΔA, the difference in the amount of each element can be calculated, for example the loss of carbon. This is given by Eq. 6.7, with $c_{\mathrm{X}(E)}$ replaced by Δc_X and A_E replaced by ΔA_E.

Error propagation

STXM raster scans inherently contain noise. As an estimate for the statistical error within the measurements, the standard error of the mean (SEM, $s_{\bar{x}}$) can be used, which is given by $s/\sqrt{N}$ (in which s is the standard deviation and N the number of measurements, in this case the number of pixels). This can be calculated from the standard deviations in pixel intensity of the studied area. From this, the SEM of other measured variables can be calculated. The standard error of the mean propagates in the same way as the standard deviation, as is given by the well-known "propagation of errors" formula:

$$s_f = \sqrt{\left(\frac{\partial f}{\partial x}\right)^2 s_x^2 + \left(\frac{\partial f}{\partial y}\right)^2 s_y^2 + \left(\frac{\partial f}{\partial z}\right)^2 s_z^2 + \ldots} \tag{6.9}$$

in which s_f represents the standard deviation of the function f, s_x represents the standard deviation of x, s_y represents the standard deviation of y, and so forth.[239] In this formula, the standard deviation can be replaced by the SEM by substituting s_x with $(\frac{s_x}{\sqrt{N_x}}) = s_{\bar{x}}$, where N_x is the number of measurements on variable x (for example the number of pixels in the image area under study) and $s_{\bar{x}}$ is the SEM. Using Eq. 6.9 we can obtain the SEM for all measured quantities. For example, the SEMs of the absorbance values are given by:

$$s_{\bar{A}} = \sqrt{\left(\frac{\partial A}{\partial \bar{I}}\right)^2 s_{\bar{I}}^2 + \left(\frac{\partial A}{\partial \bar{I}_0}\right)^2 s_{\bar{I}_0}^2} \tag{6.10}$$

Using $A = -\ln(\bar{I}/\bar{I}_0)$ and taking the derivative, we obtain:

$$s_{\bar{A}} = \sqrt{\left(-\frac{1}{\bar{I}}\right)^2 s_{\bar{I}}^2 + \left(\frac{1}{\bar{I}_0}\right)^2 s_{\bar{I}_0}^2} \tag{6.11}$$

The SEMs of the elemental densities (or loss of elemental densities in case of a non-developed sample) were calculated using Eq. 6.9, replacing all due quantities. This is straightforward yet tedious, so we will refrain from showing the full derivation.

For the cross sections, both experimental and tabulated values were used. For tabulated values, the error in σ was ignored because it is not known. For the experimentally obtained values, the SEM was calculated by:

$$s_{\bar{\sigma}_{E,\mathrm{X}}} = \frac{s_{\bar{A},E}}{\rho_{\mathrm{X}} d} \tag{6.12}$$

in which $s_{\bar{\sigma}_{E,\mathrm{X}}}$ is the SEM in the absorption cross section of element X at photon energy E, $s_{\bar{A},E}$ is the SEM in the absorbance at energy E (as given by Eq. 6.11), ρ_{X} is the elemental density of element X (in mol/cm^3) and d is the sample thickness. Elemental density was calculated using reference values for the compounds ($\rho = 1.00$ g/cm^3 for polystyrene, 1.19 g/cm^3 for polymethyl methacrylate, 7.27 g/cm^3 for tin) and the molar mass of the monomer (polymers) or atomic weight (tin). The errors in the density and thickness were neglected here. The thus obtained values for $s_{\bar{\sigma}_{E,\mathrm{X}}}$ were used to calculate contributions of these values to the error in elemental composition, making use of the propagation of errors formula (Eq. 6.9).

Results

To check the feasibility of our approach, Eq. 6.7 was first used to measure elemental concentrations of an unexposed TinOH film. A partially developed TinOH film was used for this, containing both the unexposed film ($d \approx 26$ nm) and bare silicon nitride. As a first try, we attempted to fill in tabulated values by Henke and coworkers for the absorption coefficients $\sigma_{\mathrm{X},E}$. The resulting elemental densities are shown in Fig. 6.16. Clearly, the measured elemental composition does not match the theoretical one, mainly for oxygen. Especially the ratio between oxygen and tin is quite far off. The calculated elemental composition was found to be highly dependent on the exact values for the absorption cross sections. According to Chantler,[238] errors in such values can be 50–100%. Therefore, experimental verification was found to be necessary. We performed reference measurements on compounds that have a known elemental composition: polystyrene (PS), polymethyl methacrylate (PMMA) and tin (Sn). Neglecting absorption by hydrogen, the elemental absorption coefficients can be expressed as:

$$\begin{aligned}
\sigma_{\mathrm{C}} &= \frac{A_{\mathrm{PS}}}{d_{\mathrm{PS}} \cdot \rho_{\mathrm{C,PS}}} \\
\sigma_{\mathrm{O}} &= \frac{A_{\mathrm{PMMA}} - A_{\mathrm{PMMA\ (carbon)}}}{d_{\mathrm{PMMA}} \cdot \rho_{\mathrm{O,PMMA}}} \\
\sigma_{\mathrm{Sn}} &= \frac{A_{\mathrm{Sn}}}{\rho_{\mathrm{Sn}} \cdot d_{\mathrm{Sn}}}
\end{aligned} \tag{6.13}$$

In Eq. 6.13, A_{PS} is the absorbance of the polystyrene flake, d is the flake thickness in cm, and $\rho_{\mathrm{C,PS}}$ is the density of carbon atoms in PS in mol/cm^3. This is given by $(\rho_{\mathrm{PS}}/\mathrm{MW_S}) \cdot 8$, in which ρ_{PS} is the density of polystyrene in g/cm^3, $\mathrm{MW_S}$ is

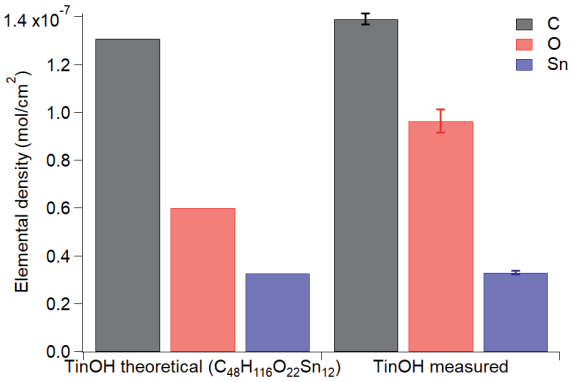

Figure 6.16: Bar chart of the theoretical elemental composition of TinOH (left, as calculated using the molecular formula) and the measured elemental composition (right) as measured using STXM. For the absorption coefficients $\sigma_{X,E}$, values were calculated by interpolation of values obtained from Henke and coworkers.[100] Error bars are the standard error of the mean (SEM). The theoretical composition was matched to the amount of tin in the experimental composition.

the molecular weight of styrene in g/mol, and 8 is the number of carbon atoms in a styrene monomer. For the PMMA measurement on oxygen, the absorbance is obtained by subtracting the absorbance that is induced by carbon ($A_{\mathrm{PMMA\ (carbon)}}$), given by $\sigma_C \cdot \rho_{C,\mathrm{PMMA}} \cdot d_{\mathrm{PMMA}}$, from the total absorbance. For PS and PMMA, a small correction for the absorption of hydrogen was applied by using tabulated values by Henke et al:[100] the known amount of carbon was converted to an amount of hydrogen, using the molecular formula.

The quality of the PS and PMMA samples was studied by measuring carbon K-edge spectra (see Fig. 6.17). A good agreement with literature spectra was found. For PS, the spectrum was compared to previous work by Outka and Stöhr.[232] The spectrum is characterized by several clear resonances. The strong absorption peak at the lowest energy, C 1s $\rightarrow$ π^* 1, corresponds to a transition to an antibonding π^* orbital on the aromatic rings. However, it also has contributions from the aliphatic side groups, which adds to the strength of this peak. Additional peaks can be assigned using the NEXAFS of benzene as a basis.[240]

The PMMA spectrum features one sharp peak at 288.5 eV corresponding to the π^* resonance of the C=O ester group. Additional weak features are present at 292, 296 and 302 eV which originate from various transitions, with the broad resonance at 302 eV corresponding to C–O σ^*.[241] For PMMA, it is known that radiation damage can occur, leading to cross-linking and to C=C bond formation.[233] The newly formed C=C π^* resonance is usually centered at 285.0 eV. This does not seem to be visible in the PMMA spectrum.

For Sn, the oxygen K-edge and Sn $M_{4,5}$-edges (480–590 eV, Fig. 6.18) were scanned

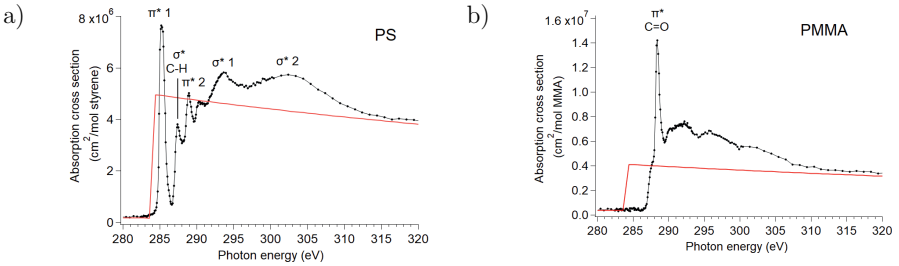

Figure 6.17: Carbon K-edge spectra of (a) polystyrene and (b) polymethyl methacrylate flakes, with a 240 nm and 77 nm thickness. The absorption coefficient is calculated in cm^2 per mol of the monomer (styrene, methyl methacrylate). The red lines show the spectra as calculated from tabulated values.[100] Peak assignments are based on refs.[232,242] for PS and refs.[233,241] for PMMA.

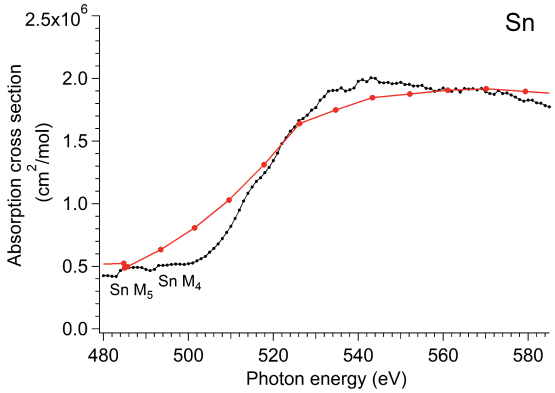

Figure 6.18: Experimental $M_{4,5}$-edge spectrum of Sn (flake, thickness approximately 177 nm, β form). This spectrum is an average of three separate measurements. The red line shows the spectrum as calculated from tabulated values.[100]

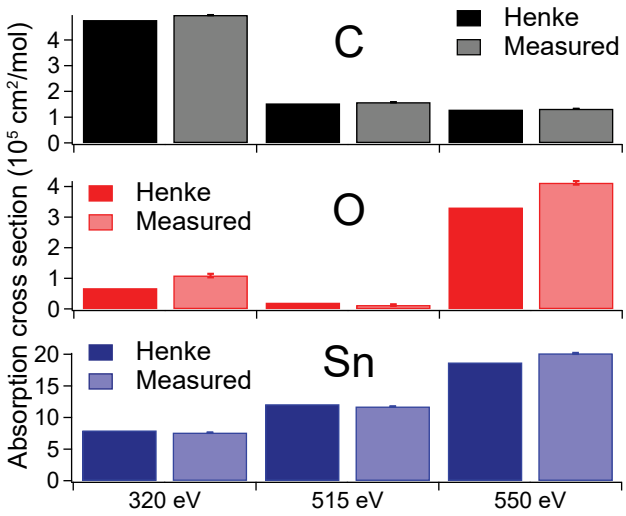

Figure 6.19: Elemental cross sections as reported by Henke et al.[100] (solid bars) and measured by reference measurements (shaded bars). Error bars are the standard error of the mean (SEM). The numerical data corresponding to this figure can be found in the ESI (Table 9.7).

to study possible contamination with oxygen. Since the Sn sample was briefly exposed to air, formation of an oxide layer on the surface is probable. As is known from previous studies, tin is not oxidized rapidly under ambient conditions, forming only a thin layer of tin (II) oxide,[243] of which the thickness is negligible compared to the total sample thickness. For comparison, spectra obtained from tabulated values (Henke et al.[100]) are additionally plotted. In this range, both the $M_{4,5}$-edges of tin (very broad, with two weak resonances at low photon energies) and oxygen K-edge (sharp resonances around 540 eV) are present. Elemental tin, tin (II) oxide (SnO) and tin (IV) oxide (SnO_2) were all studied previously by others using Electron Energy Loss Spectroscopy (EELS).[244,245] A distinct resonance was shown to be present for SnO between 535 and 540 eV. Although some weak features can be observed in this region, clearly the SnO contribution to the experimental spectrum is small. Therefore, we assumed only a very thin (3 nm) layer of SnO on both sides of the Sn flake, in line with previous results of tin oxidation at ambient temperature.[243]

The thus obtained values for the cross sections were compared to tabulated values by Henke et al. as shown in Fig. 6.19. As can be seen, the absorption cross sections are close to tabulated values, but they do not completely match them. The reason could be either experimental error or shortcomings of the tabulated values. The main difference is in the oxygen absorption coefficient at 515 eV, which was measured to be much lower ($\sim 1.6\times$). This value was obtained from the reference measurement on PMMA, subtracting absorbance caused by carbon from the total absorbance (see

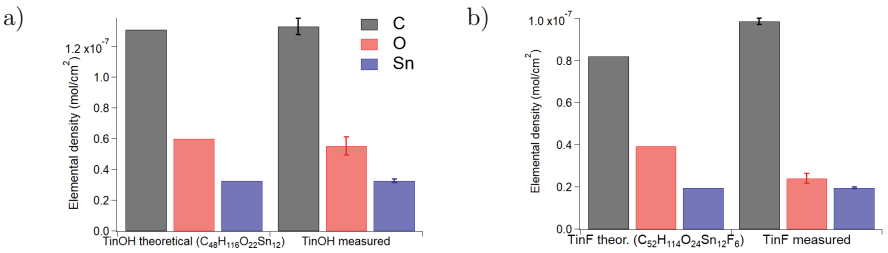

Figure 6.20: Bar chart of the theoretical and experimental compositions of (a) TinOH and (b) TinF. Error bars are the standard error of the mean (SEM). The amount of tin in the theoretical and experimental composition was assumed to be equal.

Eq. 6.13). The contribution of oxygen to the absorbance is quite small at 515 eV, as it has both a low absorption cross section and a low elemental density (2.5× lower than carbon). Therefore, this value may be more prone to errors than others, because a small deviation in absorbance already leads to a large deviation in the calculated amount of oxygen. The elemental composition of TinOH, making use of experimentally obtained elemental absorption coefficients, is shown in Fig. 6.20a. As can be seen, the experimental elemental composition matches the theoretical cross section within the error margin. However, for the closely related TinF (Fig. 6.20b), the experimental data agree less well with the theoretical composition. Clearly, the amount of oxygen has the largest uncertainty, which is a direct result of the absorption coefficient of oxygen having a relatively large error.

It is also possible to calculate the density of the elements in the film, by dividing the elemental density (in mol/cm^2) by the measured film thickness. If we add the density of all elements (in g/cm^3) together, we obtain a density of 2.5 g/cm^3 for TinOH, which is somewhat higher than the value obtained from the crystal structure of TinOH (1.84 g/cm^3),[107] TinOTs (tosylate counterions, 1.93 g/cm^3)[99] and TinCl (chloride counterions, 2.05 g/cm^3).[113]

Now that we have confirmed the feasibility of this approach, we can move towards elemental compositions of EUV-exposed films. A spin coated film of TinOH was exposed to EUV light with four different doses: 37.5 mJ/cm^2, 75 mJ/cm^2, 150 mJ/cm^2 and 375 mJ/cm^2. 37.5 mJ/cm^2 is sufficiently high to have enough material remaining after development,[161] and to be able to clearly see the exposure spot (in case of the non-developed samples). Higher doses were also studied to observe the effects of over-exposure and to track the gradual conversion to a tin oxide-like material.

STXM raster scans were recorded (320, 515 and 550 eV) at the edges of exposed areas. The resulting absorbance values were converted into elemental compositions using Eq. 6.7. The results are shown in Fig. 6.21 for samples that were developed after exposure.

It can be seen that the amount of carbon drastically decreases with increasing dose. This result is qualitatively in line with previously published elemental compositions of EUV-exposed TinOH, although the amount of lost carbon differs. Zhang

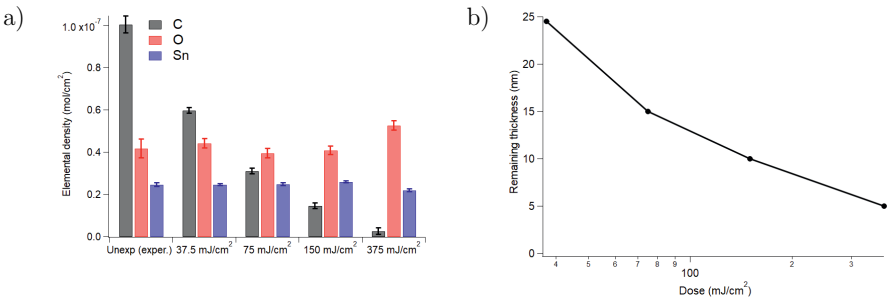

Figure 6.21: (a) Bar chart showing measured elemental composition of EUV-exposed developed TinOH. The experimental composition of the unexposed thin film was normalized to the amount of tin of the 37.5 mJ/cm^2 exposed material. (b) shows the remaining film thickness as function of EUV dose. A duplicate of these measurements can be found in the ESI (Fig. 9.25).

and coworkers report a carbon loss of only around 30% at an exposure dose of 250 mJ/cm^2.[102] The carbon amount as measured by XPS is possibly affected by surface contamination; at the low EUV dose of 10 mJ/cm^2, the XPS results indicated an *increasing* amount of carbon upon irradiation.

The carbon loss in STXM is strongly correlated with the thickness loss (see Fig. 6.21b). At 37.5 mJ/cm^2, around 40% of carbon is removed by either outgassing or the development process, giving rise to an insoluble product mixture. At this stage of conversion, on average about five butyl groups have been cleaved from the tin-oxo cage. This is reasonably in line with the model by Hinsberg,[90] which indicates that at 20 mJ/cm^2 an insoluble product is formed which has lost on average about three organic groups.

At high dose (375 mJ/cm^2), almost all carbon has disappeared while there is still film remaining. This is consistent with formation of SnO_2 as an end product at high EUV doses. At full conversion to SnO_2, the thickness would be approximately 20% of the unexposed film thickness.

The amount of tin and oxygen appears to remain approximately constant upon irradiation. This is a surprising result, since the development process is expected to remove unconverted tin-oxo cages, which contain tin. However, 37.5 mJ/cm^2 could be already higher than the dose required to obtain the maximum thickness, which means that very little unconverted material is remaining. Indeed, the thickness decreases at higher doses than 37.5 mJ/cm^2 (see Fig. 6.21b).

An increase in amount of oxygen (as observed in some cases) could be explained by reaction of intermediary reaction products with O_2, taking place during sample transfer between the exposure beamline and the STXM beamline.

The amount of tin appears to decrease at a high EUV dose (375 mJ/cm^2). A loss as a result of development is not expected at this dose because most (if not all) tin-oxo cage material should already be converted at this dose. The decrease in amount of tin could be caused by outgassing of tin-containing species upon exposure. This was

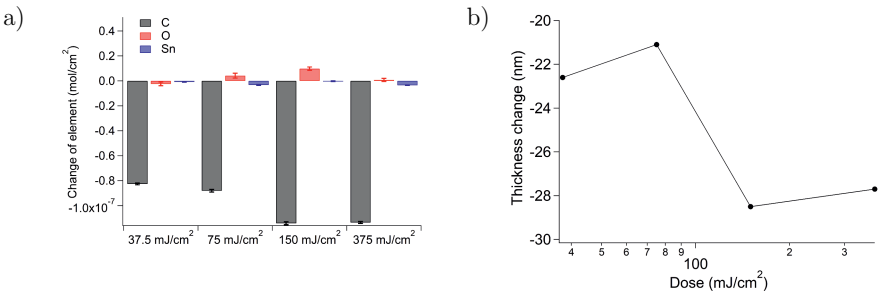

Figure 6.22: Bar chart showing measured differences in elemental composition of EUV-exposed TinOH, compared to unexposed TinOH (a). (b) shows the thickness loss as function of EUV dose. The composition for the theoretical unexposed material was calculated by assuming that the amount of tin is the same as for the 37.5 mJ/cm^2 material, and calculating the amounts of oxygen and carbon using the molecular formula.

studied separately in a measurement on exposed but non-developed material (see Fig. 6.22). Here, a small loss of tin (around 3.3×10^{-9} mol/cm^2) is also observed at 75 mJ/cm^2 and 375 mJ/cm^2. However, this observed loss of tin is not consistent because at 150 mJ/cm^2 very little loss of tin occurs. This would mean a gain of tin between 75 mJ/cm^2 and 150 mJ/cm^2, which is unexpected. This can hardly be explained by surface contamination, because any contaminant is unlikely to contain tin. The reason for this inconsistent result is therefore unclear, and loss of tin cannot really be proven or disproven using these measurements. The thickness loss (Fig. 6.22b) also showed inconsistencies, since any gain in thickness upon exposure is very unlikely. This also raises the question to what extent the initially spin coated film has a homogeneous thickness (d). Since the measured amount of elements (or elemental loss) scales with d (see Eq. 6.7), variations in film thickness could easily cause differences in the measured amount of Sn. However, it should be kept in mind that the initial thickness d is a scaling factor, and an inhomogeneous d should not have an effect on the ratios between elements.

An additional factor is uncertainty in the absorption cross sections. Although the statistical errors in the cross sections have been taken into account, these have neglected errors in thickness and density of the film, which are difficult to assess. The actual error may therefore be larger than the error bars shown in Fig. 6.20.

Apart from TinOH, the closely related TinF was also studied, with trifluoroacetate as counterion instead of hydroxide. This material is interesting because it should have an around 9% larger EUV absorption cross section (as a result of added fluorine, which is a good EUV absorber) but it was found to have lower sensitivity to both EUV and DUV.[111] The reason for the lower sensitivity is not known, but it could be related to the lower reactivity of the trifluoroacetate anion (which is much less nucleophilic and basic than OH^-). Additional research is needed to understand the reactivity issues.

The elemental composition of TinF, as function of EUV dose, is shown in Fig. 6.23.

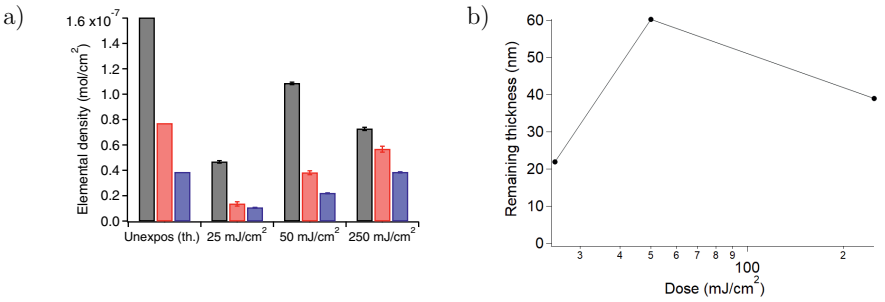

Figure 6.23: Bar chart showing measured elemental composition of EUV-exposed developed TinF (a). The composition for the theoretical unexposed material was calculated by assuming that the amount of tin is the same as for the 250 mJ/cm^2 material, and calculating the amounts of oxygen and carbon using the molecular formula. (b) shows the remaining film thickness as function of EUV dose.

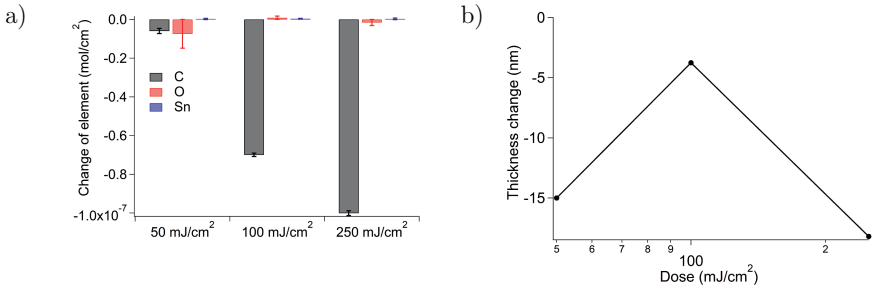

Figure 6.24: Bar chart showing measured differences in elemental composition of EUV-exposed TinF, compared to unexposed TinF. (b) shows the thickness loss as function of EUV dose.

As compared to TinOH, the results are a bit different. First, the initial thickness is probably higher since the thickness is still as high as 60 nm at an EUV dose of 50 mJ/cm^2. Furthermore, a clear loss of tin is apparent at low doses. This is attributed to development-induced tin losses (loss of tin was not observed for the non-developed sample). Conversion to insoluble material probably requires a higher dose for TinF than for TinOH. At high dose, almost all material has been converted to insoluble compounds, meaning the remaining amount of tin is higher than for low doses. Very little material is remaining at low doses, as can be seen from both the thickness measurement and the elemental composition measurement. The amount of oxygen is lower than expected at 25 mJ/cm^2, while its value is more reasonable for higher doses. The amount of carbon first decreases strongly (as a result of the development process removing most of the material), then increases at 50 mJ/cm^2 (as a result of stronger conversion, retaining more material after development), and decreases again at 250 mJ/cm^2, as a result of outgassing of carbon-containing material.

The non-developed sample (showing changes resulting from outgassing of volatile products) shows a clear decrease in the amount of carbon (see Fig. 6.24). Outgassing of tin is clearly not present, since the values for tin are very close to zero.

6.4 Conclusion

Scanning Transmission X-ray Microscopy (STXM) was used to study photo-induced chemical changes occurring in the "tin-oxo cage" material TinOH. Two methods were used: scanning the carbon K-edge, and measuring the absorbance at three different energies to obtain elemental composition. In the carbon K-edge spectrum, several features were assigned to resonant transitions, including 1s to Sn–C σ^*, C–H σ^*/3p Rydberg, and C–C σ^*. Changes in the absorption spectrum upon EUV or DUV exposure were monitored. These changes were only minor, because most carbon-containing photoproducts desorb either upon formation or in the vacuum chamber of the STXM. Although the chemical environment of the remaining butyl groups must change upon conversion of the cages, this did not lead to observable spectral changes. Therefore it was found to be difficult to obtain more chemical information for EUV-exposed samples. For DUV-exposed samples, a shift in the C–H σ^*/3p Rydberg resonance was observed. This can be attributed to carbon atoms that are selectively removed, for instance to butyl groups that are bound to 6-coordinated tin atoms.

The calculations on elemental composition involve elemental cross sections, for which both tabulated and experimental values were used. When tabulated values were used, the agreement with the theoretical composition (based on the molecular formula) was poor. Therefore, reference measurements of the elemental cross sections were carried out on polystyrene (PS) for carbon, polymethyl methacrylate (PMMA) for oxygen, and a metallic tin flake for tin. Using the obtained values in the calculation led to a better agreement with the theoretical composition for TinOH, but still imperfect agreement for TinF. The approach could be improved by performing additional measurements, for example on SnO_2 or on a polymer that contains relatively more oxygen. This would improve the reliability of the method by reducing the error in the obtained absorption coefficients, especially for oxygen. The study on elemental composition showed mainly a loss of carbon upon EUV exposure. A carbon loss of ∼40% led to an insoluble material, in which on average ∼5 butyl groups per tin-oxo cage have been removed. For the tin-oxo cage with trifluoroacetate anions (TinF), a lower reactivity was observed, requiring higher dose to achieve loss of carbon and corresponding conversion to insoluble material. This is despite TinF containing fluorine, enhancing its absorptivity. This could indicate that loss mechanisms are more prominent in TinF; possibly, absorption on fluorine does not lead to the desired solubility switch. However, the different starting thickness (∼30 nm for TinOH vs. ∼60 nm for TinF) could also play a role in the observed difference in sensitivity. No conclusive evidence was found for outgassing of tin species, neither for TinOH nor for TinF.

It can be concluded that STXM is suitable to study chemical changes upon EUV exposure. Relatively thin films (20–60 nm) were measured, which is generally difficult to achieve by other spectroscopic methods, except XPS. A limitation of this study is the relatively poor control on film thickness. Because photoproducts are likely to be lost as a result of their low molecular weight, the tin-oxo cage may not be the most suitable system to study using STXM. However, the used approach of measuring the carbon K-edge and elemental composition is clearly feasible, and could be extended to other photoresist-like systems or even to other scientific fields.

References

[1] Fleming, J. A. *The thermionic valve and its developments in radio-telegraphy and telephony*; Wireless Press, 1919.

[2] de Forest, L. The audion: A new receiver for wireless telegraphy. *Trans. Am. Inst. Electr. Eng.* **1906**, *XXV*, 735–763.

[3] de Forest, L. Demodulation of amplitude-modulated oscillations by means of non-linear elements having more than two poles of discharge tubes, US patent 879532A. 1907.

[4] de Forest, L. Evolution of the vacuum tube. *Radio News* **1930**, p. 990.

[5] Bardeen, J.; Brattain, W. The transistor, a semi-conductor triode. *Phys. Rev.* **1948**, *74*, 230.

[6] Haller, E. Germanium: from its discovery to high speed transistors. 2011; https://microlab.berkeley.edu/text/seminars/slides.

[7] Kahng, D. Electric field controlled semiconductor device, U.S. patent 3102230A. 1960.

[8] Atalla, M. Semiconductor devices having dielectric coatings, U.S. patent 3206670A. 1960.

[9] Yamada, I.; Matsuo, J.; Toyoda, N.; Kirkpatrick, A. Materials processing by gas cluster ion beams. *Mater. Sci. Eng.* **2001**, *34*, 231–295.

[10] Moore, G. Cramming more components onto integrated circuits. *Electronics* **1965**, *38*.

[11] Moore, G. E. Progress in digital integrated electronics. *Int. Electron Devices Meet. IEEE* **1975**, 11–13.

[12] E. Sperling, Quantum effects at 7/5nm and beyond. 2018; https://semiengineering.com/quantum-effects-at-7-5nm/.

[13] Nishi, Y.; Doering, R. *Semiconductor manufacturing technology*; CRC Press, 2008; pp 18–7.

[14] Mack, C. A. The new, new limits of optical lithography. *Proc. SPIE* **2014**, *5374*.

[15] Levinson, H. J. *Principles of Lithography, Second Edition*; SPIE Press, 2005.

[16] Jain, K.; Willson, C.; Lin, B. Ultrafast deep UV lithography with excimer lasers. *IEEE Electron Device Lett.* **1982**, *3*, 53–55.

[17] Vogler, K.; Klaft, I.; Voss, F.; Bragin, I.; Bergmann, E.; Nagy, T.; Niemoeller, N.; Paetzel, R.; Govorkov, S.; Hua, G. Advanced F_2-lasers for 157 nm lithography. *Proc. SPIE* **2001**, *4346*, 1175–1182.

[18] Lin, B. J. The future of subhalf-micrometer optical lithography. *Microelectron. Eng.* **1987**, *6*, 31–51.

[19] Tittnich, M. et al. A year in the life of an immersion lithography Alpha Tool at Albany NanoTech. *Proc. SPIE* **2006**, *6151*, 615101.

[20] Kinoshita, H.; Kaneko, T.; Takei, H.; Takeuchi, N.; Ishihara, S. Study on X-ray reduction projection lithography. *47th Autumn Meeting Japan Soc. Appl. Phys.* **1986**, *28-ZF-15*, 15.

[21] Silfvast, W. T.; Wood, O. R. Tenth micron lithography with a 10 Hz 37.2 nm sodium laser. *Microelectron. Eng.* **1988**, *8*, 3–11.

[22] Hawryluk, A. M.; Seppala, L. G. Soft X-ray projection lithography using an X-ray reduction camera. *J. Vac. Sci. Sci. Technol. B* **1988**, *6*, 2162–2166.

[23] Kinoshita, H.; Kurihara, K.; Ishii, Y.; Torii, Y. Soft X-ray reduction lithography using multilayer mirrors. *J. Vac. Sci. Technol. B* **1989**, *7*, 1648–1651.

[24] Kinoshita, H. History of extreme ultraviolet lithography. *J. Vac. Sci. Technol. B* **2005**, *23*, 2584–2588.

[25] Bakshi, V. *EUV lithography*; SPIE Press, 2008.

[26] Hawryluk, A. M.; Ceglio, N. M. Wavelength considerations in soft X-ray projection lithography. *Appl. Opt.* **1993**, *32*, 7062–7067.

[27] Bajt, S.; Alameda, J.; Barbee Jr., T. W.; Clift, W. M.; Folta, J.; Kaufmann, B.; Spiller, E. Improved reflectance and stability of Mo-Si multilayers. *Opt. Eng.* **2002**, *41*, 1797–1804.

[28] Torretti, F.; Schupp, R.; Kurilovich, D.; Bayerle, A.; Scheers, J.; Ubachs, W.; Hoekstra, R.; Versolato, O. O. Short-wavelength out-of-band EUV emission from Sn laser-produced plasma. *J. Phys. B* **2018**, *51*, 045005.

[29] Schupp, R.; Torretti, F.; Meijer, R. A.; Bayraktar, M.; Sheil, J.; Scheers, J.; Kurilovich, D.; Bayerle, A.; Schafgans, A. A.; Purvis, M.; Eikema, K. S. E.; Witte, S.; Ubachs, W.; Hoekstra, R.; Versolato, O. O. Radiation transport and scaling of optical depth in Nd:YAG laser-produced microdroplet-tin plasma. *Appl. Phys. Lett.* **2019**, *115*, 124101.

[30] Lee, J.; Kim, J.; Jeong, S.; Lim, M.; Koo, S.; Lim, C.-M.; Kim, Y.-S. Study on RLS trade-off resist upgrade for production ready EUV lithography. *Proc. SPIE* **2016**, *9776*, 977623.

[31] Macdonald, S. A.; Grant Willson, C.; Fréchet, M. J. Chemical amplification in high-resolution imaging systems. *Acc. Chem. Res.* **1994**, *27*, 151–158.

[32] Narasimhan, A.; Wisehart, L.; Grzeskowiak, S.; Ocola, L. E.; Denbeaux, G.; Brainard, R. L. What we don't know about EUV exposure mechanisms. *J. Photopolym. Sci. Tec.* **2017**, *30*, 113–120.

[33] Kwark, Y.-J.; Bravo-Vasquez, J. P.; Chandhok, M.; Cao, H.; Deng, H.; Gullikson, E.; Ober, C. K. Absorbance measurement of polymers at extreme ultraviolet wavelength: Correlation between experimental and theoretical calculations. *J. Vac. Sci. Technol. B* **2014**, *24*, 1822–1826.

[34] Carcasi, M.; Bassett, D.; Printz, W.; Kawakami, S.; Miyata, Y. Line pattern collapse mitigation status for EUV at 32nm HP and below. *Proc. SPIE* **2012**, *8325*, 83250K.

[35] Goldfarb, D. L.; Bruce, R. L.; Bucchignano, J. J.; Klaus, D. P.; Guillorn, M. A.; Wu, C. J. Pattern collapse mitigation strategies for EUV lithography. *Proc. SPIE* **2012**, *8322*, 832205.

[36] Montgomery, C.; Chun, J. S.; Fan, Y.-J.; Jen, S.-H.; Neisser, M.; Cummings, K. D.; Montgomery, W.; Saito, T.; Huli, L.; Hetzer, D.; Matsumoto, H.; Metz, A.; Rastogi, V. Evaluation of novel processing approaches to improve extreme ultraviolet (EUV) photoresist pattern quality. *Proc. SPIE* **2015**, *9425*, 942526.

[37] Lawson, R. A. Molecular resists for advanced lithography – design, synthesis, characterization, and simulation. Ph.D. thesis, Georgia Institute of Technology, 2011.

[38] Gallatin, G. M.; Naulleau, P.; Brainard, R. Fundamental limits to EUV photoresist. *Proc. SPIE* **2007**, *6519*, 651911.

[39] Kostinski, A. B. On the extinction of radiation by a homogeneous but spatially correlated random medium. *J. Opt. Soc. Am. A* **2001**, *18*, 1929–1933.

[40] Naulleau, P.; Anderson, C.; Chao, W.; Bhattarai, S.; Neureuther, A. Stochastics and EUV patterning in the 1x-nm regime. *J. Photopolym. Sci. Tec.* **2016**, *29*, 797–802.

[41] Kozawa, T. Effects of dose shift on line width, line edge roughness, and stochastic defect generation in chemically amplified extreme ultraviolet resist with photodecomposable quencher. *Jpn. J. Appl. Phys.* **2015**, *016503*.

[42] Montgomery, W.; McClelland, A.; Ure, D.; Roth, J.; Robinson, A. Irresistible Materials multi-trigger resist: "The journey towards high volume manufacturing readiness". *Proc. SPIE* **2017**, *10143*, 1014328.

[43] Popescu, C.; Vesters, Y.; McClelland, A.; De Simone, D.; Dawson, G.; Roth, J.; Theis, W.; Vandenberghe, G.; Robinson, A. P. G. Multi Trigger Resist for EUV Lithography. *J. Photopolym. Sci. Tec.* **2018**, *31*, 227–232.

[44] O'Callaghan, G.; Popescu, C.; McClelland, A.; Kazazis, D.; Roth, J.; Theis, W.; Ekinci, Y.; Robinson, A. P. G. Multi-trigger resist: novel synthesis improvements for high resolution EUV lithography. *Proc. SPIE* **2019**, *10960*, 109600C.

[45] Buitrago, E. et al. Sensitivity enhancement of chemically amplified resists and performance study using EUV interference lithography. *J. Micro/Nanolith. MEMS MOEMS* **2016**, *15*, 033502.

[46] Fallica, R.; Haitjema, J.; Wu, L.; Castellanos, S.; Brouwer, A. M.; Ekinci, Y. Absorption coefficient of metal-containing photoresists in the extreme ultraviolet. *J. Micro/Nanolith. MEMS MOEMS* **2018**, *17*, 1.

[47] Charache, G. W.; Maby, E. W.; Daubenspeck, T.; Bakeman, P. Lateral diffusion of sodium from peripheral sources in metal oxide semiconductor transistors. *J. Electrochem. Soc.* **1992**, *140*, 1144–1146.

[48] Shiobara, E.; Kikuchi, Y.; Mikami, S.; Sasami, T.; Kamizono, T.; Minegishi, S.; Kimoto, T.; Fujimori, T.; Watanabe, T.; Harada, T.; Kinoshita, H.; Tanaka, S. EUV resist outgassing analysis for the new platform resists at EIDEC. *Proc. SPIE* **2015**, *9776*, 97762H.

[49] Meyers, S. T.; Anderson, J. T.; Cardineau, B. J.; Edson, J. B.; Jiang, K.; Keszler, D. A.; Dardi, P. S. Organotin oxide hydroxide patterning compositions, precursors, and patterning, US Patent WO2017066319 A2. 2017.

[50] Sasaki, T.; Yokokoji, O.; Watanabe, T.; Kinoshita, H. Development of partially fluorinated EUV-resist polymers for LER and sensitivity improvement. *Proc. SPIE* **2008**, *6923*, 692347.

[51] Christianson, M. D.; Meyer, M. M.; Ongayi, O.; Valeri, D.; Wagner, M. High absorbing resists based on trifluoromethacrylate-vinyl ether copolymers for EUV lithography. *Proc. SPIE* **2013**, *8682*, 868216.

[52] Fukunaga, M.; Yamamoto, H.; Kozawa, T.; Watanabe, T. Synthesis and property of tellurium-containing polymer for Extreme Ultraviolet resist material. *J. Photopolym. Sci. Tec.* **2017**, *30*, 103–107.

[53] Bae, W. J.; Trikeriotis, M.; Sha, J.; Schwartz, E. L.; Rodriguez, R.; Zimmerman, P.; Giannelis, E. P.; Ober, C. K. High refractive index and high transparency HfO_2 nanocomposites for next generation lithography. *J. Mater. Chem.* **2010**, *20*, 5186–5189.

[54] Trikeriotis, M.; Krysak, M.; Sook, Y.; Ouyang, C.; Cardineau, B. A new inorganic EUV resist with high-etch resistance. *Proc. SPIE* **2012**, *8322*, 83220U.

[55] Chakrabarty, S.; Ouyang, C.; Krysak, M.; Trikeriotis, M.; Cho, K.; Giannelis, E. P.; Ober, C. K. Oxide nanoparticle EUV resists: toward understanding the mechanism of positive and negative tone patterning. *Proc. SPIE* **2013**, *8679*, 867906.

[56] Jiang, J.; Chakrabarty, S.; Yu, M.; Ober, C. K. Metal oxide nanoparticle photoresists for EUV patterning. *J. Photopolym. Sci. Tec.* **2014**, *27*, 663–666.

[57] Kasahara, K.; Kosma, V.; Odent, J.; Xu, H.; Yu, M.; Giannelis, E. P.; Ober, C. K. Recent progress in nanoparticle photoresist development for EUV lithography. *Proc. SPIE* **2015**, *9776*, 977604.

[58] Minami, Y.; Takahashi, S.; Minami, H.; Matsumoto, Y.; Kadoi, M.; Sekiguchi, A.; Watanabe, T. In-situ measurement of outgassing generated from EUV metal oxide nanoparticles resist during electron irradiation. *Proc. SPIE* **2018**, *10809*, 108091W.

[59] Sekiguchi, A.; Matsumoto, Y.; Isono, M.; Naito, M.; Utsumi, Y.; Harada, T.; Watanabe, T. A study on enhancing EUV resist sensitivity (2). *Proc. SPIE* **2017**, *10450*, 104501E.

[60] Carta, B. G.; Habra, N. E.; Rossetto, G.; Torzo, G.; Crociani, L.; Natali, M.; Zanella, P.; Cavinato, G.; Matterello, V.; Rigato, V.; Kaciulis, S.; Mezzi, A. Growth of hafnium dioxide thin films by MOCVD using a new series of cyclopentadienyl hafnium compounds. *Chem. Vap. Depos.* **2007**, *13*, 626–632.

[61] Ruther, R. E.; Baker, B. M.; Son, J.-H.; Casey, W. H.; Nyman, M. Hafnium sulfate prenucleation clusters and the Hf_{18} polyoxometalate red herring. *Inorg. Chem.* **2014**, *53*, 4234–4242.

[62] Son, J.-H.; Park, D.-H.; Keszler, D. A.; Casey, W. H. Acid-stable peroxoniobophosphate clusters to make patterned films. *Chem. Eur. J.* **2015**, *21*, 6727–6731.

[63] Mansergh, R. H.; Fullmer, L. B.; Park, D.-H.; Nyman, M.; Keszler, D. A. Reaction pathway: aqueous hexatantalate clusters to high-density tantalum oxide nanofilms. *Chem. Mater.* **2016**, *28*, 1553–1558.

[64] Stehlin, F.; Bourgin, Y.; Spangenberg, A.; Jourlin, Y.; Parriaux, O.; Reynaud, S.; Wieder, F.; Soppera, O. Direct nanopatterning of 100 nm metal oxide periodic structures by Deep-UV immersion lithography. *Opt. Lett.* **2012**, *37*, 4651–4653.

[65] Stehlin, F.; Wieder, F.; Spangenberg, A.; Le Meins, J.-M.; Soppera, O. Room-temperature preparation of metal-oxide nanostructures by DUV lithography from metal-oxo clusters. *J. Mater. Chem. C* **2014**, *2*, 277–285.

[66] Lin, H.-C.; Stehlin, F.; Soppera, O.; Zan, H.-W.; Li, C.-H.; Wieder, F.; Ponche, A.; Berling, D.; Yeh, B.-H.; Wang, K.-H. Deep ultraviolet laser direct write for patterning sol-gel InGaZnO semiconducting micro/nanowires and improving field-effect mobility. *Sci. Rep.* **2015**, *5*, 10490.

[67] Wu, L.; Tiekink, M.; Giuliani, A.; Nahon, L.; Castellanos, S. Tuning photoionization mechanisms of molecular hybrid materials for EUV lithography applications. *J. Mater. Chem. C* **2018**, *7*, 33–37.

[68] Wu, L.; Baljozovic, M.; Portale, G.; Kazazis, D.; Vockenhuber, M.; Jung, T.; Ekinci, Y.; Castellanos, S. Mechanistic insights in Zr- and Hf-based molecular hybrid EUV photoresists. *J. Micro/Nanolithography, MEMS, MOEMS* **2019**, *18*, 013504.

[69] Wu, L.; Liu, J.; Vockenhuber, M.; Ekinci, Y.; Castellanos, S. Hybrid EUV Resists with mixed organic shells: a simple preparation method. *Eur. J. Inorg. Chem.* **2019**, *2019*, 4136–4141.

[70] Thakur, N.; Vockenhuber, M.; Ekinci, Y.; Castellanos, S. Zinc-based metal oxo-clusters: towards enhanced EUV absorptivity. *Proc. SPIE* **2019**, *10957*, 109570D.

[71] Abel, E. W.; Stone, G. A.; Wilkinson, G. *Comprehensive Organometallic Chemistry II*; Pergamon, 1995; p 357.

[72] Zuckerman, J. *Organotin compounds: new chemistry and applications*; American Chemical Society, 1976.

[73] Davies, A. G. *Organotin chemistry, 2nd edition*; Wiley-VCH Verlag, 2004.

[74] Gielen, M. *Tin chemistry: fundamentals, frontiers, and applications*; Wiley, 2008.

[75] Sharps, M. C.; Marsh, D. A.; Zakharov, L. N.; Hutchison, J. E.; Johnson, D. W. Implications of crystal structure on organotin carboxylate photoresists. *Cryst. Res. Technol.* **2017**, *52*, 1700081.

[76] Frederick, R. T.; Diulus, J. T.; Hutchison, D. C.; Olsen, M. R.; Lyubinetsky, I.; Nyman, M.; Herman, G. S. Surface characterization of tin-based inorganic EUV resists. *Proc. SPIE* **2018**, *10586*, 1058607.

[77] Frederick, R. T.; Saha, S.; Trey Diulus, J.; Luo, F.; Amador, J. M.; Li, M.; Park, D.-H.; Garfunkel, E. L.; Keszler, D. A.; Herman, G. S. Thermal and radiation chemistry of butyltin oxo hydroxo: A model inorganic photoresist. *Microelectron. Eng.* **2019**, *205*, 26–31.

[78] Frederick, R.; Diulus, T.; Hutchison, D.; Nyman, M.; Herman, G. S. Effect of oxygen on thermal and radiation induced chemistries in a model organotin photoresist. *ACS Appl. Mater. Interfaces* **2019**, *11*, 4514–4522.

[79] Diulus, J. T.; Frederick, R. T.; Li, M.; Hutchison, D. C.; Olsen, M. R.; Lyubinetsky, I.; Árnadoóttir, L.; Garfunkel, E. L.; Nyman, M.; Ogasawara, H.; Herman, G. S. Ambient-pressure X-ray photoelectron spectroscopy characterization of radiation-induced chemistries of organotin clusters. *ACS Appl. Mater. Interfaces* **2019**, *11*, 2526–2534.

[80] Zhu, Y.; Olsen, M. R.; Nyman, M.; Zhang, L.; Zhang, J. Stabilizing γ-alkyltin–oxo Keggin ions by borate functionalization. *Inorg. Chem.* **2019**, *58*, 4534–4539.

[81] Meyers, S. T.; Keszler, D. A.; Jiang, K.; Anderson, J.; Grenville, A. Organometallic solution based high resolution patterning compositions, US Patent 0056542 A1. 2013.

[82] Meyers, S. T.; Anderson, J. T.; Edson, J. B.; Jiang, K.; Keszler, D. A.; Kocsis, M. K.; Telecky, A. J.; Cardineau, B. J. Organometallic solution based high resolution patterning compositions and corresponding methods, US Patent 0116839 A1. 2016.

[83] Prabusankar, G.; Jousseaume, B.; Toupance, T.; Allouchi, H. Sn_3 and Sn_{10} sulfonate–oxide–hydroxide clusters with two different sulfonate binding modes. *Dalt. Trans.* **2007**, *2*, 3121–3123.

[84] Prabusankar, G.; Jousseaume, B.; Toupance, T.; Allouchi, H. Organic–inorganic Sn_{12} and organic Sn_6 oxide–hydroxide clusters. *Angew. Chem. Int. Ed.* **2006**, *45*, 1255–1258.

[85] Zhu, Y.; Zhang, L.; Zhang, J. Assembly of high-nuclearity Sn_{26},Sn_{34}-oxo clusters: solvent strategies and inorganic Sn incorporation. *Chem. Sci.* **2019**, *10*, 9125–9129.

[86] Eußner, J. P.; Kusche, R. O.; Dehnen, S. Synthesis and thorough investigation of discrete organotin telluride clusters. *Chem. Eur. J.* **2015**, *21*, 12376–12388.

[87] Puff, H.; Reuter, H. Zur Hydrolyse von Monoorganylzinn-trihalogeniden III *. Isolierung und Röntgenstrukturanalyse von Verbindungen mit dem neuartigen Käfig-Ion $[(\text{i-PrSn})_{12}O_{14}(OH)_6]^{2+}$. *J. Organomet. Chem.* **1989**, *373*, 173–184.

[88] Cardineau, B.; Del Re, R.; Marnell, M.; Al-Mashat, H.; Vockenhuber, M.; Ekinci, Y.; Sarma, C.; Freedman, D. A.; Brainard, R. L. Photolithographic properties of tin-oxo clusters using extreme ultraviolet light (13.5nm). *Microelectron. Eng.* **2014**, *127*, 44–50.

[89] Van Lokeren, L.; Willem, R.; van der Beek, D.; Davidson, P.; Morris, G. A.; Ribot, F. Probing the anions mediated associative behavior of tin-12 oxo-macrocations by pulsed field gradient NMR spectroscopy. *J. Phys. Chem. C* **2010**, *114*, 16087–16091.

[90] Hinsberg, W.; Meyers, S. A numeric model for the imaging mechanism of metal oxide EUV resists. *Proc. SPIE* **2017**, *1014604*.

[91] McNaught, A. D.; Wilkinson, A. *IUPAC. Compendium of Chemical Terminology, 2nd ed. (the "Gold Book")*; Blackwell Scientific Publications, 1997; p 31.

[92] Naulleau, P.; Anderson, C.; Chao, W.; Bhattarai, S.; Neureuther, A.; Cummings, K.; Jen, S.-H.; Neisser, M.; Thomas, B. EUV resists: Pushing to the extreme. *J. Photopolym. Sci. Tec.* **2014**, *27*, 725–730.

[93] Shirai, M.; Tsunooka, I.-i. Photoacid and photobase generators: chemistry and applications to polymeric materials. *Prog. Polym. Sci.* **1996**, *21*, 1–45.

[94] Naulleau, P.; Anderson, C.; Chao, W.; Bhattarai, S.; Neureuther, A. Studying resist stochastics with the multivariate Poisson propagation model. *J. Photopolym. Sci. Tec.* **2014**, *27*, 747–750.

[95] De Simone, D.; Mao, M.; Lazzarino, F.; Vandenberghe, G. Metal containing resist readiness for HVM EUV lithography. *J. Photopolym. Sci. Tec.* **2016**, *29*, 501–507.

[96] Amador, J. M.; Decker, S. R.; Lucchini, S. E.; Ruther, R. E.; Keszler, D. A. Patterning chemistry of HafSOx resist. *Proc. SPIE* **2014**, *9051*, 90511A.

[97] Nakagawa, H.; Naruoka, T.; Nagai, T. Recent EUV resists toward high volume manufacturing. *J. Photopolym. Sci. Tec.* **2014**, *27*, 739–746.

[98] Mojarad, N.; Hojeij, M.; Wang, L.; Gobrecht, J.; Ekinci, Y. Single-digit-resolution nanopatterning with extreme ultraviolet light for the 2.5 nm technology node and beyond. *Nanoscale* **2015**, *7*, 4031–4037.

[99] Eychenne-Baron, C.; Ribot, F.; Steunou, N.; Sanchez, C.; Fayon, F.; Biesemans, M.; Martins, J. C.; Willem, R. Reaction of butyltin hydroxide oxide with *p*-toluenesulfonic acid: synthesis, X-ray crystal analysis, and multinuclear NMR characterization of $\{(BuSn)_{12}O_{14}(OH)_6\}(4\text{-}CH_3C_6H_4SO_3)_2$. *Organometallics* **2000**, *19*, 1940–1949.

[100] Henke, B. L.; Gullikson, E. M.; Davis, J. C. X-Ray interactions: photoabsorption, scattering, transmission and reflection at $E = 50$–$30{,}000$ eV, $Z = 1$–92. *At. Data Nucl. Data Tables* **1993**, *54*, 181–342.

[101] Fallica, R.; Stowers, J. K.; Grenville, A.; Frommhold, A.; Robinson, A. P. G.; Ekinci, Y. Dynamic absorption coefficients of chemically amplified resists and nonchemically amplified resists at extreme ultraviolet. *J. Micro/Nanolith. MEMS MOEMS* **2016**, *15*, 033506.

[102] Zhang, Y.; Haitjema, J.; Liu, X.; Johansson, F.; Lindblad, A.; Castellanos, S.; Ottosson, N.; Brouwer, A. M. Photochemical conversion of tin-oxo cage compounds studied using hard X-ray photoelectron spectroscopy. *J. Micro/Nanolith. MEMS MOEMS* **2017**, *16*, 023510.

[103] Haitjema, J.; Zhang, Y.; Ottosson, N.; Brouwer, A. M. Photoreactions of tin-oxo cages, model EUV photoresists. *J. Photopolym. Sci. Tec.* **2017**, *30*, 99–102.

[104] Hinsberg, W.; Houle, F.; Sanchez, M.; Wallraff, G. Chemical and physical aspects of the post-exposure baking process used for positive-tone chemically amplified resists. *IBM J. Res. Dev.* **2001**, *45*, 667–682.

[105] Mack, C. A. Lithographic optimization using photoresist contrast. *Microelectron. Manuf. Technol.* **1991**, *14*, 36–42.

[106] Ekinci, Y.; Vockenhuber, M.; Mojarad, N.; Fan, D. EUV resists towards 11nm half-pitch. *Proc. SPIE* **2014**, *9048*, 904804.

[107] Banse, F.; Toledano, P.; Maquet, J.; Sanchez, C. Hydrolysis of monobutyltin trialkoxides: synthesis and characterizations of $\{(BuSn)_{12}O_{14}(OH)_6\}(OH)_2$. *Inorg. Chem.* **1995**, *34*, 6371–6379.

[108] Mojarad, N.; Gobrecht, J.; Ekinci, Y. Interference lithography at EUV and soft X-ray wavelengths: principles, methods, and applications. *Microelectron. Eng.* **2015**, *143*, 55–63.

[109] Narasimhan, A.; Grzeskowiak, S.; Ostrander, J.; Schad, J.; Rebeyev, E.; Neisser, M.; Ocola, L. E.; Denbeaux, G.; Brainard, R. L. Studying electron-PAG interactions using electron-induced fluorescence. *Proc. SPIE* **2016**, *9779*, 97790F.

[110] Itani, T.; Kozawa, T. Resist materials and processes for extreme ultraviolet lithography. *Jpn. J. Appl. Phys.* **2013**, *52*, 010002.

[111] Zhang, Y. Organotin photoresists for extreme ultraviolet lithography. Ph.D. thesis, University of Amsterdam, 2019.

[112] Elg, D. T.; Sporre, J. R.; Panici, G. A.; Srivastava, S. N.; Ruzic, D. N. In situ collector cleaning and extreme ultraviolet reflectivity restoration by hydrogen plasma for extreme ultraviolet sources. *J. Vac. Sci. Technol. A* **2016**, *34*, 021305.

[113] Dakternieks, D.; Zhu, H.; Tiekink, E. R. T.; Colton, R. Synthesis, structure and reactions of $[(BuSn)_{12}O_{14}(OH)_6]Cl_2{\cdot}2H_2O$: solution studies using ^{119}Sn NMR and electrospray mass spectrometry. *J. Organomet. Chem.* **1994**, *476*, 33–40.

[114] Eychenne-Baron, C.; Ribot, F.; Sanchez, C. New synthesis of the nanobuilding block $\{(BuSn)_{12}O_{14}(OH)_6\}^{2+}$ and exchange properties of $\{(BuSn)_{12}O_{14}(OH)_6\}(O_3SC_6H_4CH_3)_2$. *J. Organomet. Chem.* **1998**, *567*, 137–142.

[115] Ribot, F.; Escax, V.; Martins, J. C.; Biesemans, M.; Ghys, L.; Verbruggen, I.; Willem, R. Probing ionic association on metal oxide clusters by pulsed field gradient NMR spectroscopy: the example of Sn_{12}–oxo clusters. *Chem. Eur. J.* **2004**, *10*, 1747–1751.

[116] Ribot, F.; Veautier, D.; Guillaudeu, S. J.; Lalot, T. Poly [{$(BuSn)_{12}O_{14}(OH)_6$}$(AMPS)_2$] and poly[methyl acrylate-*co*-{$(BuSn)_{12}O_{14}(OH)_6$}$(AMPS)_2$]: hybrid polymers cross-linked through electrostatic interactions. *J. Mater. Chem.* **2005**, *15*, 3973–3978.

[117] Ribot, F.; Lafuma, A.; Eychenne-Baron, C.; Sanchez, C. New photochromic hybrid organic–inorganic materials built from well-defined nano-building blocks. *Adv. Mater.* **2010**, 1496–1499.

[118] Harwood, J.; Mo, H. *Practical NMR spectroscopy laboratory guide*; Academic Press, 2016; pp 99–112.

[119] Bax, A. D.; Donald, G. D. MLEV-17-based two-dimensional homonuclear magnetization transfer spectroscopy. *J. Magn. Reson.* **1985**, *65*, 355–360.

[120] Franck, J.; Rabinowitsch, E. Some remarks about free radicals and the photochemistry of solutions. *Trans. Faraday Soc.* **1934**, *30*, 120–130.

[121] Barry, J. T.; Berg, D. J.; Tyler, D. R. Radical cage effects: the prediction of radical cage pair recombination efficiencies using microviscosity across a range of solvent types. *J. Am. Chem. Soc.* **2017**, *139*, 14399–14405.

[122] Braden, D. A.; Parrack, E. E.; Tyler, D. R. Solvent cage effects . I . Effect of radical mass and size on radical cage pair recombination efficiency. II. Is geminate recombination of polar radicals sensitive to solvent polarity? *Coord. Chem. Rev.* **2001**, *211*, 279–294.

[123] Chesta, C. A.; Mohanty, J.; Nau, W. M.; Bhattacharjee, U.; Weiss, R. G. New insights into the mechanism of triplet radical-pair combinations. The persistent radical effect masks the distinction between in-cage and out-of-cage processes. *J. Am. Chem. Soc.* **2007**, *129*, 5012–5022.

[124] Levin, P. P.; Efremkin, A. F.; Kasparov, V. V.; Khudyakov, I. V. Reactivity of benzophenone ketyl free radicals in an elongated elastomer film. *J. Phys. Chem. A* **2016**, *120*, 7484–7489.

[125] Heintz, A.; Ludwig, R.; Schmidt, E. Limiting diffusion coefficients of ionic liquids in water and methanol: A combined experimental and molecular dynamics study. *Phys. Chem. Chem. Phys.* **2011**, *13*, 3268–3273.

[126] Gottlieb, H. E.; Kotlyar, V.; Nudelman, A. NMR chemical shifts of common laboratory solvents as trace impurities. *J. Org. Chem.* **1997**, *62*, 7512–7515.

[127] Hani, R.; Geanangel, R. ^{119}Sn NMR in coordination chemistry. *Coord. Chem. Rev.* **1982**, *44*, 229–246.

[128] Evans, D. The determination of the paramagnetic susceptibility of substances in solution by Nuclear Magnetic Resonance. *J. Chem. Soc.* **1959**, 2003–2005.

[129] Friebolin, H. *Basic one- and two-Dimensional NMR spectroscopy*; Wiley, 2010.

[130] Shoaeifar, P.; Abbasian, M.; Entezami, A. A. A convenient method for preparation of amphiphilic monomethoxypoly (ethylene glycol)–polystyrene diblock copolymer by NMRP technique. *J. Polym. Res.* **2007**, *14*, 45–52.

[131] Chenneberg, L. New advances in photoredox catalysis: applications in radical chemistry synthesis and dual catalysis. Ph.D. thesis, Université Pierre et Marie Curie, Paris, 2017.

[132] Lenhardt, T.; McDade, C. E.; Bayes, K. D. Rates of reaction of butyl radicals with molecular oxygen. *J. Chem. Phys.* **1980**, *304*, 72.

[133] Eskola, A. J.; Pekkanen, T. T.; Joshi, S. P.; Timonen, R. S.; Klippenstein, S. J. Kinetics of 1-butyl and 2-butyl radical reactions with molecular oxygen: Experiment and theory. *Proc. Combust. Inst.* **2018**, *37*, 1–8.

[134] Berger, H.; Bickel, A. F. Decomposition of organic hydroperoxides. *Trans. Faraday Soc.* **1961**, *57*, 1325–1335.

[135] Michel, D.; Böhlmann, W.; Roland, J.; Mulla-Osman, S. *Molecules in interaction with surfaces and interfaces; study of conformation and dynamics of molecules adsorbed in zeolites by ^1H NMR*; Springer, 2004; pp 217–274.

[136] Tynkkynen, T.; Hassinen, T.; Tiainen, M.; Soininen, P.; Laatikainen, R. ^{1}H NMR spectral analysis and conformational behavior of *n*-alkanes in different chemical environments. *Magn. Reson. Chem.* **2012**, *50*, 598–607.

[137] Wishart, D. S. et al. HMDB: the Human Metabolome Database. *Nucleic Acids Res.* **2007**, *35*, 521–526.

[138] Habibi, H.; Hekmat-Nazemi, A.; Kamran-Pirzaman, A.; Mohammadi, A. H. Modeling viscosity of alcohols based on the CPA-EoS + f-theory. *J. Mol. Liq.* **2016**, *220*, 558–565.

[139] Macchioni, A.; Ciancaleoni, G.; Zuccaccia, C.; Zuccaccia, D. Determining accurate molecular sizes in solution through NMR diffusion spectroscopy. *Chem. Soc. Rev.* **2008**, *37*, 479–489.

[140] Miyano, Y.; Hayduk, W. Solubility of butane in several polar and nonpolar solvents and in an acetone-butanol solvent solution. *J. Chem. Eng. Data* **1986**, *31*, 77–80.

[141] Miyano, Y.; Nakanishi, K. Solubilities of 1-butene in (methanol + benzene) and (methanol + cyclohexane) at $T = 298.15$ K and $p = 40$ kPa to 102 kPa. *J. Chem. Thermodyn.* **2003**, *35*, 519–528.

[142] Weizman, H. Why are ^{1}H NMR integrations not perfect? An inquiry-based exercise for exploring the relationship between spin dynamics and NMR integration in the organic laboratory. *J. Chem. Educ.* **2008**, *85*, 294–296.

[143] Passarelli, J.; Murphy, M.; Del Re, R.; Sortland, M.; Dousharm, L.; Vockenhuber, M.; Ekinci, Y.; Neisser, M.; Freedman, D. A.; Brainard, R. L. High-Sensitivity molecular organometallic resist for EUV (MORE). *Proc. SPIE* **2015**, *9425*, 1–13.

[144] Oleksak, R. P.; Ruther, R. E.; Luo, F.; Fairley, K. C.; Decker, S. R.; Stickle, W. F.; Johnson, D. W.; Garfunkel, E. L.; Herman, G. S.; Keszler, D. A. Chemical and structural investigation of high-resolution patterning with HafSOx. *ACS Appl. Mater. Interfaces* **2014**, *6*, 2917–2921.

[145] Closser, K. D.; Ogletree, D. F.; Naulleau, P.; Prendergast, D. The importance of inner-shell electronic structure for enhancing the EUV absorption of photoresist materials. *J. Chem. Phys.* **2017**, *146*, 164106.

[146] Bhattarai, S.; Chao, W.; Aloni, S.; Neureuther, A. R.; Naulleau, P. P. Analysis of shot noise limitations due to absorption count in EUV resists. *Proc. SPIE* **2015**, *9422*, 942209.

[147] Saha, S.; Park, D.-H.; Hutchison, D. C.; Olsen, M. R.; Zakharov, L. N.; Marsh, D.; Goberna-Ferrón, S.; Frederick, R. T.; Diulus, J. T.; Kenane, N.; Herman, G. S.; Johnson, D. W.; Keszler, D. A.; Nyman, M. Alkyltin Keggin clusters templated by sodium. *Angew. Chem. Int. Ed.* **2017**, *56*, 10140–10144.

[148] Egorov, D.; Schwob, L.; Lalande, M.; Hoekstra, R.; Schlathölter, T. Near edge X-ray absorption mass spectrometry of gas phase proteins: the influence of protein size. *Phys. Chem. Chem. Phys.* **2016**, *18*, 26213–26223.

[149] Giuliani, A.; Milosavljevic, A. R.; Canon, F.; Nahon, L. Contribution of synchrotron radiation to photoactivation studies of biomolecular ions in the gas phase. *Mass Spectrom. Rev.* **2014**, *33*, 424–441.

[150] Daly, S.; Krstic, M.; Giuliani, A.; Antoine, R.; Nahon, L.; Zavras, A.; Khairallah, G. N. Gas-phase VUV photoionisation and photo-fragmentation of the silver deuteride nanocluster $[Ag_{10}D_8L_6]^{2+}$ (L = bis(diphenylphosphino)methane). A joint experimental and theoretical study. *Phys. Chem. Chem. Phys.* **2015**, *17*, 25772–25777.

[151] Zhen, J.; Castillo, S. R.; Joblin, C.; Mulas, G.; Sabbah, H.; Giuliani, A.; Nahon, L.; Martin, S.; Champeaux, J.-P.; Mayer, P. M. VUV photo-processing of PAH Cations: quantitative study on the ionization versus fragmentation processes. *Astrophys. J.* **2016**, *822*, 1–8.

[152] Fuggle, J. C.; Mårtensson, N. Core-level binding energies in metals. *J. Electron Spectrosc. Relat. Phenom.* **1980**, *21*, 275–281.

[153] Milosavljević, A. R.; Nicolas, C.; Gil, J.-F.; Canon, F.; Réfrégiers, M.; Nahon, L.; Giuliani, A. VUV synchrotron radiation: a new activation technique for tandem mass spectrometry. *J. Synchrotron Radiat.* **2012**, *19*, 174–178.

[154] Nahon, L.; de Oliveira, N.; Garcia, G.; Gil, J.-F.; Joyeux, D.; Lagarde, B.; Polack, F. DESIRS: a state-of-the-art VUV beamline featuring high resolution and variable polarization for spectroscopy and dichroism at SOLEIL. *J. Phys. Conf. Ser.* **2013**, *425*, 122004.

[155] Patiny, L.; Borel, A. ChemCalc: A building block for tomorrow's chemical infrastructure. *J. Chem. Inf. Model.* **2013**, *53*, 1223–1228.

[156] Yamamoto, H.; McCloskey, J. Calculations of isotopic distribution in molecules extensively labeled with heavy isotopes. *Anal. Chem.* **1977**, *49*, 281–283.

[157] Rockwood, A. L.; Orden, S. L. V.; Smith, R. D. Rapid calculation of isotope distributions. *Anal. Chem.* **1995**, *67*, 2699–2704.

[158] Bespalov, I.; Zhang, Y.; Haitjema, J.; Tromp, R.; van de Molen, S. J.; Brouwer, A. M.; Jobst, J.; Castellanos, S. Patterning Sn-based EUV resists with low-energy electrons. *ACS Appl. Mater. Interfaces* **2019**, *Submitted*.

[159] Feng, R.; Cooper, G.; Brion, C. E. Dipole (e,e) spectroscopic studies of benzene: quantitative photoabsorption in the UV, VUV and soft X-ray regions. *J. Electron Spectrosc. Relat. Phenom.* **2002**, *123*, 199–209.

[160] Thuéry, P.; Atoini, Y.; Harrowfield, J. The sulfonate group as a ligand: a fine balance between hydrogen bonding and metal ion coordination in uranyl ion complexes. *Dalt. Trans.* **2019**, *48*, 8756–8772.

[161] Haitjema, J.; Zhang, Y.; Vockenhuber, M.; Kazazis, D.; Ekinci, Y.; Brouwer, A. M. Extreme ultraviolet patterning of tin-oxo cages. *J. Micro/Nanolith. MEMS MOEMS* **2018**, *16*, 033510.

[162] Frederick, R. T.; Amador, J. M.; Goberna-Ferrón, S.; Nyman, M.; Keszler, D. A.; Herman, G. S. Mechanistic Study of HafSOx Extreme Ultraviolet Inorganic Resists. *J. Phys. Chem. C* **2018**, *122*, 16100–16112.

[163] de Groot, F.; Kotani, A. *Core Level Spectroscopy of Solids*; CRC Press, 2008.

[164] Argawal, B. *X-ray Spectroscopy, an Introduction*; Springer-Verlag, Berlin, 1991.

[165] Simon, M.; Journel, L.; Guillemin, R.; Stolte, W. C.; Minkov, I.; Gel, F.; Sałek, P.; Ågren, H.; Carniato, S.; Taïeb, R.; Hudson, A. C.; Lindle, D. W. Femtosecond nuclear motion of HCl probed by resonant X-ray Raman scattering in the Cl 1s region. *Phys. Rev.* **2006**, *73*, 0207061–0207064.

[166] Ghosh, A.; Pal, S.; Vaval, N. Lifetime of inner-shell hole states of Ar (2p) and Kr (3d) using equation-of-motion coupled cluster method. *J. Chem. Phys.* **2015**, *143*, 024305.

[167] Auger, P. Sur les rayons β secondaires produits dans un gaz par des rayons X. *Comptes Rendus Acad. Sci.* **1923**, *177*, 169–171.

[168] Meitner, L. Über die entstehung der β-strahl-spektren radioaktiver substanzen. *Zeitschrift für Phys.* **1922**, *9*, 131–144.

[169] Torok, J.; Del Re, R.; Herbol, H.; Das, S.; Bocharova, I.; Paolucci, A.; Ocola, L. E.; Ventrice Jr., C.; Lifshin, E.; Denbeaux, G.; Brainard, R. L. Secondary electrons in EUV lithography. *J. Photopolym. Sci. Tec.* **2013**, *26*, 625–634.

[170] Kozawa, T.; Tagawa, S. Radiation chemistry in chemically amplified resists. *Jpn. J. Appl. Phys.* **2010**, *49*, 030001.

[171] Gallatin, G. M.; Narasimhan, A. K.; Brainard, R. L.; Neisser, M. *EUV Lithography*; SPIE, 2018; pp 493–591.

[172] Fondell, M.; Gorgoi, M.; Boman, M.; Lindblad, A. An HAXPES study of Sn, SnS, SnO and SnO_2. *J. Electron Spectros. Relat. Phenomena* **2014**, *195*, 195–199.

[173] Urpelainen, S.; Caló, A.; Partanen, L.; Huttula, M.; Aksela, S.; Aksela, H.; Granroth, S.; Kukk, E. Sb_4 clusters: 4d core ionization, subsequent Auger decay, and fragmentation pathways of the Auger final states. *Phys. Rev. A - At. Mol. Opt. Phys.* **2009**, *79*, 023201.

[174] Milosavljevic, A. R.; Cerovski, V. Z.; Rankovic, M. L.; Canon, F.; Nahon, L.; Giuliani, A. VUV photofragmentation of protonated leucine-enkephalin peptide dimer below ionization energy. **2014**, 1–6.

[175] González-Magaña, O.; Reitsma, G.; Tiemens, M.; Boschman, L.; Hoekstra, R.; Schlathölter, T. Near-edge X-ray absorption mass spectrometry of a gas-phase peptide. *J. Phys. Chem. A* **2012**, *116*, 10745–10751.

[176] González-Magaña, O.; Tiemens, M.; Reitsma, G.; Boschman, L.; Door, M.; Bari, S.; Lahaie, P. O.; Wagner, J. R.; Huels, M. A.; Hoekstra, R.; Schlathölter, T. Fragmentation of protonated oligonucleotides by energetic photons and C. *Phys. Rev. A* **2013**, *87*, 032702.

[177] Hirsch, K.; Lau, J. T.; Klar, P.; Langenberg, A.; Probst, J.; Rittmann, J.; Vogel, M.; Zamudio-Bayer, V.; Möller, T.; Von Issendorff, B. X-ray spectroscopy on size-selected clusters in an ion trap: From the molecular limit to bulk properties. *J. Phys. B* **2009**, *42*.

[178] Walter, M.; Vogel, M.; Zamudio-Bayer, V.; Lindblad, R.; Reichenbach, T.; Hirsch, K.; Langenberg, A.; Rittmann, J.; Kulesza, A.; Mitrić, R.; Moseler, M.; Möller, T.; Von Issendorff, B.; Lau, J. T. Experimental and theoretical 2p core-level spectra of size-selected gas-phase aluminum and silicon cluster cations: Chemical shifts, geometric structure, and coordination-dependent screening. *Phys. Chem. Chem. Phys.* **2019**, *21*, 6651–6661.

[179] Haitjema, J.; Wu, L.; Giuliani, A.; Nahon, L.; Castellanos, S.; Brouwer, A. M. Photo-induced Fragmentation of a Tin-oxo Cage Compound. *J. Photopolym. Sci. Tec.* **2018**, *31*, 243–247.

[180] Paul, W. Electromagnetic traps for charged and neutral particles. *Rev. Mod. Phys.* **1990**, *62*, 531–540.

[181] Bari, S.; González-Magaña, O.; Reitsma, G.; Werner, J.; Schippers, S.; Hoekstra, R.; T. Sch, Photodissociation of protonated leucine- enkephalin in the VUV range of 8–40 eV. *J. Chem. Phys.* **2011**, *134*, 024314.

[182] Niemeyer, M.; Hirsch, K.; Zamudio-Bayer, V.; Langenberg, A.; Vogel, M.; Kossick, M.; Ebrecht, C.; Egashira, K.; Terasaki, A.; Möller, T.; von Issendorff, B.; Lau, J. T. Spin coupling and orbital angular momentum quenching in free iron clusters. *Phys. Rev. Lett.* **2012**, *108*, 057201.

[183] Hirsch, K.; Zamudio-Bayer, V.; Langenberg, A.; Niemeyer, M.; Langbehn, B.; Möller, T.; Terasaki, A.; von Issendorff, B.; Lau, J. T. Magnetic moments of chromium-doped gold clusters: the Anderson impurity model in finite systems. *Phys. Rev. Lett.* **2015**, *114*, 087202.

[184] You, Z.; Möckel, R.; Bergunde, J.; Dehnen, S. Organotin–oxido cluster-based multiferrocenyl complexes obtained by hydrolysis of ferrocenyl-functionalized organotin chlorides. *Chem. Eur. J.* **2014**, *20*, 13491–13496.

[185] Bouška, M.; Dostál, L.; Padělková, Z.; Lyčka, A.; Herres-Pawlis, S.; Jurkschat, K.; Jambor, R. Intramolecularly coordinated organotin tellurides: stable or unstable? *Angew. Chemie - Int. Ed.* **2012**, *51*, 3478–3482.

[186] Kmiec, K. L. Factors affecting the fragmentation of peptide ions: metal cationization and fragmentation timescale. Ph.D. thesis, Texas A&M University, 2012.

[187] Griffin, L. L.; Mcadoo, D. J. The effect of ion size on rate of dissociation: RRKM calculations on model large polypeptide ions. *J. Am. Soc. Mass Spectrom.* **1993**, *4*, 11–15.

[188] Peltz, C.; Drahos, L.; Vékey, K. SORI excitation: collisional and radiative processes. *J. Am. Soc. Mass Spectrom.* **2007**, *18*, 2119–2126.

[189] Urquhart, S. G.; Gillies, R. Rydberg - Valence Mixing in the Carbon 1s Near-Edge X-ray Absorption Fine Structure Spectra of Gaseous Alkanes. *J. Phys. Chem. A* **2005**, *2*, 2151–2159.

[190] Urquhart, S. G.; Gillies, R. Matrix effects in the carbon near edge X-ray absorption fine structure spectra of condensed alkanes. *J. Chem. Phys.* **2006**, *124*, 234704.

[191] Väterlein, P.; Fink, R.; Umbach, E.; Wurth, W. Analysis of the X-ray absorption spectra of linear saturated hydrocarbons using the Xα scattered-wave method. *J. Chem. Phys.* **1998**, *108*, 3313–3319.

[192] Weiss, K.; Weckesser, J.; Wöll, C. An X-ray Absorption Study of Saturated Hydrocarbons Physisorbed on Metal Surfaces. *J. Mol. Struct.* **1999**, *458*, 143–150.

[193] Ouchi, I.; Nakai, I.; Kamada, M.; Tanaka, S.; Hagiwara, T. Core Electron Absorption Spectra of Poly(ethylene terephthalate) and Poly(ethylene 2,6-naphthalate) Films. *Polym. J.* **1995**, *27*, 127–135.

[194] Vogel, M.; Kasigkeit, C.; Hirsch, K.; Langenberg, A.; Rittmann, J.; Zamudio-Bayer, V.; Kulesza, A.; Mitrić, R.; Möller, T.; V. Issendorff, B.; Lau, J. T. 2p core-level binding energies of size-selected free silicon clusters: Chemical shifts and cluster structure. *Phys. Rev. B* **2012**, *85*, 195454.

[195] Sharma, A.; Varshney, M.; Shin, H. J.; Chae, K. H.; Won, S. O. X-ray absorption spectroscopy investigations on electronic structure and luminescence properties of Eu:SnO_2-SnO nanocomposites. *Curr. Appl. Phys.* **2016**, *16*, 1342–1348.

[196] González-Magaña, O.; Reitsma, G.; Bari, S.; Hoekstra, R.; Schlathölter, T. Length effects in VUV photofragmentation of protonated peptides. *Phys. Chem. Chem. Phys.* **2012**, *14*, 4351–4354.

[197] Yeh, J. J.; Lindau, I. Atomic subshell photoionization cross sections and asymmetry parameters: $1 \leq Z \leq 103$. *At. Data Nucl. Data Tables* **1985**, *32*, 1–155.

[198] Coster, D.; de L. Kronig, R. A new type of Auger effect and its influence on the X-ray spectrum. *Physica* **1935**, *2*, 13–24.

[199] Gelius, U. Recent progress in ESCA studies of gases. *J. Electron Spectros. Relat. Phenomena* **1974**, *5*, 985–1057.

[200] Hiltunen, A.; Aksela, S.; Víkor, G.; Ricz, S.; Kövér, Á.; Sulik, B. High resolution carbon and oxygen K-LL Auger spectra of carbon dioxide. *Nucl. Instr. Meth. in Phys. Res. B* **1999**, *154*, 267–271.

[201] Wagner, C.; Harned, N. Lithography gets extreme. *Nat. Photonics* **2010**, *4*, 24–26.

[202] Castellanos, S.; Wu, L.; Baljozovic, M.; Portale, G.; Kazazis, D.; Vockenhuber, M.; Ekinci, Y.; Jung, T. Ti, Zr, and Hf-based molecular hybrid materials as EUV photoresists. *Proc. SPIE* **2018**, *10583*, 10583A.

[203] Lawrie, K.; Blakey, I.; Blinco, J.; Gronheid, R.; Jack, K.; Pollentier, I.; Leeson, M. J.; Younkin, T. R.; Whittaker, A. K. Extreme ultraviolet (EUV) degradation of poly(olefin sulfone)s: Towards applications as EUV photoresists. *Radiat. Phys. Chem.* **2011**, *80*, 236–241.

[204] Jefimovs, K.; Vila-Comamala, J.; Pilvi, T.; Raabe, J.; Ritala, M.; David, C. Zone-doubling technique to produce ultrahigh-resolution X-Ray optics. *Phys. Rev. Lett.* **2007**, *99*, 264801.

[205] Johnston, R.; Tomboulian, D. Absorption spectrum of beryllium in the neighborhood of the K-edge. *Phys. Rev.* **1954**, *94*, 1585–1589.

[206] Horowitz, P.; Howell, J. A. A scanning X-ray microscope using synchrotron radiation. *Science* **1972**, *178*, 608–611.

[207] de Smit, E.; Swart, I.; Creemer, J. F.; Hoveling, G. H.; Gilles, M. K.; Tyliszczak, T.; Kooyman, P. J.; Zandbergen, H. W.; Morin, C.; Weckhuysen, B. M.; de Groot, F. M. F. Nanoscale chemical imaging of a working catalyst by scanning transmission X-ray microscopy. *Nature* **2008**, *456*, 222–225.

[208] Ade, H.; Urquhart, S. *Chemical Applications of Synchrotron Radiation*; World Scientific, 2002; pp 285–355.

[209] Hitchcock, A. P.; Morin, C.; Zhang, X.; Araki, T.; Dynes, J.; Stöver, H.; Brash, J.; Lawrence, J. R.; Leppard, G. G. Soft X-ray spectromicroscopy of biological and synthetic polymer systems. *J. Electron Spectros. Relat. Phenomena* **2005**, *147*, 259–269.

[210] Lawrence, J. R.; Swerhone, G. D. W.; Leppard, G. G.; Araki, T.; Zhang, X.; West, M. M.; Hitchcock, A. P. Scanning transmission X-ray, laser scanning, and transmission electron microscopy mapping of the exopolymeric matrix of microbial biofilms. *Appl. Environ. Microbiol.* **2003**, *69*, 5543–5554.

[211] Zhu, X.; Hitchcock, A. P.; Bazylinski, D. A.; Denes, P.; Joseph, J.; Lins, U.; Marchesini, S.; Shiu, H.-W.; Tyliszczak, T.; Shapiro, D. A. Measuring spectroscopy and magnetism of extracted and intracellular magnetosomes using soft X-ray ptychography. *PNAS* **2016**, *113*, E8219–E8227.

[212] Finizio, S.; Wintz, S.; Zeissler, K.; Sadovnikov, A. V.; Mayr, S.; Nikitov, S. A.; Marrows, C. H.; Raabe, J. Dynamic imaging of the delay- and tilt-free motion of Néel domain walls in perpendicularly magnetized superlattices. *Nano Lett.* **2019**, *19*, 375–380.

[213] Muntean, L.; Planques, R.; Kilcoyne, A.; Leone, S. R.; Gilles, M.; Hinsberg, W. D. Chemical mapping of polymer photoresists by scanning transmission X-ray microscopy. *J. Vac. Sci. Technol. B Microelectron. Nanom. Struct.* **2005**, *23*, 1630–1636.

[214] Olynick, D.; Tivanski, A. V.; Gilles, M. K.; Tyliszczak, T.; Salmassi, F.; Liddle, J. A.; Liang, K.; Leone, S. R. Scanning X-ray microscopy investigations into the electron beam exposure mechanism of hydrogen silsesquioxane resists. *J. Vac. Sci. Technol. B Microelectron. Nanom. Struct.* **2006**, *24*, 3048–3054.

[215] Caster, A. G.; Kowarik, S.; Schwartzberg, A. M.; Leone, S. R.; Tivanski, A.; Gilles, M. K. Quantifying reaction spread and X-ray exposure sensitivity in hydrogen silsesquioxane latent resist patterns with X-ray spectromicroscopy. *J. Vac. Sci. Technol. B* **2010**, *28*, 1304–1313.

[216] Fallica, R.; Watts, B.; Rösner, B.; Della Giustina, G.; Brigo, L.; Brusatin, G.; Ekinci, Y. Changes in the near edge X-ray absorption fine structure of hybrid organic-inorganic resists upon exposure. *Nanotechnology* **2018**, *29*, 36LT03.

[217] Böge, M. First operation of the Swiss Light Source. *Proc. EPAC* **2002**, 39–43.

[218] Karim, W.; Tschupp, S. A.; Oezaslan, M.; Justus Schmidt, T.; Gobrecht, J.; van Bokhoven, J. A.; Ekinci, Y. High-resolution and large-area nanoparticle arrays using EUV interference lithography. *Nanoscale* **2015**, *7*, 7386–7393.

[219] Fan, D.; Ekinci, Y. Photolithography reaches 6 nm half-pitch using extreme ultraviolet light. *J. Micro/Nanolithography, MEMS, MOEMS* **2016**, *15*, 033505.

[220] Raabe, J.; Tzvetkov, G.; Flechsig, U.; Böge, M.; Jaggi, A.; Sarafimov, B.; Vernooij, M. G. C.; Huthwelker, T.; Ade, H.; Kilcoyne, D.; Tyliszczak, T.; Fink, R. H.; Quitmann, C. PolLux: A new facility for soft X-ray spectromicroscopy at the Swiss Light Source. *Rev. Sci. Instrum.* **2008**, *79*, 113704.

[221] Moffet, R. C.; Henn, T.; Laskin, A.; Gilles, M. K. Automated chemical analysis of internally mixed aerosol particles using X-ray spectromicroscopy at the carbon K-edge. *Anal. Chem.* **2010**, *82*, 7906–7914.

[222] Pöhlker, C. et al. Biogenic potassium salt particles as seeds for secondary organic aerosol in the amazon. *Science* **2012**, *337*, 1075–1079.

[223] Mikhailov, E. F.; Mironov, G. N.; Pöhlker, C.; Chi, X.; Krüger, M. L.; Shiraiwa, M.; Förster, J.-D.; Pöschl, U.; Vlasenko, S.; Ryshkevich, T.; Weigand, M.; Kilcoyne, A.; Andreae, M. Chemical composition, microstructure, and hygroscopic properties of aerosol particles at the Zotino Tall Tower Observatory (ZOTTO), Siberia, during a summer campaign. *Atmos. Chem. Phys.* **2015**, *15*, 7837–7893.

[224] Tarrio, C.; Hill, S. B.; Berg, R. F.; Bajt, S. *EUV Lithography, Second Ed.; 6A Optics Contamination*; SPIE, 2018.

[225] Levenberg, K. A method for the solution of certain non-linear problems in least squares. *Q. Appl. Math.* **1944**, *2*, 164–168.

[226] Marquardt, D. An algorithm for least-squares estimation of non-linear parameters. *SIAM J. Appl. Math.* **1963**, *11*, 431–441.

[227] Newville, M. IFEFFIT: interactive XAFS analysis and FEFF fitting. *J. Synchrotron Radiat.* **2001**, *8*, 322–324.

[228] Ravel, B.; Newville, M. ATHENA, ARTEMIS, HEPHAESTUS: data analysis for X-ray absorption spectroscopy using IFEFFIT. *J. Synchrotron Radiat.* **2005**, *12*, 537–541.

[229] Schnohr, C. S.; Ridgway, M. C. *X-ray absorption spectroscopy of semiconductors*; Springer, 2015; pp 1–26.

[230] Nečas, D.; Klapetek, P. Gwyddion: An open-source software for SPM data analysis. *Cent. Eur. J. Phys.* **2012**, *10*, 181–188.

[231] Edelman, F.; Latuta, V.; Zaitsev, B.; Khoromenko, A. The structure of silicon nitride films. *Phys. Stat. Sol.* **1978**, *50*, 573–578.

[232] Outka, D.; J. Stöhr, Curve fitting analysis of near-edge core excitation spectra of free, adsorbed, and polymeric molecules. *J. Chem. Phys.* **1988**, *88*, 3539.

[233] Zhang, X.; Jacobsen, C.; Lindaas, S.; Williams, S. Exposure strategies for polymethyl methacrylate from in situ X-ray absorption near edge structure spectroscopy. *J. Vac. Sci. Technol. B* **1995**, *13*, 1477–1483.

[234] Schmidt, N.; Hub, C.; Gnichwitz, J.-F.; Hieringer, W.; Hirsch, A.; Fink, R. Structure, morphology and interface properties of ultrathin $SnTTBPP(OH)_2$-films adsorbed on Ag(100). *Phys. Chem. Chem. Phys.* **2011**, *13*, 9839–9848.

[235] Horn, S. A. *Construction of a scanning tunneling microscope capable of precise studies of adsorbates on silicon surfaces*; Master Thesis, University of Lethbridge, 2014.

[236] Sadegh, N. *Unpublished result*; 2019.

[237] Chantler, C. T. Theoretical form factor, attenuation, and scattering tabulation for Z=1-92 from E=1-10 eV to E=0.4-1.0 MeV. *J. Phys. Chem. Ref. Data* **1995**, *24*, 71–643.

[238] Chantler, C. T. Detailed tabulation of atomic form factors, photoelectric absorption and scattering cross section, and mass attenuation coefficients in the vicinity of absorption edges in the soft X-ray (Z=30-36, Z=60-89, E=0.1 keV-10 keV), addressing convergence issues of earlier work. *J. Phys. Chem. Ref. Data* **2000**, *29*, 597–1048.

[239] Ku, H. H. Notes on the use of propagation of error formulas. *J. Res. Natl. Bur. Stand. (1934).* **1966**, *70*, 263–273.

[240] Horsley, J.; Stöhr, J.; Hitchcock, A. P.; Newbury, D.; Johnson, A.; Sette, F. Resonances in the K-shell excitation spectra of benzene and pyridine: gas phase, solid, and chemisorbed states. *J. Chem. Phys.* **1985**, *83*, 6099–6107.

[241] Wang, J.; Tyliszczak, T.; Stöver, H. Chemically selective soft X-ray patterning of polymers. *J. Synchrotron Radiat.* **2007**, *14*, 181–190.

[242] Klein, R. J.; Fischer, D. A.; Lenhart, J. L. Systematic oxidation of polystyrene by ultraviolet-ozone, characterized by near-edge X-ray absorption fine structure and contact angle. *Langmuir* **2008**, *24*, 8187–8197.

[243] Cho, S.; Yu, J.; Kang, S. K.; Shih, D.-Y. Oxidation study of pure tin and its alloys via electrochemical reduction analysis. *J. Electron. Mater.* **2005**, *34*, 635–642.

[244] Lorenz, H.; Zhao, Q.; Turner, S.; Lebedev, O. I.; Tendeloo, G. V.; Klötzer, B.; Rameshan, C.; Penner, S. Preparation and structural characterization of SnO_2 and GeO_2 methanol steam reforming thin film model catalysts by (HR)TEM. *Mater. Chem. Phys.* **2010**, *122*, 623–629.

[245] Moreno, M. S.; Egerton, R.; Rehr, J.; Midgley, P. A. Electronic structure of tin oxides by electron energy loss spectroscopy and real-space multiple scattering calculations. *Phys. Rev. B* **2005**, *71*, 035103.

Summary

This thesis is about molecular tin-oxo cage structures, which contain a core composed of twelve tin and twenty oxygen atoms. Each tin atom is attached to a hydrocarbon chain; in this work these are butyl groups. The tin-oxo cage has a 2+ charge, which is balanced by one or two negatively charged counterions.

A thin film of these tin-oxo cages can be used as a photoresist. This is a photosensitive film that changes solubility upon light exposure. A positive-tone photoresist becomes more soluble in a solvent or mixture of solvents (called developer) when it is illuminated, while a negative-tone photoresist becomes less soluble. By exposing a photoresist to a light pattern, a pattern can be written in the photoresist.

It is known that light absorption on tin-oxo cages leads to photochemical reactions in which the hydrocarbon (butyl) chains are cleaved and removed. The tin-oxo cages then bind to each other and form an insoluble network as the end product. The tin-oxo cage material therefore belongs to the negative-tone photoresist class. Better understanding of the photoreactions of tin-oxo cages is the main goal of the research described in this thesis.

Tin-oxo cages are of special interest because they contain a large number of tin atoms, while also being soluble in organic solvents. This makes them possibly applicable as photoresists for Extreme Ultraviolet (EUV) light, with a patterning wavelength of 13.5 nanometers. As a result of the ultra-short wavelength, EUV light can be used to pattern on an even smaller scale (higher *resolution*). However, EUV light is expensive to produce, which means that it is important to use this light efficiently. Tin atoms are good absorbers of EUV light; tin-containing materials could therefore need less EUV light to change solubility (higher *sensitivity*).

In **Chapter 1**, the relevance of photoresists is illustrated by showing their main application: fabrication of integrated circuits or microchips. The technique of photolithography, which is used to fabricate these chips, is discussed. EUV lithography is introduced as a new technique to decrease the size of structures that are patterned, further increasing the number of transistors that can be placed on a chip. Additionally, it is explained in more detail why metal-containing and specifically tin-containing materials are of interest for use as EUV photoresists.

In **Chapter 2**, we discuss the exposure of tin-oxo cage thin films to EUV light. In one set of experiments, large areas are exposed ("open-frame exposure") after which the remaining film thickness as a function of light dose is studied. Exposure is also performed with a nanoscale interference pattern, with alternating lines (exposed) and spaces (unexposed). The highest resolution that was obtained, is 30 nm ("Half Pitch", half the distance between two identical features). We show that the performance of the tin-oxo cage as photoresist material depends strongly on processing conditions; if the films are heated after exposure ("post-exposure bake") less EUV light is required to obtain the desired result.

In **Chapter 3**, we take a detailed look at the photochemistry of tin-oxo cages that are dissolved. We expose these tin-oxo cages to deep ultraviolet light (DUV, with a wavelength of 225 nm) in the solvents methanol or ethanol and monitor the chemical conversions using UV/Vis and NMR spectroscopy. The tin-oxo cage strongly absorbs DUV light, with an absorption maximum at 220 nm. This absorption decreases as the solution is exposed for a longer time, indicating that the tin-oxo cage undergo photochemical reactions. With UV/Vis spectroscopy, this decrease in absorption was quantified, and a quantum yield (number of bonds broken per photon) between 0.6 and 0.8 was estimated. NMR spectroscopy was used to detect and structurally identify photoproducts. It is shown that the photoreaction starts with generating radicals, most likely butyl groups that are cleaved from the central cage structure. These butyl groups react further to form products such as *n*-octane and *n*-butanol. What kind of products are obtained depends on conditions such as the presence or absence of dissolved oxygen.

In the study decribed in **Chapter 4**, we bring tin-oxo cages (without counterions or with only one counterion) into the gas phase and expose them to light. The wavelength of this light ranged from DUV (as used in Chapter 3) to vacuum UV, which is more energetic than DUV but less energetic than EUV. Photo-induced fragmentation of the cages was studied by using mass spectrometry. We show that butyl cleavage is also the main mechanism of fragmentation in the gas phase. Additionally, the ionization energy is quantified; this is the energy that is required to eject an electron from the tin-oxo cage. This energy was found to be lower for tin-oxo cages that are attached to one counterion, and is expected to be even lower in a tin-oxo cage film (in which two counterions per cage are present).

In the study described in **Chapter 5** we also bring tin-oxo cages into the gas phase, but we expose them to higher energy light (ranging from EUV to soft X-rays, which are even more energetic). It is shown that absorption of one such a high energy photon can already lead to the cleavage of several (up to at most six) butyl groups. Under some conditions, disintegration of the core is also observed. More fragmentation is observed at absorption edges, at which the photon energy corresponds to specific electronic transitions on the atoms (carbon, oxygen or tin). These electronic transitions are described in detail.

In **Chapter 6**, we study EUV-exposed thin films of tin-oxo cages, using Scanning Transmission X-ray Microscopy (STXM). This technique measures how many X-ray photons are transmitted through a thin film. We make use of STXM for two types of experiments. In the first type, transmission is measured for photon energies

around absorption edges. Important differences with the photofragmentation spectra described in Chapter 5 (without counterions) were found: the counterions have a clear effect on the ionization energy. In the second type of experiment, we measured the light absorption at three fixed energies. This enabled calculation of the elemental composition of the photo-exposed tin-oxo cage throughout the whole film, something that is difficult to achieve by most other techniques. An important conclusion is that loss of tin is negligible upon exposure of thin films of tin-oxo cages to EUV radiation.

Samenvatting

Dit proefschrift gaat over moleculaire tin-oxokooien ('tin-oxo cages'), die een kern bevatten van twaalf tin- en twintig zuurstofatomen. Aan elk tinatoom zit een koolwaterstofketen vast; in het beschreven onderzoek zijn dit butylgroepen. Elke tin-oxokooi heeft een lading van +2, die gecompenseerd wordt door één of twee negatief geladen tegenionen. Een dunne film van tin-oxokooien kan gebruikt worden als fotolak. Dit is een lichtgevoelige laag die van oplosbaarheid verandert als er licht op valt. Een positieve-toon fotolak wordt oplosbaarder door belichting, terwijl een negatieve-toon fotolak juist minder oplosbaar wordt. Door een fotolak aan een lichtpatroon bloot te stellen en vervolgens de oplosbare delen weg te wassen (ontwikkeling), kan een patroon in de laklaag worden geschreven.

De absorptie van licht door tin-oxokooien leidt tot fotochemische reacties, waarbij de koolwaterstofketens (butyl) worden afgesplitst. De tin-oxokooien binden daarna aan elkaar, wat leidt tot de vorming van een onoplosbaar netwerk als eindproduct. Het tin-oxokooi materiaal behoort hiermee tot de negatieve fotolakken. De voornaamste doelstelling van dit proefschrift is om de details van de fotoreacties van tin-oxokooien helderder te krijgen.

Tin-oxokooien zijn interessant omdat ze een groot aantal tinatomen bevatten, maar ook oplosbaar zijn in organische oplosmiddelen. Dit maakt ze potentieel toepasbaar als fotolakken voor extreem ultraviolet licht (EUV), licht met een golflengte van 13.5 nanometer. Door de ultrakorte golflengte kan met EUV-licht op nog kleinere schaal een patroon worden geschreven (hogere *resolutie*). EUV-licht is echter moeilijk en duur om te produceren, wat betekent dat efficiënt gebruik ervan belangrijk is. Tinatomen absorberen EUV-licht sterk; tinbevattende materialen hebben daarom mogelijk minder EUV-licht nodig om van oplosbaarheid te veranderen (hogere *gevoeligheid*).

In **Hoofdstuk 1** wordt de relevantie van fotolakken geschetst door hun voornaamste toepassing te laten zien: de fabricage van geïntegreerde schakelingen of microchips. De techniek van fotolithografie, die wordt gebruikt om microchips te maken, wordt besproken. EUV-lithografie wordt geïntroduceerd als een nieuwe techniek om het formaat van de structuren die worden geschreven verder te verkleinen. Dit kan

het aantal transistoren dat op een chip wordt geplaatst verder vergroten. Daarnaast wordt in meer detail beschreven waarom metaalbevattende en specifiek tinbevattende materialen interessant zijn voor gebruik als EUV-fotolakken.

In **Hoofdstuk 2** bediscussiëren we de belichting van dunne laagjes van tin-oxokooien met EUV-licht. In een reeks van experimenten worden 'grote' oppervlakten (0.5×0.5 mm^2) van de laagjes belicht ('open-frame exposure') waarna de overblijvende laagdikte na ontwikkeling als functie van de lichtdosis wordt bestudeerd. Belichting wordt ook gedaan met een interferentiepatroon op nanoschaal, met afwisselend lijnen (belicht) en ruimtes ertussen (onbelicht). De hoogste resolutie die is bereikt, is 30 nm ('Half Pitch', de helft van de afstand tussen twee identieke kenmerken). We laten zien dat het functioneren van de tin-oxokooien als fotolak sterk afhangt van de procescondities; als de laagjes worden verhit na belichting ('post-exposure bake') is minder EUV-licht nodig om het beoogde resultaat te bereiken.

In **Hoofdstuk 3** bestuderen we uitgebreid de fotochemie van tin-oxo kooien die zijn opgelost in een oplosmiddel. We belichten deze tin-oxo kooien met diep ultraviolet licht (DUV, met een golflengte van 225 nm) in de oplosmiddelen methanol of ethanol, en kijken naar de chemische omzettingen door middel van UV/Vis- en NMR-spectroscopie. De tin-oxokooien absorberen DUV-licht sterk, met een absorptiemaximum bij 220 nm. Deze absorptie neemt af naarmate de oplossing langer belicht wordt, wat erop wijst dat de tin-oxokooien chemische reacties ondergaan. Door middel van UV/Vis-spectroscopie wordt de afname in absorptie gekwantificeerd, en een kwantumopbrengst (aantal verbroken bindingen per foton) tussen 0.6 en 0.8 wordt geschat. NMR-spectroscopie wordt gebruikt om fotoproducten te detecteren en te identificeren. We laten zien dat de fotoreactie begint met het ontstaan van radicalen, waarschijnlijk butylgroepen die worden afgesplitst van de centrale kooistructuur. Deze butylgroepen reageren verder tot producten zoals *n*-octaan en *n*-butanol. Welke producten worden gevormd, hangt af van reactiecondities zoals de aan- of afwezigheid van opgelost zuurstof.

In de studie die wordt beschreven in **Hoofdstuk 4** brengen we de tin-oxokooien (zonder tegenionen of met slechts één tegenion) in de gasfase, waarna we ze aan licht blootstellen. De golflengte van het gebruikte licht varieert van DUV (zoals gebruikt in Hoofdstuk 3) tot vacuüm-ultraviolet (VUV), dat energetischer is dan DUV maar minder energetisch dan EUV. De fragmentatie van de tin-oxokooien onder invloed van licht wordt bestudeerd met massaspectrometrie. We laten zien dat butylafsplitsing ook in de gasfase het voornaamste fragmentatiemechanisme is. Ook wordt de ionisatie-energie bepaald; dit is de energie die benodigd is om een elektron weg te schieten uit de tin-oxokooi. Deze energie is lager voor tin-oxokooien die nog aan één tegenion gebonden zijn, en waarschijnlijk nog lager in een fotolak van tin-oxokooien (waarin twee tegenionen per tin-oxokooi aanwezig zijn).

In de studie beschreven in **Hoofdstuk 5** brengen we de tin-oxokooien ook in de gasfase, maar we stellen ze bloot aan licht met een hogere energie (van EUV tot zachte röntgenstraling, die nog energetischer is). We laten zien dat absorptie van één zo'n foton al kan leiden tot afsplitsing van verscheidene (tot maximaal zes) butylgroepen van één tin-oxokooi. Onder sommige condities wordt daarbij ook het gedeeltelijk uiteenvallen van de kooi waargenomen. Meer fragmentatie wordt waargenomen bij

absorptieranden, waarbij de fotonenergie correspondeert met specifieke elektronische overgangen op atomen (koolstof, zuurstof of tin). Deze elektronische overgangen worden in detail beschreven.

In **Hoofdstuk 6** bestuderen we EUV-belichte dunne laagjes van tin-oxokooien door middel van transmissie-röntgenmicroscopie (STXM). Deze techniek meet hoeveel röntgenstralen er door een dunne laag heen gaan (transmissie). We maken gebruik van STXM voor twee verschillende soorten experimenten. In het eerste soort experiment wordt transmissie gemeten voor röntgenstralen met een energie rond die van absorptieranden. Belangrijke verschillen met de fotofragmentatiespectra (zonder tegenionen) die wordt beschreven in Hoofdstuk 5 worden gevonden: de tegenionen hebben een duidelijk effect op de ionisatie-energie. In het tweede type experiment meten we de absorptie van röntgenstraling bij drie vaste energieën. Hierdoor kon de elementaire samenstelling van EUV-belichte laagjes door de hele film heen gemeten worden, iets wat lastig via de meeste andere meettechnieken te bereiken is. Een belangrijke conclusie is dat verlies van tinatomen tijdens EUV-belichting te verwaarlozen is.

Publication list

This thesis is based on the following publications:

- J. Haitjema, Y. Zhang, M. Vockenhuber, D. Kazazis, Y. Ekinci, and A. M. Brouwer, "Extreme ultraviolet patterning of tin-oxo cages", *J. Micro/Nanolitho. MEMS MOEMS*, 2017, **16**, 7. [Chapter 2]

- J. Haitjema, Y. Boeije, A.W. Ehlers, and A. M. Brouwer, "Photochemistry of tin-oxo cages in solution", *Manuscript in preparation* [Chapter 3].

- J. Haitjema, L. Wu, A. Giuliani, L. Nahon, S. Castellanos, and A. M. Brouwer, *J. Photopolym. Sci. Tec.*, 2018, **31**, 243–247 [Chapter 4]

- J. Haitjema, T.A. Schlathölter, Y. Zhang, R. Lindblad, M. Timm, C. Bülow, V. Zamudio-Bayer, B. von Issendorff, J. T. Lau, R. Hoekstra, and A. M. Brouwer, "Soft X-ray fragmentation of tin-oxo cage ions", *Manuscript in preparation* [Chapter 5]

- J. Haitjema, K. Witte, I. Bespalov, O. Lugier, N. Thakur, L. Wu, M. Vockenhuber, B. Watts, S. Castellanos, and A. M. Brouwer, "Scanning transmission X-ray microscopy on tin-oxo cage films", *Manuscript in preparation* [Chapter 6].

Other publications:

- J. Haitjema, Y. Zhang, N. Ottosson, and A.M. Brouwer, "Photoreactions of tin-oxo cages, model EUV photoresists", *J. Photopolym. Sci. Tec.*, 2017, **30**, 99-102.

- Y. Zhang, J. Haitjema, X. Liu, F. Johansson, A. Lindblad, S. Castellanos, N. Ottosson, and A.M. Brouwer, "Photochemical conversion of tin-oxo cage compounds studied using hard x-ray photoelectron spectroscopy", *J. Micro/Nanolitho. MEMS MOEMS* 2017, **16**, 023510.

- R. Fallica, J. Haitjema, L. Wu, S. Castellanos, A. M. Brouwer, and Y. Ekinci, "Absorption coefficient of metal-containing photoresists in the extreme ultraviolet", *J. Micro/Nanolitho. MEMS MOEMS*, 2018, **17**, 023505.

- Y. Zhang, J. Haitjema, M. Baljozovic, M. Vockenhuber, D. Kazazis, T. A. Jung, Y. Ekinci, and A.M. Brouwer, "Dual-tone application of a tin-oxo cage photoresist under e-beam and EUV exposure", *J. Photopolym. Sci. Tec.*, 2018, **31**, 249-255

- I. Bespalov, Y. Zhang, J. Haitjema, R.M. Tromp, S.J. van der Molen, A.M. Brouwer, J. Jobst, and S. Castellanos, "The key role of very-low-energy-electrons in tin-based molecular resists for extreme ultraviolet nanolithography", *ACS Appl. Mater. Inter.*, 2020, **12**, 9881-9889.

List of acronyms

AFM Atomic force microscopy

Bu Butyl, C_4H_9–

BuOH *n*-butanol, C_4H_9OH

CAR Chemically amplified resist

DFT Density functional theory

DOSY Diffusion-ordered spectroscopy

DUV Deep Ultraviolet

ESI Electronic supporting information

EtOH Ethanol, C_2H_5OH

EUV(L) Extreme Ultraviolet (lithography), $\lambda = 13.5$ nm

HMDS Hexamethyldisilazane or bis(trimethylsilyl)amine, $[(CH_3)_3Si]_2NH$

HOMO Highest occupied molecular orbital

HP Half pitch

HSQ Hydrogen silsesquioxane, $[HSiO_{3/2}]_n$

iPrOH Isopropyl alcohol, C_3H_7OH

IR Infra-red

IVR Internal vibrational redistribution

LER Line edge roughness

LUMO Lowest unoccupied molecular orbital

MeCN Acetonitrile, CH_3CN

MeOD Fully deuterated methanol, CD_3OD

MeOH Methanol, CH_3OH

MOSFET Metal-oxide-semiconductor field-effect transistor

MOTf$^+$ Tin-oxo cage with one trifluoromethanesulfonate anion, $[\{(BuSn)_{12}O_{14}(OH)_6\}(CF_3SO_3)]^+$

MOTs$^+$ Tin-oxo cage with one tosylate anion, $[\{(BuSn)_{12}O_{14}(OH)_6\}(C_7H_7SO_3)]^+$

NEXAFS Near-edge X-ray absorption fine structure

NMR Nuclear magnetic resonance

PAB Post-application bake/baking

PAG Photoacid generator

PEB Post-exposure bake/baking

PMMA Poly(methyl methacrylate), $[CH_2C(CH_3)(CO_2CH_3)]_n$

PMT Photomultiplier tube

PS Polystyrene, $[C_8H_8]_n$

RF Radiofrequency

SEM In Chapter 2: Scanning electron microscope/microscopy. In Chapter 6: Standard error of the mean

STXM Scanning Transmission X-ray Micro(spectro)scopy

TEMPO 2,2,6,6-tetramethylpiperidinyloxyl

TGA Thermogravimetric analysis

TinA Tin-oxo cage with acetate anions, $\{(BuSn)_{12}O_{14}(OH)_6\}(CH_3COO)_2$

TinF Tin-oxo cage with trifluoroacetate anions, $\{(BuSn)_{12}O_{14}(OH)_6\}(CF_3COO)_2$

TinM Tin-oxo cage with malonate anions, $\{(BuSn)_{12}O_{14}(OH)_6\}CH_2(COO)_2$

TinOH Tin-oxo cage with hydroxide anions, $\{(BuSn)_{12}O_{14}(OH)_6\}(OH)_2$

TinOTf Tin-oxo cage with trifluoromethanesulfonate anions, $\{(BuSn)_{12}O_{14}(OH)_6\}(CF_3SO_3)_2$

TinOTs Tin-oxo cage with tosylate anions, $\{(BuSn)_{12}O_{14}(OH)_6\}(C_7H_7SO_3)_2$

TMAH Tetramethylammonium hydroxide, $N(CH_3)_4OH$

TOCSY Total correlation spectroscopy

TOF Time-of-flight

VUV Vacuum Ultraviolet

XPS X-ray photoelectron spectroscopy

XUV Extreme ultraviolet (general term)

Acknowledgments

The research described in this thesis would not have been possible without the help of a great deal of people, and therefore I would like to thank them here (partly in Dutch).

First I would like to thank my supervisor, **Fred Brouwer**. Beste Fred, bedankt voor het delen van je kennis van (met name) fotochemie en voor het vertrouwen dat je me al die tijd hebt gegeven. Ook als het even wat minder ging, leek je altijd erop te vertrouwen dat het goed zou komen. Ook was je altijd bereid om te praten over mogelijke nieuwe richtingen die we met het onderzoek zouden inslaan en om te helpen met praktische zaken.

I would like to express my gratitude to **Kees Elsevier**, **Andries Meijerink**, **Annemieke Petrignani**, **Thomas Schlathölter**, **Petra Swiderek** and **Sander Woutersen**, for kindly inviting our invitation to be part of the committee, and for taking the time to read this manuscript.

Mijn onderzoekscarrière begon als bachelor-student in de onderzoeksgroep 'Anorganische Chemie en Katalyse' (Universiteit Utrecht), waar ik werd begeleid door **Zoran** en **Hendrik** en samenwerkte met **Jogchum**. Ik wil alledrie bedanken voor de fijne tijd die ik heb gehad en het vertrouwen dat ik van mijn begeleiders heb gekregen om mijn eerste onderzoeksproject, mijn bachelorthesis, tot een goed einde te brengen.

Als masterstudent heb ik bij de vakgroep 'Gecondenseerde materie en grensvlakken' aan de Universiteit Utrecht aan mijn masterscriptie gewerkt over energiemigratie tussen lanthanide-ionen, onder supervisie van **Freddy**, **Mathijs** en **Andries** (die tevens commissielid is). Ik heb van alledrie veel geleerd dat nog steeds van pas kwam bij het maken van deze thesis, van werken in Latex en Illustrator tot het belang van goede typografie en het vermijden van pretentieuze opmerkingen. De theses van Freddy en Mathijs heb ik (als belangrijke inspiratiebronnen) nog steeds in mijn kast staan. Hopelijk zal het Freddy, Mathijs en Andries goed doen dat ik tijdens mijn promotieonderzoek toch nog van lanthaniden gebruik heb gemaakt (de oplettende lezer mag zelf uitzoeken waar precies).

When I first started at ARCNL at the Nanophotochemistry group as an intern, our group was rather small and consisted of **Bruno**, **Sandra** and **Yu**. Bruno and Sandra were really helpful and welcoming and were always happy to offer scientific help and/or to have lunch together. As my supervisor, Yu helped me create the "magical" tin-oxo cages. Later we became colleagues and we spent a lot of time together in the lab, in the office and at synchrotron visits (the most memorable one being the first one at PSI, in which we still had to figure everything out). I thank Yu for the good supervision and the nice collaboration that lasted for almost four years. I thank **Lianjia** for the help during synchrotron visits and the always useful discussions during group meetings. Later we were paranymphs for Yu's defence, which was such a great success that I chose her to be my paranymph as well. **Olivier** and **Neha** were very nice and helpful colleagues that were always ready to help out inside and outside the lab. **Ivan** joined later, as a partner in crime during synchrotron visits and supplier of cynical jokes. His knowledge about NEXAFS and AFM has helped me a lot while writing Chapter 6. **Robbert** wil ik bedanken voor het gezelschap op kantoor (nog in het oude ARCNL-gebouw), zijn uitgebreide kennis van lasers en de altijd leuke spelletjesavonden. De mensen van het Nanocenter op AMOLF (**Bob**, **Dimitry** en **Andries**) hebben mij altijd goed kunnen helpen met nanofabricaties. Met **Wim**, **Sander** en **Claire** van ASML heb ik vaak nuttige discussies gehad over onze resultaten. Ook wil ik **Joost** en **Marjan** van ARCNL bedanken voor het regelen van allerhande zaken op de achtergrond.

Later, many other people joined the ARCNL "Nanophotochemistry" and "EUV photoresists" research groups: **Aniket**, **Carin**, **Chris**, **Felix**, **Jeremy**, **Kendra**, **Kevin**, **Lichao**, **Lotte**, **Luuk**, **Maarten**, **Marco**, **Marie-Noelle**, **Martijn**, **Najmeh**, **Paul**, **Sander**, **Unnati** and others. During this time a new group leader (**Sonia Castellanos**) joined us, initiating a new research group (EUV photoresists) in collaboration with the "Nanophotochemistry" group. Sonia's expertise and passion for scientific research were a welcome impulse to the group and her critical questions during group meetings always helped me to think further. Additionally, she has helped in the final stage of my research by critically reviewing the manuscript as a co-promotor. Last but not least, she was always up for scientific and non-scientific jokes, including making pictures of our group's researchers dressed in line-and-space-patterned shirts (unfortunately, my own shirt had an alignment error).

I have spent quite some time with the people at the "molecular photonics" group, as a guest to work in the UvA lab and to eat lunch together: **Aishwarya**, **Begüm**, **Benjamin**, **Charlotte**, **Chris**, **Dina**, **Dongdong**, **Federico**, **Hernán**, **Ivan**, **Jiayun**, **Mark**, **Rafael**, **Rebecca**, **Roberto**, **Sander**, **Tatu**, **Tomislav**, **Yanni** and many others. I thank everyone for the nice atmosphere. In particular I would like to thank the staff members for the always interesting discussions during group meetings: **Wybren-Jan**, **Hong Zhang**, **René**, and **Sander** (also committee member). Additionally, I thank **Max** for accepting the honor to be my paranymph. **Michiel** wil ik bedanken voor het onderhouden van de Ekspla-laser en nog vele andere zaken (volgens Federico is "where is Michiel" de vaakst gehoorde frase in het molecular photonics-kantoor). Verder wil ik ook **Hans** bedanken voor het managen van het chemisch lab en voor alle hulp met chemische syntheses.

For my research I have visited synchrotrons quite a few times. These are places at which experiments are conducted with high energy radiation, under high time pressure. Mainly I have visited Swiss Light Source at the Paul Scherrer Institut, Switzerland. I would like to thank **Dimitris**, **Michaela** and **Yasin** for their help at the XIL-II beamline, at which they have a powerful source of precious EUV light. Michaela and Dimitris were always ready to help us out at very early (or very late) hours and their experience kept us from making (most) mistakes. I would also like to thank **Roberto** for the nice collaboration that has lead to a publication.

Later on we also visited another beamline at the Swiss Light Source: PolLux. At one point the Nanophotochemistry/EUV photoresist groups did experiments at four SLS beamlines at the same time, which made some of us (well, only Sonia) joke that we were going to take over the entire synchrotron! At PolLux, we conducted STXM experiments on samples that were exposed to EUV light at XIL-II. I thank again my ARCNL colleagues (Neha, Lianjia and Olivier) for exposing my samples at this beamline while I was measuring other samples at PolLux. At PolLux itself we received patient help from **Katharina** (without whom we would have been helpless) who is both very friendly and very talented. She has also provided kind help reviewing Chapter 6. **Benjamin**, the group leader, was always available for interesting discussions and microtomed some useful and nice-looking tin flakes for me.

I have also twice visited another synchrotron: BESSY-II in the beautiful environment of the East Berlin neighborhood "Adlershof". I would like to thank especially **Thomas Schlathölter** (also committee member) for his kind help with the gas phase mass spectrometry setup. I am still amazed by its complexity and the seemingly effortless way he intersected it with the synchrotron beamline. He was always willing to discuss the results (in Groningen or in Amsterdam), to analyze the data and (much later) to evaluate the manuscript resulting from the two beamtimes. I would also like to thank **Ronnie**, the group leader who was also always ready to discuss things and provide corrections, and **Niklas**, who came up with the idea of the gas phase fragmentation study (if I remember correctly). During the beamtime at the NanoclusterTrap I was helped by many people: **Rebecka**, **Christine**, **Martin** and many others whose name I have probably forgotten. I would especially like to thank the group leader **Tobias Lau** for critically assessing Chapter 5.

Later I went to the SOLEIL synchrotron in France. Here I was helped by the friendly French people **Laurent** and **Alexandre**. The "dream team" (Lianjia, Sonia, Fred and me) had to solve various problems, including lost parts of tubing, but eventually we obtained some results to bring home (see Chapter 4 and Lianjia's paper).

Tijdens mijn tijd als promovendus heb ik verschillende studenten mogen begeleiden. Ik dank iedereen voor de hulp bij het onderzoek doen en hun interessante inzichten. In het bijzonder wil ik bedanken: **Daniel**, voor goed uitgevoerde UV-Vis metingen die in Hoofdstuk 3 zijn terechtgekomen, en **Eline**, die een nauwgezette analyse heeft gemaakt van de stabiliteit van de tinkooien. Ook wil ik **Yorrick** bedanken, die als bachelorstudent een grote passie had voor het onderzoek en ook erg mooie resultaten wist binnen te halen. Hij is verantwoordelijk voor een groot deel van de metingen uit Hoofdstuk 3, dat er zonder hem waarschijnlijk heel anders uit had gezien.

Naast het promoveren had ik gelukkig ook tijd voor andere zaken. Bij de Eindhovense groep schakers en wiskundigen (bestaande uit onder andere **Bas**, CM **Guus**, **Jochem**, **Martijn**, **Peter** en **Ton**) kon ik altijd ontspannen met een spelletje klaverjas. Ook bij vereniging Anderwijs heb ik leuke tijden beleefd (op de kampen en daarbuiten), waarbij ik met name nog wil bedanken: **André**, **Bouchien**, **Fieke**, **Iris**, **Jesse**, **Jos**, **Leo**, **Liesbeth**, **Marije**, **Nathalie**, **Robin** (x2) en **Saskia** (x2). Met de leden van het 'Neolyceum' had ik een aantal gezellige en interessante samenkomsten: **Britt**, **Emma** en **Niki** (en vooruit, ook een beetje **Jeffrey** al was die minder fysiek aanwezig). Als ik thuis was, had ik fijn gezelschap aan mijn huisgenoten op 'De Sterren': **Brendan**, **Daisy**, **Emiel**, **Eva**, **Fien**, **Guido**, **Javier**, **Michelle**, **Mike**, **Milou**, **Mirjam**, **Raela**, **Thelma**, **Thijs** en anderen. Het was fijn om altijd een stabiele thuisbasis te hebben waar ik regelmatig samen heb gegeten en andere leuke dingen heb gedaan. In het laatste jaar van mijn promotie verhuisde ik naar Lunetten, waar Sharell en ik gezelschap hadden van **Samoa**, een aangename huisgenoot met wie we het gezellig hebben gehad. Daar was ook een tijdje **James** aanwezig, ook een huisgenoot maar dan van een andere diersoort, die altijd bereid was om kopjes te geven of om op schoot te komen zitten.

Ik heb veel gehad aan de steun van mijn familie. Met name wil ik mijn opa en oma **Henk** en **Tineke** bedanken, bij wie ik (van jong tot oud) altijd terecht kon voor wandelen, fietsen, Scrabble spelen en hun aanstekelijke liefde voor natuur en muziek. Bij **Henny**, **Leo** en **Kristian** konden Sharell en ik altijd terecht in Oudkarspel en (tijdens onze gezamenlijke vakantie) in Oostenrijk. Het was gezellig om samen uiteenlopende spelletjes te doen en om op de bank met zijn allen samen frietjes te eten. Ook **Teddy** verdient hierbij vermelding, een grote meneer (in omvang althans) die weliswaar minder vaak kopjes geeft dan James, maar toch minstens zo lief is, vooral als zijn etensbakje leeg is.

Mijn zus **Saskia** stond altijd voor me klaar als ik hulp nodig had en ze heeft me ontelbare keren (van jongs af aan) geholpen met praktische zaken. Zij weet ook hoe het is om te promoveren en ik bewonder haar verrichtingen in de wetenschap. In mijn laatste jaar kwam **Jimi** haar vergezellen, met wie zij inmiddels samenwoont in het pittoreske Amsterdam.

Aan **Han** en **Margreeth**: het is altijd lastig om je ouders te bedanken voor alles wat ze voor je hebben gedaan, maar hierbij toch een poging. Jullie weten gelukkig allebei wat het is om onderzoek te doen en hebben mij altijd hierin gesteund. Het was fijn om, in de woorden van Saskia, een plek te hebben in Eindhoven waar we altijd langs mochten komen. Ook ben ik blij dat ik de familietraditie heb mogen hooghouden om promotieonderzoek naar dunne tinbevattende laagjes te doen.

Als laatste wil ik **Sharell** bedanken, met wie ik inmiddels samenwoon. Je bent me altijd blijven steunen, ook al heeft het schrijfproces van deze scriptie veel geduld van jouw kant gekost. Het is ontzettend fijn om zoveel tijd met je te mogen doorbrengen.